# The mineralogical and geochemical study of the Etosha meteorite from the North-West University collection


## S. Pretorius

orcid.org/0000-0002-0178-9192


Dissertation accepted in fulfilment of the requirements for the degree *Master of Science in Environmental Sciences* at the North-West University

| | |
|---|---|
| Supervisor: | Dr DM van Tonder |
| Co-supervisor: | Miss S Roopa |

Graduation May 2023

27228878

# ACKNOWLEDGEMENTS

The author would like to thank the following people for their contributions to this study:

Dr D.M. van Tonder and Ms S. Roopa, for their invaluable guidance, support and leadership for the duration of this study.

Mr L.C. Pheeha, for his guidance and assistance with the practical component of this study.

The NWU Bischoff geology museum, for providing access to the Etosha meteorite.

Dr C. Reinke at the University of Johannesburg, for his assistance with the SEM and EPMA.

Dr S. Verryn, at XRD Analytical and Consulting, for her assistance with the XRD.

Riana, at Stellenbosch University, for her assistance with the LA-ICP-MS.

Mr K. Oosthuisen and Mr M. Mashanyu, for their assistance with the cutting, polishing and other preparations of the meteorite samples.

Ms. L.C. Fourie (née Henderson) for her swift assistance with the language editing of this dissertation.

All my family and friends for their support.

Finally, my sincerest gratitude to my fiancée, Francois, for his never-ending support and love.

# ABSTRACT

The Etosha meteorite, which is part of the North-West University (NWU) collection, was found in 1970 in the Etosha National Park in Namibia. Although the meteorite has been described by previous researchers, its re-evaluation was crucial so as to be able to update the mineralogy, geochemistry and classification concerned, using modern analytical techniques. Meteorite geochemistry is very important, as it assists in understanding our solar system, which should lead to the expansion of knowledge regarding the previous and future biological and chemical evolutions that have taken place on Earth. Furthermore, the classification of meteorites is also crucial, as it enables the grouping of meteorites, and facilitates the associated understanding and description.

Polished sections of the Etosha meteorite were prepared and analysed, so as to be able to determine (1) the mineralogy and geochemistry through X-ray diffraction (XRD), portable X-ray fluorescence (pXRF) and laser ablation inductively coupled plasma mass spectrometry (LA-ICP-MS); (2) the petrographic characteristics through reflected light microscopy; and (3) the mineral chemistry through electron probe microanalysis (EPMA), as well as the classification of the Etosha meteorite. The results obtained in this study show that the Etosha meteorite contains 85-89 wt. % Fe, 5-7,8 wt. % Ni with minor amounts (± 9 wt. %) of P, Co, Cu, Cr, S and other elements. The Etosha meteorite is comprised of kamacite (α-FeNi), taenite (ɣ-FeNi), cohenite ($Fe_3C$), schreibersite ($(Fe,Ni)_3P$) , rhabdite ($(Fe,Ni)_3P$), magnetite ($Fe_3O_4$) and a possible iron phosphate. The average kamacite bandwidth is approximately 2,35 mm, classifying the meteorite as a coarse octahedrite, which does not correspond with the findings made in previous studies that classified it as a medium octahedrite. The Ga (57,01 ppm), Ge (189,77 ppm) and Ni concentrations classified the Etosha meteorite chemically as an IIAB iron meteorite.

Sub-Saharan Africa hosts many different meteorites, with the majority of meteorite discoveries having occurred in the north-western, southern and eastern parts of the region. The total mass per country, as well as the number of finds made, corresponds with this trend. Chondrites are the most common meteorite discovered, with achondrites, irons and stony-irons being second, third and fourth most common, respectively speaking. The Etosha meteorite was identified as one of eight IIAB iron meteorites found in the region, with three of the meteorites being discovered in Southern Africa, with the closest to the Etosha meteorite being the Okahandja meteorite (Namibia), with two meteorites having been discovered in South Africa, namely the Kopjes Vlei meteorite and the Hex River Mountains meteorite.

**Key terms:** Etosha meteorite, mineralogy and geochemistry, iron meteorite, coarse octahedrite, IIAB meteorite

# OPSOMMING

Die Etosha meteoriet is in 1970 ontdek in die Etosha Nasionale Park, geleë in Namibië en is tans deel van die Noord Wes Universiteit (NWU) se versameling. Hierdie meteoriet is beskryf deur vorige navorsers, maar 'n herevaluering was dringend nodig vir die opdatering van die mineralogie, geochemie asook klassifikasie van die meteoriet deur moderne analitiese tegnieke. Meteoriet geochemie is baie belangrik omdat dit help om die sonnestelsel beter te verstaan, wat kan lei tot meer kennis oor die vorige en toekomstige biologiese en chemiese evolusie van die Aarde. Verder, meteoriet klassifikasie is noodsaaklik omdat dit meteoriete groepeer en dit dan makliker maak om te verstaan en te beskryf.

Gepoleerde plaatjies van die Etosha meteoriet was voorberei en geanaliseer om (1) die mineralogie en geochemie deur middel van X-straal diffraksie (XRD), draagbare X-straalfluoressensie (pXRF) en Laser Ablasie Induktiewe Gekoppelde Plasmamassaspektrometrie LA-ICP-MS, (2) petrografiese eienskappe deur gereflekteerde lig mikroskopie, en (3) die mineral chemie deur Elektronsonde Mikro-analise (EPMA) asook die klassifikasie van die meteoriet te bepaal. Die resultate het gewys dat die Etosha meteoriet 85-89 wt. % Fe, 5-7,8 wt. % Ni en geringe hoeveelhede (± 9 wt. %) van P, Co, Cu, Cr, S en ander elemente bevat. The Etosha meteoriet bestaan uit kamasiet, taeniet, koheniet, schreibersiet, rhabdiet, magnetiet en ook n moontlike yster fosfaat. Die gemiddelde kamasiet bandwydte is ongeveer 2,35 mm, wat die meteoriet klassifiseer as n growwe oktahedriet, wat nie ooreenstem met vorige studies wat dit geklassifiseer het as 'n medium oktahedriet nie. Die Ga (57,01 ppm), Ge (189,77 ppm) en Ni konsentrasies klassifiseer die Etosha meteoriet chemies as 'n IIAB yster meteoriet.

Sub-Sahara Afrika bevat baie meteoriet ontdekkings, waarvan die meerderheid van die ontdekkings in die noordwestelike, suidelike asook oostelike areas voorkom. Die totale massa per land, asook die hoeveelheid vondse per land stem ooreen met hierdie neiging. Kondriete is die mees algemene meteoriet ontdek, terwyl akondriete, ysters en kondriet-ysters tweede, derde en vierdie meeste ontdek was. Die Etosha meteoriet was geïdentifiseer as een van agt IIAB yster meteoriete in sub-Sahara Afrika, met die Okahandja meteoriet (Namibië), en die twee meteoriete van Suid-Afrika, naamlik die Kopjes Vlei meteoriet en Hex River Mountains meteoriet wat naby aan die Etosha meteoriet gevind is.

**Sleutelterme:** Etosha meteoriet, mineralogie en geochemie, yster meteoriet, growwe oktahedriet, IIAB meteoriet

# TABLE OF CONTENTS

**ACKNOWLEDGEMENTS** ..... **I**

**ABSTRACT** ..... **II**

**OPSOMMING** ..... **I**

**LIST OF TABLES** ..... **VII**

**LIST OF FIGURES** ..... **IX**

**LIST OF ABBREVIATIONS** ..... **XV**

**LIST OF MINERAL NAMES AND THEIR CHEMICAL FORMULAS** ..... **XVII**

**CHAPTER 1 INTRODUCTION** ..... **1**

**1.1 Background** ..... **1**

**1.2 Problem statement** ..... **4**

**1.3 Research hypothesis** ..... **5**

**1.4 Research aims and objectives** ..... **5**

**1.5 Structure of the dissertation** ..... **5**

**CHAPTER 2 LITERATURE REVIEW** ..... **7**

**2.1 Introduction** ..... **7**

**2.2 Origin of meteorites** ..... **7**

**2.3 Meteorite classification and nomenclature** ..... **9**

2.3.1 Chondrites ..... 11

2.3.2 Differentiated meteorites ..... 14

2.3.2.1 Achondrites ..... 14

2.3.2.2 Martian meteorite clan ..... 14

2.3.2.3 Lunar meteorite clan ..... 15

2.3.2.4 Stony-iron meteorites ..... 15

2.3.2.5 Iron meteorites ..... 16

**2.4 Common and accessory minerals in meteorites ..... 16**

2.4.1 Minerals in iron meteorites ..... 17

**2.5 Iron meteorites ..... 22**

2.5.1 Chemical classification of iron meteorites ..... 22

2.5.2 Structural classification of iron meteorites ..... 24

2.5.2.1 Acid etching of iron meteorites ..... 25

2.5.2.2 Main and secondary structures ..... 25

2.5.3 Surface shapes and structures ..... 32

**2.6 Alternative classification schemes for meteorites ..... 34**

**2.7 The Etosha meteorite ..... 35**

**2.8 Sub-Saharan African meteorites ..... 36**

**CHAPTER 3 METHODS AND MATERIALS ..... 38**

**3.1 Introduction ..... 38**

**3.2 Sample preparation ..... 38**

3.2.1 Acid etching ..... 39

**3.3 Analytical methods ..... 40**

3.3.1 SEM ..... 40

3.3.2 EMP analysis ..... 41

3.3.3 RL microscopy ..... 42
3.3.4 pXRF ..... 43
3.3.5 XRD ..... 45
3.3.6 ICP-MS ..... 46
**3.4 Data analyses ..... 48**
3.4.1 EPMA ..... 48
3.4.2 SEM ..... 49
3.4.3 Reflected light (RL) microscopy ..... 49
3.4.4 pXRF ..... 49
3.4.5 XRD ..... 50
3.4.6 ICP-MS ..... 50
3.4.7 Sub-Saharan meteorite distribution (type, classification and locality) ..... 50
3.4.8 GIS ..... 51

**CHAPTER 4 RESULTS AND DISCUSSION ..... 52**
**4.1 Introduction ..... 52**
**4.2 Macroscopic description of Etosha meteorite ..... 52**
**4.3 Mineralogy and petrography of the Etosha meteorite ..... 57**
4.3.1 XRD ..... 57
4.3.2 Reflected light (RL) microscopy ..... 60
**4.4 Mineral chemistry of the Etosha meteorite ..... 65**
4.4.1 EPMA ..... 65
4.4.2 SEM ..... 70

**4.5 Geochemistry of the Etosha meteorite ..... 78**

4.5.1 pXRF ..... 78

4.5.2 ICP-MS ..... 80

**4.6 Classification of the Etosha meteorite ..... 82**

4.6.1 Structural classification ..... 83

4.6.2 Chemical classification ..... 85

**4.7 SSA meteorite statistics in terms of the Etosha meteorite ..... 88**

4.7.1 Meteorite types ..... 88

4.7.2 Frequency of meteorite discoveries ..... 89

4.7.3 Frequency of meteorite falls and finds ..... 90

4.7.4 Types of iron meteorites found ..... 90

4.7.5 Type of meteorite discovered versus its mass ..... 91

4.7.6 GIS ..... 92

**CHAPTER 5 CONCLUSIONS AND RECOMMENDATIONS ..... 100**

**5.1 Surface structures, mineralogy, and geochemistry of the Etosha meteorite ..... 100**

**5.2 Classification of the Etosha meteorite ..... 101**

**5.3 Sub-Saharan African meteorites and the Etosha meteorite ..... 102**

**5.4 Recommendation for further studies ..... 103**

**BIBLIOGRAPHY ..... 104**

**APPENDICES ..... 112**

**1.1 EPMA data ..... 112**

**1.2 pXRF data ..... 121**

**1.3 LA-ICP-MS data..... 125**

**1.4 Statistical data for SSA meteorites ..... 132**

# LIST OF TABLES

Table 2-1: Postulated asteroidal parent body types of most common meteorites found on Earth (Burbine *et al.*, 2002:660-663) ..... 8

Table 2-2: Petrogenetic associations of Hutchison (2004:415) that describe the origin and possible associations with parent bodies and with other types of meteorites ..... 10

Table 2-3: Chemical groups and structural classification of iron meteorites adapted from Buchwald (1977:456), with some well-known examples of the different iron meteorite types..... 23

Table 2-4: Description of the Ga (ppm) and Ge (ppm) content represented by the different Roman numerals seen in the classification of iron meteorites (Table 2-2) (Wasson, 1967:162)..... 24

Table 2-5: The structural classification of iron meteorites based on kamacite bandwidth (mm), adapted from Buchwald (1975c:66) ..... 24

Table 2-6: Meteorite shapes which have been previously mentioned and discussed in the literature, with examples of meteorites which display the characteristic shapes (Buchwald, 1975c:46) ..... 33

Table 2-7: SSA countries without available data on the date of data collection (17 October 2021) on the Meteoritical Bulletin Database (2021) ..... 37

Table 3-1: Column conditions of the CAMECA sx100 electron microprobe during analysis ..... 42

Table 3-2: Information regarding the type of ICP-MS instrument used, as well as the settings that were used for the analysis of the Etosha meteorite ..... 47

Table 3-3: Information regarding the type of laser ablation instrument used along with the ICP-MS instrument, as well as the settings that were used for the analysis of the Etosha meteorite ..... 47

Table 4-1: Mineral names and stoichiometric formulas obtained through XRD analysis, along with its occurrence in the Etosha meteorite ..... 58

Table 4-2: Average values of the pXRF data obtained (spot analysis data) of the Etosha meteorite, compared with the XRF results of Frick and Viljoen (1973:347) of the Etosha meteorite ..... 79

Table 4-3: LA-ICP-MS data obtained of the Etosha meteorite, which can be found in Appendix C ..... 81

Table 4-4: Structural classification of the Etosha meteorite based on the width of the kamacite bands, applied to both sample A and sample B by using two different methods, Buchwald (1975c:66) and Goldstein (1965:6), from the literature ..... 84

Table 4-5: Average Ni, Ga, Ge and Ir concentrations obtained by LA-ICP-MS in this study of the Etosha meteorite and historical concentrations from Wasson (1967:162), for purposes of chemical classification ..... 85

Table 4-6: Elemental abundance of Ni, Ga, Ge and Ir of the Etosha meteorite compared to other chemically similar IIAB meteorites (Okahandja – Namibia, Kopjes Vlei – South Africa, Hex River Mountains – South Africa)..... 87

Table 4-7: Meteorites of SSA that do not have coordinates of the location they were discovered in recorded (Meteoritical Bulletin Database, 2021) ..... 93

# LIST OF FIGURES

Figure 1-1: Terminologies for the different stages of a meteoroid falling to Earth, from being a meteoroid, to meteor, to fireball and ultimately to meteorite when it hits the Earth's surface, adapted from Ceplecha *et al.* (1998:330)..... 1

Figure 1-2: Chloropleth map compiled from the Meteoritical Bulletin Database (2021) for meteorites found in Africa, specifically in the SSA region, also showing the countries which have no data as well as countries which forms part of the Sahara Desert (Environmental Systems Research Institute (ESRI), 2020). With the added ★ referring to the discovery location of the Etosha meteorite. ..... 3

Figure 2-1: Meteorite classification diagram, adapted from Weisberg et al. (2006:21) and Hutchison (2004:244) explaining the different meteorites in terms of the different types as well as their subtypes that can be found on the Earth. MES = mesosiderite; PAL = pallasite; MG PAL = main-group pallasite; ES PAL = Eagle Station pallasite; PP PAL = pyroxene pallasite; SHE = shergottite; NAK = nakhlite; CHA = chassignite; OPX = orthopyroxenite; EUC = eucrite; DIO = diopside; HOW = howardite; ACA = acapulcoite; LOD = lodranite; WIN = winonaite; ANG = angrite; AUB = aubrite; URE = ureilite; BRA = brachinite. The different chondrite subtype abbreviations are explained in the text. ..... 13

Figure 2-2: An example of the Widmanstätten structure (kamacite – taenite intergrowth) which is a characteristic structure of iron meteorites, evident in a Gibeon meteorite (Tatum, 2019:2978). ..... 27

Figure 2-3: Fe-Ni two phase diagram, where α = kamacite and ɣ = taenite, adapted from Goldstein (1965:18), which explains the formation of kamacite and taenite with the decrease in temperature. ..... 27

Figure 2-4: Iso-Ni concentration at 8,5 wt. % Ni from the Fe-Ni-P ternary phase diagram showing the formation paths of three different alloys with decreasing temperature. $M_S$ = Martensite start temperature; a, b, c = alloys with different P contents; α= kamacite; ɣ = taenite and Ph = phosphide, $[FeNi]_3P$. Open circles represent data from Doan and Goldstein (1970), adapted from Yang and Goldstein (2005:242). ..... 29

Figure 2-5: The formation of the Widmanstätten structure, using the fifth mechanism explained by Yang and Goldstein (2005:245). The left side displays the microstructural development, and the right side displays the Ni profiles in kamacite and taenite, as the alloy cools down. $T_1$-$T_7$ shows different temperatures during cooldown, adapted from Yang and Goldstein (2005:245). Where α = kamacite and ɣ = taenite. ..... 31

Figure 3-1: Front view of the Etosha meteorite located in the Andries Bischoff meteorite at the NWU. Scale = 15 cm. ..... 38

Figure 3-2: Plotted points on sample A and sample B that was analysed with the NITON XL3t GOLDD+ XRF spectrometer. Scale = 10 mm. ..... 44

Figure 4-1: Front view of the Etosha meteorite located in the Andries Bischoff meteorite at the NWU. Scale = 15 cm. ..... 52

Figure 4-2: (a) Back and (b) side view of the Etosha meteorite located in the Andries Bischoff meteorite at the NWU. Scale = 15 cm. ..... 53

Figure 4-3: Regmaglypts present on the Etosha meteorite located in the Andries Bischoff meteorite at the NWU. Scale = 15 cm. ..... 54

Figure 4-4: Base view of the Etosha meteorite located in the Andries Bischoff meteorite at the NWU. Scale = 15 cm. ..... 54

Figure 4-5: Two shallow grooves on of the Etosha meteorite located in the Andries Bischoff meteorite at the NWU. Scale = 15 cm. ..... 55

Figure 4-6: Deep holes in the side of the Etosha meteorite located in the Andries Bischoff meteorite at the NWU. Scale = 15 cm. ..... 55

Figure 4-7: Unknown flat surface on the Etosha meteorite located in the Andries Bischoff meteorite at the NWU. Scale = 15 cm. ..... 56

Figure 4-8: The old cut (above) and the new cut (below), made to obtain samples of the Etosha meteorite located in the Andries Bischoff meteorite at the NWU. Scale = 15 cm. ..... 56

Figure 4-9: Newly cut surface on the Etosha meteorite located in the Andries Bischoff meteorite at the NWU. Scale = 15 cm. ..... 57

Figure 4-10: XRD diffractogram showing the peak counts and position of the different minerals obtained from the Etosha meteorite. ..... 59

Figure 4-11: Reflected light photomicrographs of the polished Etosha meteorite. Unetched. A: Screibersite forming on the kamacite-kamacite grain boundary. B: A much more developed schreibersite grain that formed on the boundary between the kamacite and the taenite. C: Broken-up schreibersite grains in a kamacite matrix. D: Schreibersite grains with a rim of cohenite, which also enters the schreibersite grain, in a kamacite matrix. E: Another kamacite-kamacite boundary with minute, euhedral rhabdite crystals that formed in 120° angles, oriented parallel to the Widmanstätten structure. F: Fine rhabdite grains in a kamacite matrix. Kam = Kamacite: Tae = Taenite; Co = Cohenite; Sch = Schreibersite; Rha = Rhabdite. ..... 62

Figure 4-12: Reflected light photomicrographs of the polished Etosha meteorite. A: Typical $\alpha_2$ structure formed by extreme heat oxidation, unetched. B: Various stages of cooling seen through different mineral rims forming, unetched. C: Schreibersite grain with a cohenite rim in a kamacite matrix, unetched. D: Intergrowth of spheroidised plessite over a taenite grain in a kamacite matrix, unetched. E: Decomposed schreibersite grain in kamacite matrix, etched (1% nitric acid). F: Neumann bands in three directions present in the kamacite grain, etched (6% nitric acid). Kam = Kamacite; Tae = Taenite; Co = Cohenite; Sch = Schreibersite; Ples = Plessite. ..... 64

Figure 4-13: Fe-Ni-P ternary diagram, adapted from Korniyenko (2009:14), with the minerals obtained through the EPMA of the Etosha meteorite plotted, where αδ = kamacite; ɣ = taenite; $M_3P = (Fe,Ni)_3P$ – schreibersite and $M_2P=(Fe,Ni)_2P$ – allabogdanite. FV = Frick and Viljoen (1973:347). ..... 66

Figure 4-14: Binary diagram of Fe-Ni, showing the different minerals present in the Etosha meteorite, determined by EPMA. FV = Frick and Viljoen (1973:347). The correlation value (R) and the coefficient of determination ($R^2$) is also displayed on the diagram. ..... 67

Figure 4-15: Individual mineral chemistries obtained through EPMA of the minerals present in the Etosha meteorite in the current study. ..... 68

Figure 4-16: Individual mineral chemistries obtained by Frick and Viljoen (1973:347) of the minerals present in the Etosha meteorite. ..... 68

Figure 4-17: Trace element quantities of different minerals present in the Etosha meteorite, compared to the results of FV = Frick and Viljoen (1973:347)..... 68

Figure 4-18: Schreibersite mineral chemistry obtained by Frick and Viljoen (1973), compared to the three possible schreibersite mineral chemistries obtained in the current study of the Etosha meteorite. Sch = Schreibersite. ..... 69

Figure 4-19: Backscattered electron (BSE) micrograph of sample B, indicating the various areas selected for EDS, showing schreibersite and cohenite (fractured phase) – 'Selected area 4' & 'Selected area 5', kamacite (matrix) – 'Selected area 1' & 'Selected area 2' and taenite (bright phase) – 'Selected area 3' & 'EDS Spot 1'. ..... 72

Figure 4-20: Backscattered electron (BSE) micrograph of sample B, indicating the various areas selected for EDS, showing schreibersite (fractured phase) – 'Selected area 2' & 'Selected area 3', kamacite (matrix) – 'Selected area 1' and high Co taenite (bright phase) – 'EDS Spot 1'..... 72

Figure 4-21: SEM EDS spectrum analysis of sample B, showing the qualitative mineral chemistries of the selected areas highlighted in Figure 4-19, as well as the mineral chemistries of schreibersite - 'Selected area 5', cohenite – 'Selected area 4', kamacite – 'Selected area 1' & 'Selected area 2' and taenite – 'Selected area 3' & 'EDS Spot 1'. ..... 73

Figure 4-22: SEM EDS spectrum analysis of sample B, showing the qualitative mineral chemistries of the selected areas highlighted in Figure 4-20, as well as the mineral chemistries of schreibersite – 'Selected area 2' & 'Selected area 3', kamacite – 'Selected area 1' and high Co taenite – 'EDS Spot 1'.... 74

Figure 4-23: Backscattered electron (BSE) micrograph of sample B, indicating the various areas selected for EDS, showing the presence of schreibersite (fractured phase) – 'Selected area 1' and magnetite (black phase) – 'EDS Spot 1'. ..... 75

Figure 4-24: Backscattered electron (BSE) micrograph of sample B, indicating the various areas selected for EDS, showing the presence of schreibersite (fractured phase) – 'Selected area 1', with possible silicates. ..... 75

Figure 4-25: SEM EDS spectrum analysis of sample B, showing the qualitative mineral chemistries of the selected areas highlighted in Figure 4-23, showing the mineral chemistries of schreibersite – 'Selected area 1' and magnetite – 'EDS Spot 1'..... 76

Figure 4-26: SEM EDS spectrum analysis of sample B, showing the qualitative mineral chemistries of the selected areas highlighted in Figure 4-24, showing the mineral chemistry of schreibersite – 'Selected area 1'..... 77

Figure 4-27: Fe (wt. %) and Ni (wt. %) binary diagram with data obtained from pXRF analysis of the Etosha meteorite (Appendix B). The correlation (R) as well as coefficient of determination ($R^2$) values are indicated on the diagram..... 80

Figure 4-28: Ga (ppm) and Ge (ppm) binary diagram with LA-ICP-MS data of the Etosha meteorite plotted (Appendix C) with the correlation (R) and the coefficient of determination ($R^2$) indicated on the diagram..... 82

Figure 4-29: Polished sections of (a) sample A, etched with 1% nitric acid (displaying a schreibersite vein), and (b) sample B, etched with 6% nitric acid. Both sample A and sample B are displaying a Widmanstätten structure. Scale bar = 10 mm..... 83

Figure 4-30: Ni (wt. %) against Ga (ppm) chemical classification diagram, adapted from Scott and Wasson (1975:529) classifying the Etosha meteorite in the IIAB chemical class..... 86

Figure 4-31: Ni (wt. %) against Ge (ppm) chemical classification diagram, adapted from Scott and Wasson (1975:529) classifying the meteorite in the IIAB chemical class..... 86

Figure 4-32: Meteorite types found in SSA. Where the added ★ refers to the Etosha meteorite type..... 89

Figure 4-33: The years in which meteorites were discovered (from 1921-2021) in SSA. Where the added ★ refers to the year in which Etosha meteorite was discovered..... 89

Figure 4-34: Find and fall occurrences in SSA. Where the added ★ indicates that the Etosha meteorite was classified as a find..... 90

Figure 4-35: Iron meteorite types, according to chemical classification. MG = main group; sHL = high-Au, low-Ni subgroup; sLL = low-Au, low-Ni subgroup; sLM = low-Au, medium-Ni subgroup; ung = ungrouped; an = anomalous; Iron = iron meteorite not yet fully classified; Iron? = possible iron not yet classified (Meteoritical Bulletin Database, 2021). Where the added ★ indicates that the Etosha meteorite is classified as a IIAB iron meteorite. .... 91

Figure 4-36: Type of meteorites found versus their average mass. Where the added ★ shows the mass of the Etosha meteorite at 111 kg. ..... 92

Figure 4-37: Map of the different meteorite types distributed over SSA (Environmental Systems Research Institute (ESRI), 2020), with the added ★ showing that the Etosha meteorite is an iron meteorite discovered in Namibia..... 94

Figure 4-38: Occurrence of different meteorite types per country (Environmental Systems Research Institute (ESRI), 2020), with the added ★ showing that the Etosha meteorite is an iron meteorite discovered in Namibia. ..... 95

Figure 4-39: Map of total mass (kg) of meteorites discovered per country (Environmental Systems Research Institute (ESRI), 2020), with the added ★ indicating that the Etosha meteorite was discovered in Namibia which displays a total mass of between 16001 and 86000 kg. ..... 96

Figure 4-40: Falls and finds in SSA per country (Environmental Systems Research Institute (ESRI), 2020), with the added ★ showing that the Etosha meteorite was discovered in Namibia which is dominated by finds. ..... 98

Figure 4-41: Iron meteorite types, similar to the Etosha meteorite, found in SSA (Environmental Systems Research Institute (ESRI), 2020), with the added ★ showing that the Etosha meteorite was discovered in the same country as the Okahandja meteorite. ..... 99

# LIST OF ABBREVIATIONS

| | |
|---|---|
| BSE | backscattered electron |
| C chondrite | carbonaceous with letter identifying type (I – Ivuna, M - Mighei, O - Ornans, V - Vigarano, K - Karoonda, R - Renazzo, B – Bencubbin, H – High metal) |
| CEMS | conversion electron Mössbauer spectroscopic |
| CMOS | complementary metal oxide semiconductor |
| EDS | energy dispersive spectrometer |
| EPMA | electron probe microanalysis |
| GIS | geographic information system |
| HED | howardite-eucrite-diogenite |
| I | intensity |
| ICP-MS | inductively coupled plasma mass spectrometry |
| LA-ICP-MS | laser ablation inductively coupled plasma mass spectrometry |
| LiF | lithium fluoride |
| LLiF | large lithium fluoride |
| LOD | limit of detection |
| LPET | large pentaerythritol |
| MORBs | mid-ocean ridge basalts |
| NWA | North-West Africa |
| NWU | North-West University |
| PET | pentaerythritol |
| POL | polarising |

| | |
|---|---|
| PU vir CHO | Potchefstroomse Universiteit vir Christelike Hoër Onderwys |
| pXRF | portable X-ray fluorescence |
| REE | rare earth elements |
| RL | reflected light |
| SDD | silicon drift detector |
| SEM | scanning electron microscopy |
| SNC | shergottites-nakhlites-chassignite |
| SSA | sub-Saharan Africa |
| TAP | thallium acid phthalate |
| WDS | wavelength dispersive spectrometer |
| XRD | X-ray diffraction |
| XRF | X-ray fluorescence |

# LIST OF MINERAL NAMES AND THEIR CHEMICAL FORMULAS

| | |
|---|---|
| kamacite | α-(FeNi) |
| taenite | ɣ-(FeNi) |
| schreibersite | $(Fe,Ni)_3P$ |
| rhabdite | $(Fe,Ni)_3P$ |
| cohenite | $Fe_3C$ |
| magnetite | $Fe_3O_4$ |
| enstatite | $MgSiO_3$ |
| troilite | FeS |
| pyroxene | $(Ca,Na)(Mg,Fe,Al)(Si,Al)_2O_6$ |
| olivine | $(Mg,Fe)_2SiO_4$ |
| plagioclase | $(Na,Ca)[(Si,Al)Al,Si_2]O_8$ |
| chromite | $FeCr_2O_4$ |
| diamond, graphite | C |
| kirschsteinite | $CaFe^{2+}SiO_4$ |
| daubréelite | $FeCr_2S_4$ |
| haxonite | $(Fe,Ni,Co)_{23}C_6$ |
| carlsbergite | CrN |

# CHAPTER 1 INTRODUCTION

## 1.1 Background

Asteroids can be described as planetesimals or small natural bodies that follow their own elliptical orbit around the Sun, taking about three to six years to complete their orbit (Gaffey *et al.*, 1993:162; Glikson & Pirajno, 2018:2). When an asteroid disintegrates, the fragments that travel to Earth are called meteoroids (Bischoff, 2001:769), as can be seen in Figure 1-1. As soon as the meteoroid enters the atmosphere of the Earth, it is heated through friction by the air particles present, which leads to the illumination of the meteoroid (Ceplecha *et al.*, 1998:329). When it is illuminated, the phenomenon is called a 'meteor', and when the illumination results in a brighter phenomenon than before, it is called a 'meteoric fireball' (Ceplecha *et al.*, 1998:329). When the meteoroid reaches the surface of the Earth, it is termed a meteorite, such as in Figure 1-1.

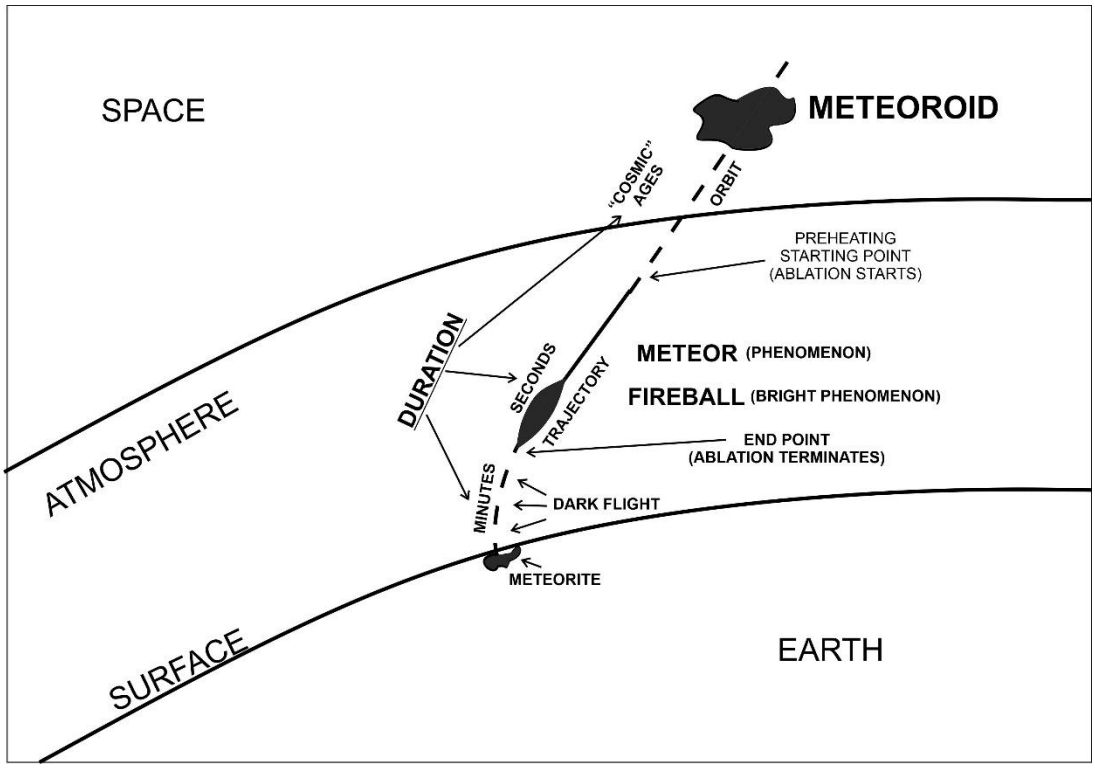


**Figure 1-1: Terminologies for the different stages of a meteoroid falling to Earth, from being a meteoroid, to meteor, to fireball and ultimately to meteorite when it hits the Earth's surface, adapted from Ceplecha *et al.* (1998:330).**

Meteorites were previously referred to as solid items that reach the Earth's surface from outer space, but this definition of meteorites is no longer valid (Rubin & Grossman, 2010:114). Although Ouknine *et al.* (2019:1) state that meteorites can be defined as "*extra-terrestrial rocks that strike*

*the Earth's surface*", Dunn (2012:1) defines them as "*fragments of planetary objects, most often of asteroids, that have broken off of their parent bodies and made their way to Earth*". Rubin and Grossman (2010:114) provide the most comprehensive and explanatory definition of a meteorite. Their definition states:

> *A meteorite is a natural, solid object larger than 10 μm in size, derived from a celestial body, that was transported by natural means from the body on which it formed to a region outside the dominant gravitational influence of that body and that later collided with a natural or artificial body larger than itself (even if it is the same body from which it was launched).*

According to Weisberg *et al.* (2006:19), the correct classification of meteorites is crucial, as such classification clusters meteorites together, which makes them easier to understand and quantify. The first and very important classification of a meteorite requires determining whether the meteorite is a 'find' or a 'fall'. According to Weisberg *et al.* (2006:20), this determination is very important, because the total amount of time that a meteorite spends on the Earth's surface determines the amount of chemical interaction that occurs with the Earth's elements. The interaction, in turn, influences the chemistry recorded when found, as a 'find' tends to show different results to those that are expected from a 'fall' (Weisberg *et al.*, 2006:20). Therefore, determining the geochemistry and mineralogy of meteorites is very important in meteoritical studies, for determining the evolution and classifications involved. Using geochemistry and mineralogy, thousands of meteorites around the world have been classified, especially on the African continent. The African continent is one of the "meteorite hot-spots", as one-sixth of the world's meteorites are on this continent (Ouknine *et al.*, 2019:1).

The Sahara region of the African continent has been proven to provide exceptional circumstances for the recovery of meteorites (Bischoff & Geiger, 1995:113). Meteorites found in the Sahara, as well as on the African continent, have been thoroughly studied in fairly recent research (e.g. Bevan (2006); Bischoff and Geiger (1995); Khiri *et al.* (2017); Ouknine *et al.* (2019)). However, the region south of the Sahara, specifically, has not received the same amount of attention, although it also presents some important occurrences of meteorites. The sub-Saharan Africa (SSA) region consists of every country on the African continent, excluding Morocco, Algeria, Tunisia, Libya and Egypt (Ouknine *et al.*, 2019:5), which can be seen in Figure 1-2. It can, thus, be seen in Figure 1-2 that the southern and north-western parts of the SSA have presented the largest number of meteorites, while moderate to small amounts of meteorites have been found in the central and eastern parts of the region.

Mauritania displays the largest number of meteorites (with 146 meteorites having been found in the country), and Niger having the second most meteorites (with 77 meteorites having been found in the country), as can be seen in Figure 1-2, which shows the distribution of meteorites across Africa. Some countries (e.g. Mozambique) lacked data when the current data was extracted.

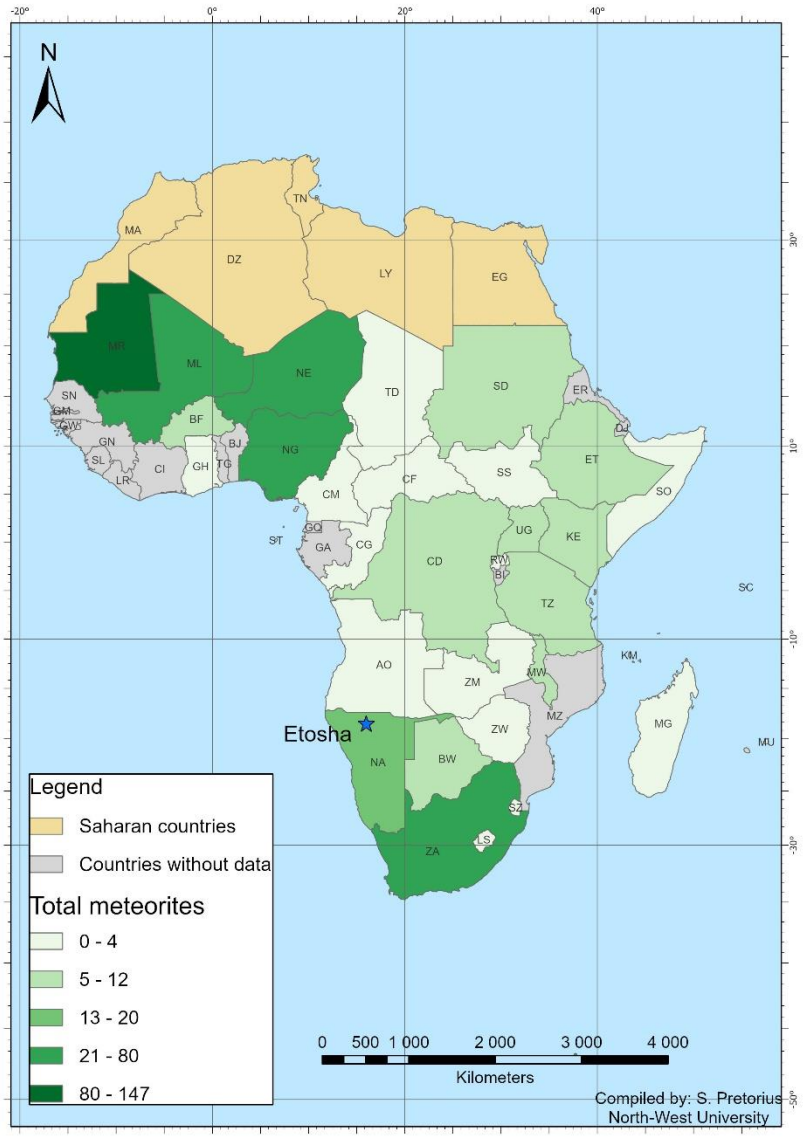


**Figure 1-2: Chloropleth map compiled from the Meteoritical Bulletin Database (2021) for meteorites found in Africa, specifically in the SSA region, also showing the countries which have no data as well as countries which forms part of the Sahara Desert (Environmental Systems Research Institute (ESRI), 2020). With the added ★ referring to the discovery location of the Etosha meteorite.**

South Africa is the country in SSA with the third most meteorites found (47 in all) (Meteoritical Bulletin Database, 2021). The reason for the high number of meteorites might be due to the large size of the country, as well as to the uniform distribution of the population of South Africa (Khiri *et al.*, 2017:653). In South Africa's neighbouring country, Namibia, 18 meteorites in total have been

found (Meteoritical Bulletin Database, 2021). Namibia is a country that is well known by meteorite scientists, as it hosts the largest and heaviest meteorite ever found, namely the Hoba meteorite (Beech, 2013:15), with a weight of 60 000 kg (or 60 tons) (Meteoritical Bulletin Database, 2021). Another neighbouring country of South Africa, Botswana, has discovered a total of 12 meteorites within its borders (Meteoritical Bulletin Database, 2021). One of the meteorites (Motopi Pan) concerned was the second meteorite ever to be observed in space, on its way to Earth (Jenniskens *et al.*, 2021:4). The phenomenon led researchers directly to the area where it fell, over the area of the Central Kalahari Game Reserve (Jenniskens *et al.*, 2021:4).

### 1.2 Problem statement

According to Dunn (2012:2), meteorites provide insight into the chemistry of the early solar system, which might help scientists improve their understanding of the previous and future chemical and biological evolution of the Earth, as the meteorites concerned can possibly contain the type of environment in which the solar system formed. One of the collections in the Geology Department (Andries Bischoff Geology Museum) of the North-West University (NWU) is a meteorite that is referred to as the Etosha meteorite, named after the Etosha National Park in Namibia, where it was found. The Etosha meteorite was collected and transported from Namibia to the NWU (then the Potchefstroomse Universiteit vir Christelike Hoër Onderwys (PU vir CHO)) in 1970 (Buchwald, 1975b:1384; Frick & Viljoen, 1973:345), where it was first studied by Frick and Viljoen in 1973. Although Frick and Viljoen (1973) investigated the petrography and chemistry of the Etosha meteorite, they did not investigate the trace elements present in the meteorite. The meteorite was classified in early sources as an octahedrite, but the classification of the type of octahedrite has differed, as Frick and Viljoen (1973:345) classified it as a medium octahedrite, while Frick and Hammerbeck (1973:16) classified it as a coarse octahedrite. The circumstances of its fall, as well as of its exact location, remain unknown (Buchwald, 1975b:1384). The investigation of the trace elements could lead to a further classification of the meteorite (Lombard, 2010:9), especially of the concentrations of Germanium (Ge), Gallium (Ga) and Iridium (Ir) contained therein (Gemelli *et al.*, 2014:57).

Weisberg *et al.* (2006:44) highlighted the importance of continuous research and of reclassifications of meteorites, mainly because such endeavour should assist in obtaining enhanced understanding of the evolution of meteorites and, in turn, of the evolution of the Earth. In recent work, conducted by Gemelli *et al.* (2014), Khiri *et al.* (2017) and Ouknine *et al.* (2019), the use of modern and advanced analytical methods and techniques has proved capable of

revealing additional information that can be used to determine the evolution and classification of meteorites. The statistics available on meteorite types and localities in the SSA region are few, due to the emphasis of the past having mainly been given to meteorites found in the Sahara Desert (Ouknine *et al.*, 2019:1) and in North-West Africa (NWA) (Ouknine *et al.*, 2017:29). Furthermore, following a preliminary investigation completed by Frick and Viljoen (1973), the need for the re-examination of the Etosha meteorite arose, which is the reasoning behind the current study.

### 1.3 Research hypothesis

If new geochemical and mineralogical data for the Etosha meteorite from the NWU collection is generated and evaluated, then the meteorite could be reclassified, based on structural and chemical schemes, making it possible to place the Etosha meteorite in the context of the distribution of meteorite types and locations in SSA.

### 1.4 Research aims and objectives

The aims of the present study are (1) to re-evaluate the mineralogy and geochemical characteristics of the Etosha meteorite, using modern analytical techniques, and (2) to classify and compare the Etosha meteorite to SSA meteorites.

The objectives to satisfy the research are to:

- investigate the meteorite occurrences of SSA, in terms of their type, classification and locality;
- investigate the mineralogy and geochemistry of the Etosha meteorite, so as to be able to determine the classification thereof; and
- compare the Etosha meteorite with the SSA meteorites already found.

### 1.5 Structure of the dissertation

This section provides a brief overview and description of the content of each chapter in this dissertation. The outline of this research study is as follows:

**Chapter 1** – The first chapter has provided a background to the study, by means of examining important definitions, and by means of providing the information required fully to comprehend the results and discussion that will be provided in Chapter 4.

**Chapter 2** – This chapter reviews the literature concerning the research topic. This review provides a comprehensive overview of all types of meteorites, but specifically focuses on iron meteorites. The common mineralogy, geochemistry, possible origin, textures and structures of iron meteorites are reviewed. Published literature on the Etosha meteorite is discussed, and a short review of the meteorites in SSA is provided.

**Chapter 3** – The sample preparation techniques, as well as the methods of analysis used in the study, are discussed in this chapter. The methods include the use of analytical techniques, X-ray diffractrometry (XRD), electron probe microanalysis (EPMA), portable X-ray fluorescence spectrometry (pXRF), inductively coupled plasma mass spectrometry (ICP-MS), scanning electron microscopy (SEM), reflected light (RL) microscopy and geographic information system (GIS).

**Chapter 4** – This chapter presents and discusses the results of the study, including historical data on meteorites in the SSA region. The results are presented in tables and graphs, photomicrographs as well as BSE images.

**Chapter 5** – This chapter provides the conclusions of the study, as well as recommendations for future studies.

# CHAPTER 2 LITERATURE REVIEW

## 2.1 Introduction

The first meteorite to have been analysed inside a laboratory dates back to the late 1760's in France, where they concluded that the meteorite did not fall from the sky, but, rather, that it was a sandstone that had been struck by lightning (Lombard, 2010:1). Around the 1800's, meteorites were first seen as extra-terrestrial objects that fell out of the sky (Khiri *et al.*, 2017:644). Since then, the number of meteorite discoveries has increased almost exponentially (Bevan, 2006:325; Bischoff, 2001:770; Khiri *et al.*, 2017:644; Ouknine *et al.*, 2017:29).

To fully understand the results to be generated, a few concepts must be discussed. These include the origin of meteorites, the classification and nomenclature of meteorites, the nature of iron meteorites and the related chemical and structural classification schemes, the common mineralogy of meteorites, and, lastly, the alternative classification schemes that may be used in their description. Next, the literature and knowledge pertaining to the Etosha meteorite will be discussed. The number of meteorites found in the sub-Saharan region of Africa, as well as the spatial distribution thereof, will also be reviewed.

## 2.2 Origin of meteorites

According to Glikson and Pirajno (2018:xvii) and Dunn (2012:2), the meteorites found on Earth originate from the main asteroid belt between Mars and Jupiter, as well from the comets in the Kuiper belt. Bischoff (2001:769) states that some meteorites might also originate from Mars and the Moon. According to Dunn (2012:17), there are approximately around 100 to 200 different parent bodies from which meteorites could originate. The assumed number of parent bodies is quite small in comparison to the total number of asteroids (approximately 600 000) present in the main belt (Dunn, 2012:17). Over half of the main asteroid belt between Jupiter and Mars consists of large asteroids, like Ceres (950 km in diameter), Vesta (530 km in diameter), Pallas (530-565 km in diameter) and Hygiea (350-500 km in diameter). Over 200 asteroids have a diameter of 100 km or more, with 700 000 to1 700 000 asteroids exceeding a diameter of 1 km (Glikson & Pirajno, 2018:4). The parental bodies, or their fragments, are generally considered to have formed in the main asteroid belt, which is assumed to be the source of most meteorites. They remained there for billions of years before being displaced as a result of a combination of collisions and thermal forces (Bottke *et al.*, 2006:821).

Asteroids are identified as parent bodies by means of analysing their spectral reflectance, as each known mineral has a specific wavelength that can be identified in the visible and near-infrared spectrum. The asteroids are grouped into specific groups, due to their visual albedo, as well as their visible spectra which can be used to group the meteorites. This is done by means of analysing the mineralogy of the meteorites, and by comparing that with the results obtained from the asteroid spectral reflectance (Burbine *et al.*, 2002:659).

Burbine *et al.* (2002:658) state that, within the approximately 100 different parent bodies that can be identified, 27 are chondritic (undifferentiated meteorites with composistions close to those of the Sun), ten are iron groups, six are differentiated achondritic (chondrites without chondrules), four are stony-iron, two are primitive achondritic and 50 are ungrouped irons. However, they also state that the presumed relationships between the ungrouped irons could lead to an approximate total of 150 parent bodies (Burbine *et al.*, 2002:658).

Meteorites most commonly originate from three different general types of asteroids, namely Carbonaceous or C-type chondrites, Siliceous or S-type asteroids and Metallic or M-type asteroids. The C-type chondrites, which occur on the outer regions of the main asteroid belt, have a very low albedo. These chondritic asteroids consist of a chemistry that closely resembles that of the sun, except for the volatile H and He. The S-type asteroids, which can be found in the inner part of the asteroid belt, display a high albedo. The asteroids concerned have a composition of metallic Fe that is mixed with Mg- and Fe-silicates. Also, various degrees of segregation and melting of metal from the silicates exists. Lastly, the M-type asteroids occupy the middle part of the main asteroid belt, have a high albedo and consist of metallic Fe. Each of the asteroid types involved constitutes a certain percentage of meteorites that fall to Earth. The C-type asteroids constitute over 75% of the known meteorites on Earth, while the S-type asteroids constitute approximately 17% of the meteorites on Earth (Glikson & Pirajno, 2018:4). Details of the most common meteorites, together with their associated parent bodies, are presented in Table 2-1.

**Table 2-1: Postulated asteroidal parent body types of most common meteorites found on Earth (Burbine *et al.*, 2002:660-663)**

| Meteorite class | Asteroid type |
|---|---|
| Ordinary chondrites | S-type asteroids |
| CM chondrites | C-type asteroids |
| HED meteorites | 4 Vesta asteroid |
| Iron meteorites, Enstatite chondrites | M-type asteroids |

## 2.3 Meteorite classification and nomenclature

Meteorite classification systems group similar meteorites, allowing researchers to communicate their results, based on a standardised nomenclature. The terminology applied in the classification of meteorites has evolved over time, although it has not always been consistently applied (Weisberg *et al*., 2006:20). Meteorites are usually given a name according to the location where the meteorite was found, or according to the name of the nearest post office, if the location lacks a name (Lombard, 2010:2; Weisberg *et al.*, 2006:20). When a meteorite is found in a desert area, like Antarctica or the Sahara, it is usually given both a name (according to its location) and a number (including the year and the number of meteorite found in that same year) (Weisberg *et al.*, 2006:20). Ouknine *et al.* (2017) found that the naming system used in assigning meteorites found in North-West Africa the acronym 'NWA', together with an accompanying number, can, at times, negatively impact on the countries in which the meteorites are found, as they do not benefit from the socio-economic value that the meteorites would otherwise offer (Ouknine *et al.*, 2017:54).

If a meteorite is affected by terrestrial processes such as weathering and erosion, but the crucial and identifiable minerals and structures remain, it will still be considered a meteorite (Rubin & Grossman, 2010:114). A meteorite can lose its status when it collides with an object that is larger than itself, and become incorporated into the larger object, which is then classified as a 'meteorite' (Rubin & Grossman, 2010:114).

The traditional classification of meteorites, rather than linking meteorites based on genetic, chemical, or mineralogical similarities, was simply a convenient way of grouping meteorites into three overall categories. The categories were based on whether the meteorites were predominantly composed of rocky material (chondritic meteorites), metallic material (iron meteorites), or mixtures (stony-iron meteorites). The categories concerned, however, formed the base for more detailed classification, as the chondrites were traditionally divided differently to the way in which the iron meteorites were (Bischoff, 2001:771).

Currently, after meteorites have been classified as a 'find' or 'fall', they can be divided up into three different classes, namely differentiated/achondrite, primitive achondrites and undifferentiated/chondrite meteorites (Bischoff, 2001:771-772; Weisberg *et al.*, 2006:20). Classification is based on chemical composition, with further classification being based on optical observation that is undertaken to determine the textural and mineralogical variation, the weathering and shock grades and the weathering features involved. Differentiated meteorites are those igneous (iron, stony-iron and achondritic) meteorites that have experienced such high temperatures that they have, at least partially, melted, having, as a result, undergone extensive

geochemical differentiation. Such meteorites originated from differentiated parent bodies with a crust, mantle and core (Bischoff, 2001:772-773; Dunn, 2012:2-3). Undifferentiated (chondrite) meteorites can be defined as meteorites originating from primitive or undifferentiated parent bodies, having undergone no melting, or any other change, since their formation (Bischoff, 2001:772-773; Dunn, 2012:2-3).

The fact that each 'group' of meteorites originates from its own astronomical object / parent body rings true only for chondrites, whereas a different term is used for differentiated meteorites, namely 'petrogenetic association'. Petrogenetic association refers to differentiated groups with the same isotopic and chemical characteristics, leading to the conclusion that they originate from the same, or from closely similar, parent bodies (Weisberg *et al.*, 2006:25,27). Hutchison (2004:415) provides valuable descriptions of the seven different petrogenetic associations that can be identified in the meteorite groups concerned. These petrogenetic associations and their descriptions can be seen in Table 2-2.

**Table 2-2: Petrogenetic associations of Hutchison (2004:415) that describe the origin and possible associations with parent bodies and with other types of meteorites**

| Petrogenetic association | Criteria and description |
|---|---|
| HED achondrites | • Similar O isotope ratios are observed |
| Mesosiderites<br>IIIAB irons<br>MGPs | • HED pyroxenes and feldspars match the ones in mesosiderites.<br>• The metal present in stony-irons is in the range of IIIAB conpositions.<br>• MGP olivines are within the range of mesosiderites.<br>• All the above have ancient crystallisation ages (4.55 – 4.65 Ga). |
| Winonaites<br>IAB / IIICD irons | • There are strong mineralogical links between chondritic inclusions of IAB irons and winonaites.<br>• Similar O isotope ratios.<br>• Ages of the chondritic silicate, metal and winonaites are 4.55 Ga. |
| Aubrites<br>Enstatite chondrites | • Similar O isotope ratios.<br>• Reduced minerals are omnipresent, however, the similarity between EH / EL and aubrite is imperfect.<br>• No less than three parent bodies may be required. |
| CR chondrites<br>CH chondrites<br>Bencubbin / Weatherford | • Olivines ~$Fo_{99}$.<br>• O isotope ratios on the mixing line and slope ~0,7.<br>• All these have an enrichment in $^{15}N$. |

| Petrogenetic association | Criteria and description |
|---|---|
| | • Metallic Ni correlates positively with Co.<br>• Very probable association. |
| H chondrites<br>IIE irons | • IIIE silicates range from chondritic (with pyroxene and H group olivine) compositions to fractionated olivine-poor igneous rocks.<br>• O isotopic ratios close to the H group.<br>• Age ranges ~4,56 – 3,5 Ga.<br>• Questionable association. |
| Carbonaceous chondrites<br>Ureilites | • The carbon contents, O isotope ratios as well as planetary noble gases suggest a link with CV / CO groups (especially the darker inclusions in CV's).<br>• Ureilites probably from numerous parent bodies. |
| L or LL chondrites<br>IVA irons | • O isotope ratios of the silicates in four iron meteorites coarsely lie on the mass fractionation line that goes through LL and L groups.<br>• Olivine absent.<br>• Pyroxenes more Mg-rich than in L-group.<br>• Silica polymorphs present.<br>• Questionable association. |

### 2.3.1 Chondrites

The composition of chondrites closely resembles that of the sun (excluding the highly volatile elements of H and He, thus including C, O, N, Ne, Mg, Si, Fe, Ni, Na, etc.) (Hutchison, 2004:5; Winter, 2014:12). These chondrites are derived from asteroids (and possibly comets) that did not experience planetary differentiation (Dunn, 2012:3). The textures present in chondrites indicate that the material involved has undergone no melting since its formation by constituent accretion (Hutchison, 2004:5). Chondrites commonly contain chondrules, along with a matrix (Weisberg *et al.*, 2006:20). Chondrules are micrometre- to 2 mm-sized spheres of previously melted silicate material, consisting predominantly of ferromagnesian silicate minerals, like olivine and pyroxene, as well as feldspathic glass and, more rarely, Fe, Ni metal and Fe-rich sulfides, as well as various refractory inclusions (Weisberg *et al.*, 2006:20). Chondrules formed as molten free-floating droplets during brief high-temperature events in the solar nebula, before being accreted to their parent asteroid (Dunn, 2012:3; Khiri *et al.*, 2017:647).

Chondrites can be further subdivided into five classes (Figure 2-1), based on their chemical composition, namely: carbonaceous chondrites (CI, CO, CV, CK, CR, etc.), which contain carbon

compounds; ordinary chondrites (L, LL and H); enstatite chondrites (EL, EH); R chondrites and K chondrites. Carbonaceous chondrites are thought to be the most primitive material in meteorites, since they are the least affected by thermal processes (Weisberg *et al.*, 2006:20). Ordinary chondrites refer to the most common type of chondrite, whereas enstatite chondrites refer to meteorites that consist primarily of the pyroxene mineral, enstatite (Dunn, 2012:3-4).

The chondrites are grouped into the three classes mentioned, due to similarities in their chemical, isotopic and petrological characteristics (Dunn, 2012:4). The carbonaceous chondrites divide up into eight different groups, as can be seen in Figure 2-1, namely CI, CM, CO, CV, CK, CR, CB and CH (Dunn, 2012:4). The above-mentioned method of nomenclature is indicated as the letter C for carbonaceous, followed by the letter identifying the type of meteorite on which the group is based (e.g. CI chondrites are based on the Ivuna meteorite, which was found in Tanzania in 1938) (Dunn, 2012:4-5).

The ordinary chondrites are divided into three different groups, as can be seen in Figure 2-1, namely H, L and LL, with the Mg/Si, Al/Si and Fe/Si ratios, as well as the Fe-Ni abundances, being used to classify the meteorites concerned into the groups mentioned (Dunn, 2012:5). The LL chondrites contain the lowest amount of metal, while the H chondrites contain the highest amount (Dunn, 2012:5). The enstatite class is divided into two groups, the EH (high amount of Fe) and the EL (low amount of Fe) (Dunn, 2012:5).

The K (Kakangari-like) chondrites are a total of three meteorites containing characteristics from all three chondrite classes. However, when their data is combined, they do not plot inside the area of the major chondrite classes (Dunn, 2012:5). Although the R, or Rumurutti-like chondrites, are compositionally similar to the ordinary chondrites, their oxygen isotope compositions are different, which means that they must have originated from another, different parent body (Dunn, 2012:5).

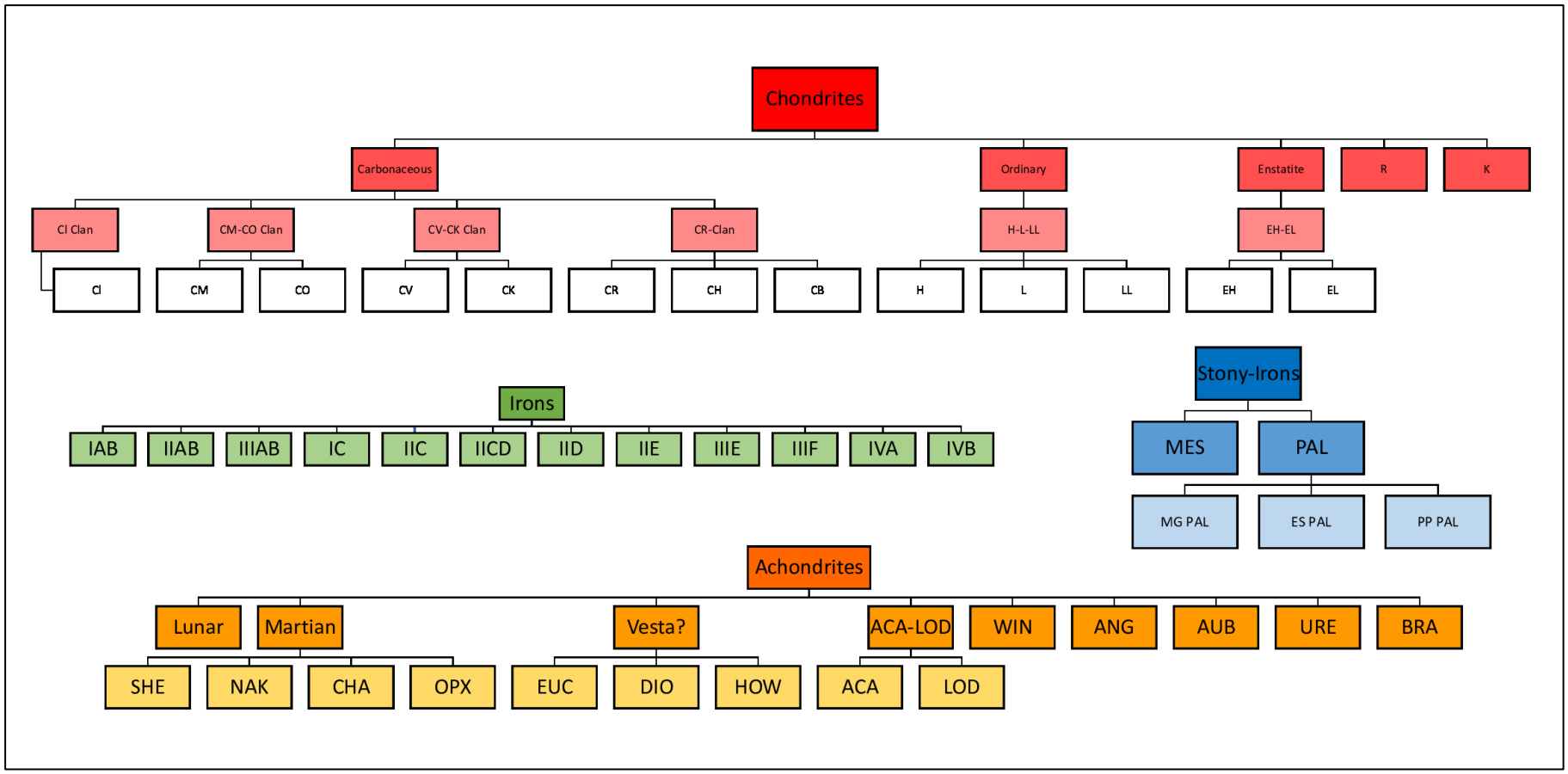


**Figure 2-1: Meteorite classification diagram, adapted from Weisberg et al. (2006:21) and Hutchison (2004:244) explaining the different meteorites in terms of the different types as well as their subtypes that can be found on the Earth. MES = mesosiderite; PAL = pallasite; MG PAL = main-group pallasite; ES PAL = Eagle Station pallasite; PP PAL = pyroxene pallasite; SHE = shergottite; NAK = nakhlite; CHA = chassignite; OPX = orthopyroxenite; EUC = eucrite; DIO = diopside; HOW = howardite; ACA = acapulcoite; LOD = lodranite; WIN = winonaite; ANG = angrite; AUB = aubrite; URE = ureilite; BRA = brachinite. The different chondrite subtype abbreviations are explained in the text.**

### 2.3.2 Differentiated meteorites

Differentiated meteorites can be described as smaller parts of asteroids that have undergone some igneous processes, like crystal fractionation or partial melting (Dunn, 2012:5). Containing a much higher diversity of meteorites than do the chondritic meteorites, their details can be seen in Figure 2-1, in the form of achondrites, stony-iron meteorites and iron meteorites.

#### 2.3.2.1 Achondrites

The achondrites can be explained as chondrites that lack any chondrules or refractory materials. The group is further reported to consist of igneous rocks (melts, partial melts, melt residues, or even recrystalised) or of breccias of igneous rock fragments from differentiated asteroids and planetary bodies, including fragments of bodies like Mars and the Moon (Dunn, 2012:5-6; Khiri *et al.*, 2017:647). Achondrites are subdivided still further, based on their chemistry, into primitive achondrites and differentiated achondrites.

Primitive achondrites, which represent achondrites where the primitive chemical affinity to their chondritic precursors was retained, are closer to their primitive chondritic parent than to other achondrites (Dunn, 2012:6; Weisberg *et al.*, 2006:20). The reason for them retaining such chondritic compositions is due to them originating from a small degree of partial melting. The five groups of achondrites are classified as primitive achondrites, consisting of lodranites, winonaites, acapulcoites, ureilites and brachinites (Dunn, 2012:6).

Differentiated achondrites, in contrast, refer to those achondrites that also contain igneous textures, but that do not share the same chemical composition as chondrites. Such achondrites, which form due to the complete melting of its precursor chondritic material, are, therefore, considered as basalts or as basaltic magma cumulates. The meteorite groups that are considered differentiated achondrites include aubrites, angrites, howardites, eucrites and diogenites, as well as the Martian and Lunar clans (Dunn, 2012:7).

#### 2.3.2.2 Martian meteorite clan

Martian meteorites, which originate from the crust of Mars, are classified as plutonic (lherzolotic and olive-phyric shergottites) and volcanic (basaltic shergottites and nakhlites) rocks. Such meteorites have also been referred to as SNC (shergottites-nakhlites-chassignite) meteorites.

The O-isotopic composition of the meteorites differs greatly from that of meteorites originating from asteroidal parent bodies, with the gases that are trapped inside the meteorites as glass containing the exact same gases that are present in the Martian atmosphere (Weisberg *et al.*, 2006:42).

#### 2.3.2.3 Lunar meteorite clan

Lunar meteorites consist of a diverse range of different rock types, including highland regolith breccias, unbrecciated and brecciated mare basalts, highland impact-melt breccias and mixed mare/highlands breccias. They share many different characteristics with samples brought back from the Apollo and Luna missions, including bulk chemical, mineralogical (with Fe/Mn ratios present in pyroxenes) and O-isotopic compositions. The meteorites concerned did not, however, originate from the same locations where the samples involved were taken (Weisberg *et al.*, 2006:42).

#### 2.3.2.4 Stony-iron meteorites

The stony-iron meteorites are differentiated meteorites consisting of only two groups, the pallasites and the mesosiderites (Figure 2-1), which both consist of nearly equal parts of rocky material (silicates) and nickel-iron metal. Such meteorites most probably originate from the mantle-core boundaries of the parental body (i.e. the asteroid) (Dunn, 2012:6; Khiri *et al.*, 2017:647; Ouknine *et al.*, 2019:2). The difference between the two groups is the type of silicate minerals that are present in them (Dunn, 2012:8).

**Mesosiderites** are classified as breccias consisting of equal amounts of Fe and Ni, but containing troilite (Weisberg *et al.*, 2006:41). Dunn (2012:8), however, states that mesosiderites contain mainly pyroxene originating from the crust of its originating asteroid. Such meteorites are considered to be various pieces from the core, as well as from the crust, that have been mixed during impact (Dunn, 2012:8).

**Pallasites** consist mainly of olivine (35-85 vol%)-metal and troilite assemblages. ‘Pallasites’ is a term that is used to group four different olivine-metal rocks, namely the main group pallasites, the Eagle Station pallasites, the pyroxene pallasites and a fourth, ungrouped pallasite, which is not included in Figure 2-1 (Weisberg *et al.*, 2006:41-42). The meteorites concerned consist of material from the mantle-core boundary (Dunn, 2012:8).

#### 2.3.2.5 Iron meteorites

The iron meteorite group, which consists mainly of iron-nickel metal, can be described as a remnant of differentiated planetesimals (Dunn, 2012:6; Khiri *et al.*, 2017:647; Ouknine *et al.*, 2019:2) (Figure 2-1). All iron meteorites consist almost only of Fe-Ni metal, which usually forms intergrowths of high-Ni and low-Ni alloys (Widmanstätten structure). According to McSween and Huss (2010:173), iron meteorites are created by the partial melting process of chondrites, which form the most common meteorite found on Earth. When the temperature of the partially melted chondritic material rises, an eutectic metal-sulfide melt is produced (McSween & Huss, 2010:173). After the melt has formed, it segregates from the silicate that is present, which then forms iron meteorites (McSween & Huss, 2010:173-174). Only the main established groups of the 12 groups of iron meteorites are indicated in Figure 2-1. However, merely 10% of the iron meteorites can be placed in the 12 groups shown (Dunn, 2012:8). According to Ouknine *et al.* (2019:2), iron meteorites are the heaviest samples of meteorites found on Earth.

## 2.4 Common and accessory minerals in meteorites

The classification of meteorites is mainly based on the similarities and differences in their petrographic characteristics, their bulk chemical composition, their oxygen isotopic composition and their mineralogy (Dunn, 2012:3; Weisberg *et al.*, 2006:19). The elements that are found in meteorites are the same as those that are found on Earth, but the isotopes that are found in meteorites differ slightly from those on Earth, due to varying initial amounts of radioactive elements, as well as different exposures to cosmic radiation (Buchwald, 1975c:75). Dunn (2012:2) explains that the mineralogy and chemistry of a meteoritic sample reflects the composition of the parent body involved.

Most newly discovered minerals in meteorites are typically trace constituents, with weight percentages of less than 1%. However, the importance of a mineral being present in a meteorite does not depend on its abundance. Minerals that are found abundantly in meteorites have abundant constituent minerals, as well as a stability field that is quite extensive, including kamacite, taenite, pyroxenes and olivine, which can be found in almost all meteorites. Rare minerals, in contrast, are considered to be rare due to their limited stability field, and to their inclusion of rare elements. The rare minerals concerned are crucial to meteoritical studies, as the detection of their presence can lead to answers being found regarding the origin of the meteorite (Mason, 1972:315).

As many as 275 to 300 different minerals can be identified in meteorites, with them being grouped into native elements, oxides, silicates, ‘sulfides, phosphides, carbides’ and ‘carbonates, sulfates, phosphates, [and] halides’ (McSween & Huss, 2010:160-162; Rubin, 1997:231). The anhydrous R, ordinary and carbonaceous chondrites consist mostly of major olivine, plagioclase, and pyroxene, with metallic Fe-Ni, chromite and troilite comprising the major opaque phases. The primitive achondrites have a similar mineralogic composition. The enstatite chondrites and achondrites (highly reduced) consist of major enstatite, kamacite, plagioclase, free silica and a silicide, as well as of Mg-, K-, Ca-, Cr-, Mn-, Ti- and Na-rich sulfides. In contrast, the aqueously altered carbonaceous chondrites consist of major complex organic compounds, magnetite, hydrous phyllosilicates, carbonates and numerous sulfides and sulfates (Rubin, 1997:231).

Howardites, eucrites and diogenites each have an orthopyroxenitic to basaltic composition, meaning that they consist mainly of major calcic plagioclase and pyroxene, as well as of accessory oxides. Ureilites, however, consist of chromian olivine, calcic and low-Ca clinopyroxene within a carbonaceous matrix, with the accessory phases being C polymorphs (diamond, chaoite, graphite and lonsdaleite), halides, metallic Fe-Ni and troilite. Angrites consist of fassaitic pyroxene, minor olivine and magnesian kirschsteinite. Martian meteorites consist of major phases of different pyroxenes and olivine, along with minor phases with various sulfides, chromite, magnetite and Ca-phosphates, whereas lunar meteorites consist of major augite, as well as of calcic plagioclase (Rubin, 1997:231).

### 2.4.1 Minerals in iron meteorites

According to Buchwald (1977:454), ten minerals can be considered as the most important minerals that are present in iron meteorites, namely kamacite (α-Fe(Ni)), taenite (ɣ-Fe(Ni)), schreibersite ($(Fe,Ni)_3P$), graphite (C), chromite ($(Mg,Fe)Cr_2O_4$), troilite (FeS), olivine ($(Mg,Fe)_2SiO_4$), daubréelite ($FeCr_2S_4$), plagioclase ($(Na,Ca)(Si,Al)_4O_8$) and enstatite ($Mg_2Si_2O_6$). However, newer literature, such as that of McSween and Huss (2010:180), have found that the most common minerals found in iron meteorites include kamacite, taenite, troilite, graphite, schreibersite, cohenite ($Fe_3C$) and chromite. The newer list of minerals appears different to that which was published in 1977, due to the use of updated and newer technologies, as well as of equipment that is used to determine the nature of the minerals present.

Kamacite and taenite are the major minerals that are present in iron meteorites, with both being iron-nickel alloys (McSween & Huss, 2010:160). The only difference between the two minerals is their nickel content. The varying Ni percentage, along with the cooling processes, tend to have a

more major effect on the structures that are present in the iron meteorite. Neither of the minerals concerned, which are both magnetic, occurs naturally in Earth rocks. The major minerals, as well as some accessory minerals commonly found in iron meteorites, are discussed in greater detail below.

***Kamacite***

The mineral kamacite, which contains up to 7,5 wt. % Ni in solid solution, displays cubic cleavage (Buchwald, 1975c:87,91), substituting for the Fe atoms in the cubic, body-centred lattice. Differing chemical groups constitute different amounts of Ni, with, for example, kamacite in hexahedrites possibly containing 5 to 5,5 wt. % Ni, whereas the kamacite in octahedrites might contain 5,5 to 7,5 wt. % Ni. Phosphorous, which can also substitute for Ni and Fe atoms in kamacite, can only occur up to 0,06 weight percentage P (Buchwald, 1975c:88).

'Swathing kamacite', which is a structure that occurs in iron meteorites, refers to the kamacite that forms rims around coarse inclusions of troilite, silicate and schreibersite. These kamacite rims can extend to widths as wide as 0,5 to 1,5 mm around schreibersite and troilite that occur specifically in group IIIA irons, but the structure might occur in all classes of iron meteorites, with the widths also tending to vary. Simply put, swathing kamacite is the first kamacite to form from taenite during the first stage of cooling. This process of solid-state transformation originates around foreign inclusions acting as heterogenous nuclei, like chromite, schreibersite, silicates and troilite. After the swathing kamacite has started forming, when the temperature of the system has dropped from about 50 to 100°C, and the rims formed are an adequate size, the majority of the taenite present will form homogenously into the Widmanstätten structure (Buchwald, 1975c:89-90).

Neumann bands, which are another characteristic feature that occurs in kamacite, can be described as mechanical, plate-shaped twin lamellae in the kamacite. The feature concerned occurs in octahedrites, hexahedrites and ataxites, or as long as a coherent kamacite phase of between 20 and 50 µm in width is present. Although the bands involved can be very narrow (1 µm) in precipitate-rich kamacite crystals, they can also reach larger widths (10 µm) in pure kamacite crystals in the same meteorite. The origin of Neumann bands can be attributed to the action of pre-atmospheric processes, like cosmic collisions, which might have occurred in remote space and at a remote time (Buchwald, 1975c:90).

### *Taenite*

Taenite, which contains between 24 wt. % and 77 wt. % Ni, can be described as austenite that occurs in meteorites (Buchwald, 1975c:92; McSween & Huss, 2010:160). When taenite occurs in octahedrites, it forms three-dimensional lamellae, or sheets, that appear to be band-shaped, in sections. Only under certain special conditions will taenite occur in hexahedrites, especially if the hexahedrites involved have undergone secondary reheating, which has led to the existence of unequilibrated structures. The composition of taenite can be variable in terms of Ni (24–77 wt. %), Co (0,3–0,8 wt. %), C (0,05–0,5 wt. %) and P (0,05–0,1 wt. %). Taenite can also be described as being much harder than the kamacite that is present in a meteorite (Buchwald, 1975c:92-93).

### *Troilite*

The pure form of troilite contains almost only FeS, with the other elements (Ni, Cu, Zn, Co, Pb, Mn, Cr) being only minor constituents of less than 1% that are present in the mineral. When troilite is exposed to shock compression and to its associated reheating, the mineral melts very easily, spreading throughout the meteorite, with it possibly partially dissolving the outer walls of cohenite, schreibersite or Ni-Fe. The process can lead to any silicate, daubréelite or chromite being subsequently fractured and included in the troilite. Thus, it can be said that troilite can be very heterogenous in composition. Troilite is described as nonmagnetic (when pure), bronze-coloured with a green tint, and strongly anisotropic. The mineral often includes some parallel oriented daubréelite lamellae. Troilite occurs as bars, dumbbells and shapeless nodules in meteorites, with the mineral being found in all types of iron meteorite (Buchwald, 1975c:106-108).

### *Plessite*

‘Plessite’ is an umbrella term that traditionally covered minerals that were neither taenite nor kamacite, but a mixture of both the minerals. Simply put, plessite is a two-phase mixture of ɣ (taenite) and α (kamacite), which develops last from the taenite retained during consistent primary cooling (Buchwald, 1975c:95). Plessite can, however, also form through the reaction of ɣ → $\alpha_2$ (martensite) → α + ɣ. Plessite was later discovered, with advanced technology, to take on a variety of forms, which are described by various neologisms, including, but not limited to, pearlitic plessite, spheroidised plessite, acicular plessite and comb plessite. Buchwald (1975c:95-100) comprehensively explains the nature of all these forms of plessite.

### *Cohenite*

The mineral cohenite, which is orthorhombic, is very closely related to cementite ($Fe_3C$), which occurs in steel. The composition of cohenite is 0,7–2,3 wt. % Ni, with 0,02–0,3 wt. % Co. The

mineral, which is pure white, can be described as being anisotropic, and, despite it being very hard (harder than schreibersite), it is, nevertheless, ductile. The reheating process of especially shocked iron meteorites leads to the recrystallisation of strained cohenite crystals. Cohenite crystals that are fractured will eventually decompose to graphite and ferrite with prolonged reheating. The mineral occurs mainly in group I iron meteorites, but it can also occur in other types of iron meteorites (Buchwald, 1975c:100-101).

***Haxonite***

Haxonite $(Fe,Ni,Co)_{23}C_6$, which is pure white and hard, is a cubic mineral that does not occur in manmade steel. The chemical composition of the mineral includes Ni (3,5–5,6 wt. %) and Co (0,05–0,4 wt. %). The mineral can be distinguished from cohenite by its isotropic behaviour under RL microscopy, as well as by the mineral's slightly lower hardness. Haxonite does not occur as coarse crystals, but, rather, as 'carbide roses', which are intricate intergrowths with schreibersite, kamacite and taenite particles. Haxonite is described as an accessory mineral that occurs in the same meteorites as does cohenite. Both haxonite and cohenite, which are thermodynamically unstable at all temperatures, are known to decompose completely into graphite and ferrite. Thus, that they are able to survive in iron meteorites is very surprising, since they will have cooled down slowly to have reached the thermodynamic equilibrium required (Buchwald, 1975c:101-103).

***Schreibersite***

Schreibersite can be described as magnetic, tetragonal, and yellow under RL. The mineral is, however, more brownish, softer, and much more brittle than is cohenite. The composition of this mineral varies greatly, as the coarse skeleton crystals, which precipitated very early and directly from the taenite concerned, show low Ni content (10–15 wt. %) and are very hard and brittle. The crystals, which precipitate later, tend to have a vermicular shape and are located in the α–γ and α–α grain boundaries, displaying a higher Ni content (20–50 wt. %), and being slightly softer and more ductile than cohenite. Schreibersite occurs in many meteorites, but not in all iron meteorites, as it does not occur in the low-Ni end of the group IVA. Only when the analytical value of P increases above 0,06 wt. % do the first minute schreibersite particles appear, but when the bulk value of P increases above 0,25 wt. %, coarse, angular schreibersite crystals form directly from the taenite phase during cooling. Another factor that directly depends on the P composition is the width of the schreibersite halos that form around the troilite crystals. However, the halos concerned inversely depend on the cooling rate involved (Buchwald, 1975c:104-105).

***Rhabdite***

The rhabdite crystals, which are tetragonal prisms of about 1 to 25 µm thickness, precipitate in the interior part of the kamacite crystal. Rhabdites, which have high Ni content (27–50 wt. %), are slightly soft and ductile, with few to no cracks. The crystals, which are plate-shaped or prismatic, are abundantly present in hexahedrites. Various subgroups can be identified in hexahedrites when looking at the clearly defined ratios of plate-shaped to prismatic rhabdites. Prismatic-shaped rhabdites occur mainly in many octahedrites, like IIB, IIIA-IIIB and I (Table 2-3) (Buchwald, 1975c:105).

***Carlsbergite***

Carlsbergite (CrN) occurs in iron meteorites as very fine, oriented laths (30 µm × 5 µm × 2 µm in size) in kamacite, and as asymmetrical grains (3–10 µm) in some of the grain boundaries. The mineral is best observed in unetched, polished sections, where it stands out in high relief, due to its hardness. Carlsbergite, which is light grey, with a characteristic rose tint, is isotropic. The mineral, which is a minor accessory in iron meteorites, is quite common (Buchwald, 1975c:103-104).

***Graphite***

Graphite appears as fine, centimetre-sized nodules, along with silicates and troilite, in group I and I-An. In other iron meteorites, the troilite-graphite nodules are either absent, or very rare. However, fine graphite lamellae and spherulites, which are the decomposition products of the other carbides mentioned above, occur in groups IIA, IID, IIID, IIIE and in various anomalous irons (Table 2-3) (Buchwald, 1975c:109).

***Daubréelite***

The mineral daubréelite, which occurs as thick, parallel bars in troilite crystals, displays a cubic spinel-type structure. Daubréelite, which is bluish in colour and isotropic, is considered as an exsolution product in troilite, forming lamellae ranging from 0,5 to 1 mm in width. The ratio of daubréelite to troilite is inversely correlated with the nodule size of the troilite, with the finer nodules of troilite exhibiting the presence of about 50 wt. % of daubréelite. The mineral occurs mainly in groups I, IIA, IIIA and IVA (Table 2-3). Although the mineral forms mainly in troilite, it can also form separate 10 to 500 µm particles in kamacite crystals. Cosmic shocks, along with their reheating, can usually destroy the daubréelite-troilite nodules, which shatter the daubréelite and partially dissolve the mineral into the melt. Afterwards, the parts of the mineral that did not

dissolve are dispersed as subangular particles (1–10 µm) in the troilite (Buchwald, 1975c:110-111).

***Chromite***

This mineral has proven to be very common in iron meteorites. Chromite can be described as a cubic spinel with distinctive octahedral cleavage, with a bluish colour and high hardness. Occurring in the form of octahedra and cubes in the troilite nodules of groups I and IIIA (Table 2-3), it can reach large dimensions (8 cm x 4 cm). Chromite occurs in various anomalous iron meteorites (Buchwald, 1975c:111-112).

***Silicates***

Silicates are common in most of the iron meteorites in the form of olivines, plagioclases, pyroxenes, and glasses. Silicates have also been proven mainly to occur in group I and I-An iron meteorites (Buchwald, 1975c:112-113).

## 2.5 Iron meteorites

### 2.5.1 Chemical classification of iron meteorites

The majority of iron meteorites display a varied range of siderophile elements, due to the processes, like fractional crystallisation, that occur in the core of asteroids (McSween & Huss, 2010:180). Siderophile elements can be described as ‘iron-loving’ elements, which form a dense metallic phase (Winter, 2014:10).

In identifying iron meteorites, approximately twelve elements are considered as the ‘fingerprints’ for discerning individual meteorites (Buchwald, 1975c:86). The elements concerned include Ni, cobalt (Co), phosphorus (P), carbon (C), sulfur (S), chromium (Cr), copper (Cu), zinc (Zn), Ga, Ge, Ir and platinum (Pt) (Buchwald, 1975c:85). However, almost all of the time, it is sufficient to classify the iron meteorite, when only the Ni and P concentrations along with the structure are known (Buchwald, 1975c:86). The Ni content of a meteorite is a very important parameter for chemical classification, as it provides information on the rate of cooling involved (Wasson, 1974:30). After determining the concentrations of Ni and P, the next elements to analyse are S and C, due to their important role in structure development (Buchwald, 1975c:86). According to Buchwald (1975c:86), Co, Cu and Zn concentrations are not very useful to know, as they tend to remain constant in the majority of cases of iron meteorites.

The most important elements for identifying individual meteorites clearly are Ge, Ir and Ga (as well as Pt to a minor extent), although they do not influence the structure as S and C do (Buchwald, 1975c:86). The Ga and Ge content of the meteorite is essential, as it signifies different core fragments of various asteroids, or even characterises the different metallic regions inside a singular parent planet (Wasson, 1967:161).

According to Buchwald (1977:456), the importance of structural classification (which used to be the main focus in the past) has shifted to chemical classification of iron meteorites, largely due to the increased amount of interest shown in the origin and genesis of meteorites in general. The classification scheme, as proposed by Buchwald (1977:456), divides iron meteorites into 13 groups, based on the P and Ni content of the iron meteorite, as well as on the trace elements that are present, as presented in Table 2-3.

**Table 2-3: Chemical groups and structural classification of iron meteorites adapted from Buchwald (1977:456), with some well-known examples of the different iron meteorite types**

| Chemical group | Structural class | Meteorite example |
|---|---|---|
| I | coarse inclusion rich Octahedrites | Canyon Diablo |
| I-An | inclusion-rich Irons | Copiapo |
| IIA | Hexahedrites | Coahuila |
| IIB | coarsest Octahedrites | Sikhote-Alin |
| IIC | plessitic Octahedrites | Ballinoo |
| IID | medium Octahedrites (10-11.5 wt. % Ni) | Carbo |
| IIIA | medium Octahedrites (7-8.8 wt. % Ni) | Cape York |
| IIIB | medium Octahedrites (8.6-10.6 wt. % Ni) | Chupaderos |
| IIIC | fine Octahedrites (10.5-13.5 wt. % Ni) | Mungindi |
| IIID | finest Octahedrites | Tazewell |
| IIIE | coarse Octahedrites | Kokstad |
| IVA | fine Octahedrites (7.5-10 wt. % Ni) | Gibeon |
| IVB | Ataxites | Hoba |
| An | anomalous Iron meteorites | Nedagolla |
| - | unclassified Iron meteorites | Armanty |

The roman numerals used for the different chemical groups represent the decreasing Ga and Ge content involved (Wasson, 1967:162), which can be seen in Table 2-4. The chemical groups concerned were determined by Lovering *et al.* (1957:273). The Ga and Ge content were graphically plotted against Ni, observing specific groups forming on the graph, which could be assigned to different chemical groups.

**Table 2-4: Description of the Ga (ppm) and Ge (ppm) content represented by the different Roman numerals seen in the classification of iron meteorites (Table 2-3) (Wasson, 1967:162)**

| Roman numeral | Ga levels (ppm) | Ge levels (ppm) |
|---|---|---|
| I | 80–95 | 300–420 |
| II | 40–62 | 130–230 |
| III | 8–24 | 15–80 |
| IV | <1–3 | <1 |
| Anomalous | - | - |

### 2.5.2 Structural classification of iron meteorites

Iron meteorites can also be classified according to the structures that are present in the meteorite, like the shape and size of the kamacite crystals that are present in the iron meteorite (Buchwald, 1975c:66). The different structural classes in which iron meteorites are divided into, along with their respective kamacite bandwidths, are presented in Table 2-5.

**Table 2-5: The structural classification of iron meteorites based on kamacite bandwidth (mm), adapted from Buchwald (1975c:66)**

| Structural class | Symbol | Kamacite bandwidth (mm) |
|---|---|---|
| Hexahedrites | H | - |
| Coarsest Octahedrites | Ogg | >3.3 |
| Coarse Octahedrites | Og | 1.3–3.3 |
| Medium Octahedrites | Om | 0.5–1.3 |
| Fine Octahedrites | Of | 0.2–0.5 |
| Finest Octahedrites | Off | <0.2 (continuous) |
| Plessitic Octahedrites | Opl | <0.2 (spindles) |
| Ataxites | D | - |
| Anomalous | Anom | Various |

Hexahedrites and ataxites can be seen not to have certain bandwidths for classification, due to the kamacite that is present in hexahedrites being significantly coarse, as well as equiaxial, while the kamacite in ataxites is not visible with the naked eye (Buchwald, 1975c:67). A meteorite should, however, be classified both by structural and chemical classification to accurately describe the meteorite so that it is universally understandable.

#### 2.5.2.1 Acid etching of iron meteorites

According to Vander Voort (1992:230), meteorite sample preparation methods closely resemble those of alloy steels. The etching technique that is commonly used to display the Widmanstätten structure in iron meteorites forms the nital etch (using $HNO_3$), with a concentration ranging from 1-5%. The acid dissolved a small portion of the meteorite, putting nickel ions in solution, displaying the structure. The 5% nital solution is quite strong, which explains why most researchers prefer to use a solution of 1 or 2%, as it tends to act much more slowly than does the 5% solution. Use of the nital solution is because it displays both the taenite and the kamacite-kamacite grain and sub-grain boundaries, along with the Neumann bands, if they are present (Vander Voort, 1992:230-231).

Nininger (1945) comprehensively explains another set of preparation and etching techniques for metallic meteorites. The etching solution that is most often used for meteorites is a 6% solution of $HNO_3$. The solution is created by means of placing approximately 30 ml of concentrated $HNO_3$ in a beaker and filling it up with distilled water, until a total volume of 500 ml is reached. When the solution is used, it can be altered according to the needs of the user (e.g. when the solution is too strong, it can be further diluted, and vice versa). When etching an octahedrite with the 6% solution, the Widmanstätten pattern takes approximately five to ten seconds to appear, with it taking up to two to five minutes for completion of the process (Nininger, 1945:82-83). The preparation and etching methods are, however, only methods that are described in the existing literature, with them not necessarily being the methods used in the current study.

#### 2.5.2.2 Main and secondary structures

According to Buchwald (1975c:125), iron meteorites are assumed to have occurred in very large parent bodies that are assumed to have protected them from any thermal loss, as well as from any cosmic radiation that might have occurred. The parent body asteroids concerned are

assumed to have constantly been hit by other celestial bodies, while the soon-to-be iron meteorites were still located deep within the parent bodies, which led to the iron meteorites involved inheriting some effects, due to their location. Finally, a quite large impact led to the parent body being broken up into small, sizable fragments that survived the violent impact that preserved the structures that formed earlier. The fragments concerned then underwent another set of collisions in space, as well as experiencing reheating when nearing the Earth. Some meteorites might also have formed new structures, due to the kinetic energy of hitting the surface of the Earth. However, the majority of meteorites were confirmed as exhibiting certain structures due to the occurrence of pre-terrestrial events (Buchwald, 1975c:125). In this section, the structures involved will be described by means of splitting them into main (Widmanstätten) and secondary structures.

***The Widmanstätten structure***

The Widmanstätten structure is a well-known structure of most iron meteorites and some stony-iron meteorites, in terms of which iron meteorites into divided into octahedrites (Os), hexahedrites (Hs), ataxites (Ds) and anomalous irons (Buchwald, 1975c:115). Previously, the Widmanstätten structure was believed to have been formed by means of direct crystallisation from a very slowly cooling melt. However, the structures concerned were later recognised as having been formed at temperatures lower than the melting temperatures, with the process involved, therefore, being rather a slow solid-state diffusion-controlled nucleation and growth process (Buchwald, 1975c:115; McSween & Huss, 2010:180).

A Widmanstätten structure, which refers to an intergrowth of kamacite and taenite in an iron meteorite, can be seen in Figure 2-2 (McSween & Huss, 2010:180). Widmanstätten patterns can be seen on the sawn, polished, and etched faces of an iron meteorite. During the process concerned, the kamacite prefers to nucleate along the octahedral planes of the taenite phase (Buchwald, 1975c:115). The final structure then forms, when the kamacite bands or plates thicken through a process of solid state diffusion, subsequently coming to touch one another (Buchwald, 1975c:115). Figure 2-2 shows the relative thinness of the kamacite bands involved.

Yang and Goldstein (2005) extensively explain five different mechanisms through which the Widmanstätten structure can form in iron meteorites. The first mechanism explains the traditional method of formation, referring to ɣ (taenite) → α (kamacite) + ɣ (taenite), which can be seen in Figure 2-3.

The mechanism explains that as the taenite is cooling, it starts to form a kamacite phase, which is in equilibrium with the taenite. The taenite phase starts to disappear as the content of the Ni

lessens. However, through computer simulations the method has been found ultimately not to lead to the formation of the Widmanstätten structure (Yang & Goldstein, 2005:240). Mechanism two explains that ɣ → ɣ + Ph → α + ɣ + Ph, and, according to Yang and Goldstein (2005:242), this mechanism can definitely lead to the creation of the Widmanstätten structure in iron meteorites with a high P content. The mechanism is best described by the presence of alloy 'a' in Figure 2-4, by means of following the dotted line representing the path that the alloy followed during cooldown.

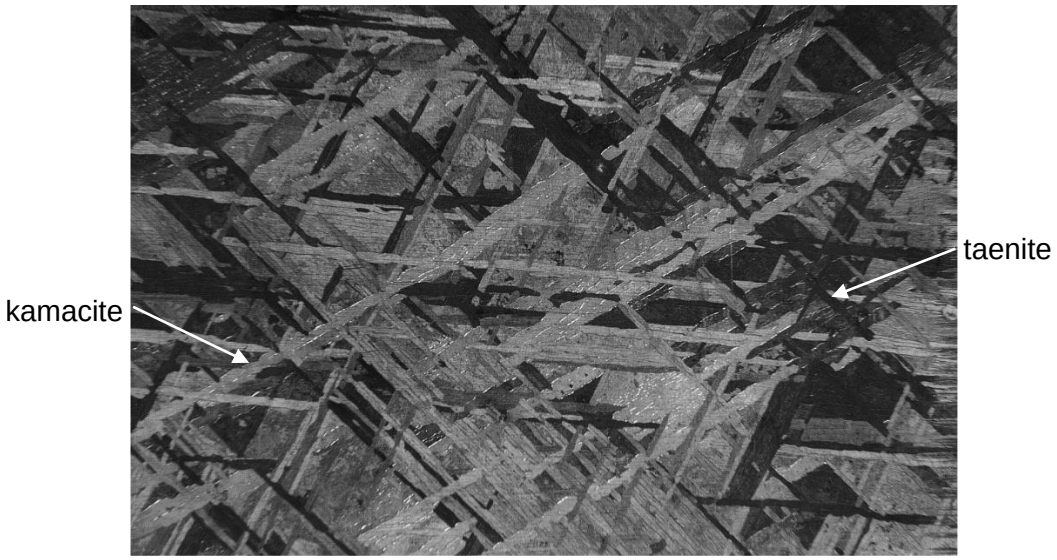


**Figure 2-2: An example of the Widmanstätten structure (kamacite – taenite intergrowth) which is a characteristic structure of iron meteorites, evident in a Gibeon meteorite (Tatum, 2019:2978).**

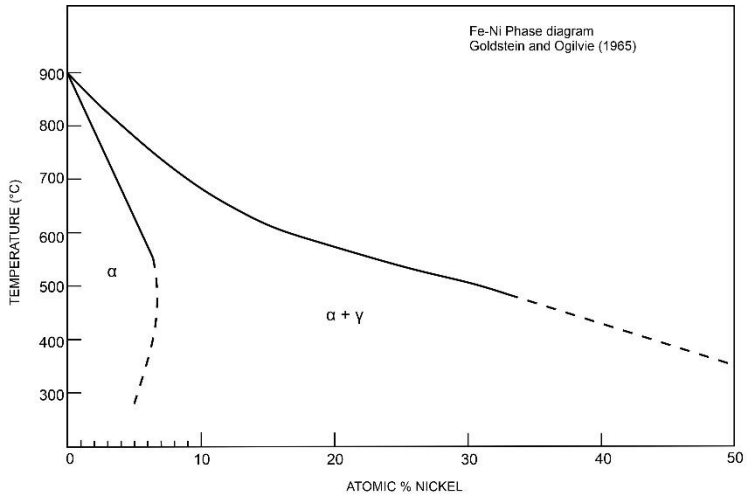


**Figure 2-3: Fe-Ni two phase diagram, where α = kamacite and ɣ = taenite, adapted from Goldstein (1965:18), which explains the formation of kamacite and taenite with the decrease in temperature.**

As alloy a starts to cool down, it reaches the ɣ + Ph phase region at ~750°C, where a phosphide is the first to form. Alloy a then reaches the α + ɣ + Ph field at ~700°C, where the α phase nucleates from the parent ɣ. The α phase continues to grow into its parent ɣ as the temperature drops. The third mechanism describes the reaction path of ɣ → (α + ɣ) → α + ɣ + Ph, which is indicated by alloy 'b' in Figure 2-4.

As alloy b cools, it reaches the (α + ɣ) field at ~700°C, with it, after further cooling, finally entering the α + ɣ + Ph phase field. The alloy does not, however, nucleate α when it enters the (α + ɣ) field. The α phase does not nucleate during this mechanism, as the alloy is much too low in P, so that it does not pass through the ɣ + Ph field before entering the α + ɣ + Ph field. The mechanism concerned has been simulated by computer programs, indicating that it is possible for the Widmanstätten structure to form only in certain low-P iron meteorites (Yang & Goldstein, 2005:242).

The fourth mechanism, which can be considered to serve as an alternative to the first mechanism, is represented by ɣ → $\alpha_2$ → α + ɣ. The mechanism is proposed to occur in two steps as the temperature drops: 1) ɣ → $\alpha_2$ and 2) $\alpha_2$ → α + ɣ. The steps concerned indicate that the ɣ fully transforms into $\alpha_2$, and that the taenite and kamacite in the Widmanstätten structure originate from the breakdown of the $\alpha_2$. However, the mechanism was concluded as not being able to produce a Widmanstätten structure in low-P iron meteorites (Yang & Goldstein, 2005:244).

Yang and Goldstein (2005:245), however, state that the $\alpha_2$ does not have to be fully transformed for it to break down into α + ɣ, as the breakdown can start during cooling. The statement refers to the fifth mechanism, which notes that ɣ → $\alpha_2$ + ɣ → α + ɣ can be seen in Figure 2-4, as alloy 'c'.

The different stages of the mechanism at different temperatures can also be seen in Figure 2-5. The ɣ cools down from very high temperatures to $T_1$ (above $M_S$), but at $T_2$, which is equal to $M_S$, the taenite starts to convert to $\alpha_2$, which displays the same Ni content as does ɣ. With further cooldown of the temperature at $T_3$, the new taenite ɣ phase starts to nucleate within the region of $\alpha_2$ (Yang & Goldstein, 2005:245). The new ɣ phase then forms epitaxially on the previous, unconverted ɣ phase, which shares a border with $\alpha_2$. At $T_4$, the $\alpha_2$ is completely converted into ɣ and α phases.

Further cooling leads to the development of an equilibrium between kamacite and taenite at $T_5$, with the two phases concerned continuing to grow until the final temperature, at $T_7$, is reached. With the various computer simulations done, mechanism five was proved to be capable of leading to the formation of the Widmanstätten structure in low-P iron meteorites (Yang & Goldstein, 2005:247).

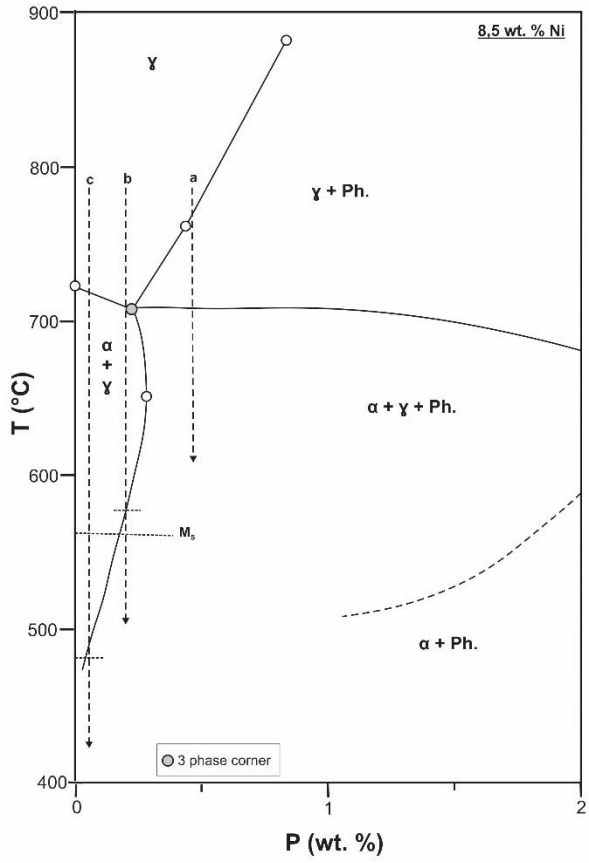


**Figure 2-4: Iso-Ni concentration at 8,5 wt. % Ni from the Fe-Ni-P ternary phase diagram showing the formation paths of three different alloys with decreasing temperature. $M_S$ = Martensite start temperature; a, b, c = alloys with different P contents; α= kamacite; γ = taenite and Ph = phosphide, $[FeNi]_3P$. Open circles represent data from Doan and Goldstein (1970), adapted from Yang and Goldstein (2005:242).**

***Secondary structures***

Iron meteorites that can be classified as falling in the same group (Figure 2-1) can display an unexpectedly large variation in terms of secondary structures, meaning that the events that caused these structures to form must have been very complex (with different intensity shocking and plastic deformation, and cycles of reheating and cooling). The secondary structures that occur in iron meteorites can be divided into four categories, namely those caused by shock-induced solid-state transformation, those caused by shock-induced plastic deformation, those caused by shock-induced melting and those caused by thermal annealing, due to shock relaxation, or to orbital reheating in Earth's atmosphere. All of the secondary structures concerned can ultimately be described, geologically, as metamorphic structures (Buchwald, 1975c:125).

The high shock pressures exerted during shock-induced solid-state transformation cause various minerals to transform to denser versions. Such transformation includes quartz, which forms coesite and stishovite, which remains metastable, and which can then be used as a form of shock

indicator. Another mineral that can be affected is feldspar, which can be fully transformed into a high-pressure phase, although the process can also occur in reverse, with the release of pressure leading to the formation of a low-density, amorphous glass (maskelynite or diaplectic feldspar glass) (Buchwald, 1975c:128).

Low rates of deformation occur during shock-induced plastic deformation, which causes the metallic matrix to be cold-worked, and the minerals present to become brecciated and distorted. The low degree of heating and deformation rates might have occurred in the hemisphere farthest from the centre of impact on the parent body. The low deformation rates might also be due to the breakup of a meteorite in the Earth's atmosphere. Broad deformation bands of kamacite, as well as shear zoned, might be seen in various meteorites, but if they are seen in large or in shower- or crater-producing meteorites, they are usually due to the impact that occurred on the Earth's surface itself. Similar deformation structures as the ones mentioned are also visible in smaller iron meteorites that did not undergo violent forces during impact with the Earth (Buchwald, 1975c:126,128).

High shock pressures that occur during shock-induced melting can, through attenuation and the reflection of shock waves at phase- and grain-boundaries, as well as at external surfaces, lead to the development of 'hot spots' in the meteorite. Such development can lead to the selective melting of quartz and silicates, which produces glass. Especially in iron meteorites, troilite is a very sensitive mineral, since it is much more compressible (shock-absorbent) than is the surrounding metal, which means that it can fully melt in situ. Cracks that may occur simultaneously may be rapidly filled with such troilite melts.

The other occurring minerals (graphite, chromite, cohenite, daubréelite, silicates and schreibersite) will either be fragmented and distributed throughout the liquid, or partially melted, forming very fine-grained structures of a ledeburitic appearance (Buchwald, 1975c:130-131).All the above-mentioned structures could have undergone further annealing after formation. Four types of annealing could have occurred, namely inside the parent body, during orbit, during atmospheric penetration and during crater formation on Earth. Annealing that occurs inside the parent body can be compared to the effects of long-term annealing of deformed material at low (close to recrystallisation) temperatures.

The structures resulting from the process include recrystallised, polygonised or recovered, according to the history, size and composition of the parent body concerned. Annealing during orbit, which occurs in the perihelial parts, would tend to recur at various times of equal intensity.

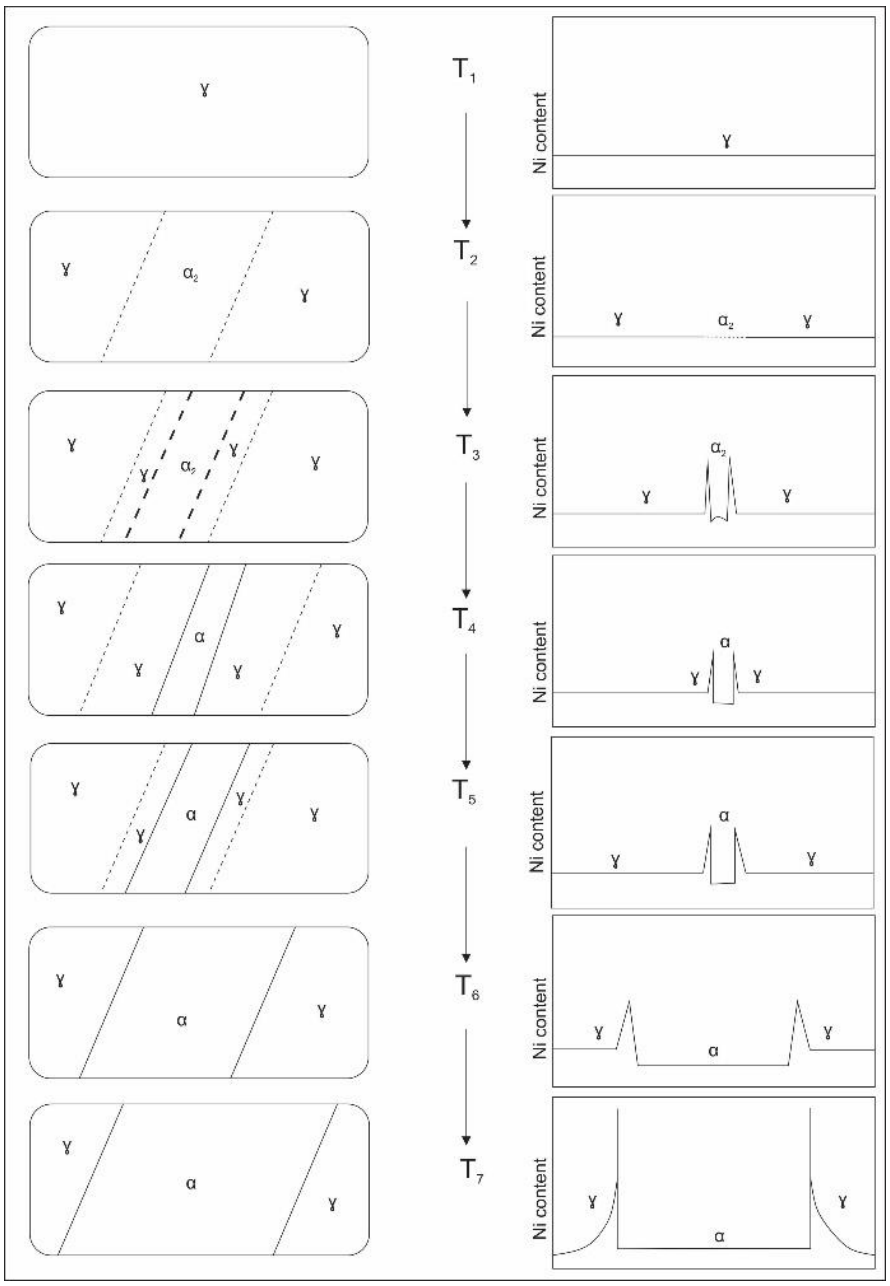


**Figure 2-5: The formation of the Widmanstätten structure, using the fifth mechanism explained by Yang and Goldstein (2005:245). The left side displays the microstructural development, and the right side displays the Ni profiles in kamacite and taenite, as the alloy cools down. $T_1$-$T_7$ shows different temperatures during cooldown, adapted from Yang and Goldstein (2005:245). Where α = kamacite and γ = taenite.**

The atmospheric reheating of the meteorite removes the exterior of the meteorites, leaving only a nucleus with a 5-20-mm-thick reheated outer crust. Lastly, the reheating during crater formation can lead to the development of different kinds of material. The near-surface material, which broke off very high up in the atmosphere and that flew independently, still displays an unchanged cosmic structure. However, the material that impacted on the Earth displays a variety of shock metamorphism (Buchwald, 1975c:131-133).

### 2.5.3 Surface shapes and structures

The shape and structure of a meteorite's surface is important for determining and investigating, because it is likely to lead to knowledge of the pre-atmospheric shape of the meteorite. The surface of any meteorite becomes severely altered when it is a 'find' and not a 'fall'. Buchwald (1975c:45) states that iron meteorites are more commonly classified as 'finds', meaning they undergo severe terrestrial corrosion that changes their ablational sculptures. A common shape that can be found in iron meteorites is angular and pyramidal (Table 2-6), which might have formed due to the boundaries of mineral-rich fracture surfaces of dodecahedral, octahedral and hexahedral orientations. However, with higher velocities and longer trajectories (more effective ablation), the angular shapes can become severely altered (Buchwald, 1975c:45).

Another common shape is that of a cone-shaped meteorite, which can be seen in Table 2-6. Such a shape develops when a meteorite adopts a stabilised flight, and when it is oriented with its pyramidal apex in the flight direction. Various structures exist that are associated with the cone shape. The structures concerned include flight markings on the meteorites that support the assumption of oriented flight, as well as elongated regmaglypts that radiate away from the apex on the skirt of the meteorite. Spilled-over ablation melts should be visible on the edge between the rear side and the cone. The rear sides of the meteorites are then likely to be flat and only slightly ablated, which probably best represents pre-atmospheric structures (Buchwald, 1975c:45).

However, it is important to know whether the meteorite involved reached the Earth's surface as one piece, or whether it broke up into various pieces, which then each had their own independent flight. Some more interesting shapes have also been found, such as those of icicles and spikes (Table 2-6), which refer to fragments of meteorites that have been separated along the grain boundaries of minerals. When a meteorite keeps tumbling during its fall to Earth, it will eventually form angular-equiaxial shapes, and possibly move in the direction of ovoid or spherical shapes. Ellipsoidal shapes, with their variations, are more common than are the spherical shapes (Buchwald, 1975c:46).

Regmaglypts are a very important surface characteristic of iron meteorites. Their structure can be described as consisting of thumblike pits / shallow holes that can be found on iron meteorite surfaces. They are formed due to turbulent supersonic airstreams, when the meteorite is falling through the atmosphere. They have also occasionally been found in chondritic meteorites. These regmaglypts usually vary in size, but, when they are very well developed, they can have a

**Table 2-6: Meteorite shapes which have been previously mentioned and discussed in the literature, with examples of meteorites which display the characteristic shapes (Buchwald, 1975c:46)**

| Rough shape of meteorite | Meteorite examples |
|---|---|
| Airfoil | Costilla Peak, Jamestown |
| Shield / very low cones | Cabin Creek, Davis Mountains |
| Low cones | Chebankol, Henbury |
| High cones | Freda, Grant |
| Spheroidal / with spheroidal parts | Bogou, Briggsdale |
| Drop / pear | Bingera, Boogaldi |
| Crescent | Bushman Land, Morradal |
| Oblate lenses (discoid) | Ballinoo, Colomera |
| Prolate lenses (ovoid-cylindrical) | Babb's Mill (Blake), Juromenha |
| Tongue | Nedagolla |
| Large, flat | Chupaderos, Campo del Cielo |
| Large, ear-shaped | Bacubirito, Tucson (Carleton) |
| Thin, flat plates | Arlington, Bingera |
| Elongated, prismatic | Guffey, Kopjes Vlei |
| Dumbbell | Savannah |
| Foot | Bald Eagle, Signal Mountain |
| Octahedral, pyramidal | Lazarev, Sikhote-Alin |
| Hexahedral, cubic | Boguslavka, Calico Rock |
| Angular, irregular | Canyon Diablo, Gibeon |
| Same re-entrant angles, extremely irregular | Bahjoi, Silver Crown |
| Spikes, icicles | Glorieta Mountains, San Cristobal |
| Rings / imperfect rings | Hex River, Kokstad |
| Bombshells, twisted slugs, slicken-sided | Canyon Diablo, Henbury |

diameter of about a tenth of the meteorite size, when measured perpendicular to their movement direction (Buchwald, 1975c:47).

On examination of certain regmaglypts, iron meteorites have been found to travel through the atmosphere in such a position that they encounter a maximum-drag orientation. However, meteorites that keep tumbling through the atmosphere will tend to lead to the regmaglypts involved being more equiaxial and more evenly distributed over the whole meteorite surface. Oriented meteorites, in contrast, contain regmaglypts that are elongated in the flight direction, and which, therefore, can indicate the apex of the meteorite (Buchwald, 1975c:48).

In the past, the creation of regmaglypts has been debated as being due to the burning of some low-melting minerals (troilite, schreibersite). However, such a supposition cannot be true, as the regmaglypts found are often spaced too densely, and tend to be much too regularly arranged, with iron meteorites with almost homogenous structures, like Gibeon, usually also displaying regmaglypts. The greater part of regmaglypts have been found to have been formed during the high velocity part of the meteorite's trajectory. Cone-shaped meteorites (Table 2-6) show a difference between the regmaglypts that are found on the flat rear side and on the tapering sides. The flat rear side shows shallow and very wide regmaglypts, while the tapering sides show deep, elongated grooves originating at, and radiating from, the apex. Fully regmaglypt-covered meteorites can, thus, be said to have very steep entries into the atmosphere, with short trajectories inside the low velocity region (Buchwald, 1975c:49).

## 2.6 Alternative classification schemes for meteorites

Specific classification schemes exist for chondrites as well. Further classification schemes can be used to divide the chondrites than that which is mentioned in section 2.3.1. Such types of classification require optical observation to determine the weathering grade, the petrologic type (mineralogical and textural variation) and the shock grade of the chondrites involved (Lombard, 2010:6). The shock effects, which can be seen by means of looking at the textural and mineralogical alteration that is present in olivine and plagioclase, can be extended to orthopyroxene in enstatite chondrites, due to the lack of olivine (Lombard, 2010:7). Weathering classification can be undertaken either just by means of examining a hand sample or by means of looking for oxidation alteration in a polished section (Lombard, 2010:8). Complete tables of petrologic type, weathering and shock classification of chondrites can be found in Lombard (2010).

## 2.7 The Etosha meteorite

The Etosha meteorite is described by Frick and Viljoen (1973:345) and by Frick and Hammerbeck (1973:16) as consisting of an approximately 111 kg mass of iron that was found, in 1970, in the Etosha National Park in Namibia (Buchwald, 1975c:1384). Frick and Viljoen (1973:345), who did not investigate the main mass as such, yet described a thin black crust identified as hematite on the small sample* provided for their investigation. They also found the matrix of the meteorite to be uniform, while the freshly cut surface had undergone some differential destruction. When the sample was etched with acid, the authors found thick kamacite lamellae of 1,0 to 1,5 mm of the Widmanstätten structure. Fanlike structures, consisting of schreibersite and cohenite, were also found in isolated areas of the meteorite matrix. Finally, they found the Widmanstätten structure to be interrupted near the fanlike textures, where the kamacite becomes more granular (Frick & Viljoen, 1973:345).

The petrographic investigation by Frick and Viljoen (1973:345) reported the presence of the following minerals: kamacite; taenite; plessite; cohenite; schreibersite; rhabdite; iron phosphate; and silicates. In the polished sections, two different areas were found to be present, in terms of texture and mineralogy. The first area was identified as being coarse-grained, containing the Widmanstätten structure and covering most of the meteorite. The other area, which is fine-grained and granular, is associated mostly with cohenite and schreibersite inclusions (Frick & Viljoen, 1973:345).

Cohenite was found to consist of coarse, elongated and anhedral grains in isolated parts of the matrix. The schreibersite appear as veins in the coarse cohenite grains, and also as ribbon-shaped inclusions along the kamacite-cohenite grain boundaries (Frick & Viljoen, 1973:346). Inside the thick kamacite lamellae, fine, prismatic, and euhedral rhabdite grains have been found as inclusions. Lastly, fine inclusions and veins (0,02 mm) of silicate were found in both the nickel-iron matrix of the meteorite, as well as in the cohenite grains (Frick & Viljoen, 1973:346-347).

Waanders and Bate (s.a.:5) determined the chemistry of the Etosha meteorite using electron microscopy and Mössbauer spectroscopy of the crust, as well as of the core, of the meteorite. The electron microscopy of the core showed that the Fe-Ni content in the kamacite lamellae has remained constant, with the Fe-Ni content of the taenite lamella showing different domains in the lamella, namely Ni-poor (25-30 wt. % Ni) and Ni-rich (>30 wt. % Ni) domains. The Mössbauer analysis of the crust revealed that the outer crust consists of 95 wt. % hematite, meaning that the crust formed either during or after the meteorite's penetration of the Earth's atmosphere. When a conversion electron Mössbauer spectroscopic (CEMS) study was undertaken into the meteorite,

three phases were discovered: a kamacite phase (83% of the meteorite), an ordered ferromagnetic noncubic phase (14% of the meteorite) and a disordered paramagnetic cubic phase (3% of the meteorite) (Waanders & Bate, s.a.:5-8).

The chemical analyses of the Etosha meteorite showed that the major elements include Ni, Fe and P, together with the minor elements, Co, and C. The Ni-rich phases of taenite and schreibersite were also found to be more enriched in Co, when compared with the other elements. In contrast, the Ni content of the kamacite decreases sharply when it occurs near the schreibersite, the Co behaves in the same way as does the Ni in the meteorite. Lastly, the Ni enrichment in the schreibersite was found to be larger than in the taenite, meaning that the Ni extraction by phosphide led to a greater concentration of Ni than did either the exsolution of Ni from the kamacite, or the exsolution of Ni from the crystallising cohenite (Frick & Viljoen, 1973:347). Frick and Viljoen (1973:347) showed that the Etosha meteorite differed in Ni content from that of the Gibeon meteorites, central Namibia. Based on the chemistry available at the time, the Etosha meteorite was considered not to be part of the Gibeon meteorite shower.

### 2.8 Sub-Saharan African meteorites

Although most meteorite searches undertaken on the African continent have been conducted in the Sahara Desert (Bevan, 2006:325), according to Khiri *et al.* (2017:651) and Khiri and Ibhi (2015:2), the majority of countries that share a border with the desert show a high recovery rate of meteorites. Such a finding can be seen in Figure 1-2, where a few countries that share a border with the Sahara Desert (such as Mauritania, Mali and Niger) display a high number of meteorites found. The Meteoritical Bulletin Database (2021) provides data for 28 of the 48 SSA countries. The countries that, as yet, lack relevant data can be seen in Table 2-7. Most of the countries that still lack such data have smaller surface areas, as can also be seen in Figure 1-2.

Various reasons exist why some countries in SSA lack meteorite data. For example, certain countries lack the necessary knowledge and skills when it comes to meteorites (Khiri *et al.*, 2015:118). Other factors that might limit meteorite recoveries are that certain areas are still covered with dense forest cover, while the population distribution of specific countries might be another such factor (Khiri *et al.*, 2015:118). Some countries might also lack data due to their possession of an unsuitable climate, as some weather conditions might speed up the weathering or oxidation of meteorites, meaning that they will be likely to last a relatively short time on the Earth's surface (Ouknine *et al.*, 2019:10).

**Table 2-7: SSA countries without available data on the date of data collection (17 October 2021) on the Meteoritical Bulletin Database (2021)**

| | |
|---|---|
| Seychelles | Togo |
| Comoros | Ivory Coast |
| Mozambique | Liberia |
| Burundi | Sierra Leone |
| Gabon | Guinea |
| Equatorial Guinea | Guinea-Bissau |
| Sao Tome & Principe | Gambia |
| Djibouti | Senegal |
| Eritrea | Cape Verde |
| Benin | Réunion |

# CHAPTER 3 METHODS AND MATERIALS

## 3.1 Introduction

Meteorite analysis requires the use of non-destructive methods of analysis, due to the fact that meteorite samples are usually small and rare, and require preservation for future study (Lombard, 2010:25). In the current chapter, the acquisition and preparation of the sample made available for the present research is discussed in detail, as well as are the analytical methods that were used to investigate the mineralogy and geochemistry of the meteorite concerned. Most of the methods used in this study are non-destructive.

## 3.2 Sample preparation

The meteorite studied is currently part of the collection of the geology museum of the NWU, Potchefstroom campus. The sample that was analysed had to be prepared before petrographic and chemical analysis could commence (Reed, 2005:149). Due to the size of the Etosha meteorite (Figure 3-1), two relatively small samples were collected and prepared for use in the analysis, which did not influence the size of the meteorite significantly. The samples were removed using a grinder with a normal steel-cutting disc.

**Figure 3-1: Front view of the Etosha meteorite located in the Andries Bischoff meteorite at the NWU. Scale = 15 cm.**

The samples were trimmed down to an appropriate size (3,5 mm × 2,5 mm) for incorporation in a polished section. The trimming was done using the Struers Accutom-50 precision cut-off machine, with a relatively thin piece of the sample being cut off by means of a diamond saw. The possibility of contamination due to the blade used cannot be eliminated because of a diamond saw with water being used. The meteorite piece was then placed in resin and left to set, whereupon it was placed in a desiccator that was attached to a DryVac air pump, so as to ensure that all the air bubbles were extracted from the piece. The sample was kept inside the desiccator for two days.

A grinding wheel with a 120-grit disc was used to reduce the size of the resin around the sample. When an appropriate size was attained. The Struers LaboPol-5 polishing machine, fitted with a 150 grit (coarse) disc, all the way to a 220-grit (fine) disc, was then used to further reduce the size of the resin. Thereafter, a 400-grit disc was used in the LaboPol-5, so as to enable the further removal of some of the resin, until the surface of the sample was exposed. DiaDuo polishing liquid, which is impregnated with diamond, was then utilised, together with a 1200-grit disc, to begin the polishing process. A 3-µm disc was ultimately used with the polishing liquid to polish the sample to its final state. The polished samples were then used for the RL microscopy and pXRF. The polished sections were coated with a carbon coating prior to analysis in the SEM and the EPMA. The XRD analyses required the use of a single 1 cm x 1 cm rough block of the sample, and not a powdered sample due to the hardness of the meteorite and difficulty that would have been encountered in preparing sufficiently fine powdered material for the analyses. The LA-ICP-MS required the 1 cm x 1 cm rough blocks to be mounted in a 2,5 cm block of resin for analysis, which also had to be polished. The two polished samples were then used for the acid etching and re-examination under RL.

### 3.2.1 Acid etching

Acid etching was done to reveal the kamacite bands of the Widmanstätten structure. The acid etching of the Etosha meteorite was conducted according to the method described in Nininger (1945), with a 1% nitric acid solution on one polished section, as well as a 6% solution on the other polished section. The sample was first ground and polished, mainly to remove the carbon coating applied during the EPMA and SEM, whereafter the sample was polished, so as to ensure that the surface was free of any scratches. After the nitric acid solution was poured into a porcelain dish, a small, soft brush was rinsed and dried. The sample was held above the dish, while the brush was dipped in the acid and then brushed over the sample, and then redipped and rebrushed. The process was repeated continuously, so as to ensure that the acid did not remain

on a single spot on the sample overly long. The process was then repeated for about five minutes, or until the structure became visible.

After the structure was visible and the etching was complete, the samples were rinsed with tap water, so as to remove any residual acid. The samples were then dried with soft paper towels and left for about ten minutes, so as to ensure that they became completely dry. Baby oil was then applied in a thin layer, so as to ensure that no oxidation could take place.

## 3.3 Analytical methods

Following the preparation of the meteorite samples, they were analysed, using different analytical methods. Each of the analytical methods will be discussed in this section, as well as the type of instrument used to conduct the analyses. The results obtained will be provided in the next chapter, together with their associated discussion.

### 3.3.1 SEM

In a SEM, a small, focused beam of electrons is scanned over a sample area, which can consist of finer particles or be a polished section (Klein & Dutrow, 2007:323). When the electron beam is scanned onto the surface of the material, backscattered electron (BSE) images and secondary electron images are produced from the radiation signals that are recorded (Klein & Dutrow, 2007:323; Lombard, 2010:27). The BSE images tend to offer important information, as they produce a greyscale image that can be compared to the chemical composition of the scanned sample, as they greyscale colour varies with the different atomic numbers of the different elements present (Bian *et al.*, 2020:1070; Lombard, 2010:28).

The SEM is used mainly for the study of the composition and the morphology on both the micro- and nano-scale (Thompson, 2017:36). Combining a SEM with an energy dispersive spectrometer (EDS) enables the determining of the composition of a sample area (Bian *et al.*, 2020:1070; Thompson, 2017:36). The advantages of the SEM include high-resolution, three-dimensional electronic imaging, along with increased and continuously adjustable magnification. The EDS also has a few advantages, fast analysis speed, ability to analyse for all the measurable elements in one line, and a higher detection efficiency (Bian *et al.*, 2020:1070). The carbon-coated polished sample was placed onto a stub, which enabled the sample to be placed into the SEM for analysis.

The meteorite sample was analysed with the SEM, so as to confirm the elements and minerals present in the sample, before placing it in the EMP. This was done to ensure that the calibration of the instrument was performed to correctly identify the minerals in the sample. The Tescan Vega3 SBH, with an EDS detector from EDAX (30 $mm^2$ Element silicon drift detector (SDD)), at the University of Johannesburg, was used for the analysis.

The beam intensity of the SEM was set to normal for a single area, after which the intensity was increased significantly, which increased the counting time. The accelerated counting resulted in sum peaks in the spectra. Automatic labelling led to some possible incorrect labelling of the sum peaks, with the minerals involved possibly then having been identified incorrectly. It is, therefore, recommended that the peak labels be revised and compared to known peaks, after the results are obtained, to ensure the correct labelling of the peaks.

### 3.3.2 EMP analysis

The EMP method utilises the X-ray spectrum to chemically analyse a localised area of a specific sample, by means of bombarding it with a focused electron beam. Although, in theory, the EMP can detect elements all the way from atomic number 4 (Be) up to atomic number 92 (U), not all EMP instruments are equipped to cope with such a large range of elements (Reed, 1995:49). When the electron beam is focused on the material, it emits X-rays back in a specific wavelength that can be analysed to determine which elements are present (Reed, 2005:1). This method of analysis is widely used, due to its high spatial resolution, its low detection limits, its accuracy, and its simple sample preparation, as well as due to it being a non-destructive, in situ method (Reed, 1995:50). SEM is closely related to the EMP, as it also utilises an electron beam, although the SEM is mainly used for imaging purposes, rather than for analysis (Reed, 2005:1).

The CAMECA sx100 EMP of the University of Johannesburg was used in this study. The column conditions of the probe are provided in Table 3-1. The analyses were done in two parts, with the first part entailing the analysis of the sample for the major elements present therein, whereas the second part analysed only a few trace elements. The intensity of the two parts differed, as a higher intensity was required to detect the trace elements that were needed for the detection of the major elements. Therefore part 1 had an intensity of only 30 nA, whereas part 2 had an intensity of 180 nA (Table 3-1). The wavelength dispersive spectrometer (WDS) has four different diffracting crystals, each of which is dedicated to a known range of X-ray wavelengths (CAMECA & Ametek, 2018:17). Another difference between the two parts consisted of a combination of the diffracting crystals used, the specifics of which can be seen in Table 3-1.

**Table 3-1: Column conditions of the CAMECA sx100 electron microprobe during analysis**

| Parameters | Part 1 (major elements) | Part 2 (trace elements) |
|---|---|---|
| **Elements analysed** | Ni, Fe, P, Cu, Co, Cr and S | P, Ga, and Ge |
| **High voltage (kV)** | 20 | 20 |
| **Current intensity (nA)** | 30 | 180 |
| **Size (µm)** | 1 | 1 |
| **Raster length (µm)** | 59 | 59 |
| **Scanning** | Off | Off |
| **Diffracting crystals used** | LiF<br>PET<br>LLiF | PET<br>TAP<br>LPET |

The EMP was calibrated before the analyses were done. The calibration samples included elements that were obtained through the SEM analysis, which were, therefore, known to be present in the meteorite samples. On completion of the calibration, the meteorite samples were inserted into the sample holder, while being secured with carbon-coated tape, and inserted into the EMP through the airlock. The samples were then analysed using the EMP, with various backscattered electron images being taken during the process. A limitation with the samples occurred on realising that one of the polished sections had small 'pits' in the centre of the sample, which affected the mineral analysis. The limitation was countered by means of increasing the zoom of the RL microscope, so as to be able to focus on the minerals without pits.

### 3.3.3 RL microscopy

RL microscopy is used to identify the minerals, textures and structures that are present in a meteorite. The RL, or ore, microscope is commonly used to examine the minerals that appear as 'opaque' under petrographic microscopes. The microscope closely resembles the traditional petrographic microscope, with the only difference being the position of the source of light, which, in the case of the RL microscope, is above the sample, so as to allow the light to reflect off its polished surface (Craig & Vaughan, 1994:1).

The Nikon Eclipse 200 POL microscope from the NWU's Potchefstroom campus was utilised in the current study. The microscope was fitted with a high definition 5.9-megapixel colour complementary metal oxide semiconductor (CMOS) image sensor, which was able to capture the images involved, with the NIS-Elements software then being used to extract the images from the

microscope. With the polished sample placed under the microscope for analysis, various photographs were taken of the minerals identified. After the sample was acid etched, it was again investigated under the RL microscope, so as to determine the thickness of the kamacite and taenite bands, for purposes of classification, as well as to discover how the etching had affected the minerals.

### 3.3.4 pXRF

The pXRF, which can be used to determine the bulk chemistry of a material, was created for the mining and metallurgical industries (Gemelli *et al.*, 2014:56). The method adopted followed the same process as that used by Gemelli *et al.* (2014). The NITON XL3t GOLDD+ XRF spectrometer of the NWU's Potchefstroom campus was used in the current study. A miniaturised X-ray tube, fitted with a silver (Ag) anode (50 kV, 200 µA, 2 W), was provided for the instrument, and an SDD was also attached that could receive different X-ray spectra at high count rates. The equipped X-ray tube can operate at much higher outputs than the instruments that are equipped with a Si(PIN) detector.

Among the different measuring modes of 'Mining', 'Soil' and 'General Metals', the 'Mining Ta/Hf' mode was utilised throughout the analysis. The use of this mode determined the concentrations of Mg, Al, Si, P, S, Cl, As, K, Ca, Ti, V, Cr, Mn, Fe, Co, Ni, Hf, Re, W, Pb, Bi, Zr, Ta, Nb, Mo, Sn, Ba, Sb, Cd, Pd, Sr, Rb, Se, Ag and Au. So as to ensure that the analysis could be optimised, such use required the instrument to be able to operate under various conditions, namely 'main' (excitation 50 kV, 40 µA), 'low' (15 kV, 133 µA) and 'light' (8 kV, 200 µA). The limit of detection (LOD) for each analyte was determined as being three times the standard deviation of the concentration measured in the samples that contained no, or only, trace amounts of the same analyte.

The pXRF had a total counting time of 120 seconds for each analysis. The built-in software of the XL3t used a correction algorithm ('Fundamental Parameters') containing corrections to the measured X-ray counts, which accounted for the differences in X-ray absorption, emission, secondary fluorescence and other phenomena that might occur. The samples were placed in the analytical plane of the instrument, with the beam diameter involved being 8 mm. The resulting spectra were then transferred onto a computer, using Niton Data Transfer 8.0.1 software. Many advantages can be gained from using such a method, which is probably why the method is so frequently used. The advantages involved include: the minimal sample preparation required; its

precise and accurate analysis of bulk chemistry; its non-destructiveness; its portability; and its rapid analysis (Gemelli *et al.*, 2014:66-67).

In the current study, the two polished samples were placed flat on the work surface, while the pXRF analyser was held perpendicular to the sample. A grid pattern was, as far as possible, followed on the samples (Figure 3-2). The method concerned was followed for both polished samples. A disadvantage encountered during the analyses was the very small size of the samples (3,5 mm × 2,5 mm), which made it difficult to follow a comprehensive grid, with the beam diameter being 8 mm. Another disadvantage was that the samples were not correctly sized (in terms of a normal thin section), preventing use of the stand. The above meant that only a rough, and imprecise, grid could be followed during the analyses, which might have affected the results negatively. Due to the large beam diameter of the pXRF instrument, some overlapping might have occurred, especially in terms of sample A. The points analysed were each assigned a number from 1 to 40 for Sample A (SA) or from 1 to 15 for Sample B (SB).

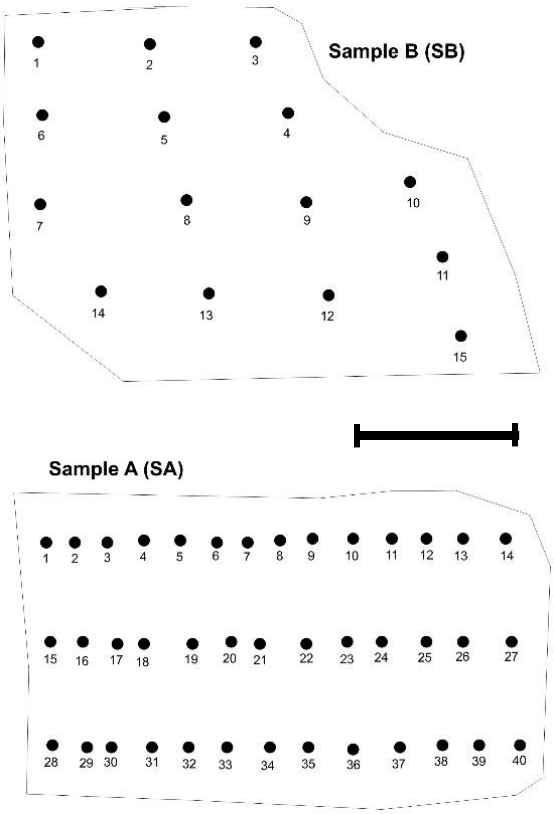


**Figure 3-2: Plotted points on sample A and sample B that was analysed with the NITON XL3t GOLDD+ XRF spectrometer. Scale = 10 mm.**

### 3.3.5 XRD

In the past, XRD techniques have been considered as vital for the analysis of crystal structures (Klein & Dutrow, 2007:308). When the X-ray beam hits an object with a three-dimensional arrangement, such as a crystal, it causes electrons in the structure to start vibrating at the same frequency as the incident X-ray beam. The electrons ultimately absorb some of the energy of the incident X-ray, which they then emit as X-radiation waves, with the same wavelength and frequency. The constructive interference of the outgoing waves is termed 'diffraction' (Klein & Dutrow, 2007:311). Two types of XRD techniques exist, namely single-crystal XRD and X-ray powder diffraction.

Single-crystal XRD refers to an X-ray beam that interacts with a single crystal, of about 1 mm or less, of a mineral in the sample. The interaction leads to the abovementioned XRD effects, which are recorded on an electronic device (Klein & Dutrow, 2007:313). X-ray powder diffraction, in contrast, refers to the original sample being ground to a fine powder, after which it is either bonded with some type of amorphous material to form a spindle, or else spread out across a glass slide. When enough powder is present after grinding, it can be placed into a special rectangular sample holder (Klein & Dutrow, 2007:317).

Another less conventional method used during XRD analysis is the method where there is no prior sample preparation, and the sample is analaysed as is. The method utilises energy dispersive XRD with back-reflection geometry and can be described as non-destructive. This method however does not take sample morphology and the positioning of the sample into consideration during analysis, even with a high-resolution configuration. This method requires low energy X-rays that have a low penetrating power. Therefore this method can be described as a surface analysis, reflection-mode XRD method (Hansford *et al.*, 2017:293). This method was utilised in this study due to the fact that the meteorite was very difficult to ground finer due to its hardness.

The Etosha meteorite sample was analysed at XRD Analytical & Consulting in Pretoria. The meteorite sample was cut to an appropriate thickness to fit into the universal sample holder. The diffractograms were produced by a Malvern Panalytical Aeris diffractometer with PIXcel detector and fixed slits with Fe-filtered Co-Kα radiation. The phases in the sample were identified using X'Pert Highscore plus software. The relative phase amounts in weight percentage were projected using the Rietveld method. The results achieved might not have been very accurate, due to the preferred orientation, as well as the crystallite size effects, which might have been a disadvantage. Another possible disadvantage of using this method is that the mineral names obtained might,

instead of reflecting the real composition of the mineral, rather reflect the composition of the mineral group concerned. Therefore, the results attained will be compared with the existing results, so as to ensure that the minerals recorded by the XRD correspond with those found in the meteorite in the previous literature.

### 3.3.6 ICP-MS

The ICP-MS technique is used to determine the presence of both trace and major elements, as well as especially the rare earth elements (REEs) that are present in the material (Ashrit *et al.*, 2018:973; Lombard, 2010:26). According to Pinto *et al.* (2012:1540), the analysis of such geological samples as rocks requires the undertaking of a very complex and long process, including the crushing, powdering and digestion of the sample for it to be viable to use in spectrometers like the ICP-MS. However, because the meteorite sample needed to be preserved for use in future studies, the sample could not be completely digested.

Laser ablation inductively coupled plasma mass spectrometry (LA-ICP-MS) was utilised in the current study to analyse the trace elements present in the meteorite, especially in terms of the concentrations of Ga, Ge and Ir, for the classification of the meteorite. The technique focuses a laser beam on the surface of the sample, which is contained within an ablation cell. The sample, which is ablated due to the beam, is turned into a gas, which is then transported as aerosols by a carrier gas into the ICP, which ionises them. After the ionisation of the aerosols, the ions with differing mass-to-charge ratios are filtered through the MS system, where they are detected by means of the detector (Hattendorf *et al.*, 2003:342 A; Liu *et al.*, 2013:3863). The main advantage of the LA-ICP-MS is its flexibility regarding what elements can be analysed (Hattendorf *et al.*, 2003:342 A), as well as its low cost and the short duration of each individual analysis (Koŝler, 2007:19). LA-ICP-MS is a widely accepted method for direct sampling of solid materials for trace elemental analysis, and it was used in this study due to its easy sample preparation.

The sample was analysed at Stellenbosch University, using the Applied Spectra Resolution 193-nm Excimer, connected to the Agilent 8800 QQQ ICP-MS. The ablation occurred in a sample cell filled with Helium (He). The ablated material was mixed with Argon (Ar), as well as with minimal Nitrogen (N), prior to being transported to the ICP-MS. The settings of the ICP-MS were initially optimised for low oxide ratios (<0,4%) and best sensitivity, while ablating on NIST612. The required elements were obtained with dwell times between 10 and 20 milliseconds, so as to reach a total sweep time of 631 milliseconds. The settings for the ICP-MS, as well as for the laser ablation, can be found in Table 3-2 and Table 3-3, respectively.

**Table 3-2: Information regarding the type of ICP-MS instrument used, as well as the settings that were used for the analysis of the Etosha meteorite**

| **ICP-MS instrument** | Agilent 8800 |
|---|---|
| **ICP-MS software** | Mass Hunter v4.5 |
| **ICP-MS settings** | |
| **RF Power (W)** | 1450 |
| **Carrier gas (L/min)** | 0,95 |
| **Sample depth (mm)** | 4 |
| **He cell gas flow (ml/min)** | n/a |
| **$H_2$ cell gas flow (ml/min)** | n/a |
| **$O_2$ cell gas flow (ml/min)** | 0,7 L/min |
| **Type of detector** | Photo multiplier |

**Table 3-3: Information regarding the type of laser ablation instrument used along with the ICP-MS instrument, as well as the settings that were used for the analysis of the Etosha meteorite**

| **Laser ablation instrument** | 193 nm Resolution M50 SE Excimer |
|---|---|
| **Controlling software** | GeoStar v10.13 |
| **Laser settings** | |
| **Frequency (Hz)** | 8 |
| **Fluence (J/cm$^2$)** | 2,8 |
| **Spot size (µm)** | 40 |
| **Ablation gas (He) flow (ml/min)** | 500 |
| **Additional gas ($N_2$) flow (ml/min)** | 3 |
| **Background acquisition time (sec)** | 20 |
| **Ablation time (sec)** | 40 |
| **Washout time (sec)** | 25 |

The calibration standards used include NIST610, BHVO-2G and Po 725 sulfide. Such standards were used, along with the standard calibration method of sample bracketing every 15 to 20 samples. The calibration of BCR-2G and BHVO-2G values was performed from GeoReM (Jochum *et al.*, 2005). The data concerned was processed by means of using the LA-ICP-MS data reduction software package, LADR, from Norris Scientific (Norris & Danyushevsky, 2018). An internal standard element ($^{57}$Fe) was used to correct for the variations that occurred in ablation

yield between the samples and standards involved (Longerich *et al.*, 1996). The final concentrations were determined by means of normalising the total element components to 100%, but by means of ensuring that the summed signal stayed proportional to the material ablated (Leach & Hieftje, 2000). The detection limit was also calculated and provided in the data.

### 3.4 Data analyses

In the current section, the presentation of the data obtained through the methods mentioned in the previous section will be discussed. The results obtained are provided in the Appendices section.

#### 3.4.1 EPMA

The results obtained through EMP were received in terms of the weight percentage of the elements present in each mineral grain analysed. Achieving such results assisted in identifying and classifying the minerals present in the meteorite. The quantities obtained in weight percentage per mineral were initially normalised, so as to ensure that the total percentage in each mineral was between 98 and 102 wt. %. The minerals were firstly grouped into major groups, according to the Fe, Ni and P percentages, which display different mineral assemblages (Klein & Dutrow, 2007:257,259). After the classification, other minor trends were noted, and additional groups were created.

The quantities of elements per mineral obtained were then plotted onto a Fe-Ni-P ternary phase diagram, so as to be able to determine the minerals concerned. The plotting was done in line with ternary diagrams being known to represent the crystallisation sequence of minerals from a melt or from the melting relations of rock compositions, as well as from the mineral assemblage present in a rock (Klein & Dutrow, 2007:256). The plotting of Fe-Ni binary diagrams was done in the R program, together with the GCDkit. The above was done while also comparing the BSE images to the mineral chemistries. After the mineral names were determined, tables were devised to show the mineral chemistries, which were then compared to the previous chemistries obtained by Frick and Viljoen (1973), so as to be able to observe any differences present in the data.

### 3.4.2 SEM

Use of the SEM method produced BSE images of the meteorites, which were used to classify the meteorite, based on the mineralogy identified in the BSE images. In addition, the composition of selected areas in the sample was produced, which assisted in identifying the minerals present in the meteorite, by means of enabling the comparing of the mineral chemistry obtained (along with its BSE image) with the results obtained with the EPMA, so as to be able to identify the minerals present in the meteorite still further. The minerals were identified by means of various structures that can also be identified in the minerals and BSE images available (Khalaf *et al.*, 2014:4819).

### 3.4.3 Reflected light (RL) microscopy

The results are presented through the use of photomicrographs that assisted in classifying the meteorite. The images obtained were used to show the different textures (Craig & Vaughan, 1994:120), structures and minerals present in the meteorite, which assisted with the meteorite classification. The RL microscope was used to identify and measure the kamacite bandwidths in the meteorite. The kamacite bandwidths were then presented, in the form of a table, so as to be able to compare them to the standard bandwidths, so as to be able to classify the meteorite structurally, according to the contents of

Table 2-5 (Buchwald, 1975c:66). The images were then used, together with the BSE images obtained from the EPMA, to identify the minerals present in the meteorite.

### 3.4.4 pXRF

The data obtained through the pXRF was provided in weight percentages of the elements present, in the format of a Microsoft Excel spreadsheet. The data had to be reworked in the Microsoft Excel spreadsheet, so as to ensure that it was in the correct format for the analyses. The R program was used for the analysis of the data, along with the GCDkit package, which was used due to its capability to manage and recalculate the whole-rock geochemistry of igneous and metamorphic rocks (Janoušek *et al.*, 2006:1256). Various graphs were created using this program, with the chemical elements concerned being compared to one another, so as to be able to determine any correlation between the specific elements involved, and comparison graphs were also created by means of comparing the meteorite data with chondrites, mid-ocean ridge basalts (MORBs), and

so on. The points analysed on the samples were plotted on the sample outlines using Surfer, version 19.

### 3.4.5 XRD

The results for XRD were obtained in peak counts, which were used for analysis. The use of peak counts led to the minerals being identified and presented as well. The peaks were used in the analyses both to show the nature of the minerals present in the meteorite and to confirm the presence of the minerals obtained through the other methods of analysis (X-ray fluorescence (XRF), EPMA, etc.) used (Ali *et al.*, 2022:4).

### 3.4.6 ICP-MS

Although the Fe was utilised as a standardisation element, a specific quantity was not used. The method used included obtaining a sum of the element totals to either 100 wt. % for the spots with very high Fe content, or else summing up the total to 85 wt. % for those spots with low Fe content, where P could be present, but was not included in the analysis (Appendix B, Table B-1). The results obtained by the LA-ICP-MS, which were given in parts per million and weight percentage, were presented in tables, as well as in geochemical graphs. The received data was organised in Microsoft Excel, after which it was processed through the R program, along with GCDkit. Binary graphs were created with Ni against the logarithmic plots of Ga and Ge, so as to establish the chemical classification of the meteorite (Scott & Wasson, 1975:529).

### 3.4.7 Sub-Saharan meteorite distribution (type, classification and locality)

Firstly, literature reviews were done to determine which African countries fall within the sub-Saharan region (Majgaard & Mingat, 2012:24). After this was established, the Meteoritical Bulletin Database (2021) was used to enter the relevant details of each country manually, noting the information available for all the meteorites found in the country. The data was then captured on Microsoft Excel, in which system it was organised and stored. However, the coverage of countries was limited, as the Meteoritical Bulletin database lacked the necessary data for approximately 20 sub-Saharan countries. Use of the method was also very time-consuming, as each country had to be searched individually, with the information pertaining to each meteorite of that country also having to be individually captured. However, the advantage of using the method was that the Meteoritical Bulletin Database (2021) contained very detailed information about most of the

relevant meteorites, and the use of Microsoft Excel facilitated the process of data capturing and organising.

The meteorite distribution in SSA was presented in the form of graphs through the use of statistical methods employed by Microsoft Excel relating to the data retrieved from the Meteoritical Bulletin Database on 17 October 2021 (Meteoritical Bulletin Database, 2021). The ‘Analyse Data’ tool on Microsoft Excel was used to identify trends and variations in the data. The graphs then created using the analysis done by Microsoft Excel included line and column graphs, pie charts and various tables created by the analysis tool.

### 3.4.8 GIS

GIS was used to create various maps by means of using the data from the Meteoritical Bulletin Database to display the distribution of meteorites in SSA. This analysis technique was used because of the many functions of GIS, including visualisation, exploration, analysis, and the identification of patterns, trends and relationships in the data, which are not so noticeable in Microsoft Excel (Reddy, 2018:48). The Microsoft Excel database mentioned above was used to import the data into ArcGIS Pro. Once the data was imported, different maps were created, highlighting the distribution of meteorites in SSA. The maps generated include the overall distribution of meteorites, the dominant type of meteorite per country, the comparison of finds and falls per country, the total weight of meteorites per country, and the amount of iron meteorites with the same classification as the Etosha meteorite per country.

ArcGIS Pro 2.7 was used to create the maps, which were exported in jpeg format with 300 dots per inch. Using GIS provides various advantages: it presents the required data in an easily understandable manner; different types of maps can be created by means of using the same datasets; and it provides various tools that can help with analysing data. However, there are also limitations to using ArcGIS. In particular, the program software is very expensive; to operate the program, extensive in-depth knowledge is required; and when a very large dataset is used, the processing time can be exceptionally long (Reddy, 2018:53).

# CHAPTER 4 RESULTS AND DISCUSSION

## 4.1 Introduction

The current chapter presents the details of (1) the relevant photographs; (2) the pertinent geochemistry; (3) the minerals identified, with their quantitative and qualitative chemistry; and (4) the petrographic/textural characteristics of the Etosha meteorite, as well as the historical data of SSA meteorites.

## 4.2 Macroscopic description of Etosha meteorite

The Etosha meteorite, which can be found in the geology museum of the NWU, is shown in Figure 4-1. The dimensions of the meteorite are 47 cm × 43 cm. The meteorite is comparatively small in size when considering its weight (111 kg).

**Figure 4-1: Front view of the Etosha meteorite located in the Andries Bischoff meteorite at the NWU. Scale = 15 cm.**

The reason for the above is that the Etosha meteorite consists mainly of Fe and Ni, so it has a high specific density (Pesonen *et al.*, 1993:402). The meteorite has also been found to be

magnetic. The shape and form of the Etosha meteorite can clearly be seen in **Error! Reference s ource not found.**(a) and (b). The overall shape of the meteorite can be described as pyramidal (Heide & Wlotzka, 1995:107), angular, asymmetric and uneven, with some sharp edges (Figure 4-1) (Buchwald, 1975c:45-46). The colour of the meteorite ranges from a dark grey to brown (from a rusty to a light brown) (**Error! Reference source not found.** (a) and (b)). Therefore, no fusion c rust can be seen on the Etosha meteorite (Buchwald, 1975b:1384), as, instead of displaying a black, leather-type texture, the outer layer is, rather, brown in colour, which is consistent with the iron oxides that form due to the rapid terrestrial weathering of a meteorite after it has landed on the Earth's surface (Heide & Wlotzka, 1995:112; Pourkhorsandi *et al.*, 2019:1752).


**Figure 4-2: (a) Back and (b) side view of the Etosha meteorite located in the Andries Bischoff meteorite at the NWU. Scale = 15 cm.**

The several large regmaglypts that can be seen on one side of the meteorite are shown in Figure 4-3. The regmaglypts concerned represent thumblike impressions that are left on the surface of the meteorite, due to the ablation that occurred during the meteorite's journey through the Earth's atmosphere, as described by Buchwald (Buchwald, 1975c:47). Both **Error! Reference source not found.** and Figure 4-3 clearly show that the regmaglypts occur throughout the surface of the meteorite, which is consistent with Buchwald (1975c:47) finding that they commonly occur in iron meteorites. Figure 4-4 indicates that the regmaglypts from the one side of the meteorite, as shown in Figure 4-3, continue to the base.

**Figure 4-3: Regmaglypts present on the Etosha meteorite located in the Andries Bischoff meteorite at the NWU. Scale = 15 cm.**

**Figure 4-4: Base view of the Etosha meteorite located in the Andries Bischoff meteorite at the NWU. Scale = 15 cm.**

Figure 4-4 indicates that there is a slight colour difference at the top of the meteorite, meaning that the heat endured during the meteorite's fall to the Earth's surface has not affected this part of the meteorite as much as it has the remainder of the surface of the meteorite. In Figure 4-4, the regmaglypts can be seen to be much larger and deeper than are those that are shown in **Error! Reference source not found.** and Figure 4-3. Another surface feature to be seen on the meteorite is the shallow grooves that are present in Figure 4-5. Whether the features have formed naturally, or whether they have resulted from human testing or sampling, is unknown. If the features are natural, they probably formed when the meteorite fell onto the Earth, when it was still

very hot and impressionable. Hasegawa (1981:293) found that the surface of a meteorite can be affected and that it can show various characteristics of when the meteorite impacts on the Earth.

**Figure 4-5: Two shallow grooves on of the Etosha meteorite located in the Andries Bischoff meteorite at the NWU. Scale = 15 cm.**

Another surface feature of unknown origin (manmade or natural) is the feature shown in Figure 4-6. The small holes that are present, running through the entire mass of the meteorite, are suspected to be manmade, due to the quality of their inside. In Figure 4-7, an extremely flat and smooth surface can be seen on the meteorite, which is also suspected of being a manmade feature on the meteorite (previous studies such as Frick and Viljoen (1973)), as the remainder of the meteorite is very uneven and rough.

**Figure 4-6: Deep holes in the side of the Etosha meteorite located in the Andries Bischoff meteorite at the NWU. Scale = 15 cm.**

**Figure 4-7: Unknown flat surface on the Etosha meteorite located in the Andries Bischoff meteorite at the NWU. Scale = 15 cm.**

In contrast to Figure 4-7, Figure 4-8 shows a slightly newer, as well as the latest, cut made on the meteorite. The latter cut, as shown in Figure 4-8, is indicated by a smooth metallic surface, which was made in 2021, while the older cut made above, which is covered with rust, was made in the early 1970's. The older cut shows that some oxidation of the meteorite has occurred since it was cut. Although different swathes do occur in the older cut, they are not as clear as are those that are present in the newer cut, with the difference concerned relating to the artefacts made by the different tools used.

**Figure 4-8: The old cut (above) and the new cut (below), made to obtain samples of the Etosha meteorite located in the Andries Bischoff meteorite at the NWU. Scale = 15 cm.**

The newly cut surface, which is shown in Figure 4-9, is already experiencing oxidation (as indicated by the red circle) only a few months after exposure to oxygen. The newly cut surface reveals the interior of the meteorite, which has a light, shiny grey/silver colour. Although no minerals can be seen with the naked eye, a crack in the meteorite can be seen in the upper right-hand corner of the cut (as indicated by the blue circle), which is probably due to the grinder having cut off the sample. Swathes in the kamacite occur in different directions, as shown in Figure 4-9.

**Figure 4-9: Newly cut surface on the Etosha meteorite located in the Andries Bischoff meteorite at the NWU. Scale = 15 cm.**

## 4.3 Mineralogy and petrography of the Etosha meteorite

### 4.3.1 XRD

The XRD analysis identified four (4) minerals, namely those of FeNi (95,7 wt. %), cohenite (2,3 wt. %), graphite (0,8 wt. %) and magnetite (1,1 wt. %). The mineral abundances inferred from the XRD spectra are shown in

Table 4-1. The most abundant mineral is FeNi (Figure 4-10), the abundance of which is attributed to the existence of iron meteorites, mainly consisting of FeNi alloy phases, like kamacite and taenite, as is presented in Buchwald (1977:460), with the former being the low-temperature alloy and the latter the high-temperature alloy. Based on the type of iron meteorite involved, which is discussed later, the high C content which the XRD attributes to the presence of graphite might be

due to the terrestrial reheating that the Etosha meteorite underwent when it entered the atmosphere of the Earth (Goldstein *et al.*, 2017:47). Therefore, graphite is seen as a contaminant, since it does not occur as a meteoric mineral in the meteorite, so it will not be discussed further in the current dissertation.

The iron meteorite consists of a crystalline material, due to the strong, narrow peaks observed in Figure 4-10 (Chauhan & Chauhan, 2014:3). At position 52° 2Θ, as well as at positions 77° 2Θ and 99° 2Θ (Figure 4-10), an enrichment of the FeNi and cohenite phases can clearly be seen, this corresponds to the standardisations of Rietveld (1969). Cohenite, despite being relatively low in abundance (possessing lower peaks), has many peaks in the analysed sample, whereas FeNi has only a few peaks, but a much higher abundance (possessing higher peaks). The presence of magnetite confirms the magnetic nature of the meteorite, as described in section 4.2.

**Table 4-1: Mineral names and stoichiometric formulas obtained through XRD analysis, along with its occurrence in the Etosha meteorite**

| Mineral | Stoichiometric formula | Occurrence (%) |
|---|---|---|
| FeNi | $Fe_{1,2}$ $Ni_{0,8}$ | 95,7 |
| Cohenite | $C_1$ $Fe_3$ | 2,3 |
| Magnetite | $Fe_3$ $O_4$ | 1,1 |
| Graphite | $H_2$ $C_1$ | 0,8 |
| **Total** | | 99,9 |

The XRD was limited to the identification of major minerals, as the EPMA obtained the mineral chemistry to support the minerals identified, as well as the additional minerals discussed later. The minerals, FeNi and cohenite, are confirmed by the findings of Frick and Viljoen (1973:347), who found kamacite, taenite and plessite (FeNi phases), as well as cohenite in the Etosha meteorite. However, magnetite is also present, which was not found in the study conducted by Frick and Viljoen (1973). Pourkhorsandi *et al.* (2019:1753) and Rubin and Grossman (2010:242) found that magnetite can form in meteorites as a terrestrial weathering product. Due to the discovery-related circumstances and the location of the Etosha meteorite, the above holds true in terms of magnetite being present in the meteorite only as a terrestrial weathering product, rather than as a meteoritic mineral.

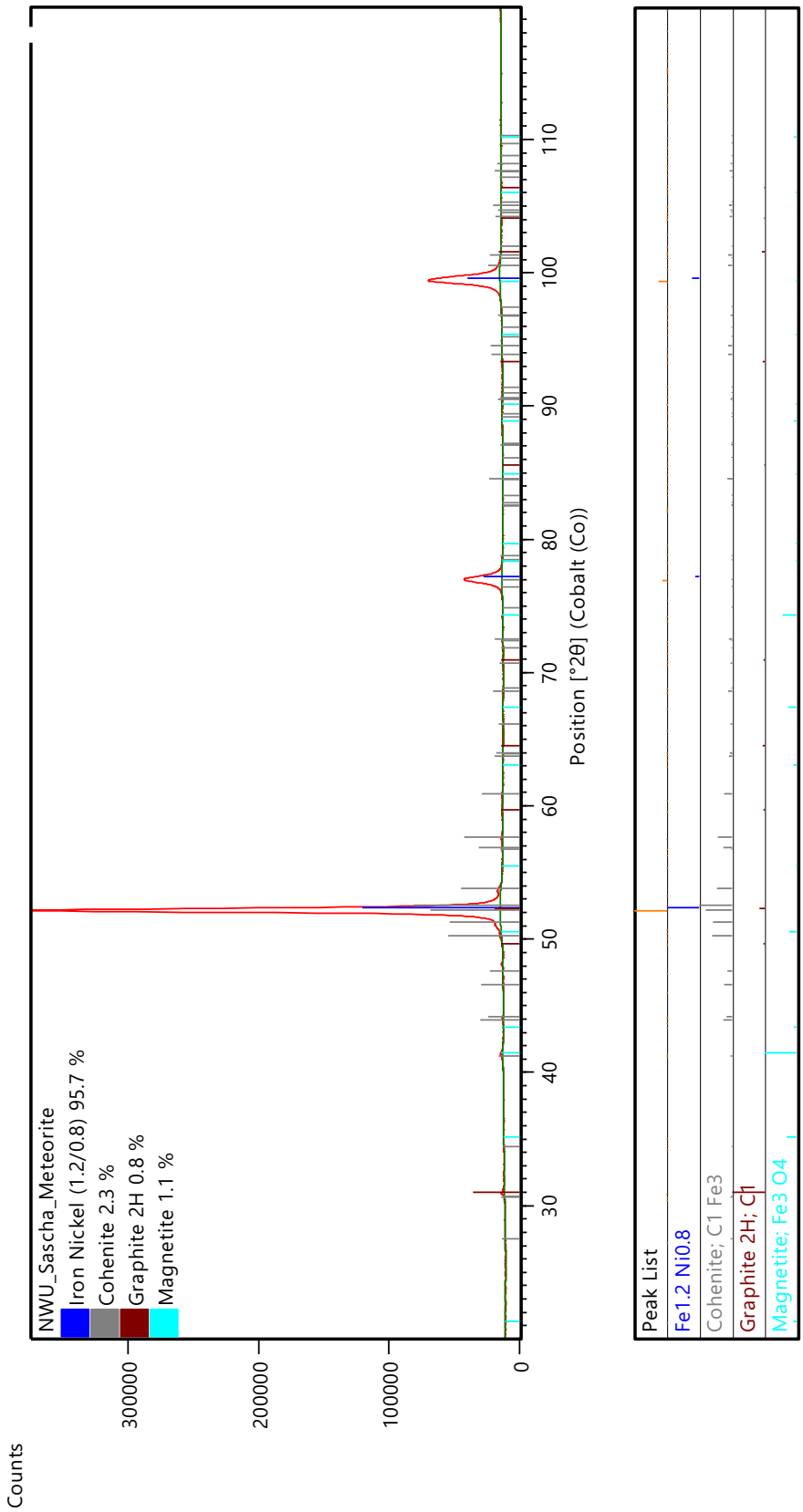


**Figure 4-10: XRD diffractogram showing the peak counts and position of the different minerals obtained from the Etosha meteorite.**

### 4.3.2 Reflected light (RL) microscopy

The Etosha meteorite was analysed under RL, due to all metallic minerals being opaque under transmitted light. The minerals that were identified under RL include kamacite, taenite, plessite, cohenite, schreibersite (and rhabdite) and silicates (Figure 4-11), which were supported by the EPMA, which confirmed the findings of Frick and Viljoen (1973:347), who, however, also found the presence of an iron phosphate. The overall texture of the unetched meteorite shows a very fine-grained matrix of kamacite, with different mineral grains being present, either in veins or in fine/coarse individual grains, whose presence was also found by Frick and Viljoen (1973:345). Some mineral grains, like schreibersite and cohenite, occur as coarse grains, whereas some taenite, plessite and rhabdite grains tend to occur as relatively fine grains. The meteorite contains many schreibersite grains, when compared to the number of cohenite grains, although the former minerals are unevenly distributed, as in the case examined by Frick and Viljoen (1973:345). Many different fractured cohenite grains are present in the meteorite, which indicates that the meteorite underwent some shock events, which are also described by (Frick & Viljoen, 1973:348), as well as spheroidised plessite. The cohenite contains mostly fine schreibersite inclusions, with it sometimes forming a rim around a schreibersite vein. Scratches are present on the samples, which are due to the sample preparation steps followed.

When etched, the meteorite displays very coarse-grained kamacite bands, interspersed with medium-sized taenite bands (in terms of a Widmanstätten structure). The schreibersite veins, however, were partially affected by the etchant (due to the removal of the Ni), despite remaining intact for most of the sample. The above-mentioned scratches became more prominent with the etching. The presence of some residual, degraded grains in the etched samples can be linked to the same grains in the unetched samples. Areas are visible in the etched samples, which are very scratched, and perhaps over-etched (i.e. with the etchant having been left for too long before being removed, which could have been due to its retention on a corner of the sample), which prevents the showcasing of any visible structures or minerals. The isotropic minerals that are present in Figure 4-11 are most likely silicates that occur within the schreibersite grains, since the presence of a moderate Si content has been recorded in the meteorite (Table 4-2). The meteorite has undergone extreme heat (Figure 4-12 A), as well as some pre-atmospheric shock (Figure 4-12 F). The structure on Figure 4-12 A has formed due to extreme heat, which caused some cracks to form, that oxidation products (black) then filled in (Buchwald, 1975c:99).

***Schreibersite***

Schreibersite, which is an iron nickel phosphide that is present in most iron meteorites, tends often to be found in the form of plates or shells around other minerals (Buchwald, 1975c:104-105). According to Yoshikawa and Matsueda (1992:258,260), seven types of schreibersite textures and chemical compositions can occur in iron meteorites, of which one, “xenomorphic and fine-grained schreibersite coexisting with kamacite”, is present in the sample, as can be seen in Figure 4-11 A. A clear boundary between kamacite grains can be seen in the bottom half of the photomicrograph, with there being fine schreibersite grains that formed along the boundary between the kamacite grains (as indicated by the white arrows) (Figure 4-11 A). Schreibersite is present as finer, less well-developed grains, as, instead of being individual grains with well-defined boundaries, they are relatively dependant on the extent of the boundary on which the schreibersite formed. Previous work conducted by Doan and Goldstein (1970:775) shows that schreibersite preferentially forms on the kamacite-taenite boundary, when the P content of the meteorite is 0,25 wt. % or lower. Similar schreibersite occurrences at the kamacite-taenite boundary were detected for the Etosha meteorite, as can be seen in Figure 4-11 B.

The schreibersite crystals seen in Figure 4-11 C are coarse skeleton crystals that probably precipitated out of solution very early on in the crystallisation process, when compared to the other schreibersite crystals (Buchwald, 1975c:104). In Figure 4-11 D and Figure 4-12 C, a grain of schreibersite can be seen, with a cohenite rim in a kamacite matrix. The schreibersite in Figure 4-11 D is fractured, mainly because the mineral is very brittle and easily shattered by cosmic events (Buchwald, 1975c:104). Various cycles of heating and cooling can be seen in Figure 4-12 B, due to the different minerals crystallising at different temperatures, meaning that the feature concerned occurred over a period. A schreibersite grain is shown in Figure 4-12 E after the meteorite sample was etched. The silicate intrusions that were seen pre-etch are no longer visible in the schreibersite grain. The schreibersite was a continuous vein (as can be seen in Figure 4-29, sample A), which decomposed partially when the etchant started to remove the Ni. The above can be seen in Figure 4-12 E, where the faint outlines of the continuous vein can still be seen in the sample (as indicated by the white arrows).

***Rhabdite***

Yoshikawa and Matsueda (1992:260) explain the presence of another texture in the meteorite, being the “idiomorphic schreibersite coexisting with kamacite” in Figure 4-11 E and F. Although the euhedral rhabdite crystals are very fine, they are oriented in specific lines, which are at approximately 120° angles, in three different directions, referring to the triple junction of

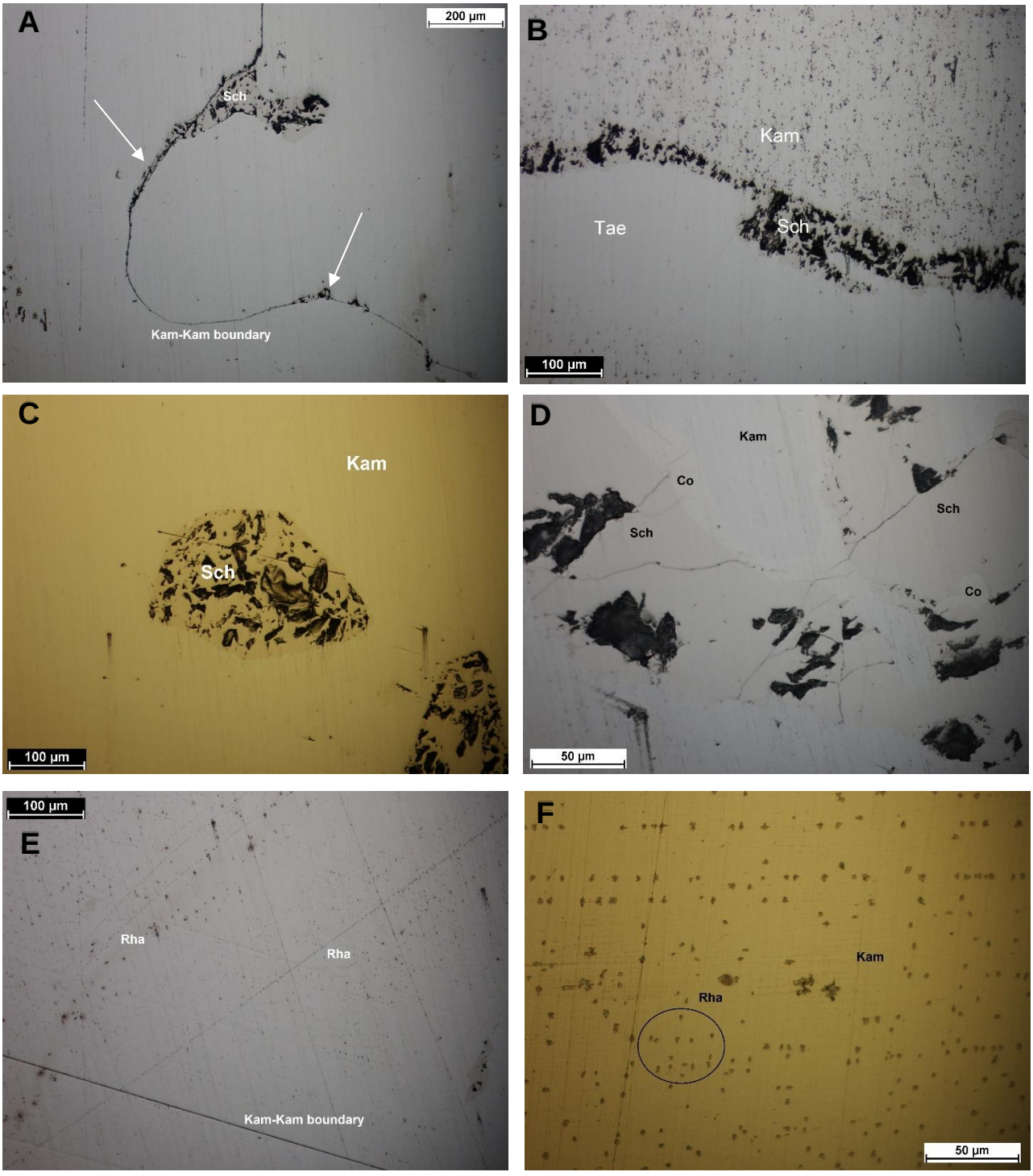


**Figure 4-11: Reflected light photomicrographs of the polished Etosha meteorite. Unetched. A: Screibersite forming on the kamacite-kamacite grain boundary. B: A much more developed schreibersite grain that formed on the boundary between the kamacite and the taenite. C: Broken-up schreibersite grains in a kamacite matrix. D: Schreibersite grains with a rim of cohenite, which also enters the schreibersite grain, in a kamacite matrix. E: Another kamacite-kamacite boundary with minute, euhedral rhabdite crystals that formed in 120° angles, oriented parallel to the Widmanstätten structure. F: Fine rhabdite grains in a kamacite matrix. Kam = Kamacite: Tae = Taenite; Co = Cohenite; Sch = Schreibersite; Rha = Rhabdite.**

recrystallised minerals (Voll, 1961:527), in the case of the kamacite. The rhabdites are known to form at the boundary between grains (Yoshikawa & Matsueda, 1992:260) (kamacite-kamacite or kamacite-taenite), which explains why the rhabdites in Figure 4-11 E are ordered in 120° angled lines, because they have formed on the boundaries of the kamacite grains.

***Kamacite and taenite (and plessite)***

The schreibersite texture in Figure 4-11 B closely resembles the one in Figure 4-11 A, although the schreibersite concerned has formed on a kamacite-taenite boundary. The formation depleted the surrounding kamacite and taenite of their Fe and Ni, while the schreibersite was forming (Goldstein, 1965:2). The $\alpha_2$ structure seen in Figure 4-12 A is usually formed when a meteorite is reheated to above 800°C for a relatively short period. When this happened, oxidation occured along the boundaries of the cracked kamacite, and the oxidation products filled the hole (Buchwald, 1975c:99). Neumann bands (which can be seen in Figure 4-12 F) are mechanical, plate-shaped twin lamellae that only occur in the kamacite bands of etched meteorites (Buchwald, 1975c:90). The Neumann bands indicate that the meteorite must have undergone shock waves much lower than 130 kbar (Buchwald, 1975c:90).

Spheroidised plessite is an intergrowth of kamacite and taenite, which forms last from the remaining taenite, when an iron meteorite is continuously cooled (Buchwald, 1975c:95). In Figure 4-12 B, the various cycles of heating and cooling can be seen through the presence of the spheroidised plessite that is present on the outer rim of the grain. The presence of the spheroidised plessite means that the taenite in the outside rim was the last remaining taenite present. In the centre, kamacite occurs, with taenite surrounding it in a lighter, less pitted area. Around the taenite, schreibersite has formed (with its silicate intrusions) a broad rim, with it having probably depleted the inner taenite of Fe and Ni. Another stage of heating and cooling must have occurred, due to the presence of another taenite rim forming around the schreibersite, once again depleting the schreibersite of its Fe and Ni (Figure 4-12 B). Another good example of the spheroidised plessite is present in Figure 4-12 D, where the plessite has formed on top of a current taenite grain. According to Buchwald (1975c:95), plessite is usually the last to form in a meteorite, which explains why the plessite in Figure 4-12 D formed on top of the taenite grain (Frick & Viljoen, 1973:345).

***Cohenite***

The cohenite not only occurs as a rim in Figure 4-11 D, but it also enters the schreibersite grain on the right-hand side. The cohenite present is not fractured like the schreibersite, because it is very hard and ductile (Buchwald, 1975c:100). The difference in hardness between the cohenite

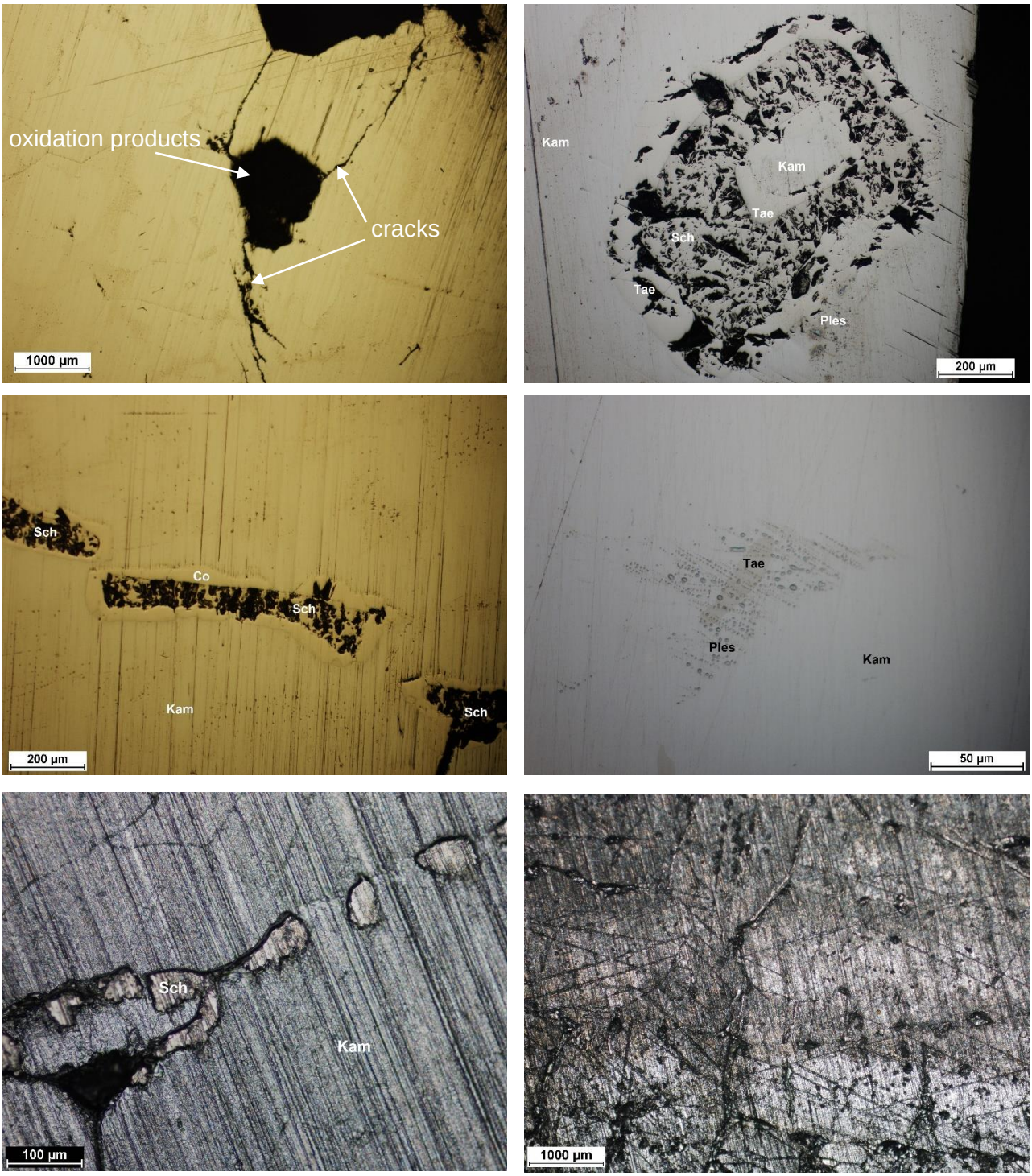


**Figure 4-12: Reflected light photomicrographs of the polished Etosha meteorite. A: Typical $\alpha_2$ structure formed by extreme heat oxidation, unetched. B: Various stages of cooling seen through different mineral rims forming, unetched. C: Schreibersite grain with a cohenite rim in a kamacite matrix, unetched. D: Intergrowth of spheroidised plessite over a taenite grain in a kamacite matrix, unetched. E: Decomposed schreibersite grain in kamacite matrix, etched (1% nitric acid). F: Neumann bands in three directions present in the kamacite grain, etched (6% nitric acid). Kam = Kamacite; Tae = Taenite; Co = Cohenite; Sch = Schreibersite; Ples = Plessite.**

and the kamacite can be seen in Figure 4-12 C, through the scratches in the image that is prominent in the kamacite matrix, with it stopping, however, at the edge of the cohenite, as the cohenite is difficult to scratch (Buchwald, 1975c:100).

The polished unetched sample showed an overall coarse-grained texture with individual minerals present in the matrix, which consisted mainly of kamacite, with the taenite forming only relatively fine crystals. The schreibersite occurred mostly as veins, or as coarse grains surrounded by cohenite rims, which is a feature that is common in iron meteorites (Clarke Junior & Goldstein, 1978:74), which was also discovered by Frick and Viljoen (1973:346). The etched sample displayed a rougher texture, as the etchant increased the depth of the scratches that were already present in the unetched sample. The etched sample displayed a coarse Widmanstätten structure, which was interrupted in parts by the schreibersite veins (Clarke Junior & Goldstein, 1978:28) and Neumann bands. Based on the existence of the Neumann bands, as well as on the nature of the filled-in cracks, the meteorite underwent pressure no higher than 130 kbar, as well as shock events and reheating and cooling events.

## 4.4 Mineral chemistry of the Etosha meteorite

### 4.4.1 EPMA

The minerals found in an iron meteorite largely depend on the fact that iron meteorites are formed from the metallic FeNi cores of asteroids (Buchwald, 1975c:76). The results obtained from the EPMA (Appendix A, Table A-1) were grouped into approximate mineral groups, based on the quantities of the major elements (Fe, Ni, P) present, and further based on the minor elements (Co, Cu, S, Cr) concerned. The different groups were then plotted on a Fe-Ni-P ternary diagram (Figure 4-13), so as to be able to determine and classify the minerals present in the meteorite, based on its mineral chemistry.

Based on the Fe-Ni-P phase diagram (Figure 4-13), the mineral chemistry results are classified, or grouped, into four major minerals. The two minerals have a very high percentage (between 88-98 wt. %) of Fe, less than 10 wt. % Ni and almost no P (cohenite: $Fe_3C$ and kamacite: α-(Fe, Ni)). A mineral is also present with little to no P, but a high percentage of Fe and a medium percentage of Ni (taenite: γ-(Ni,Fe)). The other phases have between 30 and 55 wt. % Fe, 25 to 50 wt. % Ni and 13 to 16 wt. % Ni. A mineral also exists that plot quite close to the schreibersite groups, although not closely enough to be classified as schreibersite (present as the FeNiP mineral in

Figure 4-13). The mineral displays a P and Ni content that is too low, and an Fe content that is too high to be classified as schreibersite.

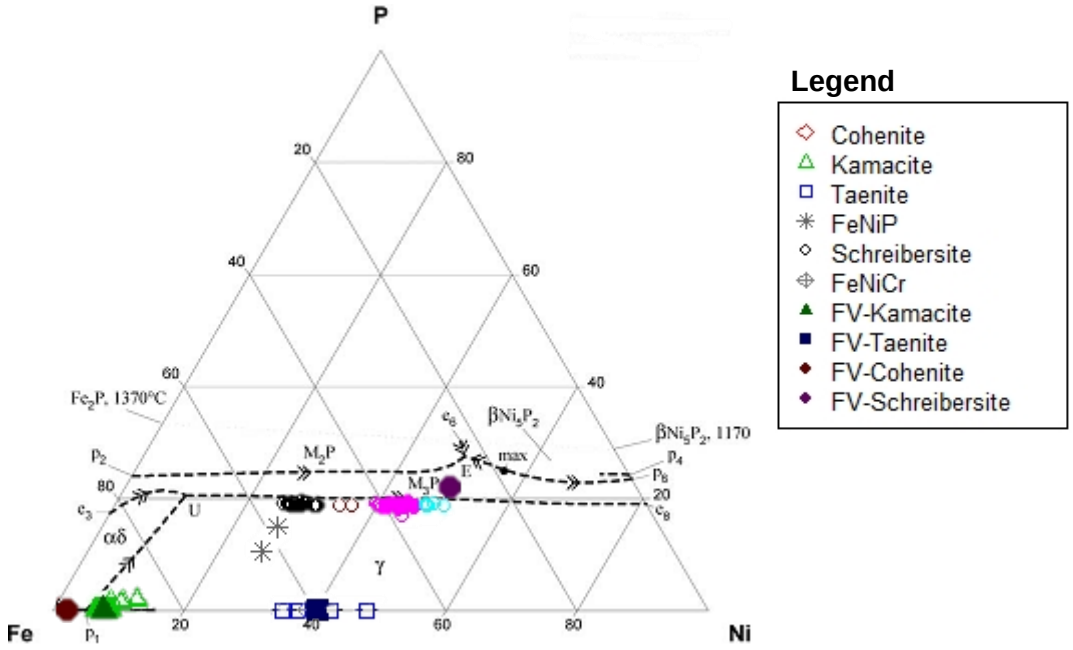


**Figure 4-13: Fe-Ni-P ternary diagram, adapted from Korniyenko (2009:14), with the minerals obtained through the EPMA of the Etosha meteorite plotted, where αδ = kamacite; ɣ = taenite; $M_3P$ = $(Fe,Ni)_3P$ – schreibersite and $M_2P$=$(Fe,Ni)_2P$ – allabogdanite. FV = Frick and Viljoen (1973:347).**

The EPMA data was plotted against the minerals created by Korniyenko (2009:14) in Figure 4-13. The group in the far left-hand corner of Figure 4-13 can be seen to be very close to the kamacite field of Korniyenko (2009:14), towards the Fe corner of the ternary diagram. The finding was confirmed by Frick and Viljoen (1973:347), which showed that the minerals were, indeed, kamacite, which can be seen in Figure 4-13. The minerals that lack P are classified as taenite in the Figure 4-13 plot in the taenite field of Korniyenko (2009:14), along with the taenite described by Frick and Viljoen (1973:347). The schreibersite groups, however, do not plot in the schreibersite field of Korniyenko (2009:14) in Figure 4-13. The mineral chemistry data classified as schreibersite has a linear trend that can fit a horizontal line, and that resembles the field of schreibersite, and, although plotting differently, the mineral can still be classified as schreibersite.

A Fe-Ni binary diagram was also created to show the relationship of the two elements and their correlation, in terms of the different mineral groups present. In Figure 4-14, Fe has a strong negative correlation with Ni, (i.e. the Fe content decreases as the Ni content increases), which is a phenomenon that was also found by Frick and Viljoen (1973:347). The Fe content of the cohenite, in the top left-hand corner of Figure 4-14, shows a small difference between the current research data and the data of Frick and Viljoen (1973). However, such a difference can be

attributed to the fact that the data from the current study was normalised to 100%. C was not analysed in the present study, meaning that C might have been present, with a lower Fe content, which might have matched the results of Frick and Viljoen (1973:347) (Figure 4-14 and Figure 4-17).

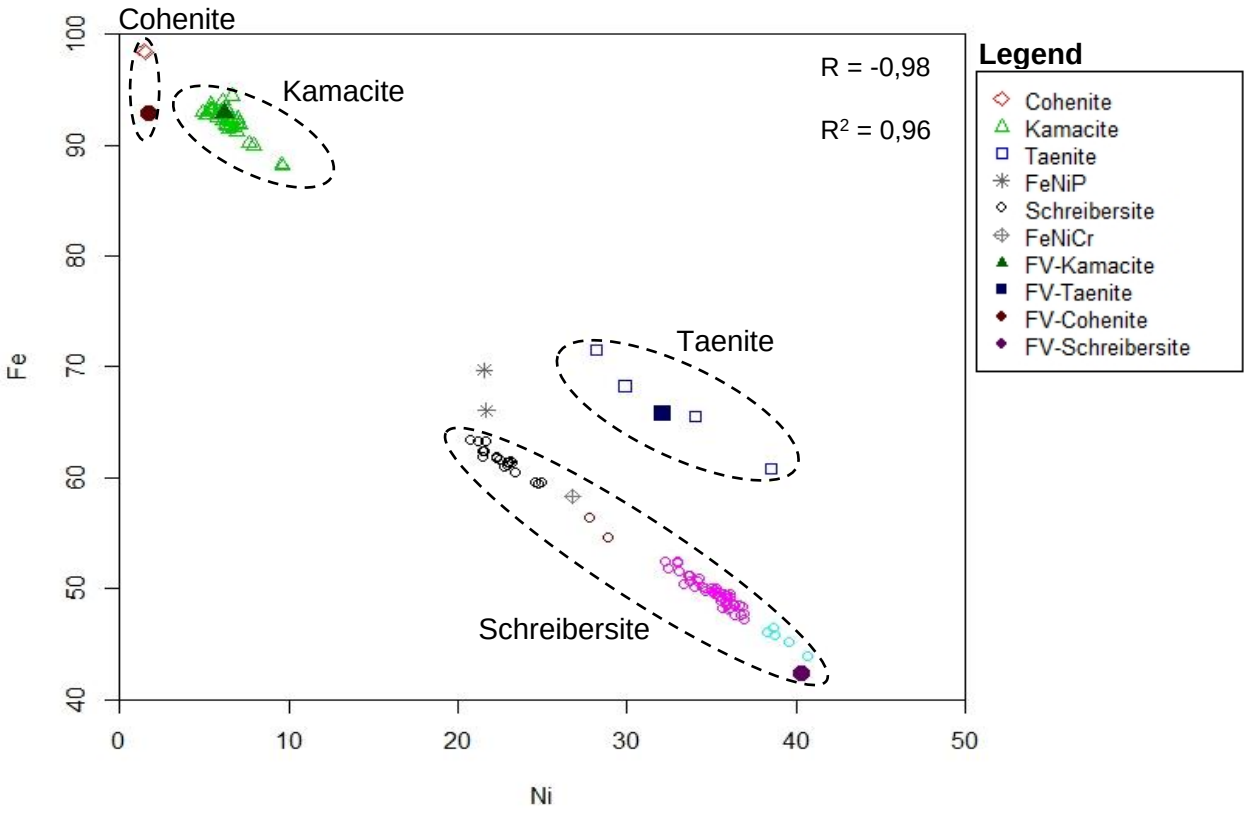


**Figure 4-14: Binary diagram of Fe-Ni, showing the different minerals present in the Etosha meteorite, determined by EPMA. FV = Frick and Viljoen (1973:347). The correlation value (R) and the coefficient of determination ($R^2$) is also displayed on the diagram.**

Table A-2 (Appendix A) displays the chemistry of the minerals present in the Etosha meteorite, compared to the results obtained by Frick and Viljoen (1973:347). In Figure 4-15 and Figure 4-16, the data is displayed through graphs reflecting the mineral chemistries involved. When comparing the graphs concerned, a clear difference can be seen in the chemistry of schreibersite. The Fe and Ni content of both the kamacite and taenite in the present study (as shown in Figure 4-15) are approximately the same as that which is given in Frick and Viljoen (1973:347) (Figure 4-16), with the trace elements showing relatively large, but still not exceptionally large, differences (Figure 4-17). The trace element chemistry of cohenite shows a large difference in C content between the findings of the present study and the findings given in Frick and Viljoen (1973:347) (keeping in mind that the C content was not analysed in the current study). Another big difference

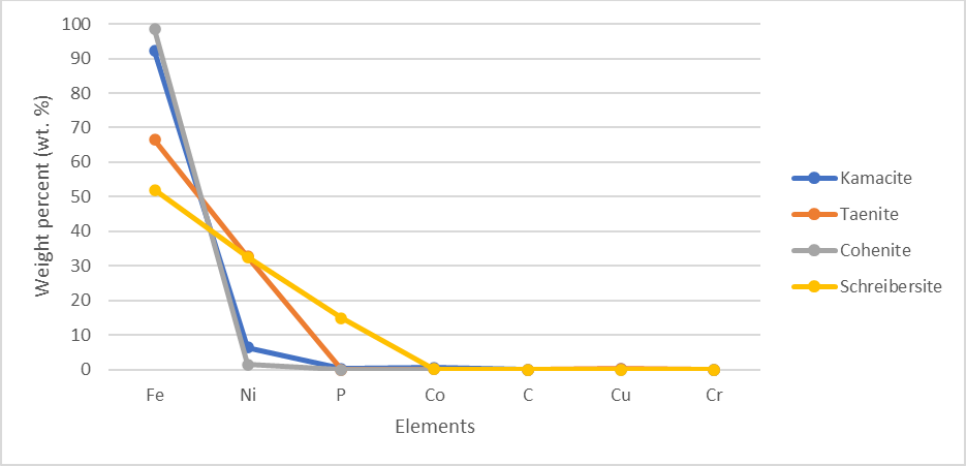


**Figure 4-15: Individual mineral chemistries obtained through EPMA of the minerals present in the Etosha meteorite in the current study.**

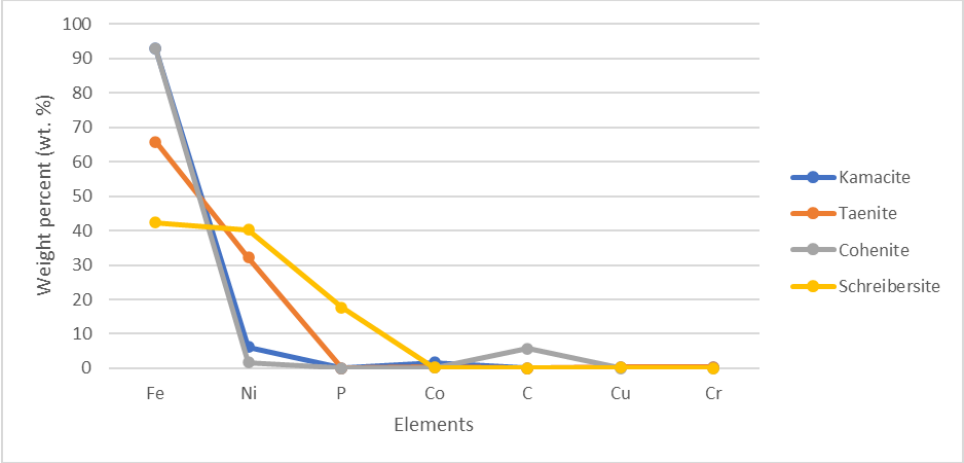


**Figure 4-16: Individual mineral chemistries obtained by Frick and Viljoen (1973:347) of the minerals present in the Etosha meteorite.**

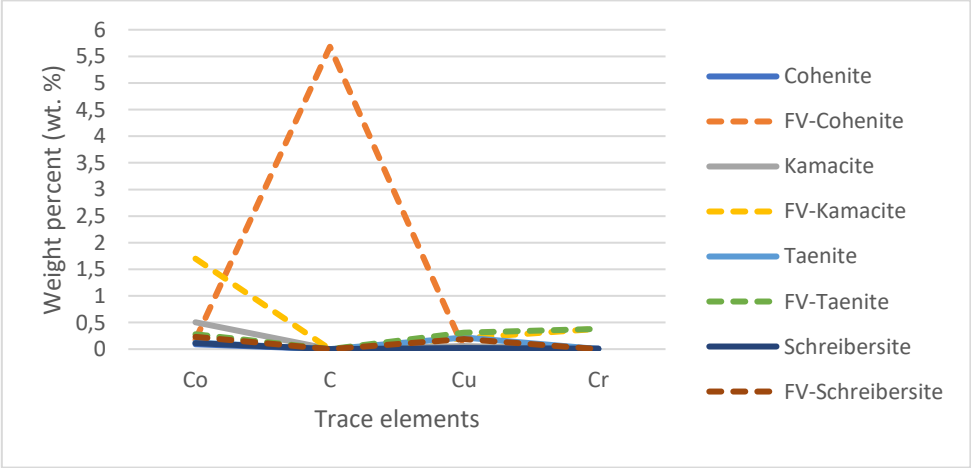


**Figure 4-17: Trace element quantities of different minerals present in the Etosha meteorite, compared to the results of FV = Frick and Viljoen (1973:347).**

between the two studies can be seen is the Co content of kamacite, with Frick and Viljoen (1973:347) study displaying a higher Co content than does the current study. The Cr content of kamacite and taenite, as noted by Frick and Viljoen (1973:347), displays slightly higher values than does that obtained in the present study (Figure 4-17).

In Figure 4-18, three chemically different schreibersite minerals were found (with one phase possibly being an iron phosphate), whereas Frick and Viljoen (1973:347) indicated only one schreibersite mineral chemistry. The schreibersite found in the current study has a much higher Fe and Ni content, as well as a much lower P content, than that which is given in Frick and Viljoen (1973:347). The lower P content might be due to the presence of a substantial number of cohenite rims present in the samples. When a cohenite rim forms around schreibersite during the cooling of a meteorite, it prevents the schreibersite from absorbing the additional P (Clarke Junior & Goldstein, 1978:71).

The 3 different types of schreibersite refer to one mineral, but with different chemical variations. The minerals all consist of the same make up of elements, but in different quantities. Schreibersite 1 contains much more iron than do its two counterparts (Figure 4-18), which might be because the schreibersite extracted an increased amount of iron from the taenite present (Clarke Junior & Goldstein, 1978:73) and because this schreibersite occurs near kamacite in a meteorite. Schreibersite 2 and 3 have Fe, Ni and P chemistries that fall within a similar range. The relationship between Fe and Ni in the schreibersite shows the presence of a strong negative correlation, as seen in Figure 4-14. The schreibersite found in the current study also showed a

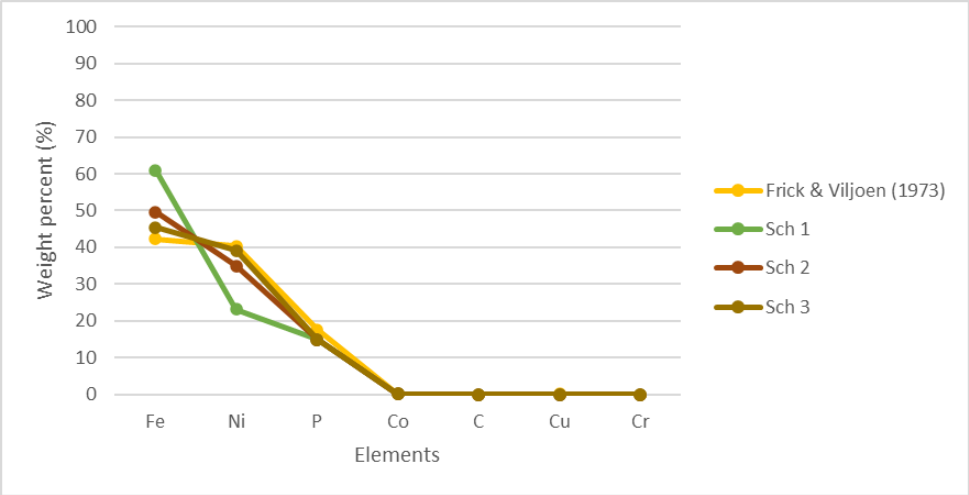


**Figure 4-18: Schreibersite mineral chemistry obtained by Frick and Viljoen (1973), compared to the three possible schreibersite mineral chemistries obtained in the current study of the Etosha meteorite. Sch = Schreibersite.**

lower trace element content, such as small variations in the amount of Co and Cu present, when compared with the values presented by Frick and Viljoen (1973:347) (Figure 4-18), which mighty be due to the differences in calibrations of the EMP instrument used (Carpenter, 2008:1151).

The presence of skeleton schreibersite crystals is confirmed by the EPMA results obtained, which found that most of the schreibersite grains found in the meteorite have a composition of Ni between 10 and 15 wt. % (Buchwald, 1975c:104). The minerals identified in the Etosha meteorite include kamacite, taenite, cohenite, schreibersite, magnetite and minor silicates. The phase areas in Figure 4-13 do not classify the minerals entirely correctly, with the discrepancy being due to the fact that, under conditions of nonequilibrium, such as those that exist on Earth, the composition range on a phase diagram might either be too small or inaccurate (ASM International, 1992:6-7), meaning that the data obtained is rarely likely to plot within the allocated phase areas. Another reason for the schreibersite not plotting completely within the allocated phase area might be due to the fact of the cohenite rims enclosing the schreibersite grains (Clarke Junior & Goldstein, 1978:71).

### 4.4.2 SEM

The SEM analysis was only done on sample B, as sample A was very pitted, which interfered with the accurate functioning of the SEM. The small holes in the sample caused the reflected signals to have incorrect intensities in relation to the minerals present, which would have led to an inaccurate analysis (Klein & Dutrow, 2007:324). Four different zones were identified, namely: (1) the fractured phase; (2) the matrix; (3) a bright zone; and (4) a black phase.

***Fractured phase***

In Figure 4-21, ‘Selected area 5’ can be seen to have significantly more Ni than do the other selected areas, with it also being the only area containing P, meaning that the grain concerned is schreibersite. This finding corresponds with the EPMA data obtained, due to the high P and Ni content, as well as due to the visible fractures presented in Figure 4-19, which is a common feature of schreibersite, due to its brittle nature (Buchwald, 1975c:104). Although all the selected areas displayed some C content, ‘Selected area 4’ displayed the presence of the largest amount of C, meaning that the grain next to the schreibersite consisted of cohenite. The above also confirms the results of the EPMA, and of the XRD, which confirmed the presence of cohenite in the sample. The above is corroborated by the findings of Frick and Viljoen (1973:347), which show cohenite to be the only mineral present containing C. The carbon coating present on the

samples had a thickness of 25 nm and was distributed evenly which means that this C content did not have an effect on the identification of minerals in the samples.

In Figure 4-22, ‘Selected area 2’ and ‘Selected area 3’ are shown to have the same makeup of elements as does ‘Selected area 5’ in Figure 4-21. However, the matrix in Figure 4-22 displays an exponentially higher P content. In Figure 4-22, the schreibersite grains (presented at the bottom and on the right of the figure) display a high amount of Co, which is a phenomenon that was also found by Frick and Viljoen (1973:347). All the areas investigated in Figure 4-22 show a high content of Fe.

The schreibersite grain (‘Selected area 1’), as shown in Figure 4-23, contains a black oxide that can be seen as ‘EDS spot 1’ in Figure 4-25. The oxide, which contains much less Fe and Ni than does the matrix, contains a significant amount of $O_2$, with it being identified as magnetite, which was found through the use of the XRD (Pourkhorsandi *et al.*, 2019:1753). Another type of schreibersite is seen in Figure 4-24, which exhibits a high Fe, Ni and P content, with a slightly higher Co content. The schreibersite grain concerned, which is much more fractured, contains more black inclusions (silicates) than do the other two types of schreibersite.

***Matrix***

All the selected areas, except for ‘EDS Spot 1’ and ‘EDS Spot 2’ in Figure 4-26, show the presence of Fe, as well as of Ni, in varying quantities. The matrix, however, showed the highest quantity of Fe present in the sample. ‘Selected area 1’ in Figure 4-22 displays an almost identical chemical composition to that of the ‘Selected area 1 and 2’ in Figure 4-21, which confirms that the matrix is kamacite throughout the two areas concerned, with kamacite being the most common mineral to be found in an iron meteorite (Buchwald, 1975c:87).

***Bright phase***

Brighter grains can be seen in the top right-hand corner of Figure 4-19, which shows a composition of Fe and Ni, with the material concerned being identified as taenite. The bright white grain (i.e. taenite) in Figure 4-20 contains Fe and Ni, and does not contain P. However, it does show a relatively high concentration of Co.

All the minerals found in the XRD, as well as in the EPMA, were confirmed by means of the SEM results found. The minerals found were kamacite, taenite, schreibersite, cohenite, magnetite and minor silicates. Frick and Viljoen (1973:347) also found that the presence of the minerals, except for the magnetite and an iron phosphate, were not confirmed in the present study. Three different

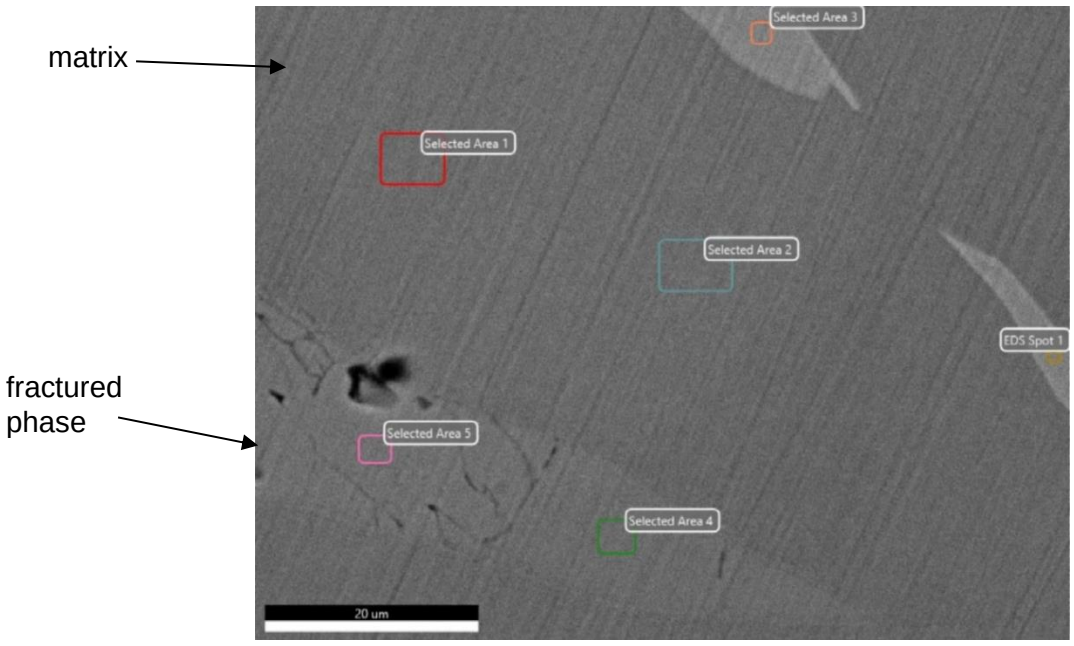


**Figure 4-19: Backscattered electron (BSE) micrograph of sample B, indicating the various areas selected for EDS, showing schreibersite and cohenite (fractured phase) – 'Selected area 4' & 'Selected area 5', kamacite (matrix) – 'Selected area 1' & 'Selected area 2' and taenite (bright phase) – 'Selected area 3' & 'EDS Spot 1'.**

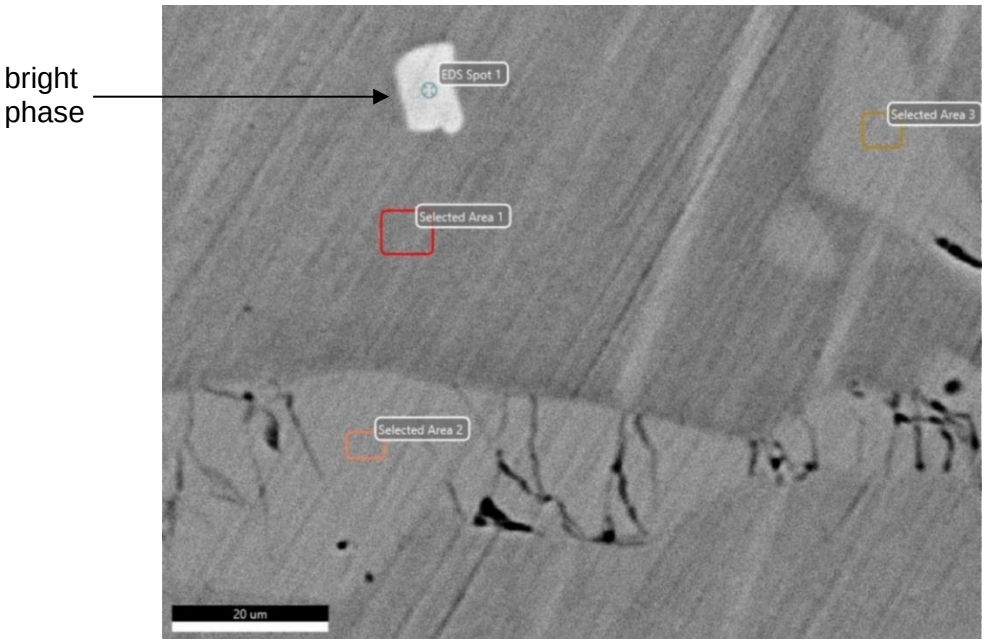


**Figure 4-20: Backscattered electron (BSE) micrograph of sample B, indicating the various areas selected for EDS, showing schreibersite (fractured phase) – 'Selected area 2' & 'Selected area 3', kamacite (matrix) – 'Selected area 1' and high Co taenite (bright phase) – 'EDS Spot 1'.**

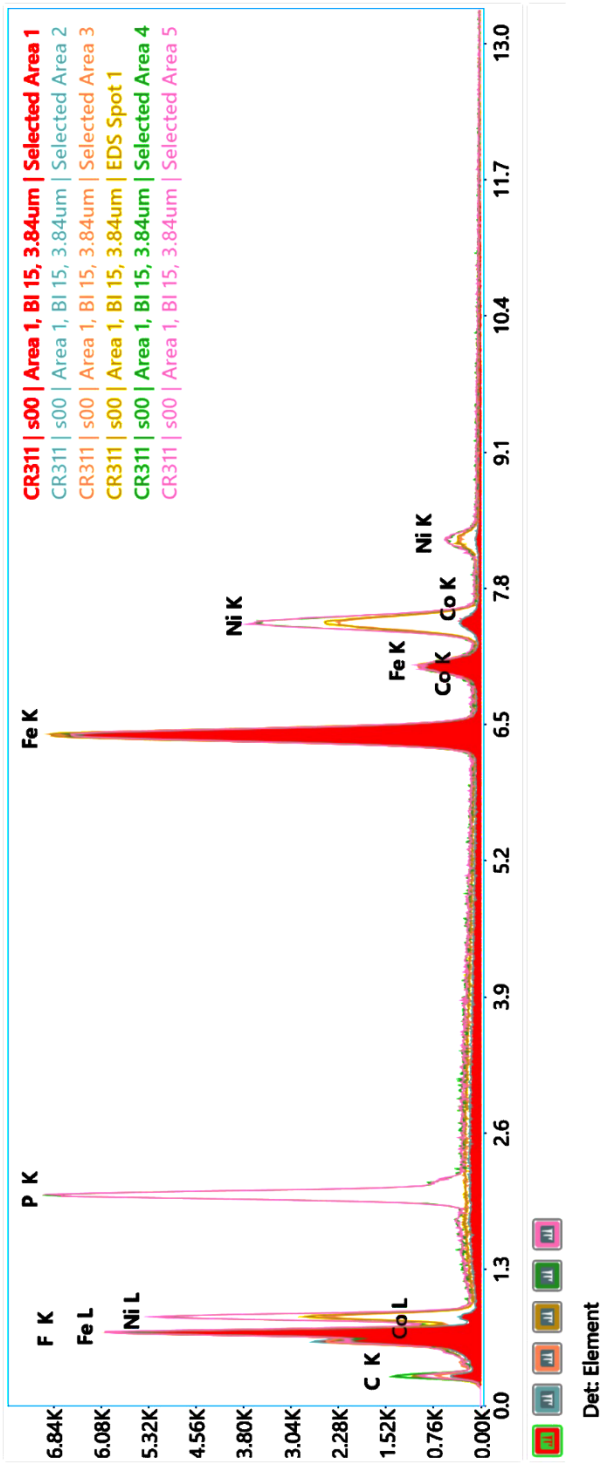


**Figure 4-21: SEM EDS spectrum analysis of sample B, showing the qualitative mineral chemistries of the selected areas highlighted in Figure 4-19, as well as the mineral chemistries of schreibersite - 'Selected area 5', cohenite – 'Selected area 4', kamacite – 'Selected area 1' & 'Selected area 2' and taenite – 'Selected area 3' & 'EDS Spot 1'.**

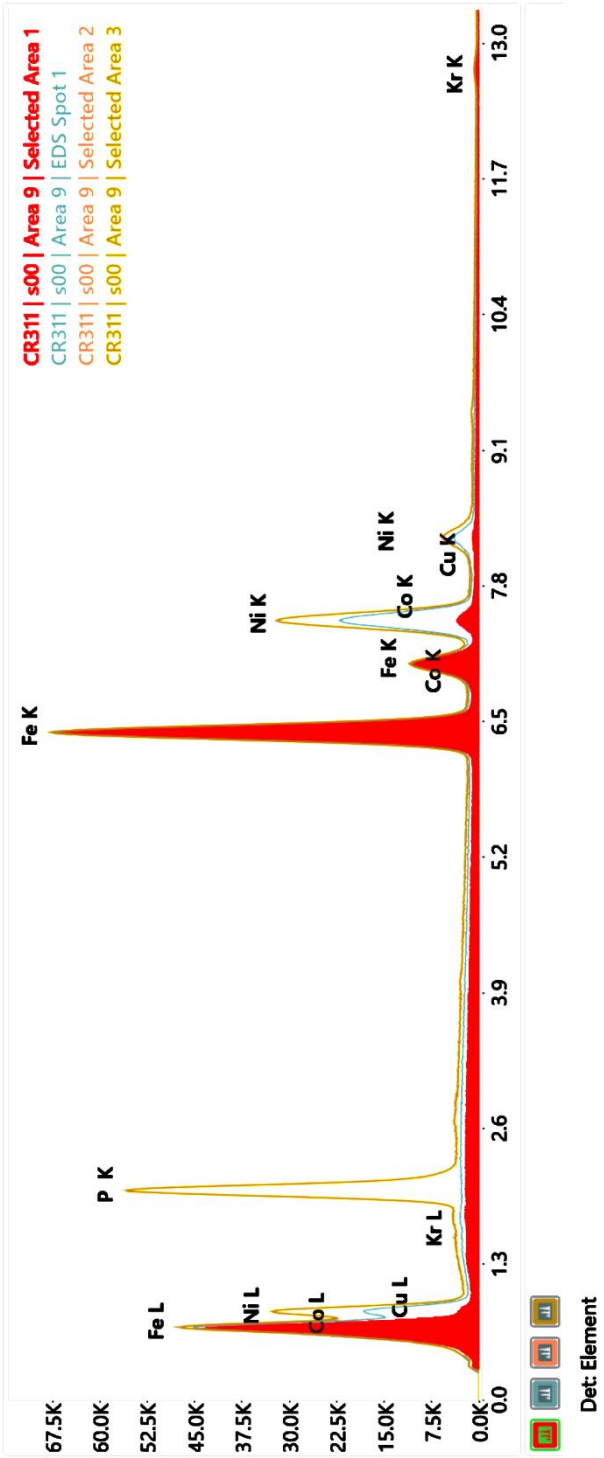


**Figure 4-22: SEM EDS spectrum analysis of sample B, showing the qualitative mineral chemistries of the selected areas highlighted in Figure 4-20, as well as the mineral chemistries of schreibersite – 'Selected area 2' & 'Selected area 3', kamacite – 'Selected area 1' and high Co taenite – 'EDS Spot 1'.**

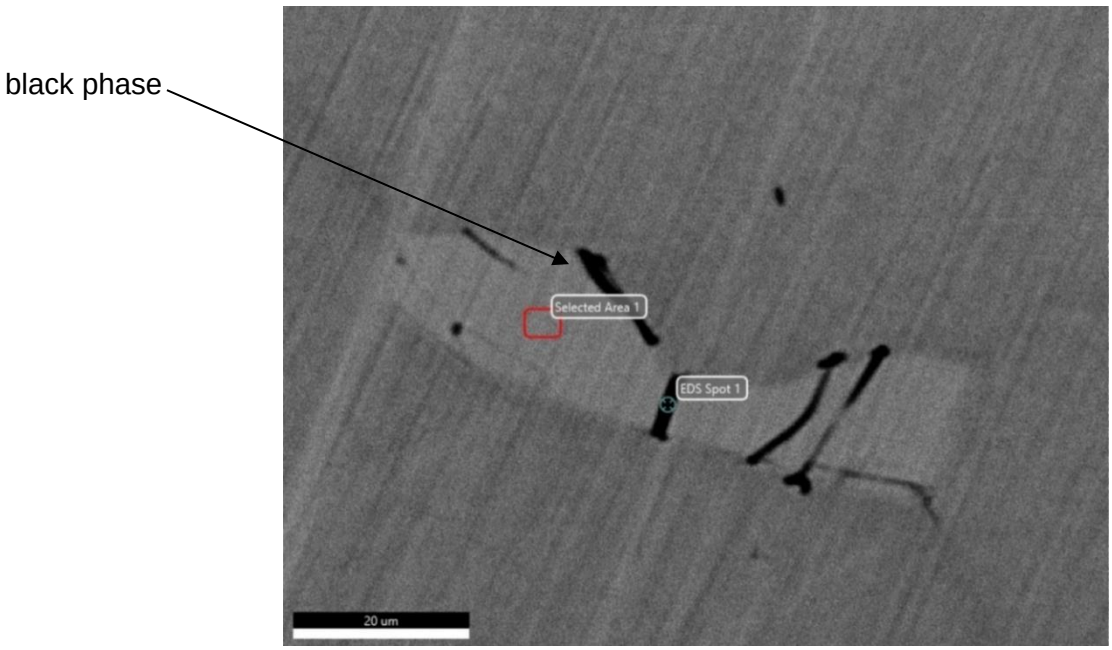


**Figure 4-23: Backscattered electron (BSE) micrograph of sample B, indicating the various areas selected for EDS, showing the presence of schreibersite (fractured phase) – 'Selected area 1' and magnetite (black phase) – 'EDS Spot 1'.**

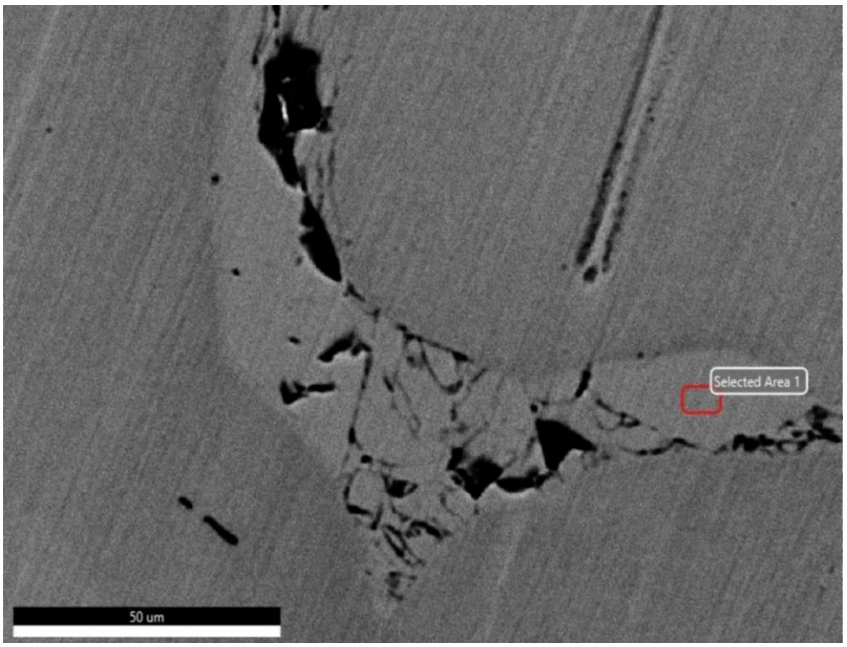


**Figure 4-24: Backscattered electron (BSE) micrograph of sample B, indicating the various areas selected for EDS, showing the presence of schreibersite (fractured phase) – 'Selected area 1', with possible silicates.**

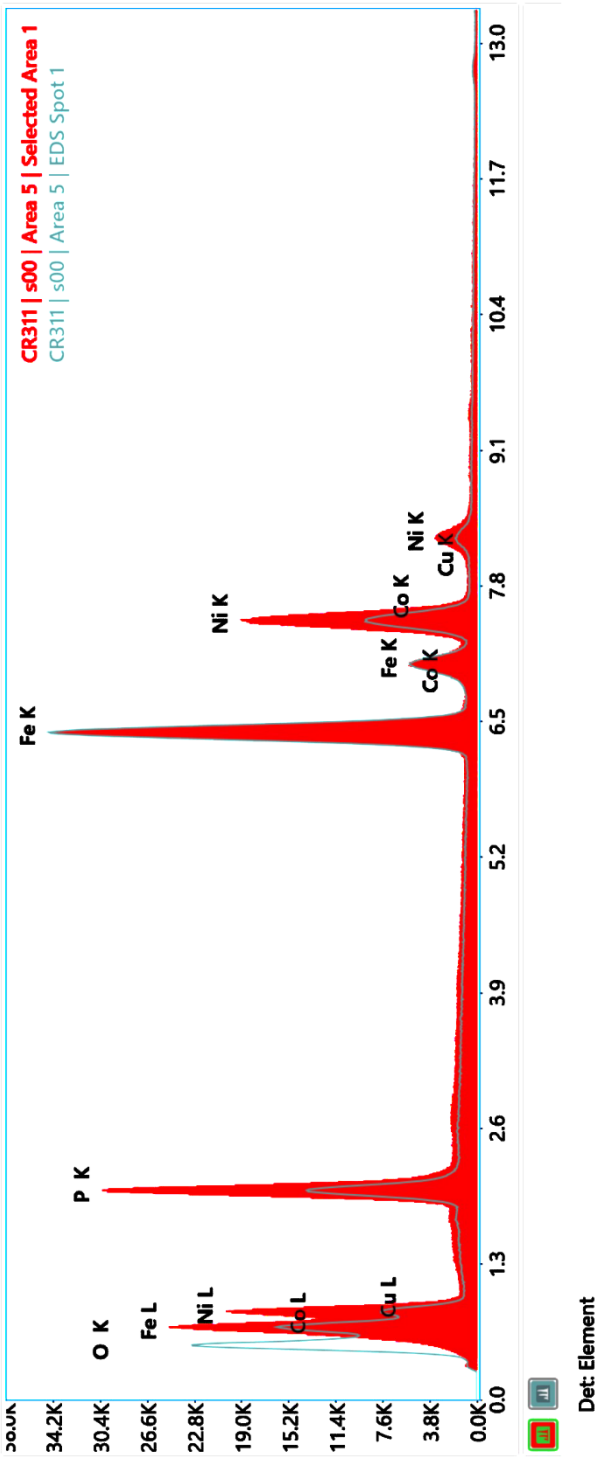


**Figure 4-25: SEM EDS spectrum analysis of sample B, showing the qualitative mineral chemistries of the selected areas highlighted in Figure 4-23, showing the mineral chemistries of schreibersite – 'Selected area 1' and magnetite – 'EDS Spot 1'.**

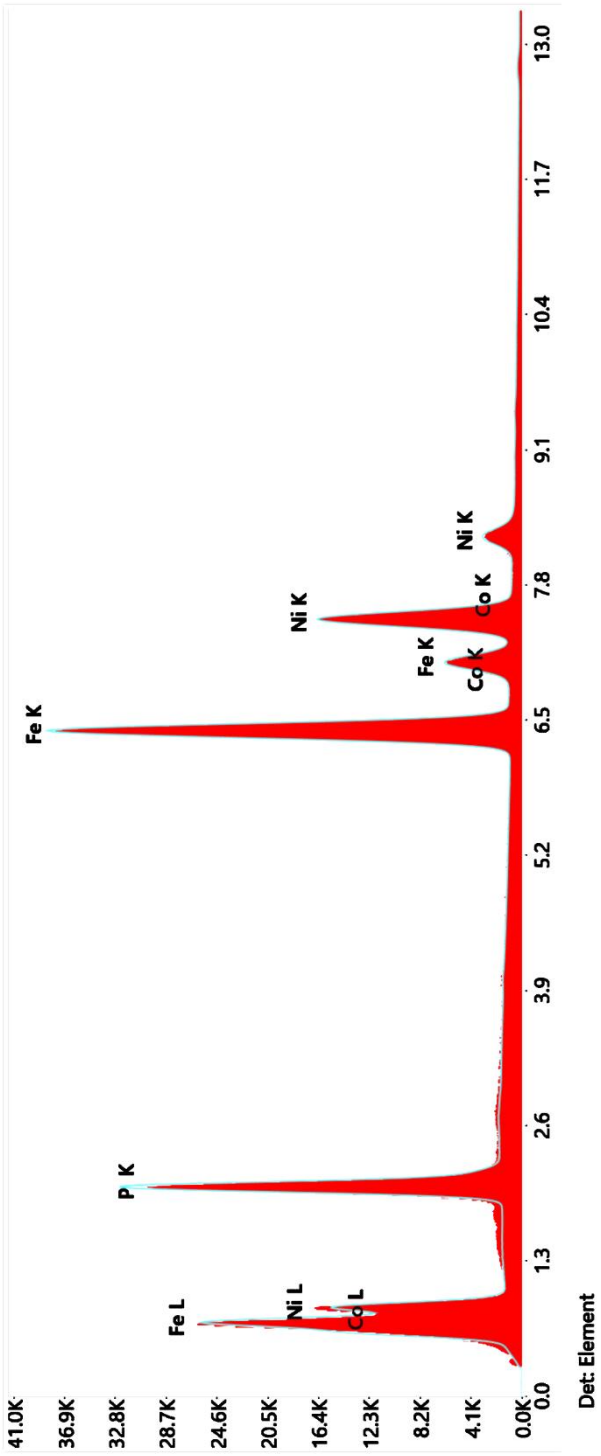


**Figure 4-26: SEM EDS spectrum analysis of sample B, showing the qualitative mineral chemistries of the selected areas highlighted in Figure 4-24, showing the mineral chemistry of schreibersite – 'Selected area 1'.**

types of schreibersite were found in the meteorite, confirming the EPMA data, which also found three different types of schreibersite minerals.

## 4.5 Geochemistry of the Etosha meteorite

### 4.5.1 pXRF

All data recorded are included in Appendix B, Table B-1, which highlights the small variation present in the chemistries of the different measurements taken across the sample. Elements generally falling below the detection limit include S and Ca, whereas Mg, Ti, Mn, and K were found to be below the detection limit in some analyses.

When the different points analysed are compared, it could be seen that point SA-27 had very low values, which were, most likely an artefact of this point being close to the edge of the sample, which might have some tarnishing, or oxidation, due to the cutting of the samples involved, or which might not be a flat surface affecting the X-rays taken. The point was, therefore, discarded, and the results were based on the remaining analyses concerned. The pXRF results showed the Fe content as ranging between 83 and 88 wt. %, the Ni as ranging between 5,0 and 5,8 wt. %, and the P as ranging between 0,17 and 0,38 wt. %. The points SA-1 to SA-14, in Sample A (Appendix A, Table A-1), have slightly lower Fe values when compared to the remainder of sample A. The whole rock chemistry obtained by Frick and Viljoen (1973:347) and the average geochemistry of the Etosha meteorite are summarised in Table 4-2. Due to specific elemental values being used for the comparison with the previous literature, the total weight percentage of the Etosha meteorite does not equal 100% in Table 4-2.

Some differences exist between the results obtained and those of Frick and Viljoen (1973:347). The difference concerned is due to the methods used in the current study (pXRF) and in the study of Frick and Viljoen (1973) (XRF). A limitation of pXRF is that the effect of textural differences on the surface of a sample is fairly difficult to understand, and can influence the readings of the instrument (Goodale *et al.*, 2012:882). The above is relevant for the sample involved, due to the kamacite bands (Widmanstätten structure) that are present, which can influence the results obtained, whereas a laboratory based XRF instrument is unaffected due to the X-ray beams used being much smaller in diameter and being more precise. The biggest difference is seen in the Fe content, in terms of which a difference of 6,59 wt. % can be seen. The other noticeable differences can be seen in the Ni, Mg, Al, Si and Ca contents. The P and Co content are in the same approximate range.

**Table 4-2: Average values of the pXRF data obtained (spot analysis data) of the Etosha meteorite, compared with the XRF results of Frick and Viljoen (1973:347) of the Etosha meteorite**

| Element | Etosha meteorite average (%) | Results obtained by Frick and Viljoen (1973:347) (weight %) |
|---|---|---|
| Fe | 85,50 | 92,09 |
| Ni | 5,37 | 6,70 |
| Mg | 1,93 | <0,05 |
| Al | 0,65 | <0,02 |
| Co | 0,35 | 0,44 |
| Si | 0,28 | 0,03 |
| P | 0,25 | 0,33 |
| K | 0,04 | 0,19 |
| Cr | 0,03 | <0,01 |
| Mn | 0,03 | <0,01 |
| Ti | 0,03 | <0,01 |
| Ca | <0,04 | <0,05 |
| S | <0,01 | <0,01 |
| C | *nd | 0,03 |
| Na | *nd | 0,09 |
| **Total** | 94,54 | 100,06 |

*nd – not determined.

The Fe and Ni weight % binary diagram in Figure 4-27, however, shows a strong positive correlation (r = 0,88) between the Fe and Ni wt. %. The differences in the elemental content of the current study, when compared to Frick and Viljoen (1973:347), can have a major impact on the types of minerals found in the present study, compared to in the previous literature. The positive correlation between Fe and Ni contrasts with the EPMA data shown in Figure 4-14, which shows a strong negative correlation (r = -0,98). The difference in correlation could be due to the EMP being much more accurate in the present instance, with it only analysing certain spots, whereas the pXRF analyses the meteorite sample as a whole, and is not as accurate as the EMP, due to the size and the distribution of minerals in the meteorite (Gemelli *et al.*, 2014:60). Since only XRF data was available from literature, both EPMA and pXRF were used in this study. To highlight the possible variations due to the technique limitations the EPMA and pXRF results were compared.

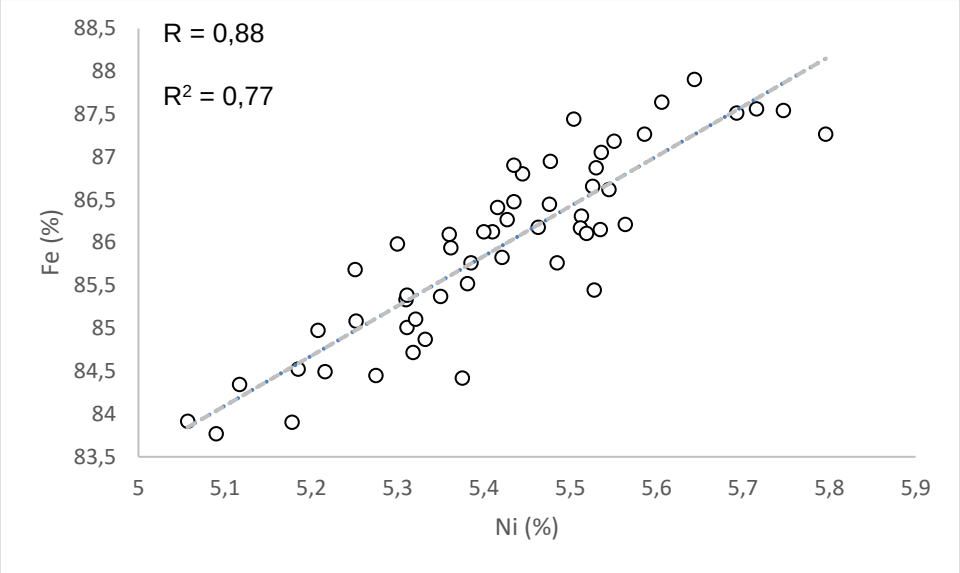


**Figure 4-27: Fe (wt. %) and Ni (wt. %) binary diagram with data obtained from pXRF analysis of the Etosha meteorite (Appendix B). The correlation (R) as well as coefficient of determination ($R^2$) values are indicated on the diagram.**

Availability of EPMA & pXRF data from older literature neccessitated the use of both techniques here to present thorough analyses. Newer technique development might have had an influence on results of XRF. A limitation of pXRF is that the effect of textural differences on the surface of a sample is difficult to understand and can influence the readings of the instrument and is not as accurate as the EPMA.

### 4.5.2 ICP-MS

The LA-ICP-MS results obtained are included in Appendix C, Table C-1. The average values of the data obtained that were calculated are presented in Table 4-3. The Fe and Ni content obtained through LA-ICP-MS is higher than is that which was found through pXRF (where Fe = 85,5% and Ni = 5,37%). The Fe and Ni values found in the current method are similar to the values obtained by Frick and Viljoen (1973:347), as shown in Table 4-2. The same range of elements were included in the results of the previously mentioned methods.

The Co content (4030,07 ppm) in the LA-ICP-MS results, however, corresponds to the pXRF values, as well as does that which was obtained by Frick and Viljoen (1973:347) (Table 4-2), as the value involved falls between the two above-mentioned values. The Co is also moderately higher than for the rest of the trace elements, with its content being the highest of the trace elements, excluding Ni, which situation was also found by Frick and Viljoen (1973:347).

**Table 4-3: LA-ICP-MS data obtained of the Etosha meteorite, which can be found in Appendix C**

| Element | Quantity |
|---|---|
| Fe | 89,17 wt. % |
| Ni | 7,87 wt. % |
| Cr | 60,20 ppm |
| Co | 4030,07 ppm |
| Cu | 134,42 ppm |
| Zn | 54,54 ppm |
| Ga | 57,01 ppm |
| Ge | 189,77 ppm |
| As | 9,16 ppm |
| Mo | 5,23 ppm |
| Ru | 1,94 ppm |
| Rh | 1,00 ppm |
| Pd | 1,83 ppm |
| Sn | 0,86 ppm |
| Sb | 0,16 ppm |
| W | 0,23 ppm |
| Ir | 0,06 ppm |
| Pt | 1,85 ppm |

The Cr content (60,20 ppm) is much lower than the values of the pXRF and of Frick and Viljoen (1973:347) study, as presented in Table 4-2. The values concerned are much more accurate than are those of the pXRF method. This is due to the LA-ICP-MS being much more rapid and accurate, due to its use of calibration standards (Makino *et al.*, 2019:1798), compared to the pXRF, which can have a lack of data quality, due to its portability, as well as to the lack of sample preparation (Adlington *et al.*, 2020:1-2).

Ga and Ge are very important in terms of the classification and description of an iron meteorite, as the two elements concerned are siderophile elements, which show a genetic relationship between the meteorites in which they are found (Buchwald, 1975c:83-84). The elements are determined and their values are obtained in iron meteorites, due to their small concentration ranges, which allow the results to be more accurate (Buchwald, 1975c:83). In Figure 4-28, the Ga values are plotted against the Ge values, with them showing a very strong positive correlation (R = 0,96) (Lovering *et al.*, 1957:275) in the Etosha meteorite, which means that the Ga content

increases along with the Ge content increase in the Etosha meteorite (Scott & Wasson, 1975:529).

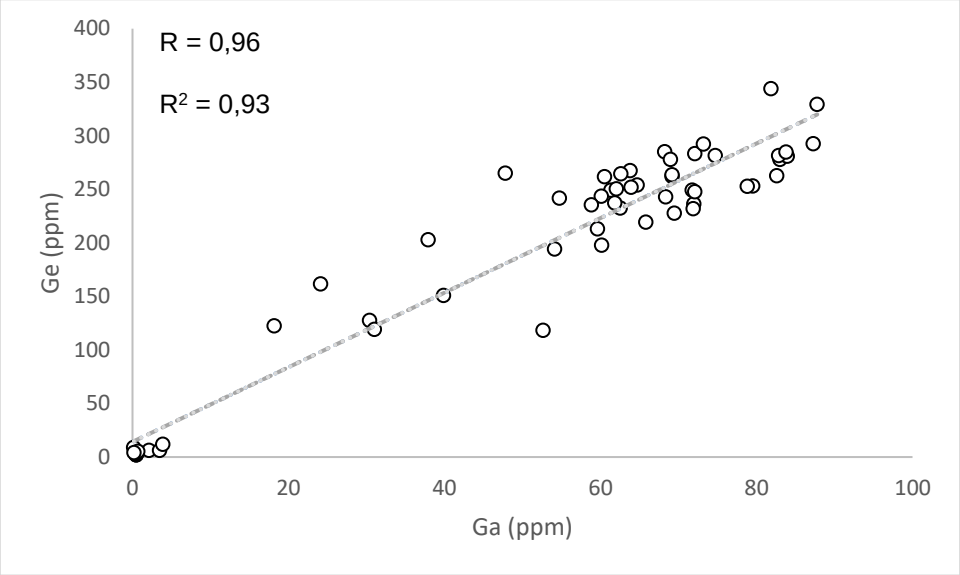


**Figure 4-28: Ga (ppm) and Ge (ppm) binary diagram with LA-ICP-MS data of the Etosha meteorite plotted (Appendix C) with the correlation (R) and the coefficient of determination ($R^2$) indicated on the diagram.**

The section confirmed the overall chemistry obtained by EPMA and SEM of the Etosha meteorite as being Fe-Ni rich with the trace elements like Co, Cu, and Cr being present in varying quantities. The Ga and Ge content was also found to be quite high when comparing it with other meteorites, which confirms the statement made by Wasson *et al.* (2007:760), who state that the IIAB meteorites tend to have higher values than do the other meteorite classes.

## 4.6 Classification of the Etosha meteorite

Wasson (1974:30) and Weisberg *et al.* (2006:44) emphasise that it is of key importance to classify a meteorite using both structural and chemical classification schemes to ensure that the classification is complete. The Etosha meteorite has been classified by Frick and Viljoen (1973) as a medium octahedrite, and by Frick and Hammerbeck (1973) as a coarse octahedrite. However, the studies involved only classify the Etosha meteorite structurally, rather than chemically.

### 4.6.1 Structural classification

The structural classification of a meteorite is done by means of measuring the bandwidths of the kamacite bands, which became prominent during the process of acid etching. The measurements are then compared to the values in

Table 2-5, so as to be able to determine the structural class of the meteorite involved. The Etosha meteorite displays the Widmanstätten structure, when etched with the 1%, as well as the 6% nitric acid (Figure 4-29).

Individual kamacite bands are visible on etched surfaces with the naked eye, as can be seen in Figure 4-29, with them being considered coarse in terms of width. The structural arrangement, therefore, suggests that the Etosha meteorite cannot be either a hexahedrite or an ataxite (

Table 2-5), as the kamacite bands are visible to the naked eye. The slight differences in the concentration of etchants used result in some variations between the features observed in the two samples, as can be seen in Figure 4-29. Sample A displays a light grey surface, with a light grey Widmanstätten structure, whereas sample B is much darker, with a darker grey surface and

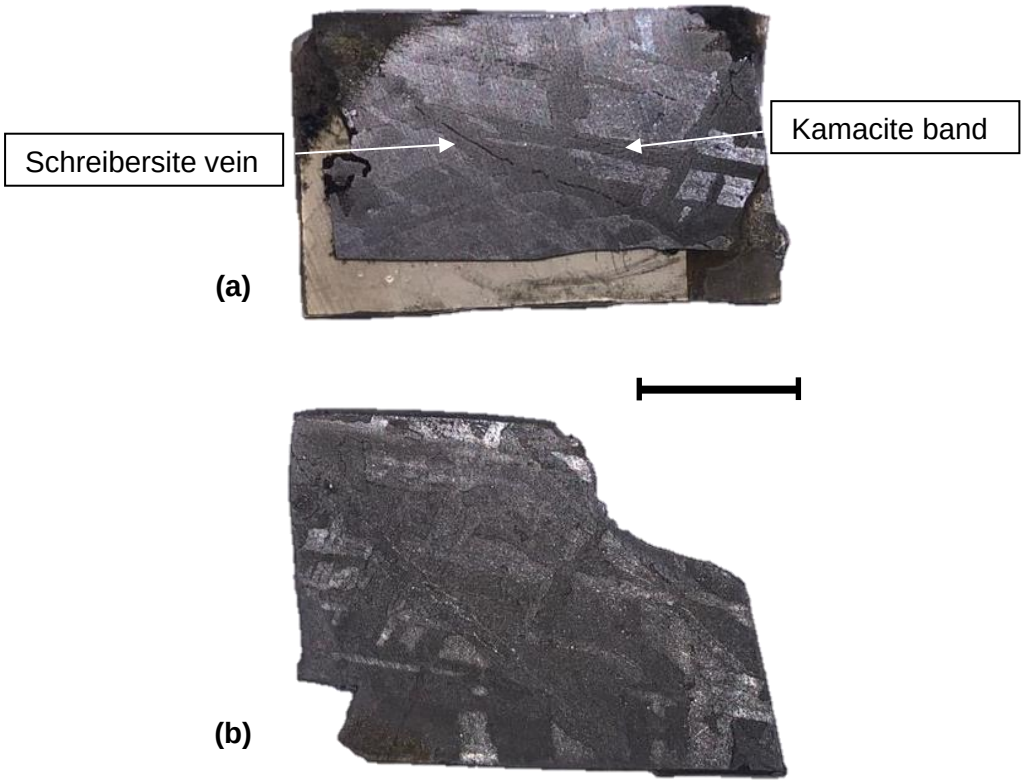


**Figure 4-29: Polished sections of (a) sample A, etched with 1% nitric acid (displaying a schreibersite vein), and (b) sample B, etched with 6% nitric acid. Both sample A and sample B are displaying a Widmanstätten structure. Scale bar = 10 mm.**

a Widmanstätten structure. The surface of sample B is also rougher than is that of sample A, which is attributed to the more concentrated acid removing more of the surface area than was removed in sample A.

The kamacite bands were analysed under RL, so as to determine the bandwidth involved. According to Buchwald (1975c:66), the classification is done by means of using the broadest kamacite band present in the sample and by means of calculating the average of its width. However, Goldstein (1965:6) states that the average kamacite bandwidth refers to the average of all of the kamacite bands together. Both of the methods concerned were, therefore, applied to determine the structural classification of the Etosha meteorite, so as to ensure that the structural classification was accurate. All kamacite bands on both samples were measured, so as to ensure that the measurements truly represent the meteorite.

The kamacite bandwidths measured in the etched samples of the Etosha meteorite are presented in Table 4-4. Both the methods of Buchwald (1975c:66) and those of Goldstein (1965:6) are presented. According to the bandwidth measurements and the classification scheme by Buchwald (1975c:66), as presented in Table 4-4, the Etosha meteorite can be classified as a coarse octahedrite, as its kamacite bands measurement falls between 1,3 mm and 3,3 mm (Table 4-4). Such classification corresponds to the classification of Frick and Hammerbeck (1973:16), although it does not correspond to the findings made by Frick and Viljoen (1973:345), as they reported kamacite bandwidth as being between 1 mm and 1,5 mm, therefore classifying the Etosha meteorite as a medium octahedrite.

**Table 4-4: Structural classification of the Etosha meteorite based on the width of the kamacite bands, applied to both sample A and sample B by using two different methods, Buchwald (1975c:66) and Goldstein (1965:6), from the literature**

| Type of measurement | Sample A | Sample B |
|---|---|---|
| Largest kamacite band average (Buchwald, 1975c:66) | 2,6 mm | 3,26 mm |
| Average of kamacite bands (Goldstein, 1965:6) | 1,96 mm | 1,61 mm |
| Classification (Buchwald, 1975c:66) | Coarse octahedrite (1,3 – 3,3 mm) | Coarse octahedrite (1,3 – 3,3 mm) |

The Etosha meteorite can structurally be compared to the Canyon Diablo (United States of America) (Buchwald, 1975a:381) and the Campo Del Cielo (Argentina) (Buchwald, 1975a:373) meteorites, which are well-known coarse octahedrites (Meteoritical Bulletin Database, 2021). The

coarse Widmanstätten structure was formed due to the very slow cooling of the meteorite during formation, which caused thick plates of kamacite to form, interspersed with medium taenite lamellae (Buchwald, 1975c:115). The structural classification should, however, correspond to the chemical classification of the meteorite, as the structural classification alone cannot comprehensively classify the meteorite.

### 4.6.2 Chemical classification

The calculated averages of the trace elements useful for the chemical classification of the meteorites obtained from LA-ICP-MS are presented in Table 4-5, along with the values used by Wasson (1967:162) for chemical classification. According to the classification made, the Etosha meteorite can be broadly classified into the Ga-Ge group II.

However, the meteorite can be further classified within the Ga-Ge group II, by means of plotting the Ni weight percentage on a logarithmic scale against Ga (Figure 4-30) and Ge (Figure 4-31), respectively. The Etosha meteorite plots completely within the IIAB field, as indicated in Figure 4-30, and partially in the IIAB field, as can be seen in Figure 4-31. Therefore, it can be said that the Etosha meteorite is an IIAB iron meteorite. The IIAB field in the diagram can be described as a grouping of the fields, IIA and IIB (Weisberg *et al.*, 2006:43). According to the chemical classification of the iron meteorites adapted from Buchwald (1977:454) and presented in Table 2-3, the IIA group corresponds to the hexahedrites, with the IIB group corresponding to coarse octahedrites. This classification, therefore, corresponds to that of Frick and Hammerbeck (1973), which states that the Etosha meteorite is a coarse octahedrite.

**Table 4-5: Average Ni, Ga, Ge and Ir concentrations obtained by LA-ICP-MS in this study of the Etosha meteorite and historical concentrations from Wasson (1967:162), for purposes of chemical classification**

| Element | Concentration | Ga-Ge group II values (Wasson, 1967:162) |
|---|---|---|
| Ni | 7,87 wt. % | 5,3-9,6 wt. % |
| Ga | 57,01 ppm | 40-62 |
| Ge | 189,77 ppm | 130-230 |
| Ir | 0,06 ppm | *nr |

*nr: element not reported

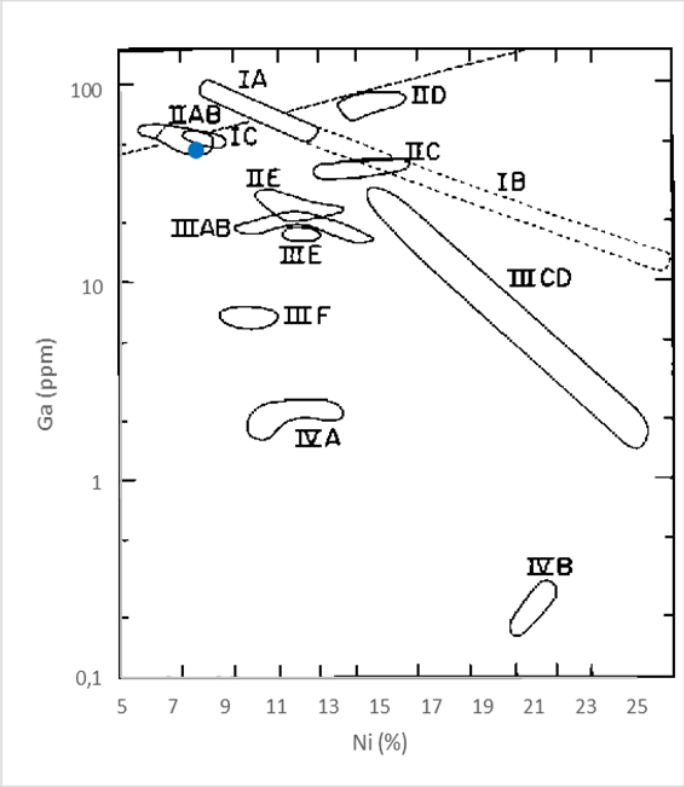


**Figure 4-30: Ni (wt. %) against Ga (ppm) chemical classification diagram, adapted from Scott and Wasson (1975:529) classifying the Etosha meteorite in the IIAB chemical class.**

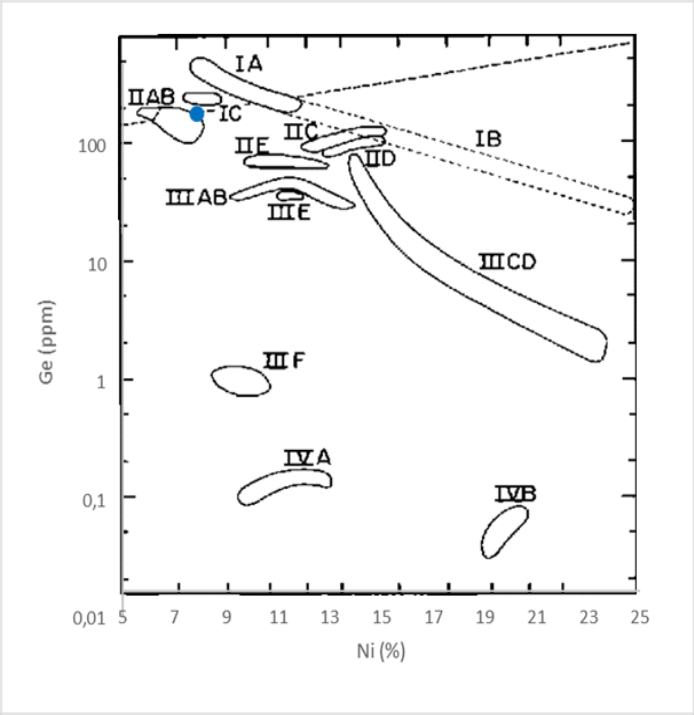


**Figure 4-31: Ni (wt. %) against Ge (ppm) chemical classification diagram, adapted from Scott and Wasson (1975:529) classifying the meteorite in the IIAB chemical class.**

The classification suggests that the Etosha meteorite is chemically similar to the Sikhote-Alin meteorite (23 tons) in Russia, the Coahuila meteorite (2,1 tons) in Mexico and the Hex River Mountains meteorite (60 kg) in South Africa (Meteoritical Bulletin Database, 2021; Scott & Wasson, 1975:536). The similarities between the different meteorites include their weight (with the Etosha meteorite weighing 111 kg) and their chemical classification, which is that of an IIAB iron meteorite.

A few selected elemental abundances (Ni, Ga, Ge and Ir) of the meteorite were compared to those of other IIAB meteorites (Okahandja, Kopjes Vlei and Hex River) that were discovered relatively close to the Etosha meteorite (Table 4-6). The Ni content of the Etosha meteorite is much higher than is that of the other meteorites. However, the Ga and Ge content is in the same range as is the Okanandja, with it being slightly lower than the Kopjes Vlei and Hex River meteorites (Table 4-6). The Ir content of the Etosha meteorite, however, is much lower than is the content of the other meteorites, as highlighted in Table 4-6.

The structural and chemical classification of the Etosha meteorite, therefore, corresponds, therefore enabling the meteorite to be classified as an IIAB coarse octahedrite. The important elemental abundances (Ni, Ga, Ge and Ir) of the Etosha meteorite correspond to those of other similar types of iron meteorites, confirming the chemical classification of the Etosha meteorite. According to Weisberg *et al.* (2006:43), the structural and chemical classification correlate with each other, with the chemical classification being inferred from the structure of the meteorite. The correlation between the chemical and structural classification is largely due to the control of the geochemistry concerned, especially in terms of the bulk Ni concentration, in relation to the Widmanstätten structure growth in the iron meteorite (Weisberg *et al.*, 2006:43).

**Table 4-6: Elemental abundance of Ni, Ga, Ge and Ir of the Etosha meteorite compared to other chemically similar IIAB meteorites (Okahandja – Namibia, Kopjes Vlei – South Africa, Hex River Mountains – South Africa)**

| Elements | Etosha | Okahandja (Buchwald, 1975a:944) | Kopjes Vlei (Buchwald, 1975a:742) | Hex River Mountains (Buchwald, 1975a:644) |
|---|---|---|---|---|
| Ni (wt. %) | 7,87 | 5,75 | 5,65 | 5,64 |
| Ga (ppm) | 57,01 | 56 | 59,9 | 60,7 |
| Ge (ppm) | 189,77 | 185 | 182 | 181 |
| Ir (ppm) | 0,06 | 9,2 | 3,1 | 4,4 |

## 4.7 SSA meteorite statistics in terms of the Etosha meteorite

The meteorite data of the sub-Saharan region of Africa has not yet been analysed in detail. Data from these meteorites was extracted from the Meteoritical Bulletin Database (2021), with various diagrams used to present the data. The explanations and discussion of the diagrams will be presented in this section.

### 4.7.1 Meteorite types

As mentioned earlier, three main types of meteorites namely chondrites, irons and stony-irons, exist according to the literature. However, to facilitate the data collection process, the meteorites were divided into four main groups, as presented in Figure 2-1, chondrites, irons, stony-irons and achondrites, which followed the same classification as Hutchison (2004:244). The achondrites include meteorites from the Martian, Lunar and howardites-eucrites-diogenites (HED) clans, angrites, aubrites, ureilites, acapulcoites, winonaites, lodranites, brachinites and the ungrouped (enstatite-rich) achondrites.

The quantities of the different meteorite types mentioned above are presented in Figure 4-32. From the data presented in Figure 4-32, it is clear that chondrites are more commonly found in SSA than are the other types of meteorite, which corroborates the worldwide trend, in terms of which the chondrites are the most common type of meteorite (Hutchison, 2004:5). Achondrites are the second most common type of meteorite, probably due to the large number of groups that are included in this meteorite classification type.

With iron meteorites being the third most common meteorite (McKenzie, 2014:35), stony-iron meteorites are the rarest type of meteorite, which corresponds with the literature concerned (McKenzie, 2014:37). However, an outlier exists that cannot be seen in Figure 4-32, which is a meteorite without a type, or whose type is ‘unknown’. The meteorite concerned, which was found in the Democratic Republic of Congo, is named Lusaka (Meteoritical Bulletin Database, 2021).

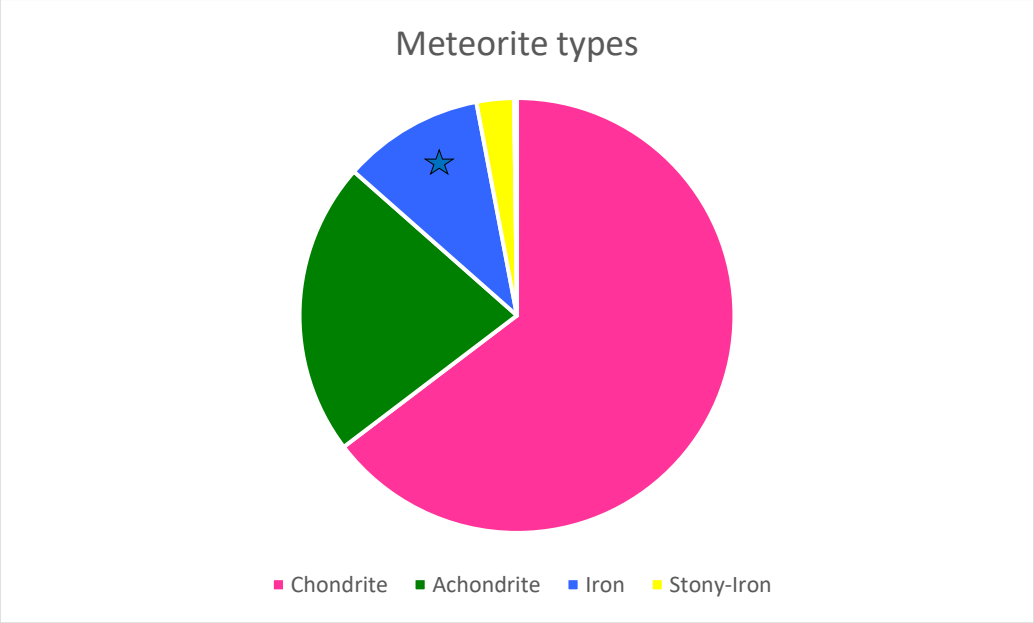


**Figure 4-32: Meteorite types found in SSA. Where the added ★ refers to the Etosha meteorite type.**

### 4.7.2 Frequency of meteorite discoveries

The frequency of discoveries of meteorites over the past century is presented in Figure 4-33. Fewer than ten meteorites, on average, were discovered, per year, up to 1997, with the discovery numbers reaching a plateau between 2004 and 2011. In 2012, the number of meteorite discoveries spiked, reaching a peak in 2019, after which it declined (Ouknine *et al.*, 2019:2).

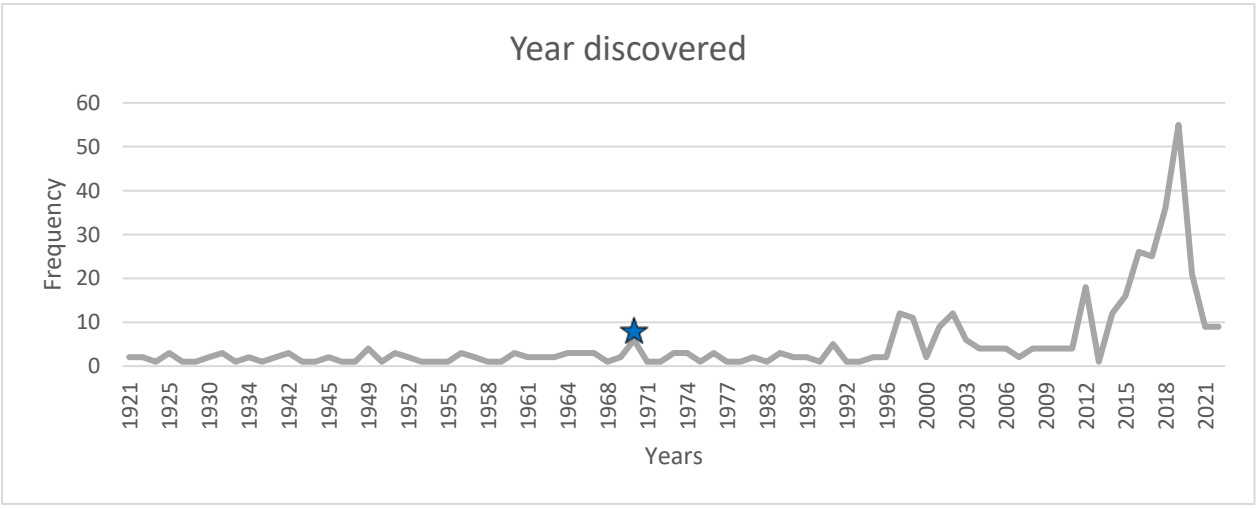


**Figure 4-33: The years in which meteorites were discovered (from 1921-2021) in SSA. Where the added ★ refers to the year in which Etosha meteorite was discovered.**

### 4.7.3 Frequency of meteorite falls and finds

The meteorite finds have been considerably more than the meteorite falls involved, as highlighted in Figure 4-34. This data corresponds to the worldwide trends in the dominating meteorite finds (McKenzie, 2014:26). The above suggests that most of the meteorites of SSA have been altered by means of terrestrial processes, which can affect their chemical analysis.

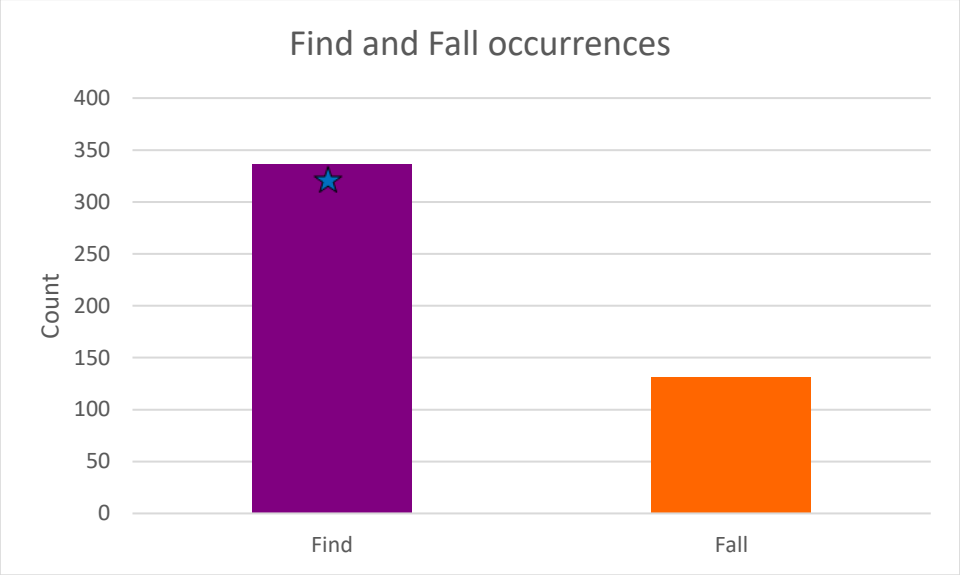


**Figure 4-34: Find and fall occurrences in SSA. Where the added ★ indicates that the Etosha meteorite was classified as a find.**

### 4.7.4 Types of iron meteorites found

The quantity of different types of iron meteorites found in SSA is presented in Figure 4-35. IIIAB iron meteorites have been the most common (10), with IIAB meteorites (the Etosha meteorite class) (7) being the second most common, and ungrouped meteorites (i.e. those that do not classify within the current chemical classes), the third most common. Figure 4-35 shows that iron meteorites are not that commonly found in comparison to chondrites (Figure 4-32).

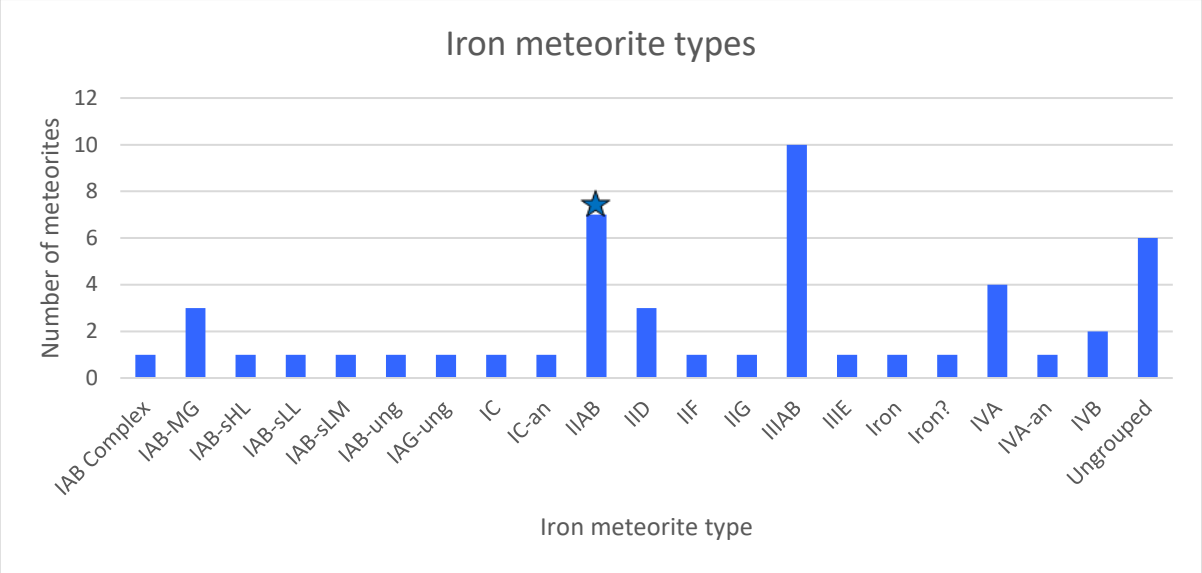


**Figure 4-35: Iron meteorite types, according to chemical classification. MG = main group; sHL = high-Au, low-Ni subgroup; sLL = low-Au, low-Ni subgroup; sLM = low-Au, medium-Ni subgroup; ung = ungrouped; an = anomalous; Iron = iron meteorite not yet fully classified; Iron? = possible iron not yet classified (Meteoritical Bulletin Database, 2021). Where the added ★ indicates that the Etosha meteorite is classified as a IIAB iron meteorite.**

### 4.7.5 Type of meteorite discovered versus its mass

The different types of meteorites found also have a corresponding average mass when found on the surface of the Earth. Their corresponding type and average mass relationship is presented in Figure 4-36. Iron meteorites represent the highest average mass, at close to 5 800 kg, whereas chondrites and achondrites have much lower average masses. The above fact can be attributed to the iron meteorites consisting mainly of Fe and Ni, and to them, therefore, being relatively dense and capable of handling intense stress, both internally and externally, meaning that the meteors concerned are unlikely to break apart easily when entering the Earth's atmosphere. In contrast, chondrites are usually incapable of handling the extreme stresses to which they are subjected when entering the atmosphere, which causes the meteors concerned to break up easily in the atmosphere, leading to many smaller pieces of meteorite falling to the Earth's surface (McKenzie, 2014:9).

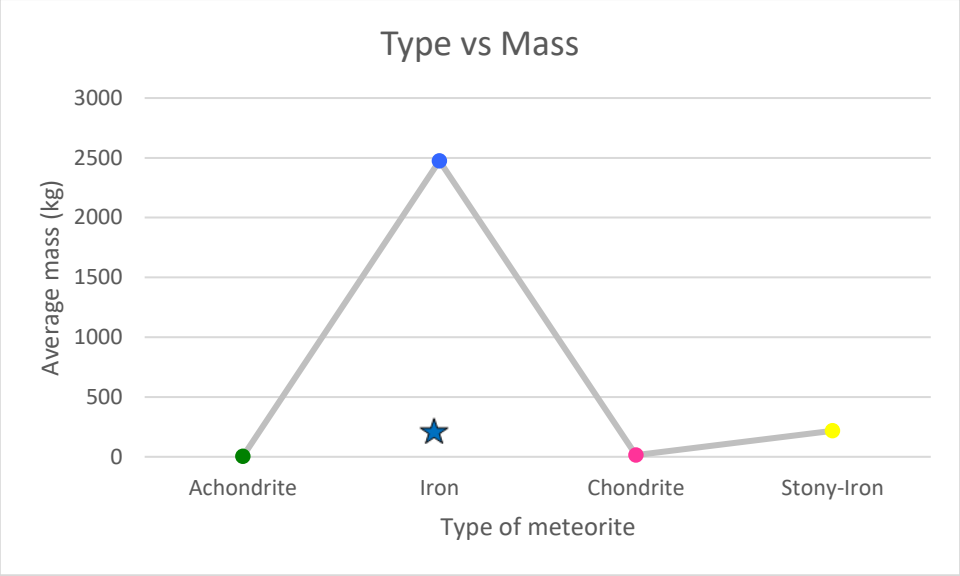


**Figure 4-36: Type of meteorites found versus their average mass. Where the added ★ shows the mass of the Etosha meteorite at 111 kg.**

### 4.7.6 GIS

In the current study, applying GIS for the representation of meteorite statistics in SSA allowed for the integration of different types of data from various sources, so as to enable the analysis and visualisation of possible trends, as well as the spatial evaluation of data (Reddy, 2018:48). Various maps were created, so as to display diverse statistical parameters of the meteorites of SSA, as well as to show the trends present, and to place the Etosha meteorite in context within the dataset concerned.

Especially in the north-western part of SSA, several meteorites lack coordinates, due to the existence of such factors as the anonymity of finders, the lack of meteorite awareness, and the high degree of commercial interest shown (Ouknine *et al.*, 2017:31-32). According to Ouknine *et al.* (2017:32), the older literature indicates that the term 'Northwest Africa' (NWA) refers to Algeria, Morocco, Nigeria, Mali, Mauritania and Niger, although they concluded that, for their study, they would only regard Algeria, Morocco, Mauritania and Mali as NWA countries. In the present study, the data pertaining to three of the abovementioned countries (namely, Mali, Mauritania and Niger) is included in Table 4-7, together with the details of a significant number of meteorites that lack coordinates. The absence of meteorites in Mauritania, Mali and Niger (Figure 4-37) is, therefore, an artefact of the prevailing situation, because the coordinates were used to plot the meteorites in the countries concerned.

**Table 4-7: Meteorites of SSA that do not have coordinates of the location they were discovered in recorded (Meteoritical Bulletin Database, 2021)**

| Country | Chondrites | Achondrites | Irons | Stony-Irons | Total |
|---|---|---|---|---|---|
| **Botswana** | 7 | - | - | - | 7 |
| **Congo DR** | 1 | - | - | - | 1 |
| **Mali** | 18 | 20 | 1 | - | 39 |
| **Mauritania** | 64 | 54 | 1 | 4 | 123 |
| **Niger** | 31 | 3 | 1 | 1 | 36 |
| **South Africa** | 2 | - | 2 | - | 4 |
| **Sudan** | 1 | 1 | - | - | 2 |

The different types of meteorites discovered over the whole of SSA are displayed in Figure 4-37 and Figure 4-38. The chondrites can be seen to be the most common meteorite discovered, which corresponds to the details presented in Figure 4-32. The only countries to have, as yet, discovered stony-iron meteorites are, clearly, South Africa, Namibia, Mali, Mauritania, Niger, Nigeria and Kenya. The location of the countries involved corresponds to the data reflected in the distribution map in Figure 1-2, which shows that the meteorite discoveries made in SSA are concentrated in southern, north-western and eastern Africa (Khiri *et al.*, 2017:653).

Iron meteorites are, however, more concentrated in the southern part of SSA, mostly in Namibia and South Africa (Ouknine *et al.*, 2019:4). Iron meteorites are more concentrated than are chondrites in the southern parts of SSA, partially due to the relatively large size of the meteorites concerned, in addition to the fact that the meteorites involved tend not to break apart as much as do others when entering the atmosphere, hence facilitating their finding (Hutchison, 2004:322; Ouknine *et al.*, 2019:4-5). Another reason for the relatively large number of iron meteorites discovered in the southern parts of SSA is their resistance to chemical and physical weathering (Ouknine *et al.*, 2019:7).

The discovery of achondritic meteorites is mainly concentrated in the north and north-western parts of SSA, most likely as a result of the climatic difference experienced between the arid and semi-arid northern parts and the tropical southern parts (Ouknine *et al.*, 2019:7). In the tropical areas, characterised by relatively high levels of precipitation and humidity, the achondrites involved tend to be much more susceptible to weathering than they are in other areas (Ouknine *et al.*, 2019:7). The apparent lack of meteorites in the tropical part of the African continent is, therefore, attributed to the high weathering rates experienced in tropical areas and the dense vegetation that makes their discovery relatively unlikely (Ouknine *et al.*, 2019:5).

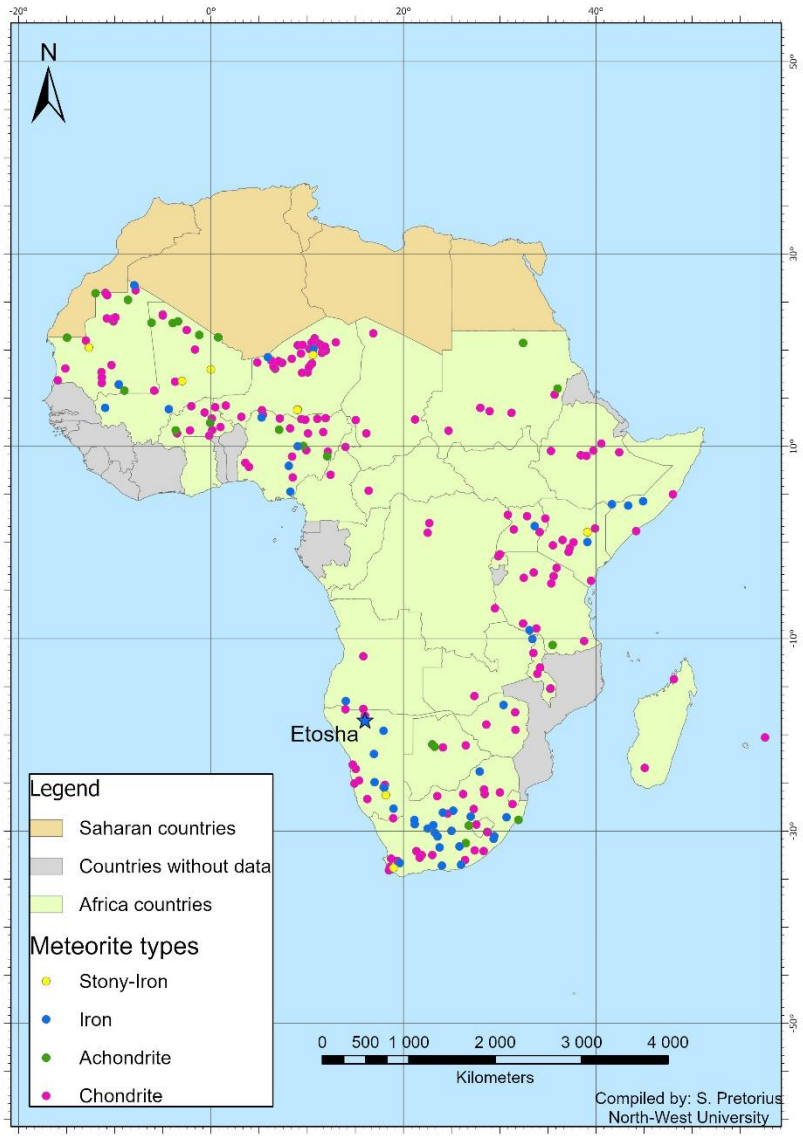


**Figure 4-37: Map of the different meteorite types distributed over SSA (Environmental Systems Research Institute (ESRI), 2020), with the added ★ showing that the Etosha meteorite is an iron meteorite discovered in Namibia.**

Many meteorites, especially in the north-western parts of SSA, lack specific coordinates on the Meteoritical Bulletin Database (2021) (Table 4-7), which is why a large difference is seen in Figure 4-38, where Mauritania and Mali display a larger number of achondrites than on the map in Figure 4-37. Another clear difference is the total number of meteorites, especially chondrites, found in the two countries (Mauritania and Mali) concerned.

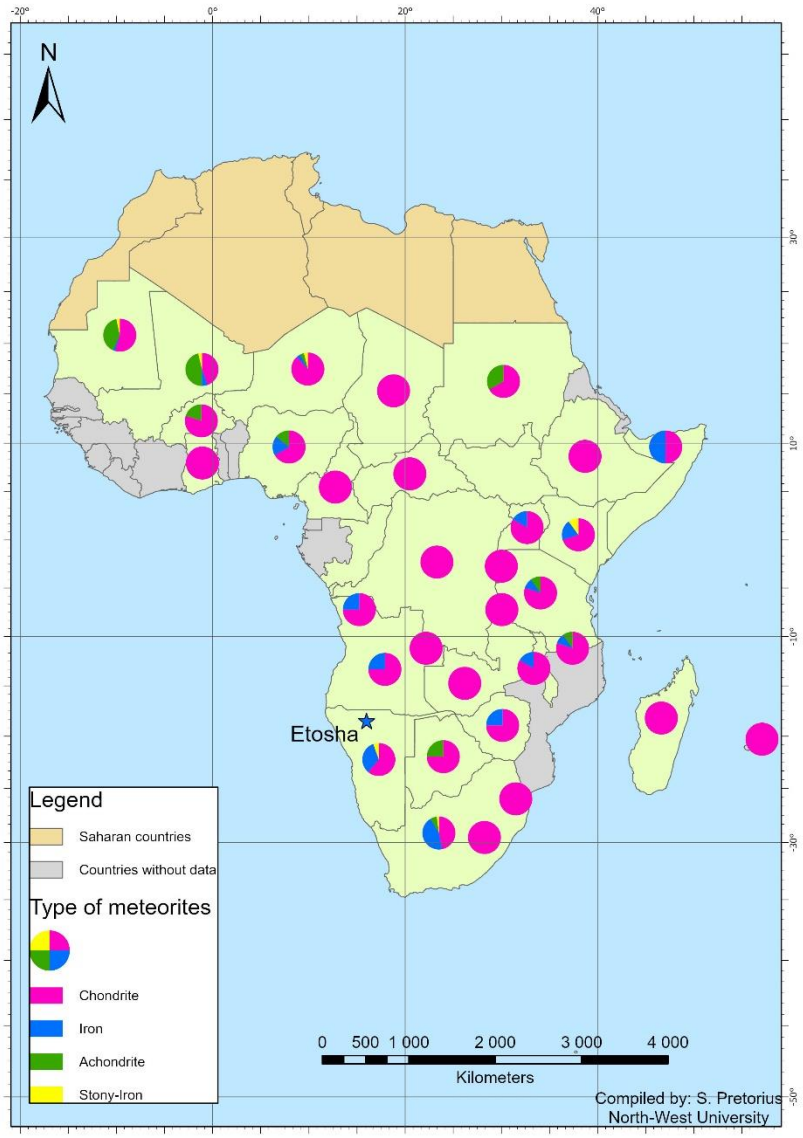


**Figure 4-38: Occurrence of different meteorite types per country (Environmental Systems Research Institute (ESRI), 2020), with the added ★ showing that the Etosha meteorite is an iron meteorite discovered in Namibia.**

South Africa and Namibia both show an almost equal number of chondrites and iron meteorites found, with few to no achondrites (Figure 4-38). The two countries also display a small number of stony-iron meteorites. On comparing Figure 4-38 with Figure 4-39, there is a clear correlation between the countries with a comparatively large number of iron meteorites and the countries that have the highest total mass (kg) of meteorites discovered. Namibia, for instance, has a large number of iron meteorites and a high total mass (kg) of meteorites (Figure 4-38 and Figure 4-39). This is due to Namibia hosting the world's largest meteorite, namely the Hoba meteorite (iron meteorite), which alone weighs close to 60 tons (McKenzie, 2014:63), as well as the Gibeon meteorite shower (consisting of iron meteorites), with a combined weight of 26 tons (Meteoritical Bulletin Database, 2021).

Although north-western SSA countries also have high total meteorite masses, such masses can be attributed to the high number of meteorites found in the countries involved (Figure 1-2 and Figure 4-39), and not to single, large meteorites, as is the case with Namibia, Tanzania and Somalia (refer to Appendix D, Table D-1). A possible reason why such northern SSA countries have a large number of discoveries is linked to their locality, namely to them bordering on the Sahara Desert (Khiri & Ibhi, 2015:2; Khiri *et al.*, 2017:653; Ouknine *et al.*, 2019:1), which is considered a hotspot for meteorite discoveries. Deserts are considered hotspots for meteorite finds, because most meteorites are difficult to distinguish from Earth rocks, when based on appearance alone, in most parts of the world, but they are much easier to identify in sandy deserts, due to their lack of vegetation and other rocks (Ouknine *et al.*, 2019:1).

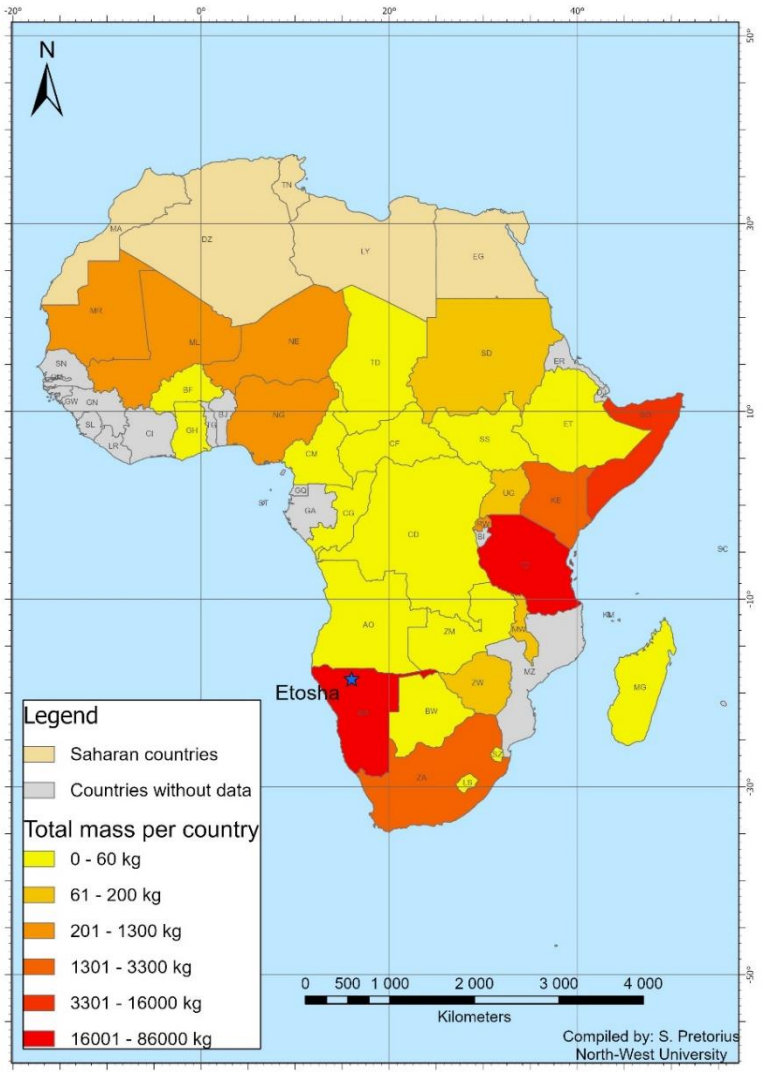


**Figure 4-39: Map of total mass (kg) of meteorites discovered per country (Environmental Systems Research Institute (ESRI), 2020), with the added ★ indicating that the Etosha meteorite was discovered in Namibia which displays a total mass of between 16001 and 86000 kg.**

Most countries with fewer than five meteorites (Figure 1-2), which are mainly concentrated in central SSA, as well as the islands of for example Mauritius and Madagascar, have mainly discovered chondrites (Figure 4-38) that are under 60 kg in weight (Figure 4-39). The finding correlates with the worldwide trend that chondrites are the most discovered meteorite type (Ouknine *et al.*, 2019:3). Chondrites are also historically known not to weigh as much as do most irons, due to their low Fe content, when they are compared to iron meteorites (Ouknine *et al.*, 2019:2).

The statistics for falls and finds in SSA are presented in Figure 4-40. The majority of falls correspond with the distribution of meteorites (Figure 1-2), which is supported by the literature (Khiri *et al.*, 2017:653), which suggests that they are concentrated in southern, north-western and eastern SSA. The available statistics also indicate the existence of more countries with both finds and falls than countries with only finds. Furthermore, a correlation exists between countries that show the highest total weight (Figure 4-39) and number of meteorites (Figure 1-2) and the countries with the most finds (Figure 4-40). The higher the number of meteorite discoveries, the higher is the probability of the meteorites concerned being classified as finds. The Etosha meteorite, which is classified as a find, was discovered in Namibia (Frick & Viljoen, 1973:345), which, incidentally, has more finds than falls.

A map that presents the IIAB meteorites found in SSA, including the Etosha meteorite, is presented in Figure 4-41. Only eight IIAB iron meteorites have been discovered in SSA, but, when compared to the other iron meteorite types (Figure 4-35), the IIAB meteorite type is the second most common type to have been found in SSA (Meteoritical Bulletin Database, 2021). As already highlighted, the IIAB meteorites closest to the locality where the Etosha meteorite was found include the Okahandja (Namibia), Kopjes Vlei (South Africa) and Hex River Mountains (South Africa) meteorites. The chemistries of the important elements used for classification (Ni, Ga, Ge and Ir) are presented in Table 4-6. Noteworthily, the IIAB iron meteorites found in SSA occur mainly on the western side of the continent.

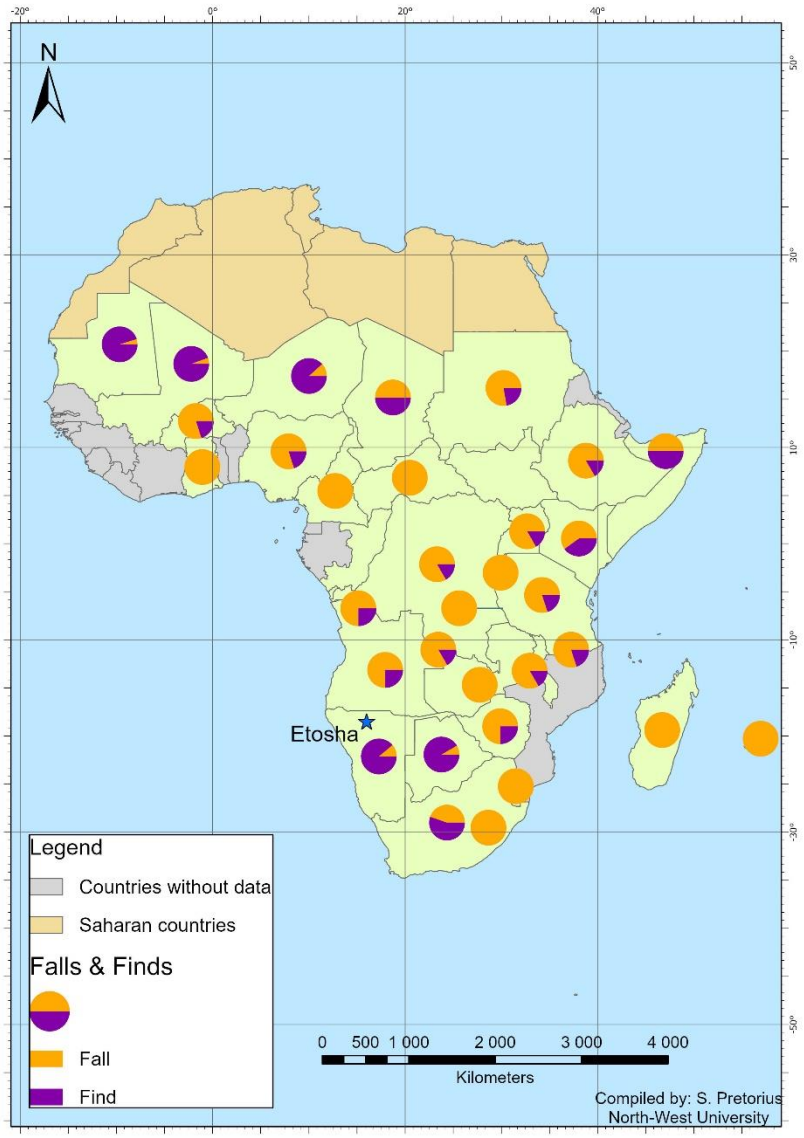


**Figure 4-40: Falls and finds in SSA per country (Environmental Systems Research Institute (ESRI), 2020), with the added ★ showing that the Etosha meteorite was discovered in Namibia which is dominated by finds.**


**Figure 4-41: Iron meteorite types, similar to the Etosha meteorite, found in SSA (Environmental Systems Research Institute (ESRI), 2020), with the added ★ showing that the Etosha meteorite was discovered in the same country as the Okahandja meteorite.**

# CHAPTER 5 CONCLUSIONS AND RECOMMENDATIONS

A comparative, re-evaluative study was done on the Etosha meteorite kept in the NWU's geological museum collection, so as to update the mineralogy, geochemistry and classification obtained by previous researchers. New information on the chemical classification was added to the existing information. The meteorite occurrences in SSA were evaluated in terms of their type, locality, and classification, so as to gain an enhanced understanding of the meteorites of the region and so as to place the Etosha meteorite in context. The study's aims and objectives will be addressed in this chapter, by means of providing a summary of the contents of the chapters in the current study. The hypothesis of the study is discussed, along with the making of recommendations for further studies.

## 5.1 Surface structures, mineralogy, and geochemistry of the Etosha meteorite

The Etosha meteorite is a find, which means that it has undergone some terrestrial weathering events, which have had an impact on some of the structures concerned. Based on the fact that no fusion crust was observed on the surface of the meteorite it was postulated that the fusion crust was lost due to oxidation (proved by the presence of magnetite in the meteorite) based on similar findings from literature. The meteorite was also shown to have undergone changes since entering the Earth's atmosphere, up until the current sample was obtained.

The Etosha meteorite, which is an iron meteorite, in general contains a limited number of minerals, mainly due to its origin in a metallic iron core of a parent body. The minerals found in the Etosha meteorite include kamacite, taenite, schreibersite (three chemical types, of which one might be an iron phosphate), cohenite and chromite. Schreibersite occurred in three different chemical variations in the Etosha meteorite because it consists of the same elements, just in different quantities. The minerals, kamacite, taenite and schreibersite, are present in larger quantities in comparison to the amounts of cohenite, magnetite and silicates. The cohenite was found mainly to occur as rims around the schreibersite, which led to the schreibersite being deprived of additional P. The result was the schreibersite minerals being plotted in the wrong phase area on the phase diagram in section 4.4. The majority of the minerals present were found to contain mainly Fe, Ni and P, with minor amounts of Co, Cu, S and Cr. The minerals identified during the EPMA investigation (kamacite, taenite, cohenite, schreibersite, magnetite and minor silicates) are commonly found in iron meteorites, as confirmed by various researchers.

The RL microscope displayed a fine-grained texture, with a kamacite matrix and schreibersite occurring as veins, or on the boundaries between the kamacite and the taenite. Neumann bands, which only became visible after the meteorite was etched with nitric acid, means that the meteorite experienced some minor high-pressure impacts while inside the core of its parent body, as well as some mild pressure (of about 130 kbar) during its journey towards Earth. The structures observed during RL microscopy also show that the meteorite underwent various stages of reheating and cooling. The coarse kamacite bands observed in the Etosha meteorite indicate that the meteorite cooled down slowly, which allowed the bands to form thick plates, leading to the formation of a coarse Widmanstätten structure.

Two methods were used to determine the chemistry of the meteorite, namely the pXRF for the major elements (Fe, Ni, P, Mg, Al, Co, Si, K, Cr, Mn, Ti, Ca, S, C, Na) and the LA-ICP-MS for the trace elements (Cr, Co, Cu, Zn, Ga, Ge, As, Mo, Ru, Rh, Pd, Sn, Sb, W, Ir, Pt), although both methods were used to analyse the Fe and the Ni in the Etosha meteorite samples. The total range of Fe content in the Etosha meteorite varies from 85,5 wt. % (pXRF) to 89,17 wt. % (LA-ICP-MS), which is slightly lower than values obtained in the original XRF results reported by previous researchers (92,09 wt. %). The Ni varied from 5,37 wt. % (pXRF) to 7,87 wt. % (LA-ICP-MS), in contrast to the previous literature that showed XRF results of 6,7 wt. % Ni. The above findings addressed objective 2: *Investigate the mineralogy and geochemistry of the Etosha meteorite to determine the classification thereof*, as new information on the mineralogy and geochemistry of the Etosha meteorite was presented, adding to the current body of scientific knowledge and data on the meteorite. The mineralogical and geochemical results were further applied in reclassifying the Etosha meteorite.

### 5.2 Classification of the Etosha meteorite

Kamacite bandwidths were used in the structural classification of the Etosha meteorite. Thick kamacite bands were found to be present in the Etosha meteorite, which measured an average of 2,35 mm bandwidth, classifying the Etosha meteorite as a coarse octahedrite, which corresponds with previous literature. The classification however also differed from previous results obtained, which measured an average kamacite bandwidth of from 1 to 1,5 mm, which classified the Etosha meteorite as a medium octahedrite. The meteorite concerned shares a structural classification with the Canyon Diablo meteorite (United States of America), as well as with the Campo Del Cielo meteorite (Argentina), although it cannot be compared with the meteorites chemically, as they lack the same chemical classification.

Previous studies did not provide a chemical classification for the Etosha meteorite. The data generated through this study made it possible to re-evaluate the Etosha meteorite by providing new information which could be applied in more modern chemical classification of meteorites. By re-evaluating and re-classifying the Etosha meteorite, in the present study, new information concerning this meteorite was generated, thus contributing to the current body of knowledge on the science of meteorites, in particular those of Sub-Saharan Africa.

By applying the data generated through this study the Etosha meteorite was re-classified as an IIAB iron meteorite. This classification on both the Ga and Ge against Ni diagrams showed this meteorite can be chemically compared to the Sikhote-Alin meteorite found in Russia and to the Coahuila meteorite found in Mexico. This study therefore contributes valuable new information to the meteorite field as this meteorite type is quite rare to find, especially in the SSA region.

The structural and chemical classification concerned therefore addressed the second part of objective 2: *Investigate the mineralogy and geochemistry of the Etosha meteorite to determine the classification thereof*.

### 5.3 Sub-Saharan African meteorites and the Etosha meteorite

The SSA region displayed a wide distribution of different types of meteorites. A general lack of meteorites exists in the tropical areas, with higher concentrations being present in countries bordering on the Sahara Desert, as well as in the southern regions of SSA, including South Africa and Namibia. The dominant type of meteorite discoveries made in SSA is that of chondrites, with stony-iron meteorites being the rarest. The frequency of meteorite discoveries was very low prior to the 1970's, with the number of discoveries increasing between 2013 and 2019, most likely due to new knowledge being distributed about meteorites, as well as to laws being promulgated to find and preserve meteorites.

The meteorite finds exceeded the number of falls in SSA, with the distribution of the countries with the highest number of falls correlating with the distribution of total meteorite discoveries, in the north-western, southern and eastern parts of the region. The total mass of meteorites found per country shows that the heaviest meteorites have mostly been found in the north-western, southern and eastern parts of the SSA region. However, the high masses in the southern and eastern regions could be attributed either to the existence of single, large meteorites or to that of large meteorite showers, whereas the large total masses in the north-western regions could be attributed to a larger number of discoveries taking place of relatively small meteorites. For

example, Namibia, which is the country with the highest total mass of meteorites found, has not yet discovered a large quantity of meteorites.

The IIIAB iron meteorite type is the most common meteorite type found in SSA, with IIAB iron meteorites, of which the Etosha meteorite is one, being the second most common. The IIAB meteorites found in SSA that can be compared to the Etosha meteorite in terms of locality include the Okahandja meteorite of Namibia and the Kopjes Vlei and Hex River Mountains meteorites, found in South Africa. Thus, the first and last objectives were addressed which stated: *Investigate the meteorite occurrences of sub-Saharan Africa in terms of their type, classification and locality* and *Compare the Etosha meteorite with the sub-Saharan Africa meteorites*.

The hypothesis of this study, “If new geochemical and mineralogical data for the Etosha meteorite from the NWU collection is generated and evaluated, then the meteorite can be reclassified, based on structural and chemical schemes, making it possible to place the Etosha meteorite in the context of the distribution of meteorite types and locations in sub-Saharan Africa” holds true, as new data was generated by the study, enabling the reclassification of the meteorite.

## 5.4 Recommendation for further studies

Both detailed whole rock geochemistry and thermobarometry can be done on the Etosha meteorite, so as to expand on the details of the origin and evolution of the meteorite. The asteroid parent body would be able to be inferred from the data, as well as the cooling rate. The undertaking of transmitted light microscopy is also recommended, due to the minor silicates that are present in the Etosha meteorite. Other minerals might, then, also be discovered that do not reflect light. The presence of graphite and magnetite found through XRD could also be confirmed through the application of automated mineralogical techniques. The undertaking of EPMA is recommended on an etched sample of the Etosha meteorite, so as to analyse the kamacite bandwidths further, in an attempt to determine their relationship with the Ni content involved.

# BIBLIOGRAPHY

Adlington, L.W., Gratuze, B. & Schibille, N. 2020. Comparison of pXRF and LA-ICP-MS analysis of lead-rich glass mosaic tesserae. *Journal of Archaeological Science: reports*, 34:1-10. 10.1016/j.jasrep.2020.102603

Ali, A., Chiang, Y.W. & Santos, R.M. 2022. X-ray diffraction techniques for mineral characterization: a review for engineers of the fundamentals, applications, and research directions. *Minerals*, 12(2):1-25. 10.3390/min12020205

Ashrit, S., Chatti, R.V., Sarkar, S., Venugopal, R. & Nair, G.U. 2018. Application of ICP-MS technique for analysis of heavy metals in LD slag fines. *Current science*, 115(5):973-977. 10.18520/cs/v115/i5/973-977

ASM International. 1992. *Alloy phase diagrams*. Vol. 3. ASM International.

Beech, M. 2013. Towards an understanding of the fall circumstances of the Hoba meteorite. *Earth, Moon, and Planets*, 111(1-2):15-30. 10.1007/s11038-013-9421-7

Bevan, A.W.R. 2006. Desert meteorites: a history. In: McCall, G.J.H., Bowden, A.J. & Howarth, R.J., eds*. The history of meteoritics and key meteorite collections: fireballs, falls and finds*. 256. London: The Geological Society. pp. 325-343.

Bian, X., Yu, W. & Song, Y. 2020. Scanning electron microscope with energy spectrum analysis in material. *Acta Microscopica*, 29(2):1068-1075.

Bischoff, A. 2001. Meteorite classification and the definition of new chondrite classes as a result of successful meteorite search in hot and cold deserts. *Planetary and space science*, 49:769-776.

Bischoff, A. & Geiger, T. 1995. Meteorites from the Sahara: find locations, shock classification, degree of weathering and pairing. *Meteoritics*, 30(1):113-122. 10.1111/j.1945-5100.1995.tb01219.x

Bottke, W.F., Nesvorny, D., Grimm, R.E., Morbidelli, A. & O'Brien, D.P. 2006. Iron meteorites as remnants of planetesimals formed in the terrestrial planet region. *Nature*, 439(7078):821-824. 10.1038/nature04536

Buchwald, V.F. 1975a. *Handbook of iron meteorites: their history, distribution, composition and structure*. Vol. 2: iron meteorites. California: University of California press.

Buchwald, V.F. 1975b. Iron Meteorites Supplement: Albuquerque-Gibeon. In. *Handbook of iron meteorites: their history, distribution, composition and structure*: University of California Press. pp. 1376-1393.

Buchwald, V.F. 1975c. *Handbook of iron meteorites: their history, distribution, composition and structure*. Vol. 1: iron meteorites in general. California: University of California press.

Buchwald, V.F. 1977. The mineralogy of iron meteorites. *Philosophical transactions of the Royal society of London, series A: mathematical and physical sciences*, 286(1336):453-491.

Burbine, T.H., McCoy, T.J., Melbom, A., Gladman, B. & Kell, K. 2002. Meteoritic parent bodies: their number and identification. In: Bottke, W.F., ed. *Asteroids III*: University of Arizona press. pp. 653-667.

CAMECA & Ametek. 2018. Electron probe microanalysis. In: Heath, J. & Kusserow, A. eds. *Microscopy and analysis*. 2nd ed. West Sussex, UK: John Wiley & Sons ltd.

Carpenter, P.K. 2008. Electron-probe microanalysis (EPMA): an overview for beginners and a status report for experts. *Microscopy and Microanalysis*, 14(2):1150-1151. 10.1017/s1431927608088806

Ceplecha, Z., Borovička, J., Elford, W.G., Revelle, D.O., Hawkes, R.L., Porubčan, V. & Šimek, M. 1998. Meteor phenomena and bodies. *Space science reviews*, 84:327-471.

Chauhan, A. & Chauhan, P. 2014. Powder XRD technique and its applications in science and technology. *Journal of analytical & bioanalytical techniques*, 5(6):1-5. 10.4172/2155-9872.1000212

Clarke Junior, R.S. & Goldstein, J.I. 1978. Schreibersite growth and its influence on the metallography of coarse-structured iron meteorites. *Smithsonian contributions to the Earth sciences*, 21:1-80.

Craig, J.R. & Vaughan, D.J. 1994. *Ore microscopy and ore petrography*. 2nd ed. New York, NY: John Wiley & Sons, inc.

Doan, A.S. & Goldstein, J.I. 1970. The ternary phase diagram, Fe-Ni-P. *Metallurgical transactions*, 1:1759-1767.

Dunn, T. 2012. Meteorites and their asteroidal parent bodies. In: Dementieva, A. & Ostrogorsky, D., eds*. Meteorites and asteroids: classification, geology and exploration*. New York: Nova Science publishers incorporated. pp. 1-38.

Environmental Systems Research Institute (ESRI). 2020. ArcGIS Pro (Version 2.7). ESRI Inc.

Frick, C. & Viljoen, E.A. 1973. The Etosha meteorite; a medium octahedrite from South West Africa. *South African Journal of Science*, 69(11):345-348.

Frick, C. & Hammerbeck, E.C.I. 1973. Catalogue of South African and South West African meteorites. *Geological survey*. Vol. 57. Pretoria: Department of mines.

Gaffey, M.J., Burbine, T.H. & Binzel, R.P. 1993. Asteroid spectroscopy: progress and perspectives. *Meteoritics*, 28:161-187.

Gemelli, M., D'Orazio, M. & Folco, L. 2014. Chemical analysis of iron meteorites using a hand-held X-Ray Fluorescence Spectrometer. *Geostandards and Geoanalytical research*, 39(1):55-69. 10.1111/j.1751-908X.2014.00291.x

Glikson, A.Y. & Pirajno, F. 2018. *Asteroids impacts, crustal evolution and related mineral systems with special reference to Australia*. Springer International Publishing. https://doi.org/10.1007/978-3-319-74545-9

Goldstein, J.I. 1965. The formation of the kamacite phase in metallic meteorites. *Journal of Geophysical Research*, 70(24):6223-6232. 10.1029/JZ070i024p06223

Goldstein, J.I., Huss, G.R. & Scott, E.R.D. 2017. Ion microprobe analyses of carbon in Fe–Ni metal in iron meteorites and mesosiderites. *Geochimica et Cosmochimica Acta*, 200:367-407. 10.1016/j.gca.2016.12.027

Goodale, N., Bailey, D.G., Jones, G.T., Prescott, C., Scholz, E., Stagliano, N. & Lewis, C. 2012. pXRF: a study of inter-instrument performance. *Journal of Archaeological Science*, 39(4):875-883. 10.1016/j.jas.2011.10.014

Hansford, G.M., Turner, S.M.R., Degryse, P. & Shortland, A.J. 2017. High-resolution X-ray diffraction with no sample preparation. *Acta crystallographica section a*, 73(Pt 4):293-311. 10.1107/S2053273317008592

Hasegawa, H. 1981. The shape of meteorites. *Memoirs of National institute of Polar research, special issue*, 20:292-299.

Hattendorf, B., Latkoczy, C. & Günther, D. 2003. Laser Ablation-ICPMS. *Analytical Chemistry*:341 A-347 A.

Heide, F. & Wlotzka, F. 1995. The meteorites. In: Heide, F. & Wlotzka, F., eds. *Meteorites*: Springer, Berlin, Heidelberg. pp. 97-168.

Hutchison, R. 2004. *Meteorites: a petrologic, chemical and isotopic synthesis*. Cambridge, United Kingdom: Cambridge University press.

Janoušek, V., Farrow, C.M. & Erban, V. 2006. Interpretation of whole-rock geochemical data in igneous geochemistry: introducing Geochemical Data Toolkit (GCDkit). *Journal of Petrology*, 47(6):1255-1259. 10.1093/petrology/egl013

Jenniskens, P., Gabadirwe, M., Yin, Q.Z., Proyer, A., Moses, O., Kohout, T., ... Botepe, K. 2021. The impact and recovery of asteroid 2018 LA. *Meteoritics & Planetary Science*, 56(4):844-893.

Jochum, K.P., Nohl, U., Herwig, K., Lammel, E., Stoll, B. & Hofmann, A.W. 2005. GeoReM: a new geochemical database for reference materials and isotopic standards. *Geostandards and Geoanalytical Research*, 29(3):333-338.

Khalaf, S.Z., Yassin, A.T., Awadh, S.M. & Jassim, R.Z. 2014. Mineralogy texture and chemistry of the Ellicott meteorite using scanning electron microscope and energy disperse spectroscopy (SEM/EDS). *Arabian Journal of Geosciences*, 8(7):4819-4831. 10.1007/s12517-014-1572-y

Khiri, F. & Ibhi, A. 2015. African meteorite falls: some statistics. In. European Planetary Science Congress, France.

Khiri, F., Ibhi, A. & Ouknine, L. 2015. Temporal and spatial distribution of meteorites falls in Africa. In. International Meteor Conference, Mistelbach. pp. 117-119.

Khiri, F., Ibhi, A., Saint-Gerant, T., Medjkane, M. & Ouknine, L. 2017. Meteorite falls in Africa. *Journal of African Earth sciences*, 134:644-657. 10.1016/j.jafrearsci.2017.07.022

Klein, C. & Dutrow, B. 2007. *The 23rd edition of the manual of mineral science*. 23rd ed. USA: J. Wiley.

Korniyenko, K. 2009. Iron-Nickel-Phosphorus. In: Effenberg, G. & Ilyenko, S., eds. *Ternary alloy systems: phase diagrams, crystallographic and thermodynamic data*. 11. Germany: Springer. pp. 1-21.

Koŝler, J. 2007. Laser ablation ICP-MS - a new dating tool in Earth science. *Proceedings of the Geologists' Association*, 118:19-24. 10.1016/S0016-7878(07)80043-5

Leach, A.M. & Hieftje, G.M. 2000. Methods for shot-to-shot normalization in laser ablation with an inductively coupled plasma time-of-flight mass spectrometer. *Journal of Analytical Atomic Spectrometry*, 15(9):1121-1124.

Liu, Y., Hu, Z., Li, M. & Gao, S. 2013. Applications of LA-ICP-MS in the elemental analyses of geological samples. *Chinese Science Bulletin*, 58(32):3863-3878. 10.1007/s11434-013-5901-4

Lombard, A. 2010. *A mineralogical and geochemical study of seven meteorites from Malawi, Namibia and Lesotho.* University of the Free State. (MSc - Dissertation).

Longerich, H.P., Jackson, S.E. & Günther, D. 1996. Inter-laboratory note: laser ablation inductively coupled plasma mass spectrometric transient signal data acquisition and analyte concentration calculation. *Journal of analytical atomic spectrometry*, 11(9):899-904.

Lovering, J.F., Nichiporuk, W., Chodos, A. & Brown, H. 1957. The distribution of gallium, germanium, cobalt, chromium and copper in iron and stony-iron meteorites in relation to nickel content and structure. *Geochimica et cosmochimica acta*, 11:263-278.

Majgaard, K. & Mingat, A. 2012. *Education in Sub-Saharan Africa*. Washington, DC: World bank.

Makino, Y., Kuroki, Y. & Hirata, T. 2019. Determination of major to trace elements in metallic materials based on the solid mixing calibration method using multiple spot-laser ablation-ICP-MS. *Journal of Analytical Atomic Spectrometry*, 34(9):1794-1799. 10.1039/c9ja00181f

Mason, B. 1972. The mineralogy of meteorites. *Meteoritics*, 7(3):309-326.

McKenzie, R. 2014. *Meteorites: a southern African perspective*. Cape Town, South Africa: Struik Nature.

McSween, H.Y. & Huss, G.R. 2010. *Cosmochemistry*. United Kingdom: Cambridge University Press.

Meteoritical Bulletin Database. 2021. https://www.lpi.usra.edu/meteor/ Date of access: 17 Oct. 2021.

Nininger, H.H. 1945. Directions for the etching and preservation of metallic meteorites. *Popular Astronomy*, 53:82-85.

Norris, A. & Danyushevsky, L. 2018. Towards estimating the complete uncertainty budget of quantified results measured by LA-ICP-MS. *Goldschmidt: Boston, MA, USA*,

Ouknine, L., Khiri, F. & Ibhi, A. 2017. African meteorites in Northwest Africa: the desired meteorites without filiation. In: Griffith, R. & Hansen, S., eds*. Meteorites*: Nova science publishers, inc. pp. 29-59.

Ouknine, L., Khiri, F., Ibhi, A., Heikal, M.T.S., Saint-Gerant, T. & Medjkane, M. 2019. Insight into African meteorite finds: typology, mass distribution and weathering process. *Journal of African Earth sciences*, 158:1-13. https://doi.org/10.1016/j.jafrearsci.2019.103551

Pesonen, L.J., Terho, M. & Kukkonen, I.T. 1993. Physical properties of 368 meteorites: implications for meteorite magnetism and planetary geophysics. In. Proceedings of the NIPR symposium on Antarctic meteorites. pp. 401-416.

Pinto, F.G., Junior, R.E. & Saint'Pierre, T.D. 2012. Sample preparation for determination of rare earth elements in geological samples by ICP-MS: a critical review. *Analytical Letters*, 45(12):1537-1556. 10.1080/00032719.2012.677778

Pourkhorsandi, H., Gattacceca, J., Rochette, P., D'Orazio, M., Kamali, H., Avillez, R., ... Jull, A.J.T. 2019. Meteorites from the Lut Desert (Iran). *Meteoritics & Planetary Science*, 54(8):1737-1763. 10.1111/maps.13311

Reddy, G.P.O. 2018. Geographic information system: principles and applications. In: Reddy, G.P.O. & Singh, S.K., eds. *Geospatial technologies in land resources mapping, monitoring and management*. Switzerland: Springer International publishing. pp. 45-62.

Reed, S.J.B. 1995. Electron probe microanalysis. In: Potts, P.J., Bowles, J.F.W., Reed, S.J.B. & Cave, M.R., eds. *The mineralogical society 6: microprobe techniques in the Earth sciences*. London: Chapman & Hall. pp. 49-89.

Reed, S.J.B. 2005. *Electron microprobe analysis and scanning electron microscopy in geology*. 2nd ed. United Kingdom: Cambridge University Press.

Rietveld, H.M. 1969. A profile refinement method for nuclear and magnetic structures. *Journal of applied crystallography*, 2:65-71.

Rubin, A.E. 1997. Mineralogy of meteorite groups. *Meteoritics & planetary science*, 32:231-247.

Rubin, A.E. & Grossman, J.N. 2010. Meteorite and meteoroid: new comprehensive definitions. *Meteoritics and Planetary Science*, 10.1111/j.1945-5100.2009.01009.x

Scott, E.R.D. & Wasson, J.T. 1975. Classification and properties of iron meteorites. *Reviews of geophysics and space physics*, 13(4):527-546.

Tatum, J.B. 2019. The Widmanstätten pattern. *Meteoritics & Planetary Science*, 54(12):2977-2984. 10.1111/maps.13403

Thompson, K. 2017. Large-area quantitative phase mapping in the scanning electron microscope. *Microscopy today*, 25(2):36-45. 10.1017/s1551929517000153

Vander Voort, G.F. 1992. A note on metallographic techniques for iron meteorites. *Materials characterization*, 29:223-241. 10.1016/1044-5803(92)90117-Z

Voll, G. 1961. New work on petrofabrics. *Geological journal*, 2(3):503-567.

Waanders, F.B. & Bate, M.D. s.a. Study by Mössbauer spectroscopy of a medium octahedrite from Etosha.

Wasson, J.T. 1967. The chemical classification of iron meteorites:I. a study of iron meteorites with low concentrations of gallium and germanium. *Geochimica et cosmochimica acta*, 31:161-180.

Wasson, J.T. 1974. *Meteorites: classification and properties*. New York: Springer-Verlag. (Minerals and rocks).

Wasson, J.T., Huber, H. & Malvin, D.J. 2007. Formation of IIAB iron meteorites. *Geochimica et cosmochimica acta*, 71(3):760-781. 10.1016/j.gca.2006.09.032

Weisberg, M.K., McCoy, T.J. & Krot, A.N. 2006. Systematics and evaluation of meteorite classification. In: Lauretta, D. & McSween, H.Y., eds*. Meteorites and the early solar system II*. pp. 19-52.

Winter, J.D. 2014. *Principles of igneous and metamorphic petrology*. 2nd ed. Harlow, UK: Pearson education.

Yang, J. & Goldstein, J.I. 2005. The formation of the Widmanstätten structure in meteorites. *Meteoritics & planetary science*, 40(2):239-253.

Yoshikawa, M. & Matsueda, H. 1992. Texture, chemical composition and genesis of schreibersite in iron meteorite. *Journal of the faculty of Science, Hokkaido University, Series 4*, 23(2):255-280.

# APPENDICES

## 1.1 EPMA data

**Table 1-1: EPMA data obtained of the important elements for mineral identification in the Etosha meteorite**

| Sample no. | Fe | Ni | P | Co | Cu | S | Cr | Total |
|---|---|---|---|---|---|---|---|---|
| **1** | 65,50 | 34,03 | 0,01 | 0,13 | 0,25 | 0,00 | 0,00 | 99,93 |
| **2** | 66,07 | 21,69 | 11,91 | 0,19 | 0,02 | 0,00 | 0,02 | 99,89 |
| **3** | 61,35 | 23,22 | 15,14 | 0,15 | 0,00 | 0,06 | 0,00 | 99,92 |
| **4** | 60,47 | 23,37 | 15,18 | 0,14 | 0,02 | 0,06 | 0,02 | 99,25 |
| **5** | 93,18 | 5,40 | 0,09 | 0,53 | 0,01 | 0,00 | 0,00 | 99,21 |
| **6** | 92,70 | 5,12 | 0,09 | 0,52 | 0,04 | 0,01 | 0,00 | 98,49 |
| **7** | 91,75 | 6,52 | 0,04 | 0,46 | 0,01 | 0,01 | 0,00 | 98,80 |
| **8** | 91,47 | 6,43 | 0,04 | 0,44 | 0,00 | 0,00 | 0,00 | 98,39 |
| **9** | 91,24 | 6,96 | 0,07 | 0,47 | 0,01 | 0,00 | 0,00 | 98,75 |
| **10** | 51,78 | 32,44 | 14,93 | 0,13 | 0,01 | 0,00 | 0,00 | 99,29 |
| **11** | 49,69 | 35,07 | 14,91 | 0,11 | 0,03 | 0,01 | 0,00 | 99,82 |
| **12** | 62,34 | 21,56 | 14,91 | 0,14 | 0,01 | 0,05 | 0,00 | 99,01 |

**Table 1-1: EPMA data obtained of the important elements for mineral identification in the Etosha meteorite**

| Sample no. | Fe | Ni | P | Co | Cu | S | Cr | Total |
|---|---|---|---|---|---|---|---|---|
| **13** | 61,90 | 21,46 | 14,69 | 0,16 | 0,00 | 0,04 | 0,00 | 98,24 |
| **14** | 62,37 | 21,46 | 14,78 | 0,16 | 0,00 | 0,06 | 0,01 | 98,83 |
| **15** | 68,27 | 29,88 | 0,00 | 0,12 | 0,20 | 0,00 | 0,00 | 98,47 |
| **16** | 60,79 | 38,55 | 0,03 | 0,11 | 0,26 | 0,01 | 0,01 | 99,75 |
| **17** | 51,12 | 33,73 | 15,28 | 0,11 | 0,04 | 0,00 | 0,01 | 100,29 |
| **18** | 50,89 | 34,28 | 15,13 | 0,11 | 0,01 | 0,02 | 0,01 | 100,45 |
| **19** | 71,51 | 28,18 | 0,01 | 0,12 | 0,16 | 0,00 | 0,01 | 100,00 |
| **20** | 94,01 | 6,08 | 0,10 | 0,50 | 0,02 | 0,01 | 0,00 | 100,70 |
| **21** | 63,31 | 21,22 | 15,31 | 0,14 | 0,02 | 0,06 | 0,00 | 100,06 |
| **22** | 63,41 | 20,69 | 15,32 | 0,15 | 0,02 | 0,06 | 0,03 | 99,69 |
| **23** | 50,60 | 34,19 | 15,32 | 0,09 | 0,02 | 0,00 | 0,00 | 100,22 |
| **24** | 50,00 | 34,97 | 15,34 | 0,10 | 0,00 | 0,01 | 0,02 | 100,43 |
| **25** | 49,93 | 35,18 | 15,50 | 0,07 | 0,03 | 0,02 | 0,00 | 100,72 |
| **26** | 61,33 | 22,95 | 15,44 | 0,25 | 0,01 | 0,05 | 0,00 | 100,02 |
| **27** | 93,20 | 5,54 | 0,10 | 0,53 | 0,01 | 0,00 | 0,00 | 99,38 |

**Table 1-1: EPMA data obtained of the important elements for mineral identification in the Etosha meteorite**

| Sample no. | Fe | Ni | P | Co | Cu | S | Cr | Total |
|---|---|---|---|---|---|---|---|---|
| **28** | 93,20 | 5,46 | 0,09 | 0,53 | 0,01 | 0,00 | 0,00 | 99,29 |
| **29** | 98,36 | 1,54 | 0,00 | 0,09 | 0,00 | 0,00 | 0,01 | 100,00 |
| **30** | 98,50 | 1,40 | 0,00 | 0,09 | 0,01 | 0,00 | 0,00 | 100,00 |
| **31** | 92,45 | 5,78 | 0,07 | 0,52 | 0,00 | 0,04 | 0,01 | 98,86 |
| **32** | 92,96 | 4,93 | 0,10 | 0,55 | 0,01 | 0,00 | 0,00 | 98,53 |
| **33** | 93,67 | 5,42 | 0,10 | 0,55 | 0,04 | 0,00 | 0,00 | 99,77 |
| **34** | 93,15 | 6,08 | 0,09 | 0,49 | 0,00 | 0,19 | 0,00 | 100,00 |
| **35** | 92,39 | 6,98 | 0,11 | 0,49 | 0,01 | 0,00 | 0,00 | 99,98 |
| **36** | 94,45 | 6,67 | 0,08 | 0,50 | 0,02 | 0,00 | 0,00 | 101,72 |
| **37** | 63,34 | 21,61 | 15,39 | 0,17 | 0,00 | 0,03 | 0,02 | 100,55 |
| **38** | 92,48 | 6,39 | 0,25 | 0,51 | 0,00 | 0,31 | 0,00 | 99,94 |
| **39** | 92,29 | 6,36 | 0,48 | 0,52 | 0,03 | 0,33 | 0,00 | 100,00 |
| **40** | 90,17 | 7,66 | 1,20 | 0,48 | 0,00 | 0,48 | 0,00 | 99,98 |
| **41** | 48,47 | 36,39 | 15,60 | 0,10 | 0,00 | 0,01 | 0,01 | 100,58 |
| **42** | 92,79 | 6,16 | 0,32 | 0,49 | 0,00 | 0,23 | 0,01 | 100,00 |

**Table 1-1: EPMA data obtained of the important elements for mineral identification in the Etosha meteorite**

| Sample no. | Fe | Ni | P | Co | Cu | S | Cr | Total |
|---|---|---|---|---|---|---|---|---|
| **43** | 92,53 | 6,54 | 0,19 | 0,54 | 0,03 | 0,15 | 0,00 | 99,97 |
| **44** | 49,23 | 36,13 | 15,16 | 0,11 | 0,02 | 0,00 | 0,00 | 100,65 |
| **45** | 48,67 | 35,90 | 15,09 | 0,10 | 0,03 | 0,02 | 0,01 | 99,82 |
| **46** | 49,35 | 35,94 | 13,44 | 0,10 | 0,05 | 0,03 | 0,01 | 98,92 |
| **47** | 92,79 | 5,74 | 0,05 | 0,51 | 0,04 | 0,01 | 0,00 | 99,15 |
| **48** | 92,17 | 6,12 | 0,09 | 0,50 | 0,04 | 0,01 | 0,00 | 98,94 |
| **49** | 48,37 | 36,78 | 15,16 | 0,08 | 0,02 | 0,01 | 0,00 | 100,42 |
| **50** | 46,41 | 38,63 | 15,08 | 0,09 | 0,02 | 0,01 | 0,01 | 100,25 |
| **51** | 47,16 | 36,94 | 14,87 | 0,10 | 0,02 | 0,01 | 0,00 | 99,10 |
| **52** | 50,05 | 35,26 | 14,50 | 0,12 | 0,05 | 0,01 | 0,00 | 99,99 |
| **53** | 49,52 | 35,17 | 14,56 | 0,10 | 0,06 | 0,01 | 0,00 | 99,42 |
| **54** | 49,37 | 35,80 | 15,24 | 0,10 | 0,03 | 0,00 | 0,01 | 100,56 |
| **55** | 91,81 | 6,29 | 0,10 | 0,54 | 0,97 | 0,18 | 0,00 | 99,89 |
| **56** | 92,31 | 6,32 | 0,13 | 0,49 | 0,58 | 0,14 | 0,00 | 99,97 |
| **57** | 52,45 | 32,29 | 15,21 | 0,10 | 0,02 | 0,01 | 0,00 | 100,06 |

**Table 1-1: EPMA data obtained of the important elements for mineral identification in the Etosha meteorite**

| Sample no. | Fe | Ni | P | Co | Cu | S | Cr | Total |
|---|---|---|---|---|---|---|---|---|
| **58** | 91,98 | 6,92 | 0,08 | 0,43 | 0,02 | 0,01 | 0,00 | 99,44 |
| **59** | 58,29 | 26,73 | 0,01 | 0,10 | 0,15 | 0,00 | 14,67 | 99,95 |
| **60** | 48,54 | 36,64 | 14,99 | 0,12 | 0,02 | 0,03 | 0,00 | 100,34 |
| **61** | 49,13 | 35,65 | 14,93 | 0,10 | 0,00 | 0,02 | 0,01 | 99,84 |
| **62** | 47,60 | 36,75 | 14,66 | 0,10 | 0,06 | 0,03 | 0,00 | 99,20 |
| **63** | 52,36 | 33,02 | 15,08 | 0,11 | 0,02 | 0,01 | 0,01 | 100,61 |
| **64** | 52,41 | 32,98 | 15,19 | 0,11 | 0,03 | 0,00 | 0,01 | 100,73 |
| **65** | 49,54 | 36,05 | 14,90 | 0,13 | 0,05 | 0,01 | 0,00 | 100,67 |
| **66** | 48,28 | 35,63 | 14,56 | 0,10 | 0,04 | 0,00 | 0,00 | 98,62 |
| **67** | 47,76 | 36,93 | 14,98 | 0,10 | 0,02 | 0,01 | 0,00 | 99,79 |
| **68** | 93,38 | 6,31 | 0,11 | 0,50 | 0,02 | 0,01 | 0,01 | 100,33 |
| **69** | 49,79 | 34,61 | 15,00 | 0,10 | 0,02 | 0,00 | 0,00 | 99,51 |
| **70** | 49,53 | 35,68 | 15,00 | 0,09 | 0,04 | 0,02 | 0,00 | 100,35 |
| **71** | 50,20 | 34,41 | 14,98 | 0,10 | 0,03 | 0,01 | 0,01 | 99,75 |
| **72** | 49,62 | 35,41 | 15,00 | 0,08 | 0,02 | 0,00 | 0,00 | 100,13 |

**Table 1-1: EPMA data obtained of the important elements for mineral identification in the Etosha meteorite**

| Sample no. | Fe | Ni | P | Co | Cu | S | Cr | Total |
|---|---|---|---|---|---|---|---|---|
| **73** | 49,71 | 34,97 | 15,00 | 0,10 | 0,02 | 0,00 | 0,00 | 99,80 |
| **74** | 49,20 | 35,41 | 14,94 | 0,08 | 0,00 | 0,01 | 0,01 | 99,65 |
| **75** | 48,49 | 35,94 | 15,03 | 0,08 | 0,03 | 0,02 | 0,00 | 99,58 |
| **76** | 48,94 | 35,56 | 15,07 | 0,12 | 0,01 | 0,01 | 0,00 | 99,69 |
| **77** | 48,85 | 35,78 | 14,94 | 0,07 | 0,03 | 0,02 | 0,00 | 99,69 |
| **78** | 50,00 | 34,66 | 14,89 | 0,10 | 0,03 | 0,00 | 0,00 | 99,68 |
| **79** | 50,17 | 34,00 | 15,01 | 0,07 | 0,06 | 0,02 | 0,01 | 99,34 |
| **80** | 48,67 | 36,23 | 14,54 | 0,12 | 0,02 | 0,01 | 0,00 | 99,58 |
| **81** | 50,45 | 33,37 | 14,70 | 0,11 | 0,00 | 0,02 | 0,02 | 98,65 |
| **82** | 50,68 | 33,75 | 14,93 | 0,11 | 0,01 | 0,02 | 0,01 | 99,51 |
| **83** | 51,19 | 33,68 | 14,99 | 0,10 | 0,00 | 0,02 | 0,00 | 99,97 |
| **84** | 88,10 | 9,63 | 1,42 | 0,49 | 0,00 | 0,33 | 0,00 | 99,98 |
| **85** | 89,94 | 7,95 | 1,33 | 0,53 | 0,03 | 0,22 | 0,00 | 100,00 |
| **86** | 69,70 | 21,55 | 8,36 | 0,34 | 0,01 | 0,01 | 0,00 | 99,97 |
| **87** | 47,65 | 36,33 | 14,74 | 0,10 | 0,01 | 0,01 | 0,00 | 98,84 |

**Table 1-1: EPMA data obtained of the important elements for mineral identification in the Etosha meteorite**

| Sample no. | Fe | Ni | P | Co | Cu | S | Cr | Total |
|---|---|---|---|---|---|---|---|---|
| **88** | 45,85 | 38,76 | 14,84 | 0,10 | 0,00 | 0,00 | 0,00 | 99,56 |
| **89** | 88,24 | 9,62 | 1,62 | 0,49 | 0,00 | 0,00 | 0,00 | 99,97 |
| **90** | 48,06 | 35,97 | 14,83 | 0,09 | 0,03 | 0,01 | 0,00 | 98,99 |
| **91** | 43,95 | 40,69 | 14,77 | 0,10 | 0,03 | 0,00 | 0,01 | 99,54 |
| **92** | 50,34 | 33,39 | 14,49 | 0,10 | 0,03 | 0,01 | 0,01 | 98,36 |
| **93** | 56,40 | 27,76 | 14,88 | 0,11 | 0,00 | 0,02 | 0,01 | 99,18 |
| **94** | 54,56 | 28,90 | 14,59 | 0,12 | 0,00 | 0,03 | 0,00 | 98,19 |
| **95** | 92,74 | 5,21 | 0,04 | 0,48 | 0,03 | 0,00 | 0,00 | 98,51 |
| **96** | 51,53 | 33,11 | 14,69 | 0,09 | 0,02 | 0,03 | 0,00 | 99,47 |
| **97** | 59,61 | 24,54 | 14,79 | 0,12 | 0,01 | 0,05 | 0,00 | 99,13 |
| **98** | 59,47 | 24,76 | 14,97 | 0,13 | 0,00 | 0,05 | 0,00 | 99,38 |
| **99** | 59,58 | 24,95 | 14,96 | 0,12 | 0,00 | 0,07 | 0,01 | 99,69 |
| **100** | 61,02 | 22,70 | 14,76 | 0,14 | 0,01 | 0,03 | 0,00 | 98,67 |
| **101** | 91,85 | 7,09 | 0,31 | 0,62 | 0,00 | 0,08 | 0,01 | 99,96 |
| **102** | 61,55 | 23,10 | 15,08 | 0,17 | 0,02 | 0,05 | 0,02 | 99,99 |

**Table 1-1: EPMA data obtained of the important elements for mineral identification in the Etosha meteorite**

| Sample no. | Fe | Ni | P | Co | Cu | S | Cr | Total |
|---|---|---|---|---|---|---|---|---|
| **103** | 61,14 | 22,96 | 14,79 | 0,16 | 0,01 | 0,07 | 0,01 | 99,13 |
| **104** | 61,33 | 23,01 | 14,93 | 0,13 | 0,01 | 0,05 | 0,02 | 99,47 |
| **105** | 51,17 | 33,63 | 14,79 | 0,08 | 0,02 | 0,03 | 0,01 | 99,72 |
| **106** | 61,58 | 22,51 | 14,80 | 0,15 | 0,03 | 0,05 | 0,01 | 99,13 |
| **107** | 61,76 | 22,31 | 14,88 | 0,14 | 0,03 | 0,05 | 0,01 | 99,17 |
| **108** | 61,84 | 22,30 | 14,79 | 0,15 | 0,02 | 0,06 | 0,00 | 99,15 |
| **109** | 91,65 | 6,37 | 1,44 | 0,46 | 0,02 | 0,05 | 0,00 | 99,98 |
| **110** | 92,19 | 6,63 | 0,07 | 0,49 | 0,01 | 0,01 | 0,01 | 99,40 |
| **111** | 92,70 | 6,30 | 0,14 | 0,54 | 0,02 | 0,00 | 0,01 | 99,71 |
| **112** | 92,04 | 6,56 | 0,11 | 0,50 | 0,02 | 0,02 | 0,00 | 99,25 |
| **113** | 91,52 | 6,70 | 0,09 | 0,48 | 0,03 | 0,00 | 0,01 | 98,82 |
| **114** | 48,19 | 36,05 | 15,13 | 0,10 | 0,03 | 0,00 | 0,00 | 99,49 |
| **115** | 46,04 | 38,30 | 15,17 | 0,09 | 0,03 | 0,00 | 0,01 | 99,62 |
| **116** | 45,16 | 39,57 | 15,23 | 0,09 | 0,05 | 0,01 | 0,00 | 100,11 |

**Table 1-2: EPMA data of the current study, compared to the results obtained by Frick and Viljoen (1973). Where FV refers to Frick and Viljoen (1973:345)**

| Results obtained in the current study | | | | | | | | | | |
|---|---|---|---|---|---|---|---|---|---|---|
| **Element** | **Kamacite (wt. %)** | | **Taenite (wt. %)** | | **Cohenite (wt. %)** | | **Schreibersite (wt. %)** | | | |
| | **This study** | **FV** | **This study** | **FV** | **This study** | **FV** | **This study (1)** | **This study (2)** | **This study (3)** | **FV** |
| Fe | 92,16 | 92,88 | 66,52 | 65,77 | 98,43 | 92,92 | 60,94 | 49,67 | 45,48 | 42,34 |
| Ni | 6,46 | 6,20 | 32,66 | 32,14 | 1,47 | 1,70 | 23,21 | 35,04 | 39,19 | 40,29 |
| P | 0,31 | - | 0,01 | - | - | - | 14,97 | 14,94 | 15,02 | 17,68 |
| Co | 0,5 | 1,70 | 0,12 | 0,28 | 0,09 | 0,18 | 0,15 | 0,10 | 0,09 | 0,23 |
| C | *na | - | *na | - | *na | 5,68 | *na | *na | *na | - |
| Cu | 0,06 | 0,21 | 0,22 | 0,31 | - | - | 0,01 | 0,02 | 0,02 | 0,19 |
| Cr | - | 0,38 | 0,01 | 0,38 | 0,01 | - | 0,01 | - | 0,01 | - |
| **Total** | **99,49** | **101,37** | **99,54** | **98,88** | **100** | **100,48** | **99,28** | **99,78** | **99,81** | **100,73** |

*na: element not analysed

## 1.2 pXRF data

**Table 1-3: Data obtained from the pXRF of both samples A and B from the points displayed in Figure 3-2**

| Sample no. | Fe (wt. %) | Ni (wt. %) | Co (wt. %) | S (wt. %) | P (wt. %) | Mg (wt. %) | Al (wt. %) | Ca (wt. %) | Si (wt. %) | Cr (wt. %) | Ti (wt. %) | Mn (wt. %) | K (wt. %) |
|---|---|---|---|---|---|---|---|---|---|---|---|---|---|
| **SA-1** | 83,77 | 5,09 | 0,4 | <0,01 | 0,2 | <1,39 | 0,46 | <0,03 | 0,21 | 0,02 | 0,03 | <0,04 | <0,04 |
| **SA-2** | 85,01 | 5,31 | 0,42 | <0,01 | 0,22 | <1,32 | 0,62 | <0,03 | 0,21 | 0,02 | 0,02 | <0,04 | <0,05 |
| **SA-3** | 83,91 | 5,06 | 0,38 | <0,01 | 0,26 | 1,49 | 0,74 | <0,03 | 0,22 | 0,03 | 0,03 | <0,03 | <0,05 |
| **SA-4** | 84,45 | 5,28 | 0,47 | <0,01 | 0,34 | 1,55 | 0,47 | <0,04 | 0,22 | 0,03 | 0,04 | 0,03 | <0,05 |
| **SA-5** | 84,87 | 5,33 | 0,37 | <0,01 | 0,32 | <1,44 | 0,73 | <0,04 | 0,23 | 0,03 | 0,02 | 0,03 | <0,05 |
| **SA-6** | 86,31 | 5,51 | 0,34 | <0,01 | 0,32 | 1,49 | 0,65 | <0,03 | 0,25 | 0,03 | 0,04 | <0,04 | <0,05 |
| **SA-7** | 85,34 | 5,31 | 0,44 | <0,01 | 0,31 | <1,25 | 0,5 | <0,03 | 0,21 | 0,03 | <0,03 | <0,04 | <0,05 |
| **SA-8** | 85,45 | 5,53 | 0,34 | <0,01 | 0,31 | <1,6 | 0,65 | <0,04 | 0,2 | 0,03 | 0,02 | <0,04 | <0,05 |
| **SA-9** | 85,12 | 5,32 | 0,44 | <0,01 | 0,34 | <1,18 | 0,91 | <0,03 | 0,22 | 0,03 | 0,05 | <0,03 | <0,05 |
| **SA-10** | 84,42 | 5,38 | 0,39 | <0,01 | 0,32 | 4,05 | 0,55 | <0,03 | 0,22 | 0,03 | 0,05 | <0,03 | <0,06 |
| **SA-11** | 83,9 | 5,18 | 0,37 | <0,01 | 0,28 | <1,15 | 0,51 | <0,03 | 0,21 | 0,03 | 0,02 | 0,03 | <0,05 |
| **SA-12** | 85,83 | 5,42 | 0,35 | <0,01 | 0,26 | <1,85 | 0,73 | <0,03 | 0,22 | 0,03 | 0,03 | <0,04 | <0,05 |
| **SA-13** | 84,34 | 5,12 | 0,33 | <0,01 | 0,2 | <1,24 | 0,82 | <0,03 | 0,2 | 0,03 | 0,04 | <0,04 | <0,05 |

**Table 1-3: Data obtained from the pXRF of both samples A and B from the points displayed in Figure 3-2**

| Sample no. | Fe (wt. %) | Ni (wt. %) | Co (wt. %) | S (wt. %) | P (wt. %) | Mg (wt. %) | Al (wt. %) | Ca (wt. %) | Si (wt. %) | Cr (wt. %) | Ti (wt. %) | Mn (wt. %) | K (wt. %) |
|---|---|---|---|---|---|---|---|---|---|---|---|---|---|
| **SA-14** | 84,52 | 5,19 | 0,36 | <0,01 | 0,18 | <1,83 | 0,56 | <0,03 | 0,41 | 0,02 | <0,02 | <0,03 | <0,05 |
| **SA-15** | 84,49 | 5,22 | 0,53 | <0,01 | 0,28 | 2,22 | 0,68 | <0,03 | 0,22 | 0,03 | 0,04 | 0,03 | <0,05 |
| **SA-16** | 85,08 | 5,25 | 0,54 | <0,01 | 0,22 | <1,2 | 0,59 | <0,03 | 0,25 | 0,02 | <0,02 | <0,04 | <0,04 |
| **SA-17** | 86,27 | 5,43 | 0,56 | <0,01 | 0,21 | <1,17 | 0,59 | <0,03 | 0,24 | 0,02 | <0,02 | <0,03 | <0,04 |
| **SA-18** | 87,9 | 5,64 | 0,54 | <0,01 | 0,19 | <1,16 | 0,56 | <0,03 | 0,24 | 0,02 | <0,02 | <0,04 | <0,04 |
| **SA-19** | 85,38 | 5,31 | 0,43 | <0,01 | 0,2 | <1,54 | 0,67 | <0,03 | 0,22 | 0,02 | 0,02 | <0,04 | <0,04 |
| **SA-20** | 84,97 | 5,21 | 0,43 | <0,01 | 0,21 | <1,33 | 0,71 | <0,03 | 0,22 | 0,02 | <0,02 | <0,03 | <0,04 |
| **SA-21** | 86,13 | 5,41 | 0,43 | <0,01 | 0,20 | 1,36 | 0,57 | <0,04 | 0,24 | 0,03 | <0,02 | <0,03 | <0,04 |
| **SA-22** | 86,09 | 5,36 | 0,3 | <0,01 | 0,24 | <2,06 | 0,71 | <0,04 | 0,25 | 0,03 | <0,02 | <0,04 | 0,04 |
| **SA-23** | 86,17 | 5,51 | 0,38 | <0,01 | 0,21 | <1,45 | 0,77 | <0,03 | 0,23 | 0,02 | <0,02 | <0,04 | <0,04 |
| **SA-24** | 86,18 | 5,46 | 0,45 | <0,01 | 0,26 | 2,21 | 0,69 | <0,03 | 0,21 | 0,02 | <0,03 | 0,03 | <0,04 |
| **SA-25** | 85,37 | 5,35 | 0,43 | <0,01 | 0,25 | <1,15 | 0,75 | <0,03 | 0,47 | 0,02 | <0,02 | <0,03 | <0,04 |
| **SA-26** | 85,68 | 5,25 | 0,41 | <0,01 | 0,23 | <1,61 | 0,61 | <0,03 | 0,47 | 0,03 | 0,02 | <0,04 | <0,05 |
| **SA-27** | 60,96 | 2,79 | 0,16 | <0,01 | 0,17 | 1,58 | 0,48 | <0,03 | 0,83 | 0,02 | 0,02 | <0,03 | <0,04 |

**Table 1-3: Data obtained from the pXRF of both samples A and B from the points displayed in Figure 3-2**

| Sample no. | Fe (wt. %) | Ni (wt. %) | Co (wt. %) | S (wt. %) | P (wt. %) | Mg (wt. %) | Al (wt. %) | Ca (wt. %) | Si (wt. %) | Cr (wt. %) | Ti (wt. %) | Mn (wt. %) | K (wt. %) |
|---|---|---|---|---|---|---|---|---|---|---|---|---|---|
| **SA-28** | 86,12 | 5,4 | 0,32 | <0,01 | 0,19 | 1,93 | 0,91 | <0,04 | 0,25 | 0,02 | <0,02 | <0,04 | <0,04 |
| **SA-29** | 86,48 | 5,44 | 0,33 | <0,01 | 0,18 | <1,35 | 0,73 | <0,04 | 0,26 | 0,02 | <0,02 | <0,03 | <0,04 |
| **SA-30** | 87,64 | 5,61 | 0,4 | <0,01 | 0,2 | <1,17 | 0,67 | <0,04 | 0,23 | 0,03 | <0,02 | <0,03 | 0,05 |
| **SA-31** | 85,94 | 5,36 | 0,37 | <0,01 | 0,2 | 2,25 | 0,72 | <0,03 | 0,25 | 0,04 | <0,02 | <0,04 | 0,04 |
| **SA-32** | 86,45 | 5,48 | 0,37 | <0,01 | 0,2 | <1,3 | 0,64 | <0,04 | 0,21 | 0,03 | <0,02 | 0,03 | <0,04 |
| **SA-33** | 86,95 | 5,48 | 0,3 | <0,01 | 0,21 | <1,08 | 0,83 | <0,05 | 0,26 | 0,04 | <0,02 | <0,04 | <0,04 |
| **SA-34** | 87,18 | 5,55 | 0,33 | <0,01 | 0,21 | 1,52 | 0,69 | <0,05 | 0,24 | 0,03 | <0,02 | <0,04 | <0,05 |
| **SA-35** | 86,65 | 5,53 | 0,29 | <0,01 | 0,21 | 2,05 | 0,74 | <0,03 | 0,23 | 0,04 | <0,02 | <0,04 | 0,05 |
| **SA-36** | 86,62 | 5,55 | 0,3 | <0,01 | 0,21 | <1,15 | 0,58 | <0,04 | 0,22 | 0,03 | <0,02 | <0,03 | <0,04 |
| **SA-37** | 87,44 | 5,5 | 0,27 | <0,01 | 0,22 | <1,56 | 0,61 | <0,03 | 0,24 | 0,04 | <0,02 | <0,03 | 0,06 |
| **SA-38** | 85,76 | 5,39 | 0,26 | <0,01 | 0,2 | 1,43 | 0,79 | <0,03 | 0,22 | 0,03 | <0,02 | <0,03 | 0,04 |
| **SA-39** | 86,8 | 5,45 | 0,29 | <0,01 | 0,21 | <1,37 | 0,69 | <0,05 | 0,22 | 0,02 | <0,02 | <0,04 | <0,06 |
| **SA-40** | 85,98 | 5,3 | 0,31 | <0,01 | 0,26 | <1,48 | 0,95 | <0,05 | 1,74 | 0,02 | <0,03 | <0,04 | <0,04 |
| **SB-1** | 86,41 | 5,42 | 0,28 | <0,01 | 0,21 | <1,94 | 0,54 | <0,05 | 0,21 | 0,02 | <0,02 | <0,04 | <0,05 |

**Table 1-3: Data obtained from the pXRF of both samples A and B from the points displayed in Figure 3-2**

| Sample no. | Fe (wt. %) | Ni (wt. %) | Co (wt. %) | S (wt. %) | P (wt. %) | Mg (wt. %) | Al (wt. %) | Ca (wt. %) | Si (wt. %) | Cr (wt. %) | Ti (wt. %) | Mn (wt. %) | K (wt. %) |
|---|---|---|---|---|---|---|---|---|---|---|---|---|---|
| **SB-2** | 86,15 | 5,54 | 0,31 | <0,01 | 0,23 | <1,42 | 0,77 | <0,04 | 0,24 | 0,02 | <0,02 | <0,04 | <0,04 |
| **SB-3** | 87,54 | 5,75 | 0,36 | <0,01 | 0,32 | <1,23 | 0,5 | <0,04 | 0,19 | 0,03 | <0,02 | 0,04 | <0,04 |
| **SB-4** | 86,87 | 5,53 | 0,27 | <0,01 | 0,29 | <0,9 | 0,53 | <0,05 | 0,23 | 0,03 | <0,03 | <0,04 | 0,04 |
| **SB-5** | 87,26 | 5,8 | 0,3 | <0,01 | 0,36 | <1,16 | 0,67 | <0,05 | 0,26 | 0,03 | <0,02 | <0,03 | <0,06 |
| **SB-6** | 86,21 | 5,56 | 0,29 | <0,01 | 0,34 | <1,15 | 0,39 | <0,05 | 0,24 | 0,03 | <0,02 | <0,04 | 0,04 |
| **SB-7** | 87,05 | 5,54 | 0,32 | <0,01 | 0,28 | <2,11 | 0,54 | <0,04 | 0,23 | 0,03 | <0,03 | <0,03 | <0,04 |
| **SB-8** | 86,9 | 5,44 | 0,31 | <0,01 | 0,25 | <1,23 | 0,53 | <0,03 | 0,24 | 0,03 | <0,02 | <0,04 | <0,04 |
| **SB-9** | 85,52 | 5,38 | 0,25 | <0,01 | 0,25 | 1,9 | 0,73 | <0,05 | 0,22 | 0,02 | <0,02 | <0,03 | <0,05 |
| **SB-10** | 86,1 | 5,52 | 0,29 | <0,01 | 0,31 | <1,45 | 0,46 | <0,04 | 0,2 | 0,04 | <0,02 | <0,03 | 0,06 |
| **SB-11** | 87,26 | 5,59 | 0,32 | <0,01 | 0,32 | 1,95 | 0,84 | <0,04 | 0,24 | 0,03 | <0,02 | 0,04 | 0,04 |
| **SB-12** | 84,72 | 5,32 | 0,21 | <0,01 | 0,31 | 2,1 | 0,7 | <0,05 | 0,21 | 0,03 | <0,02 | <0,04 | 0,05 |
| **SB-13** | 87,51 | 5,69 | 0,16 | <0,01 | 0,35 | <1,21 | 0,7 | <0,05 | 0,21 | 0,03 | <0,02 | <0,03 | 0,06 |
| **SB-14** | 87,56 | 5,72 | 0,29 | <0,01 | 0,35 | 1,81 | 0,65 | <0,05 | 0,19 | 0,04 | <0,02 | <0,04 | 0,04 |
| **SB-15** | 85,76 | 5,49 | 0,22 | <0,01 | 0,32 | <1,27 | 0,65 | <0,05 | 0,22 | 0,02 | <0,02 | <0,03 | <0,04 |

### 1.3 LA-ICP-MS data

**Table 1-4: Data obtained from LA-ICP-MS of the Etosha meteorite (trace elements in ppm)**

| Sam-ple | To-tal | Fe (wt. %) | Ni (wt. %) | Cr | Co | Zn | Ga | Ge | As | Mo | Ru | Rh | Pd | Sn | Sb | W | Ir | Pt |
|---|---|---|---|---|---|---|---|---|---|---|---|---|---|---|---|---|---|---|
| **SC1** | 100 | 98,06 | 1,83 | 137,12 | 956 | 7,56 | 2,12 | 6,26 | <1,22 | 7,49 | 0,07 | <0,05 | <0,83 | <0,44 | <0,20 | 0,32 | <0,02 | <0,18 |
| **SC2** | 100 | 98,14 | 1,73 | 156,03 | 1103 | 20,07 | 3,47 | 6,29 | <1,22 | 7,21 | 0,31 | 0,07 | <0,83 | <0,44 | <0,20 | 0,30 | 0,04 | <0,18 |
| **SC3** | 100 | 98,28 | 1,58 | 175,84 | 1205 | <3,72 | <0,48 | 2,19 | <1,22 | 7,67 | 0,22 | <0,05 | <0,83 | <0,44 | <0,20 | 0,21 | <0,02 | <0,18 |
| **SC4** | 100 | 97,75 | 2,12 | 173,98 | 1117 | 20,24 | 3,88 | 12,03 | <1,22 | 8,44 | 0,48 | 0,12 | <0,83 | <0,44 | <0,20 | 0,37 | <0,02 | 0,21 |
| **SC5** | 100 | 96,11 | 3,61 | 106,70 | 2514 | 31,54 | 30,41 | 127,69 | 5,46 | 4,49 | 1,03 | 0,77 | <0,83 | <0,44 | <0,20 | 0,28 | 0,06 | 1,24 |
| **SC6** | 100 | 98,10 | 1,76 | 121,56 | 1255 | 5,02 | <0,48 | 2,21 | <1,22 | 7,06 | 0,16 | <0,05 | <0,83 | <0,44 | <0,20 | 0,38 | <0,02 | <0,18 |
| **SC7** | 100 | 98,27 | 1,58 | 109,97 | 1351 | <3,72 | <0,48 | 2,95 | <1,22 | 6,08 | 0,33 | <0,05 | <0,83 | <0,44 | <0,20 | 0,41 | <0,02 | <0,18 |
| **SC8** | 100 | 98,18 | 1,69 | 196,36 | 1114 | <3,72 | <0,48 | 2,17 | <1,22 | 9,11 | 0,29 | <0,05 | <0,83 | <0,44 | <0,20 | 0,37 | <0,02 | <0,18 |
| **SC9** | 100 | 96,81 | 2,90 | 123,74 | 2560 | 14,86 | 31,00 | 119,10 | 6,18 | 5,13 | 2,17 | 1,03 | 0,95 | 0,61 | <0,20 | 0,54 | 0,12 | 2,98 |

**Table 1-4: Data obtained from LA-ICP-MS of the Etosha meteorite (trace elements in ppm)**

| Sam-ple | To-tal | Fe (wt. %) | Ni (wt. %) | Cr | Co | Zn | Ga | Ge | As | Mo | Ru | Rh | Pd | Sn | Sb | W | Ir | Pt |
|---|---|---|---|---|---|---|---|---|---|---|---|---|---|---|---|---|---|---|
| **SC10** | 85 | 73,59 | 11,22 | 192,01 | 1104 | 67,53 | 52,63 | 118,42 | 3,03 | 6,74 | 3,78 | 1,12 | 3,04 | 0,77 | <0,20 | 0,25 | 0,02 | 1,62 |
| **SC11** | 100 | 93,16 | 6,30 | <6,27 | 4868 | 53,56 | 61,34 | 249,17 | 10,13 | 0,44 | 1,94 | 0,86 | 1,27 | 1,20 | <0,20 | 0,12 | 0,12 | 1,65 |
| **SC12** | 100 | 92,89 | 6,63 | <6,27 | 4233 | 58,57 | 82,59 | 262,61 | 12,10 | 0,90 | 1,97 | 0,94 | 1,84 | 0,83 | <0,20 | 0,16 | <0,02 | 1,42 |
| **SC13** | 100 | 92,09 | 7,32 | <6,27 | 5370 | 35,89 | 72,09 | 283,23 | 13,34 | 1,54 | 2,56 | 0,99 | 1,37 | 1,25 | <0,20 | 0,11 | 0,07 | 1,82 |
| **SC14** | 100 | 92,57 | 6,92 | 51,40 | 4528 | 29,81 | 69,19 | 262,02 | 12,10 | 2,68 | 1,71 | 0,82 | 1,72 | 1,08 | <0,20 | 0,13 | <0,02 | 1,38 |
| **SC15** | 100 | 93,45 | 6,07 | 7,64 | 4260 | 41,53 | 60,12 | 243,65 | 10,83 | 0,77 | 1,25 | 0,88 | 1,98 | 0,79 | <0,20 | 0,16 | 0,03 | 1,48 |
| **SC16** | 100 | 92,00 | 7,17 | <6,27 | 7668 | 77,16 | 87,29 | 292,44 | 13,80 | 0,30 | 1,87 | 1,60 | 1,40 | 0,85 | 0,34 | 0,29 | 0,03 | 2,73 |
| **SC17** | 85 | 73,37 | 11,11 | <6,27 | 4670 | 39,41 | 54,13 | 194,32 | 8,80 | 0,90 | 2,50 | 1,11 | 1,56 | 0,83 | <0,20 | 0,10 | 0,03 | 2,18 |
| **SC18** | 85 | 76,05 | 8,49 | <6,27 | 4069 | 35,15 | 63,82 | 267,44 | 11,75 | 1,08 | 1,73 | 1,10 | 1,95 | 0,45 | <0,20 | 0,11 | 0,11 | 1,14 |
| **SC19** | 100 | 91,08 | 8,19 | <6,27 | 6517 | 134,73 | 81,85 | 343,85 | 10,49 | 0,70 | 2,19 | 1,41 | 2,35 | 1,36 | <0,20 | 0,16 | 0,10 | 2,64 |

**Table 1-4: Data obtained from LA-ICP-MS of the Etosha meteorite (trace elements in ppm)**

| Sam-ple | To-tal | Fe (wt. %) | Ni (wt. %) | Cr | Co | Zn | Ga | Ge | As | Mo | Ru | Rh | Pd | Sn | Sb | W | Ir | Pt |
|---|---|---|---|---|---|---|---|---|---|---|---|---|---|---|---|---|---|---|
| **SC20** | 100 | 92,47 | 7,05 | <6,27 | 4362 | 23,75 | 65,81 | 219,37 | 8,98 | 1,47 | 1,50 | 1,20 | 1,61 | 0,56 | <0,20 | 0,04 | 0,05 | 1,34 |
| **SC21** | 100 | 91,29 | 8,05 | 11,55 | 6008 | 76,29 | 82,99 | 278,05 | 10,42 | 0,78 | 2,08 | 1,28 | 1,51 | 0,89 | <0,20 | 0,06 | 0,15 | 2,20 |
| **SC22** | 100 | 92,18 | 7,18 | 15,01 | 5703 | 93,56 | 83,93 | 280,82 | 11,87 | 0,98 | 1,65 | 0,88 | 2,17 | 1,06 | 0,33 | 0,22 | <0,02 | 2,55 |
| **SC23** | 100 | 93,24 | 6,15 | <6,27 | 5561 | 57,49 | 64,72 | 254,12 | 10,91 | 0,60 | 1,16 | 0,90 | 1,57 | 0,81 | <0,20 | 0,10 | 0,02 | 2,16 |
| **SC24** | 100 | 91,65 | 7,76 | 8,26 | 5147 | 84,84 | 87,78 | 329,26 | 13,41 | 0,90 | 2,04 | 1,13 | 2,23 | 0,73 | <0,20 | 0,17 | 0,03 | 1,98 |
| **SC25** | 100 | 92,68 | 6,83 | 10,59 | 4257 | 67,73 | 69,17 | 263,55 | 11,91 | 1,11 | 2,00 | 0,98 | 1,22 | 0,70 | <0,20 | 0,17 | 0,07 | 1,69 |
| **SC26** | 100 | 91,98 | 7,24 | 6,86 | 7173 | 66,81 | 74,72 | 281,49 | 12,56 | 0,52 | 2,21 | 1,32 | 1,78 | 0,77 | <0,20 | 0,09 | 0,05 | 1,81 |
| **SC27** | 100 | 92,78 | 6,67 | <6,27 | 4916 | 53,86 | 73,20 | 292,24 | 10,87 | 0,59 | 1,74 | 1,16 | 1,75 | 0,91 | <0,20 | 0,14 | 0,05 | 1,71 |
| **SC28** | 100 | 91,10 | 8,18 | 7,17 | 6628 | 61,83 | 82,83 | 281,37 | 14,17 | 0,90 | 1,64 | 1,35 | 1,28 | 1,18 | <0,20 | 0,09 | 0,07 | 2,58 |
| **SC29** | 100 | 92,17 | 7,23 | 33,86 | 4624 | 781,29 | 83,78 | 284,88 | 14,55 | 0,58 | 1,80 | 1,06 | 1,77 | 1,07 | <0,20 | 0,25 | 0,07 | 2,16 |

**Table 1-4: Data obtained from LA-ICP-MS of the Etosha meteorite (trace elements in ppm)**

| Sam-ple | To-tal | Fe (wt. %) | Ni (wt. %) | Cr | Co | Zn | Ga | Ge | As | Mo | Ru | Rh | Pd | Sn | Sb | W | Ir | Pt |
|---|---|---|---|---|---|---|---|---|---|---|---|---|---|---|---|---|---|---|
| **SC30** | 100 | 91,70 | 7,80 | 13,65 | 4407 | 56,23 | 63,93 | 251,85 | 12,31 | 1,26 | 3,09 | 1,12 | 2,26 | 1,22 | <0,20 | 0,18 | <0,02 | 1,40 |
| **SC31** | 85 | 62,33 | 22,50 | 98,90 | 1419 | 5,00 | <0,48 | 2,79 | 1,73 | 22,99 | 3,12 | 0,87 | 2,26 | <0,44 | <0,20 | 0,17 | <0,02 | <0,18 |
| **SC32** | 85 | 66,18 | 18,62 | 63,59 | 1676 | 51,66 | 0,14 | 8,82 | 1,13 | 23,38 | 2,91 | 0,79 | 2,26 | <0,44 | 0,05 | 0,22 | <0,02 | 0,08 |
| **SC33** | 85 | 62,01 | 22,84 | 26,10 | 1222 | 21,35 | <0,48 | 3,73 | 1,64 | 26,44 | 4,36 | 1,04 | 2,31 | <0,44 | <0,20 | 0,22 | 0,01 | 0,07 |
| **SC34** | 85 | 62,60 | 22,25 | 37,84 | 1245 | 21,29 | <0,48 | 3,55 | 1,40 | 25,78 | 3,84 | 1,06 | 2,93 | <0,44 | <0,20 | 0,22 | <0,02 | 0,19 |
| **SC35** | 100 | 93,54 | 5,96 | 5,72 | 4579 | 23,81 | 37,92 | 202,88 | 8,65 | 4,44 | 3,28 | 1,38 | 1,83 | 0,41 | 0,09 | 0,44 | 0,09 | 3,01 |
| **SC36** | 85 | 65,17 | 19,66 | 62,17 | 1439 | 5,70 | 0,67 | 5,30 | 1,51 | 26,93 | 3,80 | 1,00 | 3,53 | <0,44 | <0,20 | 0,25 | <0,02 | 0,89 |
| **SC37** | 100 | 93,70 | 5,75 | 3,36 | 5187 | 12,54 | 24,11 | 161,73 | 5,90 | 5,05 | 2,16 | 0,94 | 1,36 | 0,30 | 0,04 | 0,32 | 0,07 | 2,35 |
| **SC38** | 100 | 91,73 | 7,70 | 4,01 | 5168 | 19,99 | 47,81 | 264,95 | 11,78 | 5,22 | 4,66 | 1,78 | 1,64 | 0,48 | 0,05 | 0,51 | 0,14 | 3,52 |
| **SC39** | 85 | 62,50 | 22,33 | 126,54 | 1409 | 10,77 | 0,19 | 4,19 | 1,95 | 23,68 | 3,38 | 0,93 | 2,18 | <0,44 | <0,20 | 0,13 | <0,02 | <0,18 |

**Table 1-4: Data obtained from LA-ICP-MS of the Etosha meteorite (trace elements in ppm)**

| Sam-ple | To-tal | Fe (wt. %) | Ni (wt. %) | Cr | Co | Zn | Ga | Ge | As | Mo | Ru | Rh | Pd | Sn | Sb | W | Ir | Pt |
|---|---|---|---|---|---|---|---|---|---|---|---|---|---|---|---|---|---|---|
| **SC40** | 100 | 93,99 | 5,42 | 18,14 | 5601 | 48,87 | 18,15 | 122,60 | 5,56 | 5,94 | 2,29 | 0,93 | 1,13 | 0,20 | 0,08 | 0,40 | 0,10 | 2,14 |
| **SC41** | 100 | 92,73 | 6,78 | <6,27 | 4457 | 36,04 | 60,53 | 261,83 | 10,06 | 2,96 | 2,29 | 0,87 | 1,37 | 0,87 | <0,20 | 0,17 | 0,06 | 2,62 |
| **SC42** | 100 | 92,05 | 7,34 | 8,55 | 5567 | 32,31 | 62,55 | 232,36 | 9,63 | 2,77 | 1,97 | 0,77 | 1,41 | 0,55 | <0,20 | 0,23 | <0,02 | 2,19 |
| **SC43** | 100 | 92,73 | 6,75 | 53,65 | 4568 | 52,60 | 68,24 | 285,25 | 10,33 | 2,71 | 1,32 | 0,92 | 1,79 | 0,58 | <0,20 | 0,11 | <0,02 | 2,03 |
| **SC44** | 100 | 92,65 | 6,81 | 9,34 | 4847 | 42,97 | 79,54 | 253,06 | 13,53 | 2,73 | 2,10 | 1,18 | 1,61 | <0,44 | <0,20 | 0,30 | <0,02 | 2,52 |
| **SC45** | 100 | 91,33 | 8,21 | <6,27 | 4084 | 35,36 | 69,45 | 227,69 | 11,11 | 2,31 | 1,92 | 1,02 | 2,50 | 1,62 | <0,20 | 0,09 | <0,02 | 2,24 |
| **SC46** | 100 | 92,42 | 7,03 | <6,27 | 4980 | 29,03 | 68,37 | 242,94 | 8,64 | 2,57 | 2,08 | 0,92 | 1,32 | 1,37 | 0,27 | 0,09 | <0,02 | 1,89 |
| **SC47** | 100 | 91,55 | 7,94 | 7,22 | 4597 | 41,36 | 71,78 | 249,15 | 10,25 | 2,46 | 2,42 | 1,12 | 1,66 | 1,06 | 0,23 | 0,28 | 0,08 | 2,59 |
| **SC48** | 100 | 94,45 | 5,13 | 8,11 | 3752 | 31,15 | 58,83 | 235,61 | 8,95 | 2,30 | 1,45 | 0,65 | 1,50 | <0,44 | <0,20 | 0,35 | <0,02 | 1,70 |
| **SC49** | 100 | 93,42 | 5,96 | <6,27 | 5654 | 30,23 | 71,98 | 236,50 | 7,88 | 2,95 | 2,02 | 0,81 | 1,72 | 1,33 | <0,20 | 0,18 | 0,09 | 1,70 |

**Table 1-4: Data obtained from LA-ICP-MS of the Etosha meteorite (trace elements in ppm)**

| Sam-ple | To-tal | Fe (wt. %) | Ni (wt. %) | Cr | Co | Zn | Ga | Ge | As | Mo | Ru | Rh | Pd | Sn | Sb | W | Ir | Pt |
|---|---|---|---|---|---|---|---|---|---|---|---|---|---|---|---|---|---|---|
| **SC50** | 100 | 93,13 | 6,38 | 7,71 | 4400 | 26,56 | 60,15 | 197,80 | 9,21 | 1,20 | 1,22 | 1,05 | 1,48 | 0,66 | <0,20 | 0,24 | 0,07 | 1,46 |
| **SC51** | 100 | 93,57 | 5,89 | 24,14 | 4822 | 43,44 | 62,05 | 250,36 | 9,50 | 2,43 | 1,52 | 0,81 | 2,51 | 0,74 | <0,20 | 0,25 | 0,07 | 1,57 |
| **SC52** | 100 | 91,37 | 8,03 | 9,66 | 5475 | 51,02 | 72,10 | 247,82 | 8,53 | 2,76 | 1,31 | 1,07 | 1,22 | 1,55 | <0,20 | 0,27 | 0,03 | 2,53 |
| **SC53** | 85 | 73,49 | 11,13 | 10,60 | 3411 | 18,39 | 39,88 | 150,93 | 5,84 | 4,26 | 1,37 | 0,82 | 2,07 | 0,60 | <0,20 | 0,17 | 0,05 | 1,45 |
| **SC54** | 100 | 92,08 | 7,46 | 16,75 | 4025 | 34,48 | 62,60 | 264,59 | 10,75 | 2,86 | 1,83 | 0,99 | 2,28 | 0,61 | <0,20 | 0,13 | 0,05 | 1,39 |
| **SC55** | 100 | 92,84 | 6,61 | 13,59 | 4961 | 51,76 | 71,90 | 231,77 | 8,74 | 3,46 | 1,40 | 1,10 | 1,85 | 0,68 | <0,20 | 0,16 | 0,06 | 2,17 |
| **SC56** | 100 | 90,94 | 8,52 | <6,27 | 4819 | 46,64 | 68,96 | 277,89 | 12,66 | 3,10 | 1,78 | 1,16 | 1,65 | 1,00 | <0,20 | 0,19 | 0,07 | 1,82 |
| **SC57** | 100 | 93,92 | 5,60 | 8,25 | 4260 | 46,13 | 59,63 | 212,99 | 9,13 | 2,86 | 2,04 | 0,85 | 1,58 | 1,13 | <0,20 | 0,24 | <0,02 | 1,56 |
| **SC58** | 100 | 93,25 | 6,22 | 13,70 | 4770 | 42,07 | 54,74 | 241,84 | 9,55 | 2,16 | 1,29 | 0,88 | 1,62 | 0,65 | <0,20 | 0,33 | 0,03 | 1,55 |
| **SC59** | 100 | 92,88 | 6,57 | 351,91 | 4548 | 52,91 | 61,81 | 237,39 | 9,36 | 3,86 | 1,65 | 1,08 | 1,53 | 0,91 | <0,20 | 0,26 | 0,04 | 2,23 |

**Table 1-4: Data obtained from LA-ICP-MS of the Etosha meteorite (trace elements in ppm)**

| Sam-ple | To-tal | Fe (wt. %) | Ni (wt. %) | Cr | Co | Zn | Ga | Ge | As | Mo | Ru | Rh | Pd | Sn | Sb | W | Ir | Pt |
|---|---|---|---|---|---|---|---|---|---|---|---|---|---|---|---|---|---|---|
| **SC60** | 100 | 92,56 | 6,83 | <6,27 | 5612 | 47,27 | 78,82 | 252,73 | 10,64 | 2,80 | 2,12 | 1,12 | 2,37 | 0,52 | <0,20 | 0,46 | 0,06 | 2,48 |

## 1.4 Statistical data for SSA meteorites

**Table 1-5: Statistics of SSA meteorites with coordinates (decimal degrees) (Meteoritical Bulletin Database, 2021)**

| Name | Latitude | Longitude | Year | Mass (kg) | Fall/Find | Type | Classification |
|---|---|---|---|---|---|---|---|
| **ANGOLA** | | | | | | | |
| Chitado | -17.35 | 13.97 | 1966 | - | Fall | Chondrite | L6 |
| Ehole | -17.3 | 15.83 | 1961 | 2,4 | Fall | Chondrite | H5 |
| Jolomba | -11.85 | 15.83 | 1974 | 0,483 | Fall | Chondrite | LL6 |
| Otchinjau | -16.5 | 14 | 1919 | 30 | Find | Iron | IVA |
| **BOTSWANA** | | | | | | | |
| Kalahari 001* | - | - | - | 0,15 | Find | Chondrite | H4/5 |
| Kalahari 002* | - | - | - | 0,141 | Find | Chondrite | H5 |
| Kalahari 003* | - | - | - | 0,827 | Find | Chondrite | H5/6 |
| Kalahari 004* | - | - | - | 0,087 | Find | Chondrite | H5 |
| Kalahari 005* | - | - | - | 0,22 | Find | Chondrite | H5 |
| Kalahari 006* | - | - | - | 0,157 | Find | Chondrite | H5 |
| Kalahari 007* | - | - | - | 0,072 | Find | Chondrite | H4 |

**Table 1-5: Statistics of SSA meteorites with coordinates (decimal degrees) (Meteoritical Bulletin Database, 2021)**

| Name | Latitude | Longitude | Year | Mass (kg) | Fall/Find | Type | Classification |
|---|---|---|---|---|---|---|---|
| Kalahari 008 | -20.98 | 22.98 | 1999 | 0,585 | Find | Achondrite | Lunar - Anorth |
| Kalahari 009 | -20.98 | 22.98 | 1999 | 13,5 | Find | Achondrite | Lunar - Basalt |
| Mabe | -21.3 | 24.1 | 1999 | 0,378 | Find | Chondrite | H5 |
| Matsitama | -21.09 | 26.49 | 1999 | 0,187 | Find | Chondrite | H4/5 |
| Motopi Pan | -21.25 | 23.24 | 2018 | 0,215 | Fall | Achondrite | Howardite |
| **BURKINA FASO** | | | | | | | |
| Béréba | 11.65 | -3.65 | 1924 | 18 | Fall | Achondrite | Eucrite-mmict |
| Bilanga | 12.45 | -0.08 | 1999 | 25 | Fall | Achondrite | Diogenite |
| Gao-Guenie | 11.65 | -2.18 | 1960 | - | Fall | Chondrite | H5 |
| Gao-Guenie (b) | 11.65 | -2.18 | 2002 | 0,344 | Find | Chondrite | CR |
| Gasseltepaoua | 14.15 | -2.04 | 2000 | - | Fall | Chondrite | H5 |
| Guibga | 13.5 | -0.68 | 1972 | 0,288 | Fall | Chondrite | L5 |
| Komin Yanga | 11.7 | 0.14 | 2014 | 0,678 | Find | Chondrite | H5 |
| Nadiabondi | 12 | 1 | 1956 | 8,17 | Fall | Chondrite | H5 |

**Table 1-5: Statistics of SSA meteorites with coordinates (decimal degrees) (Meteoritical Bulletin Database, 2021)**

| Name | Latitude | Longitude | Year | Mass (kg) | Fall/Find | Type | Classification |
|---|---|---|---|---|---|---|---|
| Ouadangou | 12.9 | 0.08 | 2003 | 4,44 | Fall | Chondrite | L5 |
| Pê | 11.33 | -3.54 | 1989 | - | Fall | Chondrite | L6 |
| **CAMEROON** | | | | | | | |
| Galim (a) | 7.05 | 12.43 | 1952 | 0,0361 | Fall | Chondrite | LL6 |
| Galim (b) | 7.05 | 12.43 | 1952 | 0,028 | Fall | Chondrite | EH3/4-an |
| Guidder | 9.92 | 13.98 | 1949 | 0,968 | Fall | Chondrite | LL5 |
| **CENTRAL AFRICAN REPUBLIC** | | | | | | | |
| Bali | 5.38 | 16.38 | 1907 | 1 | Fall | Chondrite | CV3 |
| **CHAD** | | | | | | | |
| Andila | 12.79 | 21.2 | 2014 | 0.5 | Fall | Chondrite | L6 |
| Bardaï | 21.76 | 16.85 | 2005 | 8 | Find | Chondrite | H3-5 |
| Djermaia | 12.73 | 15.05 | 1961 | 3.95 | Fall | Chondrite | H |
| Massenya | 11.35 | 16.15 | 1958 | 0.612 | Find | Chondrite | H5 |
| **CONGO DR** | | | | | | | |

**Table 1-5: Statistics of SSA meteorites with coordinates (decimal degrees) (Meteoritical Bulletin Database, 2021)**

| Name | Latitude | Longitude | Year | Mass (kg) | Fall/Find | Type | Classification |
|---|---|---|---|---|---|---|---|
| Alberta | 2 | 22.67 | 1949 | 0,625 | Fall | Chondrite | L |
| Essebi | 2.88 | 30.83 | 1957 | 0,5 | Fall | Chondrite | C2-ung |
| Kalaba | -6.83 | 29.5 | 1951 | 0,95 | Fall | Chondrite | H4 |
| Lusaka* | - | - | 1951 | - | Fall | Unknown | Unknown |
| Yambo | 1 | 22.5 | 1951 | 0,004 | Fall | Chondrite | H5 |
| Yambo no. 2* | - | - | 1975 | 0,003 | Find | Chondrite | L3 |
| **eSWATINI** | | | | | | | |
| Dwaleni | -27.2 | 31.32 | 1970 | 3.23 | Fall | Chondrite | H4-6 |
| **ETHIOPIA** | | | | | | | |
| Ankober | 9.53 | 39.72 | 1942 | 6.5 | Fall | Chondrite | H4 |
| Bouri | 10.27 | 40.57 | 1996 | 9.1 | Find | Chondrite | H4 |
| Gursum | 9.37 | 42.42 | 1981 | 34.65 | Fall | Chondrite | H4/5 |
| Holetta | 9.07 | 38.42 | 1923 | 1.42 | Fall | Chondrite | Uncl |
| Nejo | 9.5 | 35.33 | 1970 | 2.45 | Fall | Chondrite | L6 |

**Table 1-5: Statistics of SSA meteorites with coordinates (decimal degrees) (Meteoritical Bulletin Database, 2021)**

| Name | Latitude | Longitude | Year | Mass (kg) | Fall/Find | Type | Classification |
|---|---|---|---|---|---|---|---|
| Wolamo | 9 | 39 | 1964 | 0.167 | Fall | Chondrite | OC |
| **GHANA** | | | | | | | |
| Bawku | 11.08 | -0.18 | 1989 | 1.557 | Fall | Chondrite | LL5 |
| **KENYA** | | | | | | | |
| Balambala | 0.06 | 39.12 | 2018 | 60.5 | Find | Iron | IIF |
| Bojiyare | 1.45 | 39.91 | 2018 | 102 | Find | Chondrite | L5 |
| Bur-Abor | 3.98 | 41.65 | 1997 | 290 | Find | Iron | IIIAB |
| Duruma | -4 | 39.5 | 1853 | 0.577 | Fall | Chondrite | L6 |
| Gatuto | -0.57 | 37.29 | 2020 | 25 | Fall | Chondrite | L6 |
| Kuresoi | -0.3 | 35.53 | 2014 | 0.555 | Fall | Chondrite | L6 |
| Meru | 0 | 37.67 | 1945 | 6 | Fall | Chondrite | LL6 |
| Rumuruti | 0.27 | 36.53 | 1934 | 0.067 | Fall | Chondrite | R3.8-6 |
| Sericho | 1.09 | 39.1 | 2016 | 2800 | Find | Stony-Iron | Pallasite |
| Thika | -1 | 37.15 | 2011 | 14.2 | Fall | Chondrite | L6 |

**Table 1-5: Statistics of SSA meteorites with coordinates (decimal degrees) (Meteoritical Bulletin Database, 2021)**

| Name | Latitude | Longitude | Year | Mass (kg) | Fall/Find | Type | Classification |
|---|---|---|---|---|---|---|---|
| **LESOTHO** | | | | | | | |
| Thuathe | -29.33 | 27.58 | 2002 | 45.3 | Fall | Chondrite | H4/5 |
| **MADAGASCAR** | | | | | | | |
| Benenitra | -23.45 | 45.08 | 2018 | 20 | Fall | Chondrite | L6 |
| Maromandia | -14.2 | 48.1 | 2002 | 6 | Fall | Chondrite | L6 |
| **MALAWI** | | | | | | | |
| Chisenga | -10.06 | 33.4 | 1988 | 3.92 | Fall | Iron | IIIAB |
| Dowa | -13.67 | 33.92 | 1976 | 0,642 | Fall | Chondrite | Uncl |
| Kota-Kota | -13.02 | 34.2 | 1905 | 0,334 | Find | Chondrite | EH3 |
| Machinga | -15.21 | 35.24 | 1981 | 93.2 | Fall | Chondrite | L6 |
| Mtola | -11.5 | 33.5 | 1944 | 1,1 | Fall | Chondrite | Uncl |
| Zomba | -15.18 | 35.28 | 1899 | 0,008 | Fall | Chondrite | L6 |
| **MALI** | | | | | | | |
| Chergach | 23.7 | -5.01 | 2007 | 100 | Fall | Chondrite | H5 |

**Table 1-5: Statistics of SSA meteorites with coordinates (decimal degrees) (Meteoritical Bulletin Database, 2021)**

| Name | Latitude | Longitude | Year | Mass (kg) | Fall/Find | Type | Classification |
|---|---|---|---|---|---|---|---|
| Dar el Kahal | 22.1 | -2.54 | 2013 | 85 | Find | Chondrite | H5-6 |
| Et Tamat 001 | 17.99 | -12.68 | 2021 | 1.2 | Find | Stony-Iron | Mesosiderite |
| N'Goureyma | 13.85 | -4.38 | 1900 | 37.5 | Fall | Iron | Ungrouped |
| NWA 512 | 23.6 | -5 | 1999 | 8 | Find | Chondrite | L4 |
| NWA 513 | 23.6 | -5 | 1999 | 1 | Find | Chondrite | L4/5 |
| NWA 5960* | - | - | 2009 | 0.147 | Find | Achondrite | Martian - Shergottite |
| NWA 5982* | - | - | 2009 | 1.4 | Find | Achondrite | Eucrite-pmict |
| NWA 6234* | - | - | 2010 | 0.557 | Find | Achondrite | Martian - Shergottite |
| NWA 6710* | - | - | 2011 | 0.744 | Find | Achondrite | Martian - Shergottite |
| NWA 7370 | 22.83 | -6.18 | 2009 | 2.29 | Find | Achondrite | Diogenite-olivine |
| NWA 7500* | - | - | 2012 | 2.04 | Find | Achondrite | Martian - Shergottite |
| NWA 7756* | - | - | 2010 | 0.124 | Find | Achondrite | Eucrite |
| NWA 8537* | - | - | 2014 | 0.131 | Find | Chondrite | LL5/6 |

**Table 1-5: Statistics of SSA meteorites with coordinates (decimal degrees) (Meteoritical Bulletin Database, 2021)**

| Name | Latitude | Longitude | Year | Mass (kg) | Fall/Find | Type | Classification |
|---|---|---|---|---|---|---|---|
| NWA 8701* | - | - | 2014 | 0.072 | Find | Achondrite | Lunar - Feldsp. breccia |
| NWA 10416* | - | - | 2015 | 0.964 | Find | Achondrite | Martian |
| NWA 11209* | - | - | 2015 | 0.05 | Find | Achondrite | Eucrite-unbr |
| NWA 11302* | - | - | 2016 | 0.09 | Find | Achondrite | Eucrite-unbr |
| NWA 11471* | - | - | 2017 | 0.345 | Find | Chondrite | LL3 |
| NWA 11575* | - | - | 2016 | 0.598 | Find | Chondrite | AStony-ung |
| NWA 11691* | - | - | 2016 | 0.049 | Find | Chondrite | H6 |
| NWA 11782* | - | - | 2018 | 25.7 | Find | Chondrite | L3 |
| NWA 11788* | - | - | 2017 | 10.44 | Find | Achondrite | Lunar - feldsp. breccia |
| NWA 11851* | - | - | 2018 | 0.227 | Find | Achondrite | Lunar - feldsp. breccia |
| NWA 11898* | - | - | 2018 | 0.768 | Find | Achondrite | Lunar - feldsp. breccia |
| NWA 11899* | - | - | 2017 | 16 | Find | Achondrite | Howardite |

**Table 1-5: Statistics of SSA meteorites with coordinates (decimal degrees) (Meteoritical Bulletin Database, 2021)**

| Name | Latitude | Longitude | Year | Mass (kg) | Fall/Find | Type | Classification |
|---|---|---|---|---|---|---|---|
| NWA 12593* | - | - | 2017 | 0.333 | Find | Achondrite | Lunar - frag. breccia |
| NWA 12692* | - | - | 2019 | 0.373 | Find | Chondrite | LL3.00 |
| NWA 12758* | - | - | 2019 | 2.4 | Find | Chondrite | AStony-ung |
| NWA 12767* | - | - | 2018 | 6.31 | Find | Iron | Ungrouped |
| NWA 12837* | - | - | 2019 | 4.15 | Find | Achondrite | Martian - Shergottite |
| NWA 12869* | - | - | 2019 | 4.3 | Find | Chondrite | AStony-prim |
| NWA 13113* | - | - | 2019 | 1.485 | Find | Chondrite | L4 |
| NWA 13116* | - | - | 2019 | 15.4 | Find | Chondrite | H6 |
| NWA 13178* | - | - | 2019 | 1.876 | Find | Chondrite | CO3 |
| NWA 13182* | - | - | 2019 | 0.083 | Find | Chondrite | LL3 |
| NWA 13221* | - | - | 2019 | 1.097 | Find | Chondrite | L4 |
| NWA 13313* | - | - | 2019 | 0.987 | Find | Chondrite | L3-6 |
| NWA 13621* | - | - | 2020 | 1.608 | Find | Achondrite | Lunar - feldsp. breccia |
| NWA 13755* | - | - | 2020 | 0.125 | Find | Chondrite | LL3 |

**Table 1-5: Statistics of SSA meteorites with coordinates (decimal degrees) (Meteoritical Bulletin Database, 2021)**

| Name | Latitude | Longitude | Year | Mass (kg) | Fall/Find | Type | Classification |
|---|---|---|---|---|---|---|---|
| NWA 13888* | - | - | 2018 | 2 | Find | Chondrite | H5 |
| NWA 14011* | - | - | 2020 | 5.01 | Find | Achondrite | Diogenite |
| NWA 14041* | - | - | 2021 | 11.7 | Find | Achondrite | Lunar - feldsp. breccia |
| NWA 14088* | - | - | 2021 | 2.7 | Find | Achondrite | Lunar - troct. anorth. |
| NWA 14172* | - | - | 2020 | 0.23 | Find | Chondrite | CK5 |
| NWA 14266* | - | - | 2019 | 0.475 | Find | Chondrite | L4/5 |
| Siratik | 14 | -11 | 1716 | 1.7 | Find | Iron | IIAB |
| Taoudenni | 22.79 | -3.97 | 2007 | 24.37 | Find | Achondrite | Diogenite |
| Taoudenni 002 | 22.98 | -3.43 | 2021 | 14.51 | Find | Achondrite | Martian - Shergottite |
| Tihigrin | 16.72 | -3.73 | 2020 | 6.53 | Fall | Chondrite | L4 |
| Timbuktu | 16.79 | -3 | 2015 | 5.5 | Find | Stony-Iron | Mesosiderite-B4 |
| Tisserlitine 001 | 21.33 | 0.73 | 2019 | 57.41 | Find | Achondrite | Lunar - feldsp. breccia |
| Tisserlitine 002 | 21.58 | -1.22 | 2021 | 0.541 | Find | Achondrite | Diogenite |

**Table 1-5: Statistics of SSA meteorites with coordinates (decimal degrees) (Meteoritical Bulletin Database, 2021)**

| Name | Latitude | Longitude | Year | Mass (kg) | Fall/Find | Type | Classification |
|---|---|---|---|---|---|---|---|
| Trifir | 20.05 | -1.68 | 1956 | 1 | Find | Chondrite | L6 |
| **MAURITANIA** | | | | | | | |
| Adam Talha | 22.99 | -10.15 | 2005 | 0.259 | Find | Chondrite | LL3.2 |
| Aioun el Atrouss | 16.4 | -9.57 | 1974 | 1 | Fall | Achondrite | Diogenite-pm |
| Aioun el Atrouss 002 | 16.43 | -9.58 | 2015 | 17.2 | Find | Iron | IIAB |
| Bassikounou | 15.78 | -5.9 | 2006 | 29.56 | Fall | Chondrite | H5 |
| Bir Moghrein | 25.91 | -11.99 | 2016 | 11 | Find | Achondrite | Diogenite-olivine |
| Boumdeid (2003) | 17.71 | -11.37 | 2003 | 0.19 | Fall | Chondrite | L6 |
| Boumdeid (2011) | 17.17 | -11.34 | 2011 | 3.6 | Fall | Chondrite | L6 |
| Chinguetti | 20.25 | -12.68 | 1920 | 4.05 | Find | Stony-Iron | Mesosiderite-B1 |
| Dayet el Aam | 26.73 | -7.97 | 2012 | 4.98 | Find | Iron | IIAB |
| Dekkaliat | 15.8 | -9 | 2020 | 1.83 | Find | Achondrite | Diogenite |
| El Hammami | 23.28 | -10.82 | 1997 | 240 | Find | Chondrite | H5 |
| EHOH 001 | 25.23 | -8.62 | 2019 | 12.16 | Find | Achondrite | Eucrite-unbr |

**Table 1-5: Statistics of SSA meteorites with coordinates (decimal degrees) (Meteoritical Bulletin Database, 2021)**

| Name | Latitude | Longitude | Year | Mass (kg) | Fall/Find | Type | Classification |
|---|---|---|---|---|---|---|---|
| Galb Inal | 21.3 | -14.97 | 2011 | 1.05 | Find | Achondrite | Lunar |
| Kiffa | 16.58 | -11.33 | 1970 | 1.5 | Fall | Chondrite | H5 |
| Mederdra | 16.85 | -15.93 | 2019 | 1.552 | Find | Chondrite | R4-5 |
| Mhabes el Hamra | 26.23 | -7.82 | 2018 | 23.1 | Fall | Chondrite | H4/5 |
| Mreïra | 25.96 | -10.96 | 2012 | 6 | Fall | Chondrite | L6 |
| Noktat Addagmar | 25.7 | -10.78 | 2006 | 0.779 | Find | Chondrite | LL5 |
| NWA 1717 | 21 | -13 | 2002 | 6.03 | Find | Chondrite | LL5-6 |
| NWA 2282* | - | - | 2003 | 0.155 | Find | Chondrite | L6 |
| NWA 2305* | - | - | 2003 | 0.94 | Find | Chondrite | L5/6 |
| NWA 5829* | - | - | 2008 | 0.99 | Find | Chondrite | H5 |
| NWA 6117* | - | - | 2002 | 1.75 | Find | Chondrite | L6 |
| NWA 6275* | - | - | 2010 | 0.001 | Find | Achondrite | Lunar - feldsp. breccia |
| NWA 6697* | - | - | 2010 | 0.067 | Find | Chondrite | C2-ung |
| NWA 7291* | - | - | 2012 | 0.681 | Find | Chondrite | R3-5 |

**Table 1-5: Statistics of SSA meteorites with coordinates (decimal degrees) (Meteoritical Bulletin Database, 2021)**

| Name | Latitude | Longitude | Year | Mass (kg) | Fall/Find | Type | Classification |
|---|---|---|---|---|---|---|---|
| NWA 7292* | - | - | 2012 | 0.0099 | Find | Achondrite | Eucrite |
| NWA 7293* | - | - | 2012 | 1.034 | Find | Chondrite | H5 |
| NWA 7294* | - | - | 2012 | 0.209 | Find | Achondrite | Ureilite |
| NWA 7295* | - | - | 2012 | 0.995 | Find | Chondrite | H5 |
| NWA 7415* | - | - | 2012 | 0.0405 | Find | Achondrite | Eucrite |
| NWA 7416* | - | - | 2012 | 0.0191 | Find | Achondrite | Howardite |
| NWA 7417* | - | - | 2012 | 37 | Find | Chondrite | L6 |
| NWA 7418* | - | - | 2012 | 0.216 | Find | Chondrite | LL6-melt breccia |
| NWA 7419* | - | - | 2012 | 0.386 | Find | Chondrite | H~6§ |
| NWA 8165* | - | - | 2012 | 0.125 | Find | Chondrite | LL6 |
| NWA 8166* | - | - | 2012 | 0.225 | Find | Chondrite | L6 |
| NWA 8167* | - | - | 2012 | 0.435 | Find | Achondrite | Ureilite |
| NWA 8168* | - | - | 2012 | 1.2 | Find | Achondrite | Ureilite |
| NWA 8563* | - | - | 2014 | 9.13 | Find | Achondrite | Eucrite-mmict |

**Table 1-5: Statistics of SSA meteorites with coordinates (decimal degrees) (Meteoritical Bulletin Database, 2021)**

| Name | Latitude | Longitude | Year | Mass (kg) | Fall/Find | Type | Classification |
|---|---|---|---|---|---|---|---|
| NWA 8586* | - | - | 2014 | 0.705 | Find | Achondrite | Lunar - feldsp. breccia |
| NWA 8651* | - | - | 2014 | 0.598 | Find | Achondrite | Lunar |
| NWA 8653* | - | - | 2014 | 0.214 | Find | Achondrite | Martian - Shergottite |
| NWA 10263* | - | - | 2015 | 1.015 | Find | Achondrite | Lunar - feldsp. breccia |
| NWA 10459* | - | - | 2012 | 0.047 | Find | Achondrite | Howardite |
| NWA 10519* | - | - | 2015 | 18.2 | Find | Achondrite | Enst achon-ung |
| NWA 10602* | - | - | 2015 | 1.96 | Find | Achondrite | Eucrite-melt breccia |
| NWA 10603* | - | - | 2015 | 0.3 | Find | Achondrite | Eucrite-melt breccia |
| NWA 10670* | - | - | 2014 | 0.887 | Find | Chondrite | CV3 |
| NWA 10710* | - | - | 2016 | 1.065 | Find | Achondrite | Eucrite-unbr |
| NWA 10714* | - | - | 2015 | 0.178 | Find | Chondrite | CO3 |
| NWA 10715* | - | - | 2015 | 0.073 | Find | Chondrite | R3 |
| NWA 10716* | - | - | 2015 | 0.151 | Find | Achondrite | Eucrite-mmict |

**Table 1-5: Statistics of SSA meteorites with coordinates (decimal degrees) (Meteoritical Bulletin Database, 2021)**

| Name | Latitude | Longitude | Year | Mass (kg) | Fall/Find | Type | Classification |
|---|---|---|---|---|---|---|---|
| NWA 10717* | - | - | 2015 | 0.03 | Find | Achondrite | Ureilite |
| NWA 10718* | - | - | 2015 | 0.017 | Find | Chondrite | CO3.0 |
| NWA 10719* | - | - | 2015 | 0.397 | Find | Chondrite | CK5 |
| NWA 10720* | - | - | 2015 | 1.015 | Find | Achondrite | Martian - Nakhlite |
| NWA 10810* | - | - | 2016 | 0.402 | Find | Achondrite | Lunar |
| NWA 10890* | - | - | 2016 | 0.281 | Find | Achondrite | Ureilite |
| NWA 10891* | - | - | 2016 | 0.482 | Find | Chondrite | CO3.2 |
| NWA 10892* | - | - | 2016 | 0.25 | Find | Chondrite | CK3 |
| NWA 10893* | - | - | 2016 | 0.677 | Find | Achondrite | Ureilite |
| NWA 10894* | - | - | 2016 | 2.52 | Find | Achondrite | Eucrite-cm |
| NWA 10895* | - | - | 2016 | 2.53 | Find | Achondrite | Acapulcoite |
| NWA 11042* | - | - | 2016 | 0.09 | Find | Chondrite | AStony-prim |
| NWA 11043* | - | - | 2016 | 0.544 | Find | Achondrite | Martian - Shergottite |
| NWA 11082* | - | - | 2016 | 0.39 | Find | Achondrite | Ureilite |

**Table 1-5: Statistics of SSA meteorites with coordinates (decimal degrees) (Meteoritical Bulletin Database, 2021)**

| Name | Latitude | Longitude | Year | Mass (kg) | Fall/Find | Type | Classification |
|---|---|---|---|---|---|---|---|
| NWA 11088* | - | - | 2016 | 1.34 | Find | Chondrite | H6§ |
| NWA 11089* | - | - | 2016 | 0.45 | Find | Chondrite | LL6 |
| NWA 11090* | - | - | 2016 | 0.955 | Find | Chondrite | L6-melt breccia |
| NWA 11091* | - | - | 2016 | 0.99 | Find | Chondrite | L6 |
| NWA 11119* | - | - | 2017 | 0.453 | Find | Chondrite | AStony-ung |
| NWA 11210* | - | - | 2016 | 2.93 | Find | Chondrite | H4 |
| NWA 11236* | - | - | 2014 | 2.36 | Find | Chondrite | H4-6 |
| NWA 11377* | - | - | 2017 | 0.982 | Find | Achondrite | Aubrite |
| NWA 11431* | - | - | 2017 | 0.524 | Find | Achondrite | Martian - Shergottite |
| NWA 11444* | - | - | 2017 | 1.323 | Find | Achondrite | Lunar - melt breccia |
| NWA 11481* | - | - | 2016 | 4.04 | Find | Achondrite | Diogenite |
| NWA 11500* | - | - | 2016 | 0.04 | Find | Chondrite | H6 |
| NWA 11551* | - | - | 2017 | 0.447 | Find | Achondrite | Howardite |
| NWA 11582* | - | - | 2017 | 0.565 | Find | Chondrite | L~6§ |

**Table 1-5: Statistics of SSA meteorites with coordinates (decimal degrees) (Meteoritical Bulletin Database, 2021)**

| Name | Latitude | Longitude | Year | Mass (kg) | Fall/Find | Type | Classification |
|---|---|---|---|---|---|---|---|
| NWA 11702* | - | - | 2017 | 0.033 | Find | Chondrite | LL6 |
| NWA 11704* | - | - | 2018 | 1.127 | Find | Achondrite | Eucrite-pmict |
| NWA 11729* | - | - | 2017 | 0.345 | Find | Achondrite | Eucrite-an |
| NWA 11774* | - | - | 2018 | 0.439 | Find | Stony-Iron | Mesosiderite |
| NWA 11787* | - | - | 2017 | 23.5 | Find | Achondrite | Lunar - feldsp. breccia |
| NWA 11789* | - | - | 2017 | 5.49 | Find | Achondrite | Lunar - feldsp. breccia |
| NWA 12188* | - | - | 2018 | 0.209 | Find | Achondrite | Ureilite |
| NWA 12200* | - | - | 2018 | 0.076 | Find | Chondrite | CK6 |
| NWA 12240* | - | - | 2017 | 1.808 | Find | Chondrite | H4 |
| NWA 12243* | - | - | 2018 | 0.164 | Find | Achondrite | Eucrite-pmict |
| NWA 12248* | - | - | 2018 | 0.037 | Find | Achondrite | Lunar - feldsp. breccia |
| NWA 12270* | - | - | 2018 | 1.3 | Find | Achondrite | Lunar - feldsp. breccia |

**Table 1-5: Statistics of SSA meteorites with coordinates (decimal degrees) (Meteoritical Bulletin Database, 2021)**

| Name | Latitude | Longitude | Year | Mass (kg) | Fall/Find | Type | Classification |
|---|---|---|---|---|---|---|---|
| NWA 12305* | - | - | 2018 | 13.5 | Find | Chondrite | L6 |
| NWA 12320* | - | - | 2018 | 4.46 | Find | Achondrite | Angrite |
| NWA 12505* | - | - | 2017 | 0.081 | Find | Chondrite | R3 |
| NWA 12548* | - | - | 2019 | 0.151 | Find | Chondrite | H3 |
| NWA 12552* | - | - | 2019 | 0.866 | Find | Chondrite | H6-melt breccia |
| NWA 12566* | - | - | 2018 | 2.9 | Find | Stony-Iron | Mesosiderite C3 |
| NWA 12634* | - | - | 2019 | 0.052 | Find | Chondrite | L/LL3 |
| NWA 12693* | - | - | 2018 | 0.551 | Find | Chondrite | H4 |
| NWA 12893* | - | - | 2018 | 0.056 | Find | Chondrite | L6-melt breccia |
| NWA 12956* | - | - | 2017 | 0.162 | Find | Achondrite | Eucrite-pmict |
| NWA 12967* | - | - | 2019 | 4.6 | Find | Stony-Iron | Mesosiderite |
| NWA 12968* | - | - | 2019 | 0.257 | Find | Achondrite | Eucrite-br |
| NWA 12980* | - | - | 2019 | 1.3 | Find | Achondrite | Lunar - melt breccia |
| NWA 12984* | - | - | 2017 | 0.85 | Find | Iron | Ungrouped |

**Table 1-5: Statistics of SSA meteorites with coordinates (decimal degrees) (Meteoritical Bulletin Database, 2021)**

| Name | Latitude | Longitude | Year | Mass (kg) | Fall/Find | Type | Classification |
|---|---|---|---|---|---|---|---|
| NWA 13119* | - | - | 2019 | 7 | Find | Achondrite | Lunar - feldsp. breccia |
| NWA 13174* | - | - | 2016 | 0.083 | Find | Chondrite | LL5 |
| NWA 13250* | - | - | 2019 | 2.57 | Find | Achondrite | Martian - Shergottite |
| NWA 13269* | - | - | 2019 | 0.74 | Find | Achondrite | Eucrite-unbr |
| NWA 13368* | - | - | 2020 | 1.105 | Find | Achondrite | Martian - Nakhlite |
| NWA 13373* | - | - | 2018 | 0.92 | Find | Chondrite | H5 |
| NWA 13374* | - | - | 2018 | 3.07 | Find | Chondrite | L6 |
| NWA 13375* | - | - | 2018 | 1.382 | Find | Chondrite | L6 |
| NWA 13390* | - | - | 2017 | 0.113 | Find | Achondrite | Lunar - frag. breccia |
| NWA 13398* | - | - | 2019 | 9.25 | Find | Chondrite | H5§ |
| NWA 13399* | - | - | 2018 | 8.87 | Find | Chondrite | H5§ |
| NWA 13402* | - | - | 2017 | 5.64 | Find | Chondrite | H5§ |
| NWA 13403* | - | - | 2019 | 3.32 | Find | Chondrite | L6§ |

**Table 1-5: Statistics of SSA meteorites with coordinates (decimal degrees) (Meteoritical Bulletin Database, 2021)**

| Name | Latitude | Longitude | Year | Mass (kg) | Fall/Find | Type | Classification |
|---|---|---|---|---|---|---|---|
| NWA 13405* | - | - | 2019 | 2.66 | Find | Chondrite | H6§ |
| NWA 13407* | - | - | 2019 | 2.82 | Find | Chondrite | L5§ |
| NWA 13433* | - | - | 2020 | 24.7 | Find | Achondrite | Eucrite-unbr |
| NWA 13472* | - | - | 2018 | 0.814 | Find | Chondrite | LL4-6 |
| NWA 13565* | - | - | 2020 | 1.085 | Find | Stony-Iron | Mesosiderite |
| NWA 13604* | - | - | 2019 | 0.258 | Find | Chondrite | L6 |
| NWA 13640* | - | - | 2020 | 0.935 | Find | Achondrite | Winonaite |
| NWA 13684* | - | - | 2020 | 0.17 | Find | Chondrite | CK5 |
| NWA 13685* | - | - | 2020 | 0.486 | Find | Chondrite | R3-6 |
| NWA 13686* | - | - | 2020 | 0.341 | Find | Chondrite | R5 |
| NWA 13697* | - | - | 2019 | 8.29 | Find | Chondrite | L5 |
| NWA 13700* | - | - | 2020 | 1.46 | Find | Chondrite | LL6 |
| NWA 13721* | - | - | 2017 | 0.286 | Find | Chondrite | L6 |
| NWA 13741* | - | - | 2020 | 0.257 | Find | Chondrite | LL3-5 |

**Table 1-5: Statistics of SSA meteorites with coordinates (decimal degrees) (Meteoritical Bulletin Database, 2021)**

| Name | Latitude | Longitude | Year | Mass (kg) | Fall/Find | Type | Classification |
|---|---|---|---|---|---|---|---|
| NWA 13742* | - | - | 2020 | 0.272 | Find | Achondrite | Eucrite |
| NWA 13761* | - | - | 2018 | 0.162 | Find | Chondrite | L6§ |
| NWA 13842* | - | - | 2019 | 8.2 | Find | Chondrite | H5 |
| NWA 13951* | - | - | 2021 | 4.3 | Find | Achondrite | Lunar - feldsp. breccia |
| NWA 13954* | - | - | 2020 | 4.5 | Find | Chondrite | AStony-ung |
| NWA 13992* | - | - | 2021 | 1.035 | Find | Achondrite | Lunar - frag. breccia |
| NWA 14022* | - | - | 2018 | 1.635 | Find | Chondrite | L6§ |
| NWA 14106* | - | - | 2017 | 1.39 | Find | Chondrite | H6 |
| Nouakchott | 18.12 | -15.13 | 2008 | 0.309 | Find | Chondrite | L5 |
| Rhall Amane 001 | 23.29 | -10.17 | 2005 | 0.224 | Find | Chondrite | H4 |
| Rhall Amane 002 | 23.39 | -9.94 | 2005 | 0.383 | Find | Chondrite | LL6 |
| Tichit 001 | 18.44 | -10.34 | 2014 | 68 | Find | Chondrite | H5 |
| Zerga | 20.25 | -12.68 | 1973 | 0.076 | Find | Chondrite | LL6 |
| **MAURITIUS** | | | | | | | |

**Table 1-5: Statistics of SSA meteorites with coordinates (decimal degrees) (Meteoritical Bulletin Database, 2021)**

| Name | Latitude | Longitude | Year | Mass (kg) | Fall/Find | Type | Classification |
|---|---|---|---|---|---|---|---|
| Mauritius | -20 | 57 | 1801 | 0,22 | Fall | Chondrite | LL5-6 |
| **NAMIBIA** | | | | | | | |
| Asab | -25.43 | 17.92 | 1999 | 1,53 | Find | Chondrite | H5 |
| Aus | -26.67 | 16.25 | - | 0,03 | Find | Chondrite | L |
| Etosha | -18.5 | 16 | 1970 | 110.7 | Find | Iron | IC |
| Gibeon | -25.5 | 18 | 1836 | 26000 | Find | Iron | IVA |
| Gobabeb | -23.55 | 15.03 | 1969 | 27 | Find | Chondrite | H4 |
| Hoba | -19.58 | 17.92 | 1920 | 60000 | Find | Iron | IVB |
| Itzawisis | -26.27 | 18.18 | 1946 | 0,35 | Find | Stony-Iron | Pallasite, PES |
| Karasburg | -27.67 | 18.97 | 1964 | 12 | Find | Iron | IIIAB |
| Korra Korrabes | -25.2 | 18.08 | 1996 | 140 | Find | Chondrite | H3 |
| Maltahöhe | -24.92 | 16.98 | 1991 | 22.27 | Find | Iron | IAB-sLM |
| Namib Desert | -24.75 | 15.37 | 1979 | 1 | Find | Chondrite | H4 |
| Okahandja | -21.98 | 16.93 | 1926 | 6.58 | Find | Iron | IIAB |

**Table 1-5: Statistics of SSA meteorites with coordinates (decimal degrees) (Meteoritical Bulletin Database, 2021)**

| Name | Latitude | Longitude | Year | Mass (kg) | Fall/Find | Type | Classification |
|---|---|---|---|---|---|---|---|
| Ovambo | -18 | 16 | 1900 | 0,122 | Fall | Chondrite | L6 |
| Rooikop 001 | -23.08 | 14.72 | 1991 | 1,039 | Find | Chondrite | H5 |
| Rooikop 002 | -23.08 | 14.72 | 1991 | 0,903 | Find | Chondrite | L5 |
| Rooikop 003 | -23.08 | 14.72 | 1991 | 0,902 | Find | Chondrite | L4/5 |
| St. Francis Bay | -25.07 | 14.88 | 1976 | 0,532 | Find | Chondrite | L6 |
| Witsand Farm | -28.67 | 18.92 | 1932 | 0,066 | Fall | Chondrite | LL4 |
| **NIGER** | | | | | | | |
| Adrar Bous | 20.5 | 9 | 2001 | 0.36 | Find | Chondrite | EL5 |
| Adrar Chiriet | 19.64 | 9.36 | 2003 | 0.926 | Find | Chondrite | L6 |
| Adrar Madet | 18.5 | 10.4 | 1997 | 1.113 | Find | Chondrite | H5/6 |
| Adrar Madet 002 | 18.61 | 10.49 | 2002 | 2.2 | Find | Chondrite | LL3 |
| Adrar Yaouelt | 17.68 | 10.04 | 2002 | 2.73 | Find | Chondrite | H5 |
| Aïr | 19.08 | 8.38 | 1925 | 24 | Fall | Chondrite | L6 |
| Areshima | 18.21 | 10.18 | 1999 | 0.114 | Find | Chondrite | LL3.7 |

**Table 1-5: Statistics of SSA meteorites with coordinates (decimal degrees) (Meteoritical Bulletin Database, 2021)**

| Name | Latitude | Longitude | Year | Mass (kg) | Fall/Find | Type | Classification |
|---|---|---|---|---|---|---|---|
| Arlit | 18.67 | 7.34 | 2002 | 0.0201 | Find | Chondrite | H5 |
| Assamakka | 19.27 | 5.92 | 2002 | 4.4 | Find | Iron | IVA-an |
| Birni N'konni | 13.77 | 5.3 | 1923 | 0.56 | Fall | Chondrite | H4 |
| Capot Rey | 20.13 | 10.21 | 2004 | 38 | Find | Chondrite | H5 |
| Dosso | 13.05 | 3.17 | 1962 | 1.25 | Fall | Chondrite | L6 |
| Gouchi 001 | 13.82 | 9 | 2019 | 0.189 | Find | Chondrite | R4 |
| Grein 001 | 21.23 | 10.76 | 1997 | 0.71 | Find | Chondrite | H3 |
| Grein 002 | 20.71 | 11.12 | 1997 | 0.609 | Find | Chondrite | EL4/5 |
| Grein 003 | 20.57 | 11.35 | 1997 | 0.491 | Find | Chondrite | H6 |
| Grein 005 | 20.1 | 10.62 | 2015 | 52.5 | Find | Iron | IIIAB |
| Maigatari-Danduma | 12.83 | 9.38 | 2004 | 4.63 | Fall | Chondrite | H5/6 |
| Mount Tazerzait | 18.7 | 4.8 | 1991 | 110 | Fall | Chondrite | L5 |
| Niger (C2)* | - | - | 1969 | 0.02 | Find | Chondrite | CM2 |
| Niger (L6)* | - | - | 1967 | 0.003 | Fall | Chondrite | L6 |

**Table 1-5: Statistics of SSA meteorites with coordinates (decimal degrees) (Meteoritical Bulletin Database, 2021)**

| Name | Latitude | Longitude | Year | Mass (kg) | Fall/Find | Type | Classification |
|---|---|---|---|---|---|---|---|
| Niger (LL6)* | - | - | 1967 | 0.003 | Fall | Chondrite | LL6 |
| NWA 12322* | - | - | 2018 | 35.3 | Find | Chondrite | CV3 |
| NWA 12484* | - | - | 2018 | 1.1 | Find | Chondrite | L3 |
| NWA 12607* | - | - | 2019 | 15.2 | Find | Chondrite | H~5§ |
| NWA 12608* | - | - | 2019 | 4.46 | Find | Chondrite | H~6§ |
| NWA 12609* | - | - | 2019 | 0.61 | Find | Chondrite | H~5§ |
| NWA 12610* | - | - | 2019 | 0.385 | Find | Chondrite | H~5§ |
| NWA 12611* | - | - | 2019 | 0.355 | Find | Chondrite | L~6§ |
| NWA 12612* | - | - | 2019 | 0.43 | Find | Chondrite | L~6§ |
| NWA 12613* | - | - | 2019 | 0.32 | Find | Chondrite | H~5§ |
| NWA 12614* | - | - | 2019 | 0.31 | Find | Chondrite | H~5§ |
| NWA 12615* | - | - | 2019 | 0.185 | Find | Chondrite | L~5§ |
| NWA 12616* | - | - | 2019 | 0.275 | Find | Chondrite | H~5§ |
| NWA 12617* | - | - | 2019 | 0.25 | Find | Chondrite | L~6§ |

**Table 1-5: Statistics of SSA meteorites with coordinates (decimal degrees) (Meteoritical Bulletin Database, 2021)**

| Name | Latitude | Longitude | Year | Mass (kg) | Fall/Find | Type | Classification |
|---|---|---|---|---|---|---|---|
| NWA 12618* | - | - | 2019 | 0.35 | Find | Chondrite | L~6§ |
| NWA 12619* | - | - | 2019 | 0.15 | Find | Chondrite | H~5§ |
| NWA 12620* | - | - | 2019 | 0.085 | Find | Chondrite | H~5§ |
| NWA 12621* | - | - | 2019 | 0.3 | Find | Chondrite | H~5§ |
| NWA 12622* | - | - | 2019 | 36.1 | Find | Chondrite | L~6§ |
| NWA 12831* | - | - | 2019 | 0.151 | Find | Achondrite | Lunar - fedsp. breccia |
| NWA 12923* | - | - | 2017 | 5.5 | Find | Chondrite | H5-melt breccia |
| NWA 12924* | - | - | 2018 | 5.7 | Find | Chondrite | H5-melt breccia |
| NWA 13006* | - | - | 2019 | 3.96 | Find | Iron | IIIAB |
| NWA 13132* | - | - | 2017 | 180 | Find | Chondrite | L5/6 |
| NWA 13219* | - | - | 2019 | 0.113 | Find | Achondrite | Eucrite-cm |
| NWA 13248* | - | - | 2018 | 70 | Find | Chondrite | H5-melt breccia |
| NWA 13281* | - | - | 2019 | 50 | Find | Chondrite | L5 |
| NWA 13579* | - | - | 2019 | 0.719 | Find | Stony-Iron | Pallasite |

**Table 1-5: Statistics of SSA meteorites with coordinates (decimal degrees) (Meteoritical Bulletin Database, 2021)**

| Name | Latitude | Longitude | Year | Mass (kg) | Fall/Find | Type | Classification |
|---|---|---|---|---|---|---|---|
| NWA 13756* | - | - | 2020 | 0.201 | Find | Chondrite | R4 |
| NWA 14010* | - | - | 2018 | 1.085 | Find | Chondrite | CV3 |
| NWA 14170* | - | - | 2019 | 0.141 | Find | Chondrite | LL7 |
| NWA 14171* | - | - | 2020 | 0.271 | Find | Chondrite | L-melt rock |
| NWA 14187* | - | - | 2021 | 0.548 | Find | Chondrite | LL6 |
| Pétèlkolé | 14.05 | 0.42 | 1995 | 0.189 | Fall | Chondrite | H5 |
| Point Berliet | 20.54 | 9.54 | 2001 | 42 | Find | Chondrite | H5 |
| Séguédine | 20.82 | 12.97 | 2002 | 0.444 | Find | Chondrite | H6 |
| Tafassasset | 20.76 | 10.44 | 2000 | 114 | Find | Chondrite | AStony-prim |
| Tassédet 001 | 18.07 | 6.67 | 2001 | 0.56 | Find | Chondrite | H5 |
| Tassédet 002 | 18.24 | 6.52 | 2001 | 0.009 | Find | Chondrite | H5 |
| Tassédet 003 | 18.3 | 6.51 | 2001 | 0.013 | Find | Chondrite | H5 |
| Tassédet 004 | 18.68 | 7.4 | 2016 | 405 | Find | Chondrite | H5-melt breccia |
| Tassédet 005 | 18.83 | 7 | 2018 | 50 | Find | Chondrite | L6 |

**Table 1-5: Statistics of SSA meteorites with coordinates (decimal degrees) (Meteoritical Bulletin Database, 2021)**

| Name | Latitude | Longitude | Year | Mass (kg) | Fall/Find | Type | Classification |
|---|---|---|---|---|---|---|---|
| Tazizilet | 17.64 | 9.44 | 2006 | 0.996 | Find | Chondrite | L5 |
| Tiffa 001 | 19.95 | 11.93 | 1997 | 26.9 | Find | Chondrite | H5 |
| Tiffa 002 | 19.7 | 11.53 | 1997 | 4.71 | Find | Chondrite | H4/5 |
| Tiffa 003 | 20.01 | 11.87 | 1997 | 0.329 | Find | Chondrite | L6 |
| Tiffa 004 | 19.96 | 11.88 | 1997 | 1.362 | Find | Chondrite | H5 |
| Tiffa 005 | 19.92 | 11.88 | 1997 | 0.327 | Find | Chondrite | H5 |
| Tiffa 006 | 19.91 | 11.88 | 1997 | 0.56 | Find | Chondrite | H5 |
| Tiffa 007 | 20.2 | 11.59 | 2001 | 9.25 | Find | Chondrite | H5 |
| Tiffa 008 | 20.36 | 11.85 | 2001 | 1.149 | Find | Chondrite | CO3 |
| Tiffa 022 | 19.49 | 10.59 | 2021 | 0.729 | Find | Stony-Iron | Mesosiderite |
| Tillaberi | 14.25 | 1.53 | 1970 | 3 | Fall | Chondrite | L6 |
| Timmersoi | 18.92 | 6.25 | 1966 | 0.516 | Find | Chondrite | L5 |
| Zinder | 13.78 | 8.97 | 1999 | 0.046 | Find | Stony-Iron | Pallasite, ungrouped |
| Zinder 003* | - | - | 2019 | 0.803 | Find | Achondrite | Eucrite-melt breccia |

**Table 1-5: Statistics of SSA meteorites with coordinates (decimal degrees) (Meteoritical Bulletin Database, 2021)**

| Name | Latitude | Longitude | Year | Mass (kg) | Fall/Find | Type | Classification |
|---|---|---|---|---|---|---|---|
| **NIGERIA** | | | | | | | |
| Aba Panu | 8.28 | 3.57 | 2018 | 160 | Fall | Chondrite | L3 |
| Akwanga | 8.92 | 8.43 | 1959 | 3 | Fall | Chondrite | H5 |
| Bununu | 10.02 | 9.58 | 1942 | 0.357 | Fall | Achondrite | Howardite |
| Demsa | 9.46 | 12.15 | 2006 | 5 | Fall | Chondrite | H6 |
| Gashua | 12.85 | 11.03 | 1984 | 4.16 | Fall | Chondrite | L6 |
| Geidam | 12.92 | 11.92 | 1950 | 0.725 | Fall | Chondrite | H5 |
| Git-Git | 9.6 | 9.92 | 1947 | 0.48 | Fall | Chondrite | L6 |
| Goronyo | 13.27 | 5.4 | 2001 | 11 | Find | Chondrite | H4 |
| Gujba | 11.49 | 11.66 | 1984 | 100 | Fall | Chondrite | CBa |
| Kabo | 11.85 | 8.22 | 1971 | 13.4 | Fall | Chondrite | H4 |
| Karewar | 12.9 | 7.15 | 1949 | 0.18 | Fall | Chondrite | L6 |
| Katagum | 11.33 | 10.08 | 1999 | 1.5 | Fall | Chondrite | L6 |
| Kilabo | 12.77 | 9.8 | 2002 | 19 | Fall | Chondrite | LL6 |

**Table 1-5: Statistics of SSA meteorites with coordinates (decimal degrees) (Meteoritical Bulletin Database, 2021)**

| Name | Latitude | Longitude | Year | Mass (kg) | Fall/Find | Type | Classification |
|---|---|---|---|---|---|---|---|
| Mayo Belwa | 8.97 | 12.08 | 1974 | 4.85 | Fall | Achondrite | Aubrite |
| Ohuma | 6.75 | 8.5 | 1963 | 7.7 | Fall | Chondrite | L5 |
| Oyo | 7.88 | 3.96 | 2019 | 1.975 | Find | Chondrite | LL4 |
| Richa | 10 | 9 | 1960 | 1.5 | Find | Iron | IID |
| Sokoto | 13.01 | 5.25 | 2008 | 30 | Fall | Iron | IIIAB |
| Udei Station | 7.95 | 8.08 | 1927 | 103 | Fall | Iron | IAB-ung |
| Uwet | 5.28 | 8.25 | 1903 | 54 | Find | Iron | IIAB |
| Zagami | 11.73 | 7.08 | 1962 | 18 | Fall | Achondrite | Martian - Shergottite |
| **RWANDA** | | | | | | | |
| Ruhobobo | -1.45 | 29.83 | 1976 | 466 | Fall | Chondrite | L6 |
| **SOMALIA** | | | | | | | |
| Bur-Gheluai | 5 | 48 | 1919 | 120 | Fall | Chondrite | H5 |
| El Ali | 4.29 | 44.9 | 2020 | 15200 | Find | Iron | IAB Complex |
| Ergheo | 1.17 | 44.17 | 1889 | 20 | Fall | Chondrite | L5 |

**Table 1-5: Statistics of SSA meteorites with coordinates (decimal degrees) (Meteoritical Bulletin Database, 2021)**

| Name | Latitude | Longitude | Year | Mass (kg) | Fall/Find | Type | Classification |
|---|---|---|---|---|---|---|---|
| Uegit | 3.82 | 43.33 | 1921 | 252 | Find | Iron | IIIAB |
| **SOUTH AFRICA** | | | | | | | |
| Bellsbank | -28.08 | 24.08 | 1955 | 38 | Find | Iron | IIG |
| Benoni | -26.17 | 28.42 | 1943 | 3.88 | Fall | Chondrite | H6 |
| Bowden | -33 | 26.4 | 1907 | 0,603 | Find | Chondrite | H5 |
| Britstown | -30.58 | 23.55 | 1910 | 0,544 | Find | Iron | IAG-ung |
| Bulls run* | - | - | 1964 | 2.25 | Fall | Iron | Iron? |
| Cape of Good Hope | -33.5 | 26 | 1793 | 136 | Find | Iron | IVB |
| Christiana | -27.9 | 25.15 | 2004 | 127.9 | Find | Iron | IVA |
| Cold Bokkeveld | -33.13 | 19.38 | 1838 | 5.2 | Fall | Chondrite | CM2 |
| Cronstad | -27.7 | 27.3 | 1877 | 3.65 | Fall | Chondrite | H5 |
| Daniel’s Kuil | -28.2 | 24.57 | 1868 | 1,064 | Fall | Chondrite | EL6 |
| De Hoek | -29.38 | 23.1 | 1960 | 20.93 | Find | Iron | Ungrouped |
| Deelfontein | -30.18 | 23.27 | 1932 | 28 | Find | Iron | IAB-MG |

**Table 1-5: Statistics of SSA meteorites with coordinates (decimal degrees) (Meteoritical Bulletin Database, 2021)**

| Name | Latitude | Longitude | Year | Mass (kg) | Fall/Find | Type | Classification |
|---|---|---|---|---|---|---|---|
| Diep Rivier | -33.75 | 18.57 | 1906 | 1 | Fall | Chondrite | L6 |
| Ellisras | -23.83 | 27.92 | 1970 | 2.07 | Find | Iron | Iron |
| Hex River Mountains | -33.32 | 19.62 | 1882 | 60 | Find | Iron | IIAB |
| Idutywa | -32.1 | 28.33 | 1956 | 3.46 | Fall | Chondrite | H5 |
| Jackalsfontein | -32.5 | 21.9 | 1903 | 48 | Fall | Chondrite | L6 |
| Karee Kloof | -31.6 | 25.8 | 1914 | 92.1 | Find | Iron | IAB-sLL |
| Kokstad | -30.55 | 29.42 | 1884 | 341 | Find | Iron | IIIE |
| Kopjes Vlei | -29.3 | 21.15 | 1914 | 13.6 | Find | Iron | IIAB |
| Kouga Mountains | -33.62 | 24 | 1903 | 1170 | Find | Iron | IIIAB |
| Leeuwfontein | -25.67 | 28.37 | 1912 | 0,46 | Fall | Chondrite | L6 |
| Lichtenberg | -26.15 | 26.18 | 1973 | 4 | Fall | Chondrite | H6 |
| Macibini | -28.83 | 31.95 | 1936 | 1,995 | Fall | Achondrite | Eucrite-pmict |
| Malvern | -29.45 | 26.77 | 1933 | 0,807 | Fall | Achondrite | Eucrite-pmict |
| Maria Linden* | - | - | 1925 | 0,114 | Fall | Chondrite | L4 |

**Table 1-5: Statistics of SSA meteorites with coordinates (decimal degrees) (Meteoritical Bulletin Database, 2021)**

| Name | Latitude | Longitude | Year | Mass (kg) | Fall/Find | Type | Classification |
|---|---|---|---|---|---|---|---|
| Merweville | -32.76 | 21.68 | 1977 | 6.97 | Find | Chondrite | L5 |
| Molteno | -31.25 | 26.47 | 1953 | 0,15 | Fall | Achondrite | Howardite |
| Morokweng | -26.37 | 23.52 | 2004 | 0,75 | Find | Chondrite | LL6 |
| Moshesh | -30.1 | 28.72 | | 200 | Find | Chondrite | H |
| Mount Ayliff | -30.82 | 29.35 | 1907 | 13.6 | Find | Iron | IAB-MG |
| Muizenberg | -34.1 | 18.47 | 1880 | 4.61 | Find | Chondrite | L6 |
| Natal* | - | - | 1973 | 0,0014 | Fall | Chondrite | Uncl |
| N'Kandhla | -28.57 | 30.7 | 1912 | 17.2 | Fall | Iron | IID |
| Orange River | -30 | 25 | 1855 | 148.8 | Find | Iron | IIIAB |
| Piquetberg | -32.87 | 18.72 | 1881 | 0,037 | Fall | Chondrite | H |
| Queen's Mercy | -30.12 | 28.7 | 1925 | 7 | Fall | Chondrite | H6 |
| Rateldraai | -28.83 | 21.13 | 1909 | 549 | Find | Iron | IIIAB |
| St. Mark's | -32.02 | 27.42 | 1903 | 13.78 | Fall | Chondrite | EH5 |
| Schaap-Kooi | -32.08 | 21.33 | 1910 | 2.7 | Find | Chondrite | H4 |

**Table 1-5: Statistics of SSA meteorites with coordinates (decimal degrees) (Meteoritical Bulletin Database, 2021)**

| Name | Latitude | Longitude | Year | Mass (kg) | Fall/Find | Type | Classification |
|---|---|---|---|---|---|---|---|
| Simondium | -33.85 | 18.95 | 1907 | 1,6 | Find | Stony-Iron | Mesosiderite-A4 |
| South African Railways* | - | - | 1938 | 47 | Find | Iron | IVA |
| Vaalbult | -29.75 | 22.5 | 1921 | 11.8 | Find | Iron | IAB-MG |
| Victoria West | -31.7 | 23.75 | 1860 | 2.95 | Find | Iron | IAB-sHL |
| Winburg | -28.5 | 27 | 1881 | 50 | Find | Iron | IC-an |
| Witklip Farm | -26 | 30 | 1918 | 0,022 | Fall | Chondrite | H5 |
| Wittekrantz | -32.5 | 23 | 1880 | 2.2 | Fall | Chondrite | L5 |
| **SUDAN** | | | | | | | |
| Al Zarnkh | 13.66 | 28.96 | 2001 | 0.7 | Fall | Chondrite | LL5 |
| Almahata Sitta | 20.75 | 32.41 | 2008 | 3.95 | Fall | Achondrite | Ureilite-an |
| Khor Temiki | 16 | 36 | 1932 | 3.2 | Fall | Achondrite | Aubrite |
| Kidairat | 14 | 28 | 1983 | 100 | Fall | Chondrite | H6 |
| Kingai | 11.63 | 24.68 | 1967 | 0.674 | Fall | Chondrite | H6 |
| New Halfa | 15.37 | 35.68 | 1994 | 12 | Fall | Chondrite | L4 |

**Table 1-5: Statistics of SSA meteorites with coordinates (decimal degrees) (Meteoritical Bulletin Database, 2021)**

| Name | Latitude | Longitude | Year | Mass (kg) | Fall/Find | Type | Classification |
|---|---|---|---|---|---|---|---|
| Northeast Africa 001* | - | - | 2002 | 0.262 | Find | Achondrite | Lunar - Anorth |
| Northeast Africa 006* | - | - | 2016 | 0.7 | Find | Chondrite | L5/6 |
| Umm Ruaba | 13.47 | 31.22 | 1966 | 1.7 | Fall | Chondrite | L5 |
| **TANZANIA** | | | | | | | |
| Chela | -3.67 | 32.5 | 1988 | 2.94 | Fall | Chondrite | H4 |
| Ishinga | -8.93 | 33.8 | 1954 | 1,3 | Fall | Chondrite | H |
| Ivuna | -8.42 | 32.43 | 1938 | 0,705 | Fall | Chondrite | CI1 |
| Karatu | -3.5 | 35.58 | 1963 | 2.22 | Fall | Chondrite | LL6 |
| Malampaka | -3.13 | 33.52 | 1930 | 0,47 | Fall | Chondrite | H |
| Mbosi | -9.12 | 33.07 | 1930 | 16000 | Find | Iron | Ungrouped |
| Ngare Sero | -2.63 | 35.89 | 2017 | 2.23 | Find | Chondrite | L5 |
| Peramiho | -10.67 | 35.5 | 1899 | 0,165 | Fall | Achondrite | Eucrite-mmict |
| Rupota | -10.27 | 38.77 | 1949 | 6 | Fall | Chondrite | L4-6 |
| Ufana | -4.27 | 35.35 | 1957 | 0,189 | Fall | Chondrite | EL6 |

**Table 1-5: Statistics of SSA meteorites with coordinates (decimal degrees) (Meteoritical Bulletin Database, 2021)**

| Name | Latitude | Longitude | Year | Mass (kg) | Fall/Find | Type | Classification |
|---|---|---|---|---|---|---|---|
| **UGANDA** | | | | | | | |
| Awere | 2.72 | 32.83 | 1968 | 0.134 | Fall | Chondrite | L4 |
| Hoima | 1.35 | 31.47 | 2003 | 0.1677 | Fall | Chondrite | H6 |
| Maziba | -1.22 | 30 | 1942 | 4.98 | Fall | Chondrite | L6 |
| Mbale | 1.07 | 34.17 | 1992 | 150 | Fall | Chondrite | L5/6 |
| Mount Moroto | 2.5 | 34.75 | 1995 | 0.752 | Find | Chondrite | L6 |
| Soroti | 33.63 | 1.7 | 1945 | 2.05 | Fall | Iron | Ungrouped |
| **ZAMBIA** | | | | | | | |
| Monze | -15.97 | 27.35 | 1950 | - | Fall | Chondrite | L6 |
| **ZIMBABWE** | | | | | | | |
| Mafuta | -16.9 | 30.41 | 1984 | 71.5 | Find | Iron | IID |
| Magombedze | -19.48 | 31.65 | 1990 | 0,667 | Fall | Chondrite | H3-5 |
| Mangwendi | -17.65 | 31.6 | 1934 | 22.3 | Fall | Chondrite | LL6 |
| Nkayi | -18.93 | 28.6 | 2009 | 100 | Fall | Chondrite | L6 |

*Without coordinates in the Meteoritical Bulletin Database (2021)